Feedback from deeply embedded low- and high-mass protostars

Surveying hot molecular gas with *Herschel*

Universiteit Leiden

Feedback from deeply embedded low- and high-mass protostars

Surveying hot molecular gas with *Herschel*

PROEFSCHRIFT

ter verkrijging van
de graad van Doctor aan de Universiteit Leiden,
op gezag van de Rector Magnificus prof. mr. C. J. J. M. Stolker,
volgens besluit van het College voor Promoties
te verdedigen op woensdag 24 september 2014
klokke 11.15 uur

door

Agata Karska
geboren te Inowrocław, Polen
op 8 juni 1985

Promotiecommissie

Promotor: Prof. dr. E. F. van Dishoeck   Leiden University,
                                                         Max-Planck-Institut für extraterrestrische Physik
Co-Promotor: Dr. G. J. Herczeg   Kavli Institute, Beijing

Overige leden: Prof. dr. A. G. G. M. Tielens   Leiden University
                              Prof. dr. H. J. A. Röttgering   Leiden University
                              Prof. dr. P. Caselli   Max-Planck-Institut für extraterrestrische Physik
                              Prof. dr. N. J. Evans II   University of Texas
                              Dr. B. Nisini   Istituto Nazionale di Astrofisica (INAF), Rome
                              Dr. E. Sturm   Max-Planck-Institut für extraterrestrische Physik

Dedicated to the entire PACS team

Cover: Artist's view of low-mass star forming regions.

9 789462 592797

"Ignorancja nasza jest oceanem ogólnoświatowym, zaś wiedza pewna
– pojedynczymi wysepkami na tym oceanie"

– Stanisław Lem
[Our ignorance is like the world's ocean, while our limited knowledge
– like individual islands on this ocean]

Contents

Introduction

The origin of our Solar System can be studied by observations of currently forming protostars in our Galaxy. Tracing the evolution of protostars that will eventually resemble our Sun is fundamental to understand our own origins. Low-mass stars ($M \sim 0.08$–$1.5\ M_\odot$) dominate the star formation in galaxies both in total mass and number (Kroupa 2002, Chabrier 2003). The less numerous high-mass stars ($M \gtrsim 8\ M_\odot$) strongly influence the formation of low-mass stars via strong radiation, winds, and injection of heavy elements and are therefore equally important to study (Zinnecker & Yorke 2007, Krumholz et al. 2014).

One of the most interesting aspects of star formation is the scale of material condensation needed to form a star: from about ~ 10 particles per cm^3 in the interstellar medium, $\sim 10^4$ cm^{-3} in molecular clouds, $\sim 10^6$ cm^{-3} in dense cores and filaments, to $\sim 10^{24}$ cm^{-3} in stellar cores (Mottram et al. 2013). The gravitational collapse alone is however too efficient by a factor of ~ 20 in forming stars compared to the actual observed star formation rates (Leroy et al. 2008, Evans et al. 2009) and must be slowed down by some combination of turbulence, radiation, outflows, and magnetic fields (Evans 1999, Krumholz et al. 2014).

The inclusion of 'feedback' in simulations of star formation has a profound effect on the accretion, multiplicity, and mass of protostars, with implications for the shape of the initial mass function and formation of star clusters (Offner et al. 2014, Bate et al. 2014, Krumholz 2014). Feedback processes in low- and high-mass star forming regions are associated with high temperatures ($\gtrsim 100$K) and are thus not traced by the emission from cold dust. Instead, the high-temperature gas is being cooled in far-infrared molecular transitions (Goldsmith & Langer 1978). Quantifying this line emission is therefore crucial to identify additional physical processes in the surroundings of young stars and ultimately estimate their impact on the molecular clouds (Bate et al. 2014, Sales et al. 2014) and galaxy formation (Vogelsberger et al. 2014).

Validation of those simulations requires that the basic physical phenomenon are quantitiatively understood: *What are the physical conditions of the gas (temperature, density) in low- and high-mass star forming regions? What are the dominant physical processes responsible for the gas heating (shocks, ultraviolet radiation)? How does the evolution proceed to the point where the envelope is fully dispersed and the stars become visible in the optical light? How does the process differ for stars of different mass?*

Temperatures and densities of the physical regimes involved in the star formation process are best probed by far-infrared lines of in particular CO and H_2O whose excitation depends on the local physical conditions. The combination of excitation studies and spectroscopy at high enough angular resolution presents the ideal tools to quantify which physical mechanisms are responsible for the gas heating.

This thesis presents spectral observations of low- and high-mass star forming regions at different evolutionary stages using the PACS instrument (Poglitsch et al. 2010) on board the 3.5 m *Herschel Space Observatory* (Pilbratt et al. 2010a) that allow us to quantify the far-infrared emission at unprecedented detail and shed new light on the feedback from deeply embedded protostars.

Table 1.1 – Physical characteristics of interstellar and circumstellar clouds

Name	Density (cm^{-3})	Temperature (K)	Extinction (mag)	Examples
Diffuse cloud	10^2	30-100	1	ζ Oph
Translucent cloud	10^3	15-50	1-5	HD 154368
Dense PDR	$10^4 - 10^5$	50-500	< 10	Orion Bar
Molecular cloud	10^2	10-20	> 10	Perseus cloud
Dense core	$\gtrsim 10^5$	8-15	10-100	L1544
Protostellar envelope				
low-mass	$10^4 - 10^6$	8-100	10-100	L 1527
high-mass	10^4-10^7	20-100	50-500	AFGL 2591

Notes. The table presents typical physical parameters and is based on Table 2 from van Dishoeck et al. (2013), but with envelope parameters split into low- and high-mass protostars based on van der Tak et al. (2000, 2013), Jørgensen et al. (2002), Kristensen et al. (2012). The examples for diffuse and translucent clouds are the objects along their line-of-sight.

1.1 Interstellar medium and sites of star formation

Galaxies are mostly empty volumes with only a small fraction of space filled by stars and their planetary systems (e.g. ~3×10^{-10} of space in Milky Way, Tielens 2010). Everything in between stars is referred to as interstellar medium (ISM). The main visual manifestations of the otherwise hidden ISM are nebulosities seen around some young stars (e.g. reflection nebulae in the Pleiades) and some evolved stars (e.g. planetary nebulae and supernova remnants). In general, the diffuse and cold ISM is best revealed by absorption lines. The youngest stars are formed in the densest condensations of the ISM, which are opaque to visual light and seemingly devoid of stars.

Physical conditions in various clouds in the cold phase of the ISM are summarized in Table 1.1. The regions range from low-density diffuse and translucent clouds to dense photodissociation regions (PDRs, Tielens & Hollenbach 1985), illuminated by far-ultraviolet photons from nearby OB stars (FUV; $6 - 13.6$ eV). Molecular clouds are regions with densities comparable to some PDRs but higher visual extinction (A_V) and thus more efficient UV shielding. The high density, low temperature regions of molecular clouds are dense cores, the sites of star formation. When the collapse begins, most of the material will accumulate in the envelope, the mass reservoir for the forming star(s).

Most stars in our Galaxy form in the Giant Molecular Clouds, which have masses as high as ~ $10^{6.5}$ M$_\odot$ (Rosolowsky 2005) and projected areas of a few 10^3 pc^2 (Solomon et al. 1987). The most local star formation, however, occurs in smaller clouds, like the Perseus molecular cloud with $M \sim 7 \cdot 10^3$ M$_\odot$ and total area of 73 pc^2 (Evans et al. 2014). Even smaller are the Bok globules, clouds with masses of 1-100 M$_\odot$. The most striking common characteristics of those seemingly different environments are the uniform distribution of stellar masses that they form ('initial mass function') and the small number of stars formed given the available reservoir of gas and dust (Bastian et al. 2010). The star formation efficiency, defined as a fraction of stellar mass to the total mass in the cloud and

stars, is only about 3-6% in the nearby molecular clouds (Padoan et al. 2014).

Simulations of molecular clouds reproduce the shape of initial mass function and low star formation efficiencies when feedback from protostars is included (Krumholz et al. 2014). For example, feedback from outflows driven by low-mass protostars adds turbulence to the cloud, while UV heating suppresses the fragmentation and slows down the infall of material onto the protostar (Offner et al. 2014, Bate et al. 2014, Krumholz 2014). On the other hand, recent results from extinction mapping and from the 'Herschel Gould Belt Survey' show large similarities between the stellar and pre-stellar core mass functions (within a factor of 3), suggesting that no additional physical processes are required, i.e. the role of feedback is not dominant (Alves et al. 2007, André et al. 2010, 2014). A better understanding of physics and chemistry in the immediate surroundings of protostars is therefore needed to resolve these discrepant results and link the star formation on local and global scales.

1.2 Evolution before the main sequence

1.2.1 From dense cores to stars and planets

Figure 1.1 illustrates the key phases of low-mass star formation. The star formation begins once enough cold material condenses in the dense core, leading to its collapse under self-gravity (i.e. the criteria for Jeans instability are satisfied, Jeans 1928). Larson (1969) first described the main stages of this collapse, in particular the *Initial isothermal phase* when, due to pressure gradients, the small region with high density quickly develops in the core center; the *Formation of the opaque core*, where adiabatic collapse leads to the formation of the first hydrostatic core (radius of ~5 AU and mass of ~5 Jupiter masses) and the *Formation of the second (stellar) core*, triggered by dissociation of H_2.

The formation of the stellar core marks the beginning of the Class 0 phase. During this phase, referred to by Larson as the *main accretion phase*, material from the dense envelope is accreted to the star-disk system, quickly increasing the mass of the central protostar. The infall / accretion of material on the rotating protostar in the presence of magnetic fields leads to the launching of bipolar jets in the direction perpendicular to the disk, see recent review by Frank et al. (2014). The collimated jets carve out cavities in the surrounding envelope, exposing the material to the stellar winds and UV photons. As a result, wider-angle bipolar outflows are formed, with shocks and entrainment occurring along the cavity walls. Such a low-mass protostar with its envelope and outflows is altogether referred to as a *young stellar object* (YSO).

The subsequent evolution of a protostar is determined by accretion onto the disk/star system and simultaneous dispersal of the envelope by the outflows (Class I). The UV radiation from the growing central star penetrates deeper into the envelope, while the jets carry less material as the accretion rate decreases and eventually stops. Once the envelope disappears (Class II), a central pre-main sequence star surrounded by a circumstellar disk becomes visible. The gas from the disk is trapped in the giant planets or dispersed by the strong stellar wind and radiation. Subsequently, the grains in the disk coagulate to larger
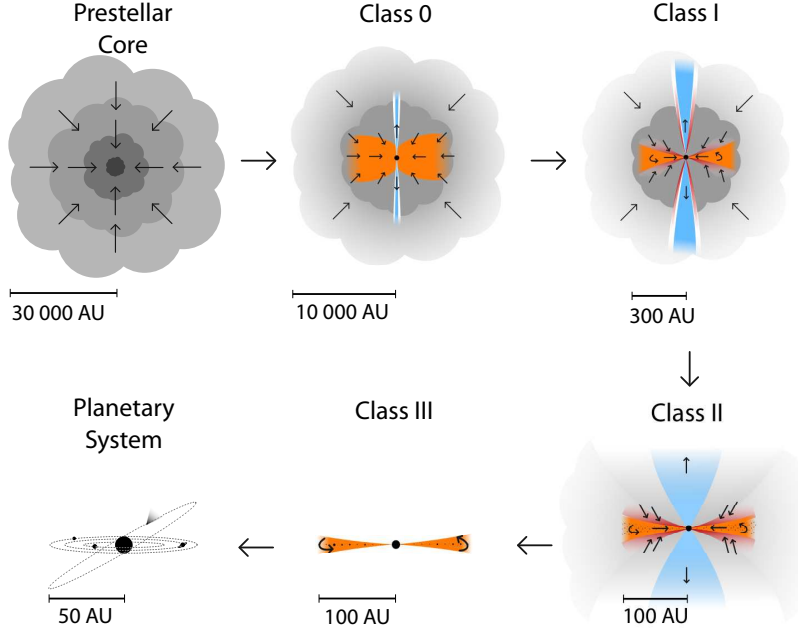
Figure 1.1 – Evolution of a collapsing dense core to a Sun-like star with a planetary system. The physical scales are indicated for each evolutionary stage. Adapted from Persson (2013).

particles, leading to the planetesimal and planet formation (Class III).

The evolution of protostars is therefore driven by the relative amount of mass in the envelope (M_{env}), central protostar ($M_\star$), and the disk (M_{disk}). Physical classification based on the masses distinguishes four main Stages ((0-III), Robitaille et al. 2006, 2007) that ideally should correspond to more phenomenological Classes used in this thesis and in Figure 1.1. In the Stage 0 sources the envelope mass is much larger than that of the central protostar, $M_{env} \gg M_\star$. In Stage I, the envelope mass becomes less than the mass of the protostar, $M_\star > M_{env}$. In Stage II, the disk mass is larger than that of the envelope, $M_{disk} > M_{env}$. Unfortunately, determining masses directly from observations is difficult (Crapsi et al. 2008) and therefore alternative methods of classification have been developed.

1.2.2 Observational classification of young stellar objects

The evolution of young stellar objects is revealed by the shapes of their spectral energy distributions (SEDs). The SEDs of Class 0 sources are dominated by emission from cold dust, whereas the contribution from the star-disk system increases gradually in more evolved Class I/II sources (Figure 1.2 and Chapter 2). Several methods are used to quan-
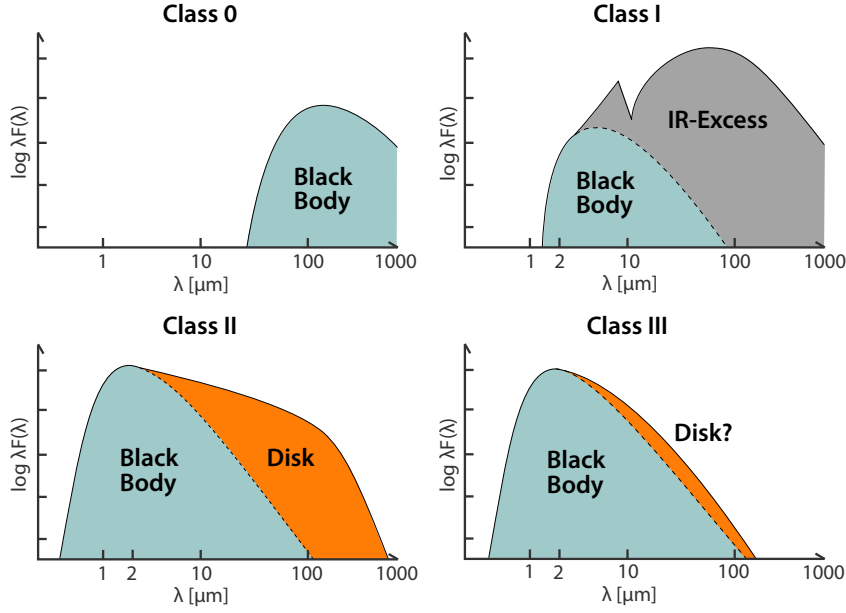
Figure 1.2 – Spectral energy distributions of low-mass young stellar objects. Class 0 sources are characterized by a single black-body spectrum from the cold envelope peaking at ~100 μm (no emission in near-IR). Class I sources have lower extinction and thus a protostellar black body spectrum slowly appears in the near-IR with a large IR excess ('rising SED') at longer wavelengths due to the remaining envelope and growing disk. Class II sources have flat or falling SEDs consisting of a pre-main sequence (T Tauri) stellar black-body and disk emission at mid- to far-IR. Class III sources show a stellar spectrum (more luminous than the main-sequence stars) with a possible weak contribution from the remaining disk. Figure by M. Persson.

tify the SEDs and construct the age sequences of protostars (for detailed discussion, see Evans et al. 2009).

Their main shortcoming is the uncertainty in the outflow/disk geometry, which can severely alter the shape of the SED. For example, when the disk is viewed face-on, mid-IR emission is easily detected by looking down the outflow cone, mimicking the more evolved sources. On the other hand, the edge-on disks hide the protostellar contribution, and the SED is thus dominated by the cold envelope making the source appear less evolved.

Table 1.2 summarizes how Class 0 and I sources are defined using different classification methods. The method based on the spectral index, α, introduced by Lada & Wilking (1984) and extended by Greene et al. (1994), uses the SED between 2 and 20 μm and is not suitable for classification of Class 0 sources. Bolometric temperature, T_{bol}, defined as the temperature of a blackbody with the same flux-weighted mean frequency as the actual SED, is calculated over the entire spectrum and divides sources into Class 0 and I at 70

Table 1.2 – Classification of Class 0/I protostars

Method	Class 0	Class I	Reference
α^a	–	0.3	Lada & Wilking (1984), Greene et al. (1994)
T_{bol}	< 70	$70 < T_{bol} < 650$	Myers & Ladd (1993), Chen et al. (1995)
L_{submm}/L_{bol}	> 200	< 200	André et al. (1993), Young & Evans (2005)
$L_{bol}^{0.6}/M_{env}$	$< 2^b$	2^b	Bontemps et al. (1996)
$L_{FIRL}/L_{bol}{}^c$	$\sim 10^{-2}$	$\sim 10^{-3}$	Giannini et al. (2001), Nisini et al. (2002b)

Notes. [a] Spectral index, $\alpha = d\log(\lambda S(\lambda))/d\log\lambda$, calculated using SED between 2 and 20 μm (λ is the wavelength and $S(\lambda)$ is the flux density at that wavelength). Class 0 sources with SEDs resembling a blackbody spectrum at $T \sim 15 - 30$ K could not be classified in this scheme due to non-detections in mid-IR wavelengths. [b] For a protostar with bolometric luminosity $L_{bol} = 1$ L$_\odot$. [c] Far-infrared line cooling, L_{FIRL}, is the sum of $L_{O_I} + L_{CO} + L_{H_2O} + L_{OH}$.

K (Myers & Ladd 1993). According to models of collapsing cores by Young & Evans (2005), the ratio of source luminosity longwards of 350 μm and its bolometric luminosity is a good indicator of the ratio of mass in the star and the envelope (see also, André et al. 1993); the L_{bol}/L_{submm} ~200 marks the transition from Class 0 to I. A tight correlation between envelope mass and bolometric luminosity in Class 0/I protostars led Bontemps et al. (1996) to describe the evolutionary stage using the $L_{bol}^{0.6}/M_{env}$ ratio.

Far-IR lines are not sensitive to extinction and are often optically thin (e.g. highly-excited CO lines); as such, they provide an alternative to continuum slopes for determining the evolutionary stage. Giannini et al. (2001) introduced a parameter L_{FIRL}, the total line luminosity of species emitting in the far-IR, which decreases for more evolved sources. The underlying assumption was that the dominant excitation mechanism of far-IR emission (most likely outflow shocks) decreases in strength with evolution. If that is indeed the case, L_{FIRL} could serve as the most accurate evolutionary tracer of protostellar evolution.

1.3 Heating and cooling in deeply-embedded protostars

1.3.1 Processes leading to gas heating

Figure 1.3 illustrates the main physical components of low-mass YSOs that can give rise to far-IR line emission. Possible components include (i) the inner part of the envelope heated by the accretion luminosity (hot core); (ii) the entrained outflow gas; (iii) UV-heated gas along the cavity walls; (iv) shocks along the outflow cavity walls where the wind from the young star directly hits the envelope; (v) bow shocks at the tip of the jet where it impacts the surrounding cloud; (vi) internal working surfaces within the jet; and (vii) a disk embedded in the envelope. The contribution of these components to the far-IR emission from deeply-embedded YSOs is evaluated and discussed below.
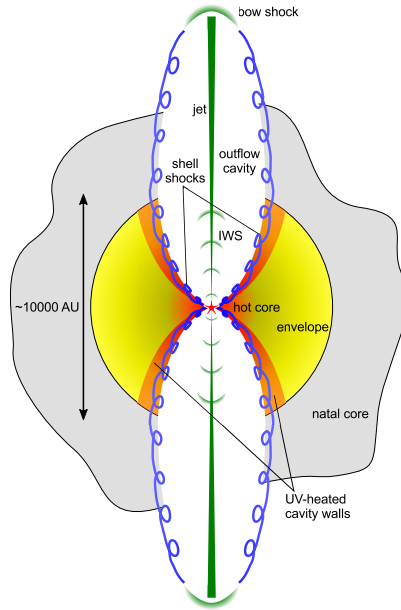
Figure 1.3 – Cartoon of a low-mass young stellar object with various physical components and their nomenclature indicated. IWS stands for internal working surfaces. The spatial scales correspond to low-mass protostars and do not resolve the ~100 AU disk surrounding the protostar. Figure by R. Visser, adapted from van Dishoeck et al. (2011).

1.3.1.1 Envelope heating by protostellar luminosity

The main source of protostellar luminosity during the Class 0/I phase is the *accretion luminosity* produced from the gravitational energy of the infalling gas from the dense collapsing envelope, through the disk, and onto the star in extremely hot ($>10^5$ K) accretion shocks. This luminosity heats mostly the inner parts of the envelope, since the large amount of dust quickly absorbs most of the protostellar radiation and re-radiates it in the form of far-IR continuum. The gas is then heated through gas-dust collisions. However, a fraction of the envelope cooling is also predicted to occur via atoms and molecules (Ceccarelli et al. 1996, Doty & Neufeld 1997, for early models of line emission from low- and high-mass envelopes, respectively).

Far-IR H_2O emission was initially interpreted as arising purely from the collapsing envelope in Class 0/I sources (Ceccarelli et al. 1999) based on the single beam observations ($\sim$ 80″) with the Long-Wavelength Spectrometer on board the *Infrared Space Observatory* (ISO) (Kessler et al. 1996, Clegg et al. 1996). However, small maps with the same instrument revealed that the emission is extended and more likely originates in the outflow (Nisini et al. 1999). Recently, Visser et al. (2012) concluded that the envelope cooling accounts for less than 1% of the total H_2O emission and only a few percent of CO
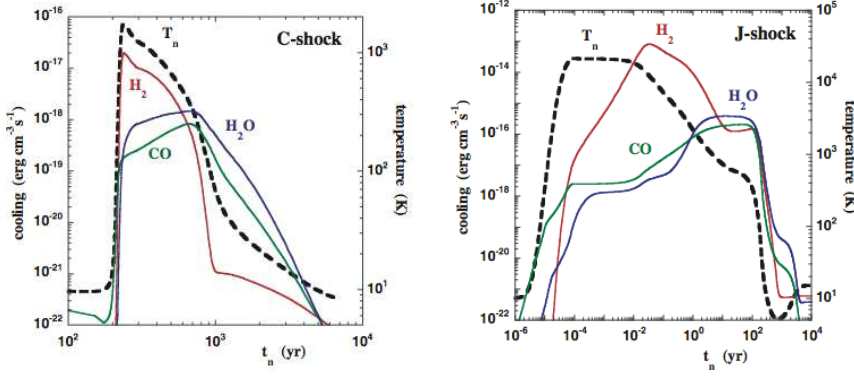
Figure 1.4 – Rates of molecular cooling as a function of flow time of neutrals in $C-$ (left) and $J-$type (right) shocks with v=20 km s^{-1} and pre-shock density of the ambient medium $n = 10^5$ cm^{-3}. The temperature structure through the shock is shown on the right vertical axis. Adapted from Flower & Pineau des Forêts (2010).

emission observed towards low-mass protostars with *Herschel*/PACS.

1.3.1.2 Shocks in outflow cavities and jets

Large-scale shocks are produced by the bipolar jets and protostellar winds impacting the envelope along the cavity walls. Theoretically, shocks are divided into two main types, the 'continuous' (C-type) and 'jump' (J-type) shocks, based on a combination of magnetic field strength, shock velocity, density, and level of ionization (Draine 1980, Draine et al. 1983, Hollenbach et al. 1989, Hollenbach 1997).

In $C-$type shocks, which occur in regions with strong magnetic fields and low ionization fractions, the weak coupling between the ions and neutrals results in a continuous change in the gas parameters (for an example of temperature profile, see Figure 1.4). Peak temperatures of a few 10^3 K allow the molecules to survive the passage of the shock, which is therefore referred to as non-dissociative.

In $J-$type shocks, physical conditions change in a discontinuous way, leading to higher peak temperatures than in C shocks of the same speed and for a given density (Figure 1.4). Depending on the shock velocity, J shocks are either non-dissociative (velocities below about ~ 30 km s^{-1}, peak temperatures of about a few 10^4 K) or dissociative (peak temperatures even exceeding 10^5 K), but the molecules efficiently reform in the dense post-shock gas (Figure 1.4).

Cooling of post-shock gas by H$_2$ is dominant in the outflow shocks, but negligible for lower$-T$ gas due to a lack of low-lying rotational states and the large level spacing in H$_2$ (Goldsmith & Langer 1978). But even in regions with sufficiently high temperatures, mid-IR H$_2$ emission is strongly affected by extinction in the dense envelopes of young protostars (Davis et al. 2008, Maret et al. 2009). The far-IR rotational transitions of H$_2$O

9
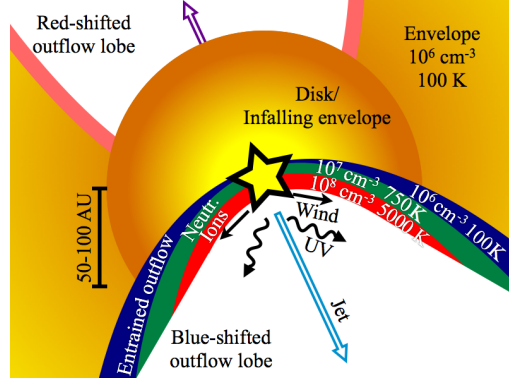
Figure 1.5 – Cartoon illustrating the inner regions of protostellar envelope where UV radiation from the protostar can dissociate the shocked gas and produce high$-J$ CO emission ($J_{up} \gtrsim 24$). Adopted from Kristensen et al. (2013).

and CO are thus a better diagnostic of the shock type, shock velocity, and the pre-shock density of the medium (Hollenbach et al. 1989, Kaufman & Neufeld 1996, Flower & Pineau des Forêts 2010, 2012).

The characteristics of the first complete far-IR spectra of low-mass Class 0/I protostars obtained with ISO /LWS indicated an origin in the two distinct shocks (Giannini et al. 2001, Nisini et al. 2002b). The molecular emission was attributed to the slow, $C-$type shock in the cavity walls and the bright [O I] emission arising from the $J-$type shock in the jet and / or bow-shock. A fraction of the [O I] emission was also attributed to the UV heating from the protostar. The [O I] contribution to the total cooling was higher for the more evolved sources.

This general picture finds support in the recent observations with *Herschel*, even though the details of the shock characteristics are still strongly debated. The [O I] emission is generally explained by $J-$type shocks (van Kempen et al. 2010b, Benedettini et al. 2012, Dionatos et al. 2013, Lee et al. 2013, Santangelo et al. 2013), but a convincing detection of the high velocity component is seen only towards low-mass source HH46 (van Kempen et al. 2010b). The molecular emission is attributed to slow ($v \sim 15 - 40$ km s^{-1}), non-dissociative $C-$ or $J-$type shocks, depending on the assumptions on the (spatially unresolved) size of the emitting region and the exact species (CO, H$_2$O, OH, H$_2$) that are treated together. An alternative explanation for the very high$-J$ CO emission is dissociative shocks due to strong UV irradiation proposed by Kristensen et al. (2013), see Figure 1.5.

1.3.1.3 Ultraviolet heating and gas entrainment in the outflow cavity walls

The first observations of ^{13}CO $J = 6 - 5$ in low-mass protostars showed unexpectedly intense, extended line emission that could not be accounted for by the models of collapsing
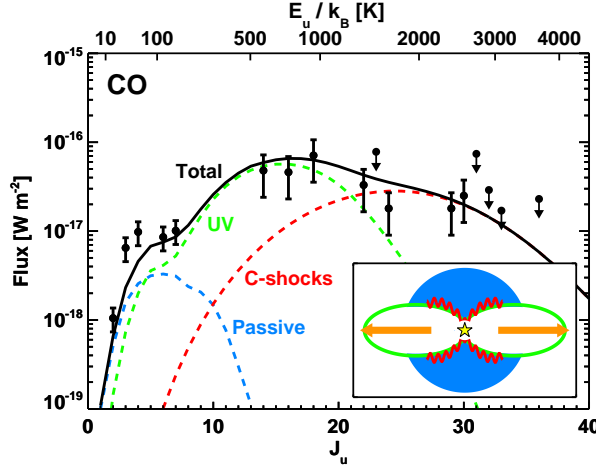
Figure 1.6 – CO fluxes observed with *Herschel* / PACS and APEX telescope (J_u<10) with model predictions from a passively heated envelope (blue), a UV-heated cavity (green), and small-scale shocks in the cavity walls (red). The black line is the sum of the three. A cartoon of the different components is shown in the inset. Adopted from van Kempen et al. (2010b).

envelopes (Spaans et al. 1995, Hogerheijde et al. 1997). Spaans et al. (1995) explained this puzzling excess emission with additional heating of cavity walls by the ultraviolet photons from the ~10,000 K boundary layer where the accretion stream hits the star, scattered in the low-density outflow cavities. van Kempen et al. (2009a) adopted this model to describe the extended CO $J = 6 - 5$ emission in the HH46, but with additional UV photons created in the dissociative J−type shocks originating in the internal working surfaces in the jet and / or in the bow-shock at the tip of the jet (Neufeld & Dalgarno 1989).

The UV heating was subsequently invoked to explain the bulk of CO $J_{up} \sim 10 - 20$ emission detected with *Herschel* / PACS (van Kempen et al. 2010b, Visser et al. 2012). In models of HH 46 (Figure 1.6), 45% of the total CO emission is excited by UV heating, 48% is excited in small scale C−type shocks, and 7% is excited in the passively heated envelope (Visser et al. 2012). Modeling of two additional sources in Visser et al. (2012) showed that the contribution of the UV heating to the total line cooling increases as the protostar evolves, from ~20% in the young Class 0 protostar up to ~80% in Class I/II protostar.

Yıldız et al. (2012) used the velocity-resolved profiles of CO isotopologues to directly measure the amount of gas traced by CO $2 - 1$ to $10 - 9$ lines in the envelope, outflow, and UV heated component (see Figure 1.7). First, the density and temperature gradients in the envelope were modeled using the continuum maps. The narrow $C^{18}O$ line profiles produced in the envelope emission were used to constrain the CO abundance profile in the envelope (following the approach in Jørgensen et al. 2002). Subsequently, the resulting envelope structure was used to calculate the fraction of ^{13}CO emission that arises from
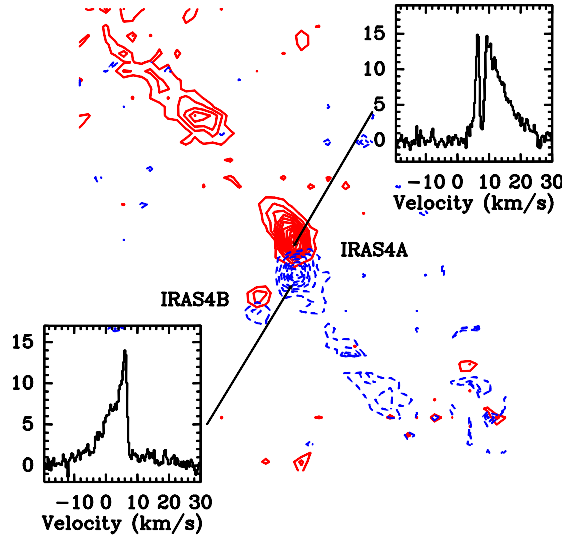
Figure 1.7 – ^{12}CO 6-5 line profiles at the blue and red outflow positions of NGC 1333 IRAS 4A. The integrated emission in the blue (-20 to 2.7 km s^{-1}) and red (10.5 to 30 km s^{-1}) velocity ranges with respect to the source velocity is shown as contours. Figure by U. A. Yıldız, based on Yıldız et al. (2012).

the envelope. The excess emission from the observations was proposed to arise in the UV-heated component (following van Kempen et al. 2009a,b), since the narrow shape of ^{13}CO line profiles and the low abundances of ^{13}CO with respect to the CO made the outflow origin unlikely. The emission in the broad component in the ^{12}CO line was interpreted as arising in the entrained outflow gas with a kinetic temperature of $\sim$ 100 K. The amount of gas mass in the UV-heated and the outflow components was found to be comparable.

1.3.2   Main cooling channels

Any single dust grain located in Class 0/I envelopes absorbs ultraviolet photons from the central protostar, heats up, and then cools by emitting radiation at far-infrared wavelengths. This cooling channel is the dominant source of far-IR continuum radiation. The resulting far-IR continuum is thus an excellent tracer of envelope properties (size, density, temperature) that can be derived from simple modified blackbody fitting (e.g. Goicoechea et al. 2012) or more complicated radiative transfer models (e.g. Young & Evans 2005, Kristensen et al. 2012). On the other hand, the dust emission does not trace the warm gas of young stellar objects that is heated directly by shocks or the photoelectric effect in other physical components and can only be studied using lines.

Goldsmith & Langer (1978) made the first predictions of molecular and atomic line emission from dense interstellar clouds. Although the knowledge of abundances of vari-
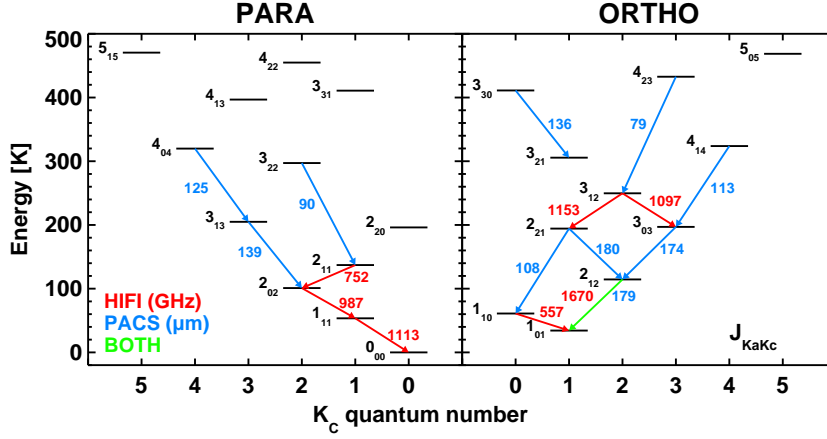
Figure 1.8 – Energy levels of ortho- and para-H_2O with some important transitions observed in the WISH program with *Herschel* / PACS (in μm) and *Herschel* / HIFI (in GHz) indicated (adopted from van Dishoeck et al. 2011). In fact, as many as ~ 65 H_2O lines were detected with PACS in NGC 1333 IRAS 4B (Herczeg et al. 2012).

ous species was scarce, the models based on the energy level structure, Einstein coefficient for spontaneous emission (A), and the collision rate coefficients were mostly correct. For densities $\gtrsim 10^4$ cm^{-3} and $T \sim 10$ K, a large number of species including H_2O, hydrides (e.g. OH), molecular ions (emitting in the sub-millimeter regime), and diatomic molecules (e.g. CO) dominated the total line cooling. Neufeld & Kaufman (1993) extended these predictions to warmer gas ($T \gtrsim 100$) of similar densities, focusing on H_2, H_2O, and CO, and suggested that H_2O may be even the dominant coolant in such gas if its predicted high abundances are correct. The other reasons for the dominant role of H_2O, CO, and a possible importance of OH, in gas cooling are discussed below.

1.3.2.1 H_2O

The routes of H_2O formation include ion-molecule reactions at $T \sim 10$ K, very efficient high temperature neutral-neutral reactions in shocked gas ($T \gtrsim 230$ K), and formation on the grains (ice abundances as high as 10^{-4}) followed by evaporation into the gas phase at $T \sim 100$ K (van Dishoeck et al. 2011, 2013). In dense and relatively warm environments of young protostars, the abundances of H_2O are expected to be high.

H_2O is an asymmetric rotor molecule with a large number of energy levels contributing to the total cooling (Figure 1.8). Rotational levels are characterized by rotational quantum number J and two additional quantum numbers K_A and K_C, which relate to the projection of the angular momentum on the axes of symmetry. The nuclear spins of the two hydrogen atoms can be either parallel or anti-parallel, resulting in a grouping of the rotational levels into ortho ($K_A + K_C$ = odd) and para ($K_A + K_C$ = even) ladders.

13

The large dipole moment (μ_D=1.85 D) of H_2O and the high frequencies (ν) of the transitions result in relatively large spontaneous radiative rates compared to other molecules, proportional to $\mu_D^2 \nu^3$ (Einstein A coefficients). Therefore, H_2O is de-excited by line emission (radiation) and not by collisions in protostellar envelopes, where densities are a few orders of magnitude lower than the critical density needed for thermalization. That implies that the level population typically cannot be described by a Boltzmann distribution at the gas kinetic temperature; the rotational temperature calculated based on H_2O lines is therefore set by a combination of the temperature and density.

Giannini et al. (2001) first quantified the role of H_2O in the total gas cooling in Class 0 protostars using the complete far-infrared spectra obtained with ISO/LWS. H_2O, CO, and [O I] were found to contribute each $\sim$ 30% of the total gas cooling, with the remaining emission originating in OH. Nisini et al. (2002b) extended this study to Class I sources and demonstrated a decrease in molecular cooling as a protostar evolves.

1.3.2.2 CO

CO is the second most abundant molecule in the ISM after H_2 ($CO/H_2 = 10^{-4}$) with level energies scaling as $\propto J(J + 1)$ (Figure 1.9). Due to the relatively high mass of the molecule the levels are closely spaced, with the few lowest$-J$ transitions lying at sub-/mm wavelengths and $J \gtrsim 10$ in the far-IR. In contrast to H_2O, CO has a very small dipole moment (μ_D=0.1 D) and its low$-J$ transitions are easily collisionally excited even at low densities, providing a better diagnostic of gas kinetic temperature.

CO lines with upper levels as high as J_{up} = 49 and 36 CO lines in total have been detected with *Herschel*/PACS towards low-mass young stellar objects (Herczeg et al. 2012, Goicoechea et al. 2012, Green et al. 2013, Manoj et al. 2013). Such a large number of transitions contribute a significant fraction of the total line cooling, but can also prove useful in determining the physical conditions of gas (its temperature and density) in young protostars. In fact, many protostars observed with PACS show CO emission at two (rotational) temperatures, $\sim$ 350 K and $\gtrsim$ 700 K, suggesting that the origin is in two distinct physical components (van Kempen et al. 2010b, Visser et al. 2012). Alternatively, the origin is in a single low-density, hot component (Neufeld 2012, Manoj et al. 2013). In either case, the physical origin(s) is not yet fully understood.

1.3.2.3 OH

OH is a free radical i.e., it has one unpaired electron, and thus its energy levels are divided into two ladders corresponding to opposite orientations of the unpaired electron spin with respect to Λ, the projection of angular momentum on the molecular axis (Figure 1.9). The levels are further split into two configurations, depending on whether the symmetry axis of the unpaired electron orbital motion is coincident or orthogonal to the internuclear axis (Λ-doubling). The interaction between the spins of the unpaired electron and the hydrogen nucleus results in magnetic hyperfine splitting (Tennyson 2005).

Although the OH abundances are not as high as those of CO, the cooling in OH can be important in regions where the high temperature route of H_2O formation is at play (at

14
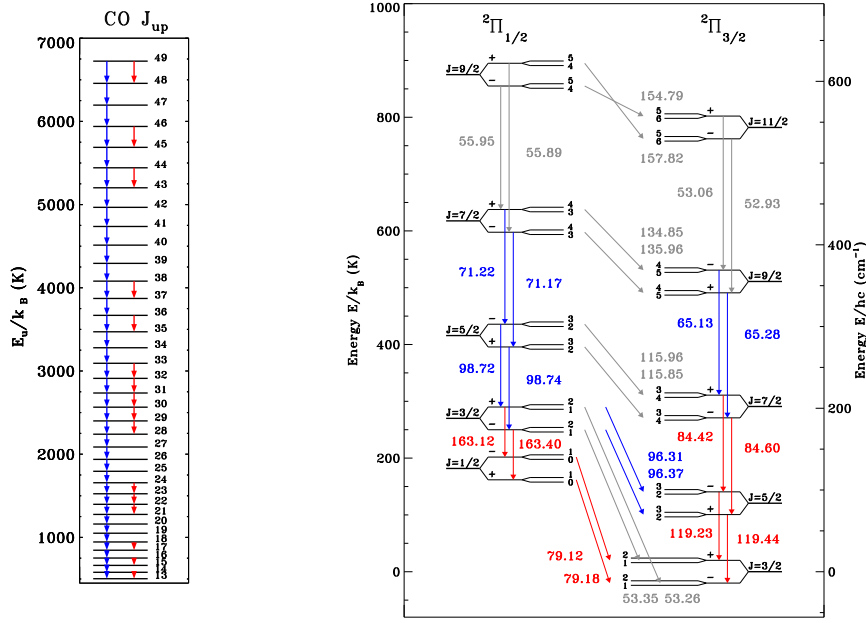
Figure 1.9 – Energy levels of CO (right) and OH (left) observed with *Herschel* / PACS. Blue arrows indicate transitions detected towards low-mass protostars in the full-spectrum mode, while red arrows indicate the lines targeted and detected towards most sources in the WISH program. The OH diagram is adopted from Wampfler et al. (2013).

$T \gtrsim 230$ K). The backward reaction leading to the H_2O destruction and OH formation requires hydrogen in the atomic form and therefore depends on the local UV field or presence of dissociative shocks (Wampfler et al. 2013). These conditions can occur in $J-$type shocks along the jet or in a bow shock or in UV-irradiated cavity shocks in low-mass young stellar objects and thus explain the relatively large OH cooling, $\sim 3\%$ in Class 0 and $\sim 20\%$ in Class I sources (this thesis, Karska et al. 2013).

1.4   *Herschel* / PACS

Herschel was a 3.5 m space telescope operating from mid-2009 to mid-2013 at the L2 point located $1.5 \; 10^9$ m 'behind' the Earth as viewed from the Sun (Pilbratt et al. 2010a). The telescope was equipped with three complementary instruments designed for observations at the far-infrared and submillimeter wavelengths:

- HIFI – the Heterodyne Instrument for the Far-Infrared (de Graauw et al. 2010) –

15

a single pixel heterodyne spectrometer observing at 480-1910 GHz (157-625 μm) with very high spectral resolving power, R= $\lambda/\Delta\lambda \gtrsim 10^6$ (d$v \sim 0.1$ km s^{-1}) and diffraction limited beam of ~11-45".

- PACS – the Photodetector Array Camera and Spectrometer (Poglitsch et al. 2010) – consists of two subinstruments: an imaging photometer and an integral-field spectrometer, both sensitive to emission at $50-210\,\mu$m with blue and red bands observed simultaneously. The photometer consisted of two bolometer arrays with 16×32 and 32×64 pixels covering a field of view 1.75'×3.5' in the 60-85 μm / 85-125 μm and 125-210 μm bands. The spectrometer consisted of a 5×5 array of spaxels, each corresponding to 9.4"×9.4" on the sky, and a total field of view of 47"×47". The spectral resolving power is R~ $1000 - 5500$ (d$v \sim 60 - 320$ km s^{-1}) depending on the grating order.

- SPIRE – the Spectral and Photometric Imaging Receiver (Griffin et al. 2010) – an imaging photometer and an imaging Fourier transform spectrometer observing at 194-672 μm with spectral resolution R~ $40 - 1000$ at 250 μm.

A more detailed description of the PACS spectrometer and its comparison to the Long Wavelength Spectrometer on ISO are presented in the following sections.

1.4.1 PACS spectrometer

The key scientific goal of the PACS spectrometer was to provide medium resolution observations (R~ 1500) of weak spectral lines on top of a much stronger far-infrared continuum, particularly of extragalactic sources (Poglitsch et al. 2010). In order to achieve the required sensitivity, but also the sufficient baseline coverage and high tolerance to pointing errors without compromising spatial resolution, the integral-field unit (IFU) design was selected.

In the PACS IFU spectrometer, the two dimensional image from the 5×5 array is transformed by the image slicer into a one dimensional entrance slit for the grating spectrometer, as illustrated in Figure 1.10. The spectrometer consists of two Ge:Ga photoconductors arrays (for blue and red bands) with 16 spectral elements and 25 spatial pixels (*spaxels*), that determine the spectral and spatial resolution of the instrument.

The grating is operated in the 1st, 2nd, and 3rd orders to cover the full wavelength range, with special order sorting filters suppressing contributions by other orders. The respective wavelengths are 102-210 μm (1st order), 71-105 μm (2nd), and 51-73 μm (3rd), but the order overlap regions and spectrum > 190 μm is not instantly usable (see Appendix A in Herczeg et al. 2012).

The resolving power increases non-linearly with wavelength, with R~1000-2000 in the 1st order, R~1500-3000 in the 2nd order, and R~2500-5500 in the 3rd order. The corresponding velocity resolution ranges from ~90 km s^{-1} in the 3rd order observation of the [O I] line at 63 μm to ~300 km s^{-1} in the CO 24-23 line at 108 μm. As a result, typically the lines are spectrally unresolved (Gaussian shape), with only a few sources showing high-velocity wings in the [O I] profiles. Spectral coverage (covered by 16 pixels)
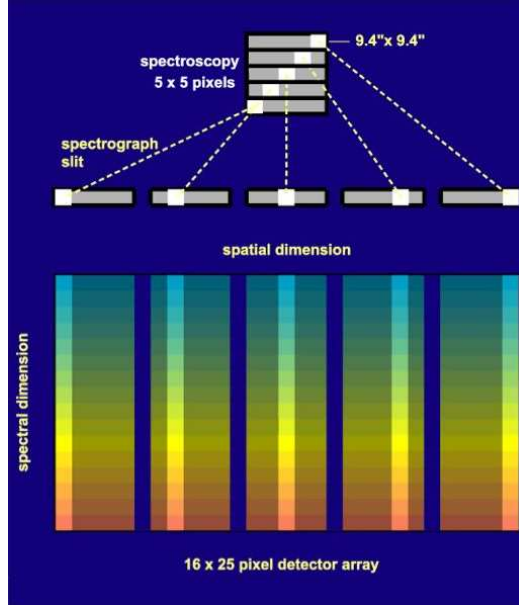
Figure 1.10 – Integral-field spectroscopy with PACS. The 5×5 array of spaxels is re-arranged by the image slicer along the entrance slit of the grating spectrograph to observe simultaneously all 25 spectra. Adopted from the PACS Observer's Manual (http://herschel.esac.esa.int/Docs/PACS/html/pacs_om.html).

is about $1400\,\mathrm{km\,s^{-1}}$ at 63 μm and 3000 at 108 μm, with typically 1-2 pixels per full width half maximum (FWHM), respectively.

The telescope point spread function (PSF) is asymmetric, with the size increasing with wavelength and not diffraction limited below ~130 μm. As a consequence of the fixed size of the spaxels, the fraction of the PSF viewed by the spaxels differs depending on the wavelength. At 63 μm, the central spaxel views 70% of a perfect point-source emission, while at 186 μm (CO 14-13) only 42 % is captured. It is thus important to account for the flux outside the central spaxel, in particular when comparing line fluxes at different wavelengths.

The two main observing schemes on PACS were the line spectroscopy and the range spectroscopy modes. The line spectroscopy mode allows observations of small spectral regions ($\Delta\lambda$ ~0.5-2 μm) around selected lines and is particularly well suited for deep integrations. The range spectroscopy mode provides the full spectrum from ~ 50 to 210 μm but the spectral sampling within a resolution element is about 3-4 times coarser than in the line spectroscopy mode.

For both schemes, the chopping / nodding or the wavelength switching techniques were employed to subtract the far-IR background emission. In the chop/nod mode, spectroscopy of the region at a distance up to 6′ from the source was used to correct for

17

emission unrelated to the source. In cases where the contamination was still high at those distances, the signal is modulated by moving the line over about half of the FWHM and the differential line profile is measured.

1.4.2   Comparisons to ISO / LWS

The ISO/LWS was the only instrument before PACS that offered the access to the complete far-IR window, with a spectral range of 45-197 μm (Kessler et al. 1996, Clegg et al. 1996). The telescope was operational in 1995-1997.

ISO had a relatively small diameter of 0.6 m and thus the LWS beam was $\sim 80''$, nearly an order of magnitude larger than in case of *Herschel* / PACS. As a consequence, the spatial information of the line and continuum emission was lacking. The emission in a single beam from protostars was often contaminated by nearby sources, their outflows, and the PDR emission from the cloud.

A factor of ~ 6 increase in the telescope diameter and the IFU design of the PACS instrument provides an improved spatial resolution. As a consequence, the spatial extent of line emission coupled with the more accurate excitation analysis allows us to trace the origin of far-IR line and continuum emission. In particular, the [O I] and [C II] emission patterns demonstrate whether the emission is dominated by the large scale cloud PDR or a protostar.

The spectral resolving power of LWS was ~200, about a factor of 10 lower than PACS. The Fabry-Perot mode offered a higher spectral resolution, but the sensitivity was so low that only a few brightest sources could be observed. The higher spectral resolution and sensitivity of PACS with respect to LWS was therefore crucial to detect weak molecular lines, especially on top of the bright continuum. The CO lines up to $J_{\mathrm{up}} = 49$ are detected in NGC1333 IRAS4B (20 more lines than with ISO!) and reveal two components on CO diagrams (Herczeg et al. 2012, Goicoechea et al. 2012, Manoj et al. 2013, Green et al. 2013). The detections of H_2O lines in Class I sources improve our understanding of the evolution of molecular cooling from Class 0/I protostars and allow us to model the physical conditions at which H_2O is produced (Herczeg et al. 2012).

1.4.3   WISH, DIGIT, and WILL programs

This thesis uses data from three large *Herschel* programs: WISH, DIGIT, and WILL. The 'Water in Star forming regions with Herschel' (WISH) is a guaranteed-time key program on *Herschel* with the primary goal to probe the physical and chemical processes in young stellar objects using H_2O and related species (van Dishoeck et al. 2011). The effects of evolution and environment on the molecular emission are studied by targeting sources at various evolutionary stages (from pre-stellar cores to Class II) and masses (low-, intermediate-, and high-mass protostars). The HIFI spectra of selected lines (Figure 1.8) are complemented with PACS maps in the line spectroscopy mode. Full PACS spectra are acquired for only 4 Class 0 sources. Fully-sampled maps of a few sources are obtained at the protostellar or outflow position (e.g. Nisini et al. 2010a), with most of the sources observed in a single pointing.

The 'Dust, Ice, and Gas in Time' (DIGIT) open time key program uses the full PACS 50-210 μm spectra of about 30 Class 0/I protostars to quantify the dust and gas evolution in the far-IR (Green et al. 2013). All the targeted sources have good quality mid-IR and sub-mm observations, which together with PACS spectra allow the determination of the full SED and the search for and analysis of solid-state features. The full inventory of far-IR gas lines provides a unique measurement of total far-infrared line cooling and is a useful guide for analysis of WISH / PACS data, where mostly selected lines were targeted.

The 'William Herschel Line Legacy' (WILL) survey obtained PACS and HIFI spectra toward an unbiased flux-limited sample of low-mass protostars newly discovered in the recent *Spitzer* and Herschel Gould Belt imaging surveys (e.g. Evans et al. 2009, André et al. 2010). Its main aim is to study the physics and chemistry of H_2O and related species in star-forming regions in a statistically significant way by doubling the sample of low-mass protostars observed in the WISH and DIGIT programs.

1.5 This thesis

The central theme of this thesis is the feedback from protostars onto their surroundings during the first 0.5 million years of protostellar life (Dunham et al. 2014). The feedback is elucidated by means of astrochemistry – the molecules and atoms are used as tracers of physical conditions of the emitting gas and the associated physical processes. Far-infrared spectroscopy from the *Herschel Space Observatory* (2009-2013) unravels the spatial scales and energetics of the protostellar feedback at unprecedented detail. Large *Herschel* surveys of protostars at various evolutionary stages and masses reveal global properties of young stellar objects and their evolution during the deeply-embedded stage that cannot be studied at visible wavelengths. The most important questions specifically addressed in this thesis are the following.

- What is the origin of far-infrared emission in the surroundings of young stellar objects? Can we quantify the feedback from protostars on envelope spatial scales using molecular lines of CO, H_2O, and OH, and atomic [O I]?
- What is the role of shocks and ultraviolet radiation in low-mass protostars and on which scales?
- What is the cooling budget of hot gas in deeply-embedded protostars? Which feedback processes determine the total line cooling?
- How do physical processes responsible for the gas heating change with evolution? How robust is the total gas cooling as an evolutionary tracer?
- What is the impact of protostellar mass on the properties of the far-infrared emission? Are the dominant excitation mechanisms of CO the same in low- and high-mass star forming regions?

These questions are addressed in the following chapters. The names of the projects on *Herschel* where the data come from are shown in brackets next to the chapter titles.

Chapter 2 – *Far-IR cooling lines in low-mass young stellar objects* [WISH]

A spectral survey of 18 low-mass protostars reveals rich molecular and atomic far-infrared emission. CO lines from $J =$14-13 to $J = 49 - 48$ and even highly-excited H_2O lines (for example, the H_2O 8_{18}–7_{07} line with the upper level energy above 1000 K) are detected. Boltzmann diagrams of CO show two temperature components, at ~350 K and ~700 K, whereas H_2O diagrams show a single component at ~150 K and a significant scatter due to subthermal excitation. A broad range of corresponding gas physical conditions is found using non-LTE radiative transfer calculations. Similar patterns of spatially-extended H_2O and CO emission and their strong flux correlations found in the survey indicate high-densities ($n_H \gtrsim 10^6$ cm^{-3}) and moderately-high temperatures ($T_{kin} \gtrsim 350$ K) of the exciting gas. Comparisons to shock models yield consistent results suggesting that *H_2O and CO originate most likely in non-dissociative shocks*. In contrast, at least a fraction of OH and [O I] emission originates in a different physical component, since no spatial or strong flux correlations are found between those species and CO or H_2O. Dissociative shocks at the point of direct impact of the wind on the dense envelope are the most likely excitation mechanism, since only a small fraction of [O I] emission is seen in the high-velocity wings tracing a hidden atomic jet. The total far-infrared gas cooling budget is dominated by H_2O and CO (up to 50%) with an increasing contribution of [O I] for more evolved sources (up to 30% of total cooling). The absolute value of the total gas cooling and its ratio with the source bolometric luminosity decrease with evolution from Class 0 to Class II sources and therefore are useful evolutionary tracers.

Chapter 3 – *Far-IR molecular lines from low- to high-mass star forming regions* [WISH]

A survey of 10 high-mass star forming regions extends the study of low-mass protostars from Chapter 2 to more massive objects. Rich far-infrared molecular spectra are detected at the central position of PACS maps. Many H_2O lines are detected in absorption against the bright continuum emission, in particular at shorter wavelengths, and do not contribute to the gas cooling. Instead, the total cooling is dominated by CO (typically ~75%) and [O I] (~20%) with a minor contribution of H_2O and OH (below ~1%). Even though CO transitions up to $J_{up} \sim 29$ are detected, only one temperature component at ~ 300 K is seen on the CO rotational diagrams. In contrast with low-mass protostars, radiative transfer modeling shows that most of CO emission originates from the quiescent envelope (up to 70-100 %), except the highest$-J$ lines that require an additional physical component (shocks). H_2O rotational temperatures are ~250 K, about 100 K higher than for the low-mass protostars due to higher envelope densities and temperatures. Across the wide luminosity range from ~ 1 to 10^6 $L_\odot$, the far-IR line cooling strongly correlates with the bolometric luminosity, in agreement with studies of low-mass protostars, but the relative amount of cooling of hot gas to the dust cooling ratio decreases by more than an order of magnitude from low to high-mass protostars.

Chapter 4 – *Shockingly low water abundances in Herschel / PACS observations of low-mass protostars in Perseus* [WILL]

A large and uniform sample of young protostars (22 objects) located exclusively in the Perseus molecular cloud is observed in selected transitions of H_2O, CO, and OH. Line ratios of the same and different species are used as diagnostics of shocks resulting from the envelope-outflow interactions. Changes in absolute line fluxes and line ratios as a function of shock velocity and pre-shock density are discussed and compared with steady-state non-dissociative and dissociative shocks from the literature. Observed line ratios of the same species are well-reproduced by existing models of non-dissociative $C-$shocks with velocities $\gtrsim 20$ km s^{-1} and pre-shock densities of $\sim 10^5$ cm^{-3}. In contrast, model line ratios of H_2O / CO, H_2O / OH, and CO / OH are overestimated with respect to the observations by one to two orders of magnitude. The most likely reasons for these discrepancies are too large H_2O abundances and too small OH abundances produced in the shock models. Inclusion of illumination of shocks by ultraviolet radiation from the protostellar environment should allow to reconcile the models with observations.

Chapter 5 – *Physics of deeply-embedded low-mass protostars: evolution of shocks, ultraviolet radiation, and mass loss rates* [WISH, DIGIT, WILL]

A combined survey of 90 low-mass protostars sheds more light on the physical components and their evolution giving rise to the far-infrared emission observed with *Herschel* / PACS. Rich molecular spectra are detected towards 70 out of 90 sources, including ~ 30 sources with the detection of highly-excited H_2O and CO emission. Median CO rotational temperatures are ~ 320 K and ~ 690 K, in line with previous studies. The total cooling in CO decreases as the protostar evolves, but the [O I] emission is surprisingly similar in the Class 0 and I stages. Comparison of [O I] line emission to the shock models implies a necessary contribution from dissociative $J-$shocks and / or UV irradiation of outflow cavities. The [C II] emission, on the other hand, must originate in photodissociation regions, characterized by densities of $10^4 - 10^{5.5}$ cm^{-3} and UV fields of 10-100 times the average interstellar radiation field. The increasing role of UV in the more evolved sources is testified by the decrease of the H_2O / OH ratio from Class 0 to Class I stages. A similar decrease is not seen in the H_2O / [O I] ratio, implying that in Class I sources a large fraction of [O I] emission comes from the H_2O photodissociation in the outflow cavities and not from the jet. As a consequence, the mass loss rates calculated from the [O I] luminosity, of order 10^{-8} M$_\odot$ yr^{-1}, are upper limits to the jet ejection rates. Nevertheless, these rates are up to about an order of magnitude lower than those determined for the entrained outflow gas from the CO 3-2 and CO 6-5 maps, especially for the most deeply embedded sources. In contrast, Class I sources show larger [O I]/CO mass flux rates than the Class 0 sources, suggesting that the jet evolves from molecular to atomic form during the embedded phase.

The main conclusions from this thesis are summarized below.

1. Far-infrared molecular line emission is ubiquitous in star forming regions (Chapters 2-5). 80% of low-mass protostars show detections of CO, H_2O, and OH lines. 40% of those sources show also highly-excited lines of CO and H_2O (Chapter 5).

2. Spatial extent of molecular line emission is typically of order ~ 1000 AU, with a few sources with extended emission up to $\sim 10,000$ AU in the CO outflow direction. The [O I] emission is often extended on the same spatial scales along the outflow direction.

3. Rotational diagrams of CO show uniformly two components in low-mass protostars, corresponding to temperatures of ~ 320 K and ~ 690 K (Chapters 2, 5). The ~ 300 K component is detected in protostars with a broad range of luminosities, from ~ 1 to $10^6\ L_\odot$ (Chapter 3). Despite the similarities in the CO ladders, the contribution from the envelope to the far-IR CO emission increases 10 times from low- to high-mass protostars (Chapter 3).

4. Evolutionary stage affects the ratio of molecular and atomic cooling more than the mass of a protostar. In contrast, $L_{\text{FIRL}}/L_{\text{bol}}$ decreases only by a factor of 4 from Class 0 to Class I and more than 20 times from low- to high-mass star forming regions (Chapters 2, 3).

5. Shocks are the main source of hot ($T \gtrsim 300$ K) and dense ($n \sim 10^6$ cm^{-3}) gas in low-mass protostars (Chapters 2, 4, 5). Non-dissociative $C-$shocks produce most of the observed molecular emission, but dissociative shocks are needed to explain the [O I] and OH lines as well as the highly-excited CO and H_2O lines (Chapters 4, 5).

6. UV irradiation of shocks needs to be implemented in the next-generation of shock models (Chapters 4, 5). The UV fields are of order 10-100 times the average interstellar radiation field (Chapter 5).

Feedback processes from low- and high-mass star forming regions are therefore successfully identified in the far-IR spectra from *Herschel* / PACS emission. Characteristics of shocks and UV radiation presented here provide additional means to test the origin of protostellar outflows and the launching mechanisms of jets, as well as the scales on which feedback processes occur. Determination of relative jet and UV contributions to the [O I] emission as the protostar evolves is becoming possible with the German REceiver for Astronomy at Terahertz Frequencies (GREAT) instrument on board the Stratospheric Observatory for Infrared Astronomy (SOFIA) which offers [O I] spectroscopy with spectral resolution $\lesssim 1$ km s^{-1}.

A complementary view of the feedback processes in the young stellar objects is being provided by sub-millimeter observations with the Atacama Large Millimeter/submillimeter Array (ALMA). Spatially resolved down to ~ 100 AU scales emission from ^{13}CO $J_{\text{up}} < 8$

transitions will fully explore the importance of ultraviolet heating, while, for example, SiO observations will continue to constrain the shock characteristics originating in the outflow-envelope interactions.

High spatial resolution (0.4-0.8") spectral maps from the Mid-Infrared Instrument (MIRI) on the *James Webb Space Telescope* (to be launched in late 2018) will eventually allow us to study hot gas around protostars using the unique mid-IR diagnostics (5-28 μm) on spatial scales similar to ALMA.

Even though *Herschel* is no longer operational, the large amount of data collected in its archives still awaits further exploration. In particular, complete surveys of protostars in nearby molecular clouds will help to develop theoretical models of star formation and protostellar evolution, and their feedback on the surroundings.

Water in star forming regions with *Herschel* (WISH) III. Far-infrared cooling lines in low-mass young stellar objects

A. Karska, G. J. Herczeg, E. F. van Dishoeck, S. F. Wampfler, L. E. Kristensen,
J. R. Goicoechea, R. Visser, B. Nisini, I. San José-García, S. Bruderer, P. Śniady, S. Doty,
D. Fedele, U. A. Yıldız, A. O. Benz, E. Bergin, P. Caselli, F. Herpin, M. R. Hogerheijde,
D. Johnstone, J. K. Jørgensen, R. Liseau, M. Tafalla, F. van der Tak, and F. Wyrowski

25

Abstract

Context. Understanding the physical phenomena involved in the earlierst stages of protostellar evolution requires knowledge of the heating and cooling processes that occur in the surroundings of a young stellar object. Spatially resolved information from its constituent gas and dust provides the necessary constraints to distinguish between different theories of accretion energy dissipation into the envelope.

Aims. Our aims are to quantify the far-infrared line emission from low-mass protostars and the contribution of different atomic and molecular species to the gas cooling budget, to determine the spatial extent of the emission, and to investigate the underlying excitation conditions. Analysis of the line cooling will help us characterize the evolution of the relevant physical processes as the protostar ages.

Methods. Far-infrared Herschel-PACS spectra of 18 low-mass protostars of various luminosities and evolutionary stages are studied in the context of the WISH key program. For most targets, the spectra include many wavelength intervals selected to cover specific CO, H_2O, OH, and atomic lines. For four targets the spectra span the entire 55-200 μm region. The PACS field-of-view covers $\sim 47''$ with the resolution of $9.4''$.

Results. Most of the protostars in our sample show strong atomic and molecular far-infrared emission. Water is detected in 17 out of 18 objects (except TMC1A), including 5 Class I sources. The high-excitation H_2O 8_{18}–7_{07} 63.3 μm line ($E_u/k_B = 1071$ K) is detected in 7 sources. CO transitions from $J = 14 - 13$ up to $J = 49 - 48$ are found and show two distinct temperature components on Boltzmann diagrams with rotational temperatures of $\sim$350 K and $\sim$700 K. H_2O has typical excitation temperatures of $\sim$150 K. Emission from both Class 0 and I sources is usually spatially extended along the outflow direction but with a pattern that depends on the species and the transition. In the *extended* sources, emission is stronger off source and extended on 10,000 AU scales; in the *compact* sample, more than half of the flux originates within 1000 AU of the protostar. The H_2O line fluxes correlate strongly with those of the high−J CO lines, both for the full array and for the central position, as well as with the bolometric luminosity and envelope mass. They correlate less strongly with OH fluxes and not with [O I] fluxes. In contrast, [O I] and OH often peak together at the central position.

Conclusions. The PACS data probe at least two physical components. The H_2O and CO emission very likely arises in non-dissociative (irradiated) shocks along the outflow walls with a range of pre-shock densities. Some OH is also associated with this component, most likely resulting from H_2O photodissociation. UV-heated gas contributes only a minor fraction to the CO emission observed by PACS, based on the strong correlation between the shock-dominated CO 24-23 line and the CO 14-13 line. [O I] and some of the OH emission probe dissociative shocks in the inner envelope. The total far-infrared cooling is dominated by H_2O and CO, with the fraction contributed by [O I] increasing for Class I sources. Consistent with previous studies, the ratio of total far-infrared line emission over bolometric luminosity decreases with the evolutionary state.

2.1 Introduction

Stars form in collapsing dense molecular cores deep inside interstellar clouds (see reviews by di Francesco et al. 2007, Bergin & Tafalla 2007, Lada 1999). Star formation is associated with many physical phenomena that occur simultaneously: infall from the envelope, action of jets and winds resulting in shocks, outflows sweeping up surrounding material, and UV heating of outflow cavity walls (Shu et al. 1987, Spaans et al. 1995, Bachiller & Tafalla 1999). In the earliest phases of star formation (Class 0 and I objects; André et al. 1993, 2000), the interaction between the jet, wind, and the dense envelope is particularly strong and produces spectacular outflows (Arce et al. 2007).

Atomic and molecular tracers are needed to probe the physical conditions and to evaluate and disentangle the energetic processes that occur in the Class 0/I young stellar objects. Low$-J$ (J 6, E_u/k_B 116 K) rotational transitions of carbon monoxide (CO) are among the most widely used tracers (Bontemps et al. 1996), but are only sensitive to the cold gas, T 100 K, from both the envelope and the entrained outflow material. Nevertheless, spectrally resolved profiles of CO and ^{13}CO 6–5 allowed van Kempen et al. (2009a) and Yıldız et al. (2012) to attribute the narrow emission lines to the heating of the cavity walls by UV photons (see also Spaans et al. 1995). High-density tracers such as SiO (n_{H2} 10^5 cm^{-3}) have been used to study fast J-type shocks produced at bow shocks where the jet plunges into the cloud (Bachiller et al. 2001). At the same time, theoretical studies of line cooling from dense cores predict that most of the released energy is produced in between these two extreme physical regimes and emitted mainly in atomic [O I], high$-J$ CO and H$_2$O rotational transitions in the far-infrared spectral region in addition to H$_2$ mid-infrared emission (Goldsmith & Langer 1978, Takahashi et al. 1983, Neufeld & Kaufman 1993, Ceccarelli et al. 1996, Doty & Neufeld 1997). Therefore, to study the energetics of young stellar objects (YSOs) and, in particular, the relative importance of different energetic processes as a function of the evolutionary state of a YSO, line observations in the $\sim 50 - 200\,\mu$m spectral region are necessary.

The Long-Wavelength Spectrometer onboard the Infrared Space Observatory has for the first time offered spectral access to the complete far-IR window (Kessler et al. 1996, Clegg et al. 1996). Many CO rotational transitions from $J = 14 - 13$ to $J = 29 - 28$ (for NGC1333-IRAS4) and several H$_2$O lines up to $E_u/k_B \sim 500$ K have been detected in Class 0 sources (Giannini et al. 2001, Maret et al. 2002). On the other hand, H$_2$O remained undetected in Class I sources, the exception being the outflow position of HH46. CO emission was generally found to be weaker than H$_2$O, whereas the fine structure lines of [O I] and [C II] dominates the ISO spectra (Nisini et al. 2002b). The gas cooling budget calculations show similar contributions from lines of CO, H$_2$O, [O I], and OH in Class 0 sources to a smaller extent. Moreover, an evolutionary trend toward a gradual decrease in molecular luminosity and total line luminosity was established as the objects evolve from the Class 0 to Class I phases. This trend was interpreted as the result of weaker shocks and less shielded UV radiation in the later phase of protostellar evolution (Nisini et al. 2002b).

The Photodetector Array Camera and Spectrometer (PACS) (Poglitsch et al. 2010) on

27

board the *Herschel* Space Observatory (Pilbratt et al. 2010a)[1] with 25 $9\rlap{.}''4 \times 9\rlap{.}''4$ spatial pixels provides an 8× improvement in spatial resolution as compared to ISO/LWS. The PACS field of view of $\sim 47''$ is smaller than the $80''$ ISO beam, but in many cases it still covers the full extent of the emission from nearby YSOs. For a typical distance of 200 pc to our objects (Table 4.1), regions of ~ 9400 AU are observed and resolved down to ~ 1880 AU. The higher sensitivity and better spectral resolution provides an important improvement in the quality of the spectra. PACS is thus well suited for studies of atomic and molecular emission in the Class 0/I objects, as demonstrated by PACS results on individual Class 0/I sources and their outflows (van Kempen et al. 2010b,a, Nisini et al. 2010a, Herczeg et al. 2012, Benedettini et al. 2012, Goicoechea et al. 2012). These results have already indicated relative differences in the gas cooling budget from different sources and differences in spatial distributions of emission between different molecules. Visser et al. (2012) have modeled these early data with a combination of shocks and UV heating along the cavity wall. The strong [O I] and OH emission also suggests there are dissociative shocks in the close vicinity of the protostar (van Kempen et al. 2010b).

In our paper, we address the following questions. How does a YSO affect its surrounding cloud and on what spatial scales? What are the dominant gas cooling channels for deeply embedded YSOs? What do they tell us about the physical components and conditions that cause excitation of the observed lines? How do all of these processes change during the evolution from the Class 0 to the Class I stage? To this end, we present Herschel-PACS spectroscopy of 18 Class 0/I YSOs targeting a number of CO, H_2O, OH, and [O I] lines obtained as part of the 'Water in star forming regions with Herschel' (WISH) key program (van Dishoeck et al. 2011). WISH observes about 80 protostars at different evolutionary stages (from prestellar cores to circumstellar disks) and masses (low-, intermediate-, and high-mass) with both the Heterodyne Instrument for the Far-Infrared (HIFI; de Graauw et al. 2010) and PACS. Our paper only focuses on low-mass YSOs and is closely associated to other WISH papers. Specifically, Kristensen et al. (2012) studies the spectrally resolved 557 GHz H_2O line observed towards all our objects with HIFI. Wampfler et al. (2013) analyzes the same sample of sources but focuses on the excitation of OH in the Class 0/I sources, whereas full PACS spectral scans of two sources are published by Herczeg et al. (2012; NGC1333-IRAS4B) and Goicoechea et al. (2012; Ser SMM1). A synthesis paper discussing the HIFI, PACS, and SPIRE data being obtained in WISH and other programs is planned at the final stage of the program.

The paper is organized as follows. Section 2 introduces the source sample and explains the observations and reduction methods; §3 presents results that are derived directly from the observations; §4 focuses on the analysis of the data; §5 provides the discussion of the results in the context of the available models, and §6 summarizes the conclusions.

---

[1] Herschel is an ESA space observatory with science instruments provided by European-led Principal Investigator consortia and with important participation from NASA.

2.2 Observations

2.2.1 Sample selection

We used PACS to observe 18 out of 29 Class 0/I objects selected in the low-mass part of the WISH key program. The WISH source list consists of nearby ($D \lesssim 450$ pc), well-known young stellar objects for which ample ground-based single dish and interferometer observations are available (for details concerning the WISH program see van Dishoeck et al. 2011). The remaining 11 sources, that were not targeted with PACS within WISH were observed in the 'Dust, Gas and Ice in Time' key program (DIGIT, PI: N. Evans; Green et al. 2013, Dionatos et al. subm., Jørgensen et al., in prep., Lee et al., in prep.).

Table 4.1 presents our sample of objects together with their basic properties. Bolometric luminosities and temperatures were derived using our new PACS data supplemented with observations found in the literature (see §2.4 for spectral energy distribution discussion). Envelope masses are from Kristensen et al. (2012), which includes a discussion of the impact of new PACS measurements on the derived physical parameters.

2.2.2 Observing strategy

The far-IR spectra were obtained with PACS, an integral field unit with a 5×5 array of spatial pixels (hereafter *spaxels*). Each spaxel covers $9\rlap{.}''4 \times 9\rlap{.}''4$, providing a total field of view of $\sim 47'' \times 47''$. The full wavelength coverage consisted of three grating orders (1st: 102-210 μm; 2nd: 71-105 μm; or 3rd: 51-73 μm), two of which were always observed simultaneously (one in the blue, $\lambda < 105$ μm, and one in the red, $\lambda > 102$ μm, parts of the spectrum). The velocity resolution ranges from $\sim$75 to 300 km s^{-1}, depending on the grating order and the wavelength. The highest spectral resolution is obtained at the shortest wavelengths, below 65 μm. Two nod positions were used for chopping 3$'$ on each side of the source. Typical pointing accuracy is better than 2$''$.

Two observing schemes were used in our program: line spectroscopy mode to cover short spectral regions and range spectroscopy mode to cover the full far-IR SED. Line spectroscopy mode uses small grating steps to provide deep integrations and to fully sample the spectral resolution over short (0.5-2 μm) wavelength intervals. This mode was used to observe selected lines for 16 of 18 objects from our sample (Ser SMM1 and NGC1333-IRAS2A are the exceptions). We targeted 12 H$_2$O lines ($E_u/k_B \sim 100 - 1320$ K), 12 CO lines ($E_u/k_B \sim 580 - 3700$ K), and 4 OH doublets ($E_u/k_B \sim 120 - 291$ K), as well as the [O I] and [C II] lines (full list of available lines is included in Table 2.A.1). BHR71 and Ser SMM4 were only observed in a limited number of scans within the WISH program; range spectroscopy observations of those sources are analyzed in DIGIT (Jørgensen et al. in prep. and Dionatos et al. subm., respectively).

The range spectroscopy mode uses large grating steps to quickly scan the full 50-210 μm wavelength range with Nyquist sampling of the spectral resolution. This mode achieves a spectral resolution of $R = \lambda/\Delta\lambda \approx$1000-1500 over the full spectral range, which includes 37 high$-J$ CO transitions, as well as 140 H$_2$O transitions ($J < 10$, $E_u/k_B < 2031$ K) and 11 OH doublets. NGC1333-IRAS2A, 4A, 4B, and Ser SMM1 were observed with

29

Table 2.1 – Catalog information and source properties.

Nr	Object	D	L_{bol}	T_{bol}	$M_{env}{}^a$
		(pc)	($L_\odot$)	(K)	($M_\odot$)
1	NGC1333-IRAS2A	235	35.7	50	5.1
2	NGC1333-IRAS4A	235	9.1	33	5.6
3	NGC1333-IRAS4B	235	4.4	28	3.0
4	L1527	140	1.9	44	0.9
5	Ced110-IRS4	125	0.8	56	0.2
6	BHR71	200	14.8	44	2.7
7	IRAS15398^b	130	1.6	52	0.5
8	L483	200	10.2	49	4.4
9	Ser SMM1	230	30.4	39	16.1
10	Ser SMM4	230	1.9	26	2.1
11	Ser SMM3	230	5.1	38	3.2
12	L723	300	3.6	39	1.3
13	L1489	140	3.8	200	0.2
14	TMR1	140	3.8	133	0.2
15	TMC1A	140	2.7	118	0.2
16	TMC1	140	0.9	101	0.2
17	HH46	450	27.9	104	4.4
18	RNO91	125	2.6	340	0.5

Notes. Sources above the horizontal line are Class 0, sources below are Class I. Source coordinates and references are listed in van Dishoeck et al. (2011). Positional angles of CO 6-5 outflows will be presented in Yıldız et al. (in prep.).
[a] Envelope mass at 10 K from Kristensen et al. (2012). [b] The difference between the pointing coordinates and the coordinates derived from 2D Gaussian fits to PACS continuum observations in multiple wavelengths is (9″1 ± 0.2,8″0 ± 0.3).
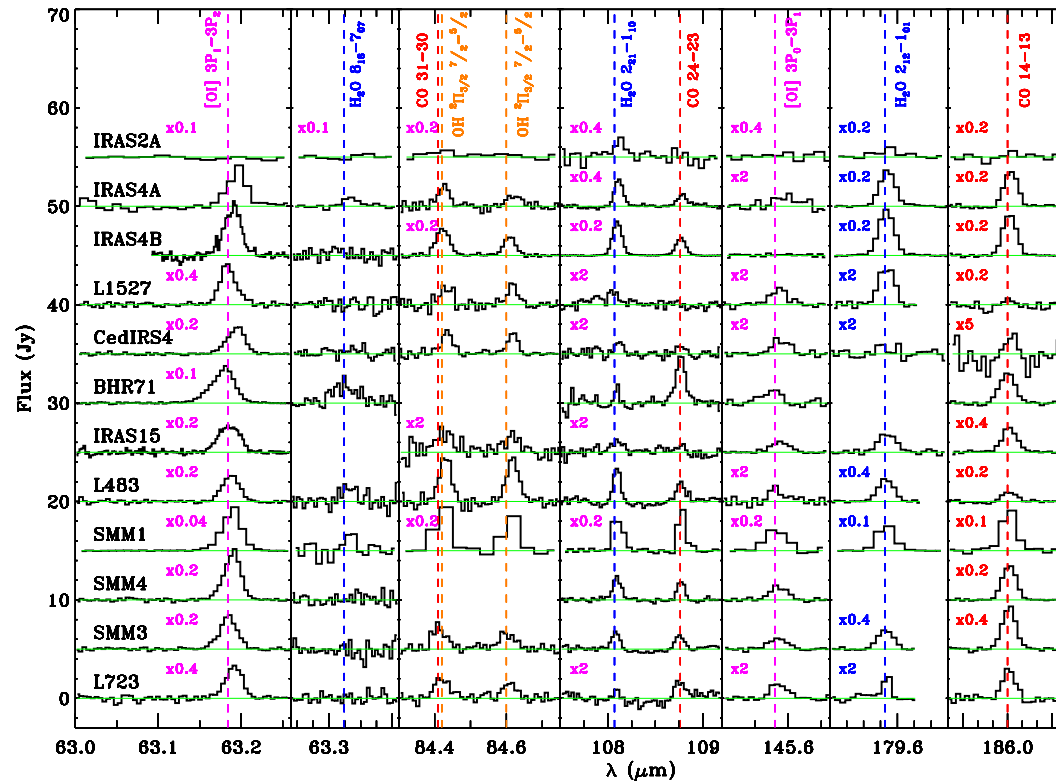
Figure 2.1 – Line survey of Class 0 sources at the on-source position. Spectra are extracted from the central spaxel only for the well-pointed sources (for mispointed sources see text) and continuum subtracted. No correction for point spread function is made. Dashed lines show laboratory wavelengths of [O I] (pink), OH (orange), CO (red), and H_2O (blue). BHR71 and Ser SMM4 were not observed in all the lines within our program (see text).
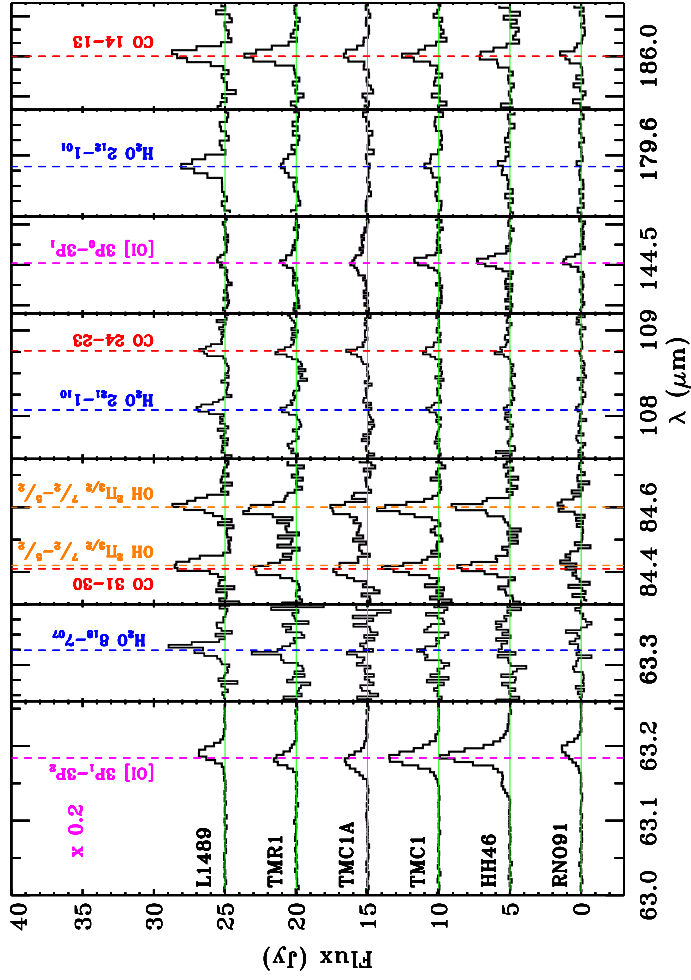
Figure 2.2 – Same as Figure 2.1 but for Class I sources.

full range spectroscopy within WISH. The NGC1333-IRAS2A data were taken during the science demonstration phase, when the optimal PACS settings were not yet known. The data are therefore of poorer quality than the other full range spectroscopy observations.

2.2.3 Reduction methods

Both line spectroscopy and range spectroscopy basic data reduction were performed with the Herschel Interactive Processing Environment v.8 (HIPE, Ott 2010). The flux was normalized to the telescopic background and calibrated using Neptune observations. Spectral flatfielding within HIPE was used to increase the signal-to-noise ratio (for details, see Herczeg et al. 2012 Green et al. 2013). The overall flux calibration is accurate to ~ 30%, based on the flux repeatability for multiple observations of the same target in different programs, cross-calibrations with HIFI and ISO, and continuum photometry. The 5×5 datacubes were further processed with IDL.

Since the spaxel size stays fixed, whereas the Herschel beam size increases with wavelength, the wavelength-dependent loss of radiation in a spaxel for a well-centered point source is observed to be ~30% in the blue to ~60% in red parts of the spectra (see PACS Observers Manual). Most of the radiation that leaks outside a given spaxel is captured by the adjacent ones. However, the far-IR emission from many Class 0/I objects is spatially extended on scales of $> 10''$, which are resolvable by PACS. For these sources the central spaxel fluxes corrected for the point spread function (PSF) using the standard wavelength-dependent values provided by the Herschel Science Center largely underestimate the total emission from the source. Thus, in this paper, either a sum of 25 spaxels (for lines at λ 100 μm) or a sum of the spaxels with detected emission (for weak lines at λ 100 μm) are taken to calculate line fluxes used for most of the analysis. The only exceptions are in §3.1 and in §4.3, where central spaxel fluxes corrected for the PSF using the standard factors are calculated in order to study the emission in the direct vicinity of the YSOs. All line fluxes are listes in Tables 2.A.2 and 2.A.3.

The approach to use the sum of the fluxes of all spaxels results in a lower signal-to-noise ratio of the detected lines; some of the weak lines become undetected. Therefore, we developed the 'extended source correction' method, which provides wavelength-dependent correction factors for the brightest spaxel(s). This method is well suited for the extended, Class 0/I sources. The details of the method are given in Appendix B; it is primarily applied to sources for which full line scans are available.

The PACS maps show that Herschel was mispointed for some of our objects. Continuum emission of BHR71, IRAS15398 and TMR1 peaks in between a few spaxels. In the case of IRAS15398, our observations were centered on the 2MASS position, which is offset by ~10'' from the far-infrared source position as determined from SCUBA maps by Shirley et al. (2000). Continuum emission from TMC1 and TMC1A peaks off-center in the PACS array, but is well confined to a single spaxel.

2.2.4   Spectral energy distributions

Radiation from the inner regions of a YSO is absorbed by dust in the envelope and re-emitted in the far-IR. As the evolution proceeds, the spectral energy distribution (SED) due to cold dust of a young Class 0 source evolves to a warmer Class I SED with emission also observed at shorter wavelengths. Therefore, SEDs are a useful starting guide for estimating the evolutionary stage of a YSO (Lada 1999, André et al. 2000). PACS continuum observations cover the SED peak of these embedded sources and thus provide a more accurate determination of bolometric luminosity (L_{bol}) and bolometric temperature (T_{bol}) than previously available.

Based on our PACS continuum measurements and the literature measurements, new values of L_{bol} and T_{bol} have been calculated. They are included in Table 4.1 and were also presented by Kristensen et al. (2012). The details of the calculations, the continuum values at different PACS wavelengths, and the actual SEDs are presented in Appendix C.

2.3   Results

2.3.1   Emission spectra

PACS spectroscopy of our sources reveals rich emission line spectra superposed on the dust continuum emission. Several transitions of the CO, H_2O, and OH molecules, as well as atomic emission from [O I] are detected. Emission in the [C II] line is only rarely detected and associated with the young stellar object.

Figure 2.1 presents a line inventory at the on-source position for Class 0 sources (central spaxel[2]). The Class 0 spectra show detections of at least one line of H_2O, CO, OH, and [O I] each for every object (all except NGC1333-IRAS2A, which has a high upper limit). The H_2O 2_{12}-1_{01} line at 179.5 μm is the strongest observed water line and often the strongest far-IR line in general, only comparable with CO 14-13 and [O I] 63.2 μm lines. CO transitions from $J = 14 - 13$ to $J = 48 - 47$ are detected in the richest spectra; typically CO emission from transitions higher than $J = 31 - 30$ is either weak or undetected. The OH $^2\Pi_{3/2}$ $J = 7/2 - 5/2$ doublet at 84 μm is detected for all sources, except NGC1333-IRAS2A. The discussion of other OH transitions can be found in Wampfler et al. (2013). The [O I] $^3P_1 - ^3P_2$ and $^3P_0 - ^3P_1$ lines at 63.2 μm and 145.5 μm are detected for all sources except NGC1333-IRAS2A (both lines undetected) and NGC1333-IRAS4B (the 145.5 μm line undetected).

For Class I objects, on-source spectra are presented in Figure 2.2. At least one water line is detected in all Class I sources except TMC1A; H_2O in RNO91 is detected when a few lines are co-added. Unlike the case of the Class 0 sources in our sample, the H_2O 2_{12}-1_{01} ($E_u/k_B = 114$ K) line at 179.5 μm is no longer the strongest water or molecular line. For all sources except HH46, the H_2O 2_{21}-1_{10} line ($E_u/k_B = 194$ K) at 108.07 μm or the H_2O 3_{03}-2_{12} line ($E_u/k_B = 196$ K) at 174.63 μm is the strongest water line, whereas CO

---

[2] For mispointed sources: TMR1, TMC1A, and TMC1 spaxel 32, corresponding to the continuum peak, is shown; for IRAS15398, where continuum emission falls into a few spaxels, only spaxel 23 is shown.
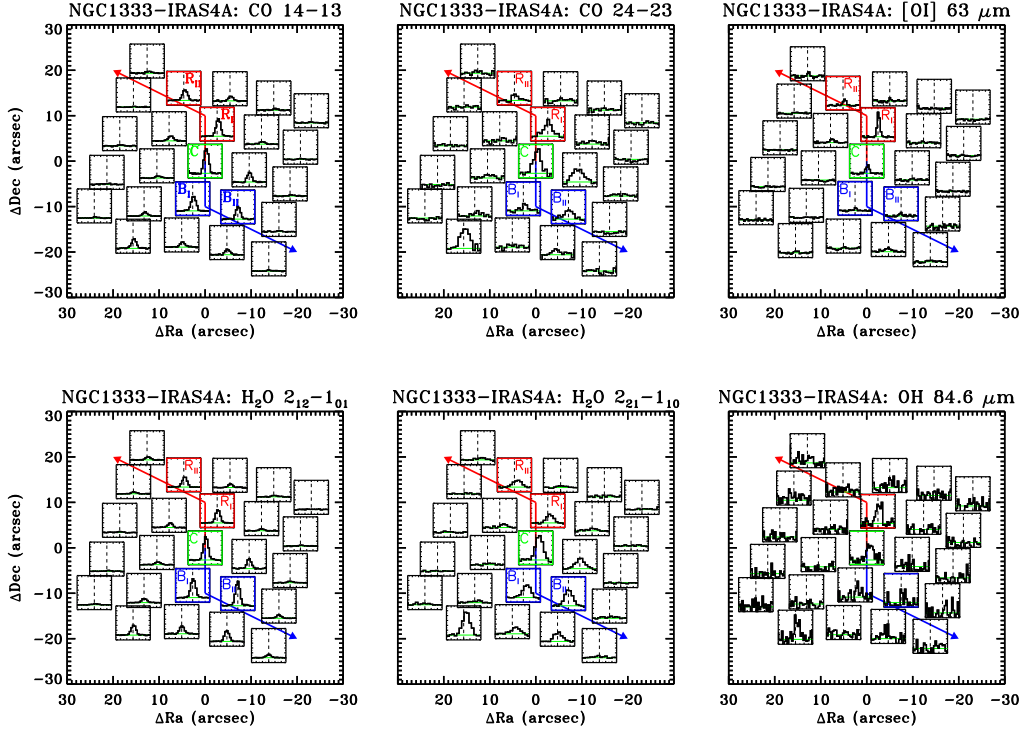
Figure 2.3 – PACS spectral maps of the Class 0 source NGC1333-IRAS4A in the CO 14-13, CO 24-23, [O I] 63.2 μm, H_2O 2_{12}-1_{01}, H_2O 2_{21}-1_{10} and OH 84.6 μm lines. The center of each spaxel box corresponds to its position on the sky with respect to the pointed source coordinates from van Dishoeck et al. (2011); shown boxes are smaller than the actual spaxel sizes. Wavelengths in microns are translated to the velocity scale on the X-axis using laboratory wavelengths of the species and cover the range from -550 to 550 km s^{-1}, except for the OH 84.6 μm lines where -400 to 400 km s^{-1} is shown. The Y-axis shows fluxes normalized to the brightest spaxel on the map separately for each species in a range -0.2 to 1.2. Outflow directions are drawn in blue and red lines based on CO 6-5 APEX CHAMP$^+$ sub-mm maps (Yıldız et al. 2012 and in prep.) that traces the warm entrained gas ($T \sim 100$ K). Two red outflow (R_I, R_{II}), on-source (C) and blue outflow (B_I, B_{II}) spaxels are marked with letters. IRAS4A spectra at those positions in different species are shown in Appendix D. The contribution from NGC1333-IRAS4B, located at (22.5″,-22.8″) with respect to IRAS4A, is seen in the S-E part of the map.

16-15 or CO 18-17 and OH 84.6 μm lines are the strongest molecular lines. The CO lines are typically weaker from Class I than from Class 0 objects, up to a factor of 10 compared with the brightest Class 0 sources, and the CO 24-23 is even undetected for one Class I object, RNO91. On the other hand, the OH 84.6 μm line and both fine-structure [O I] lines are seen in all sources. The [O I] line at 63.2 μm is always the strongest emission line in the far-IR spectrum of the Class I sources. The profiles of the [O I] line at 63.2 μm are

35
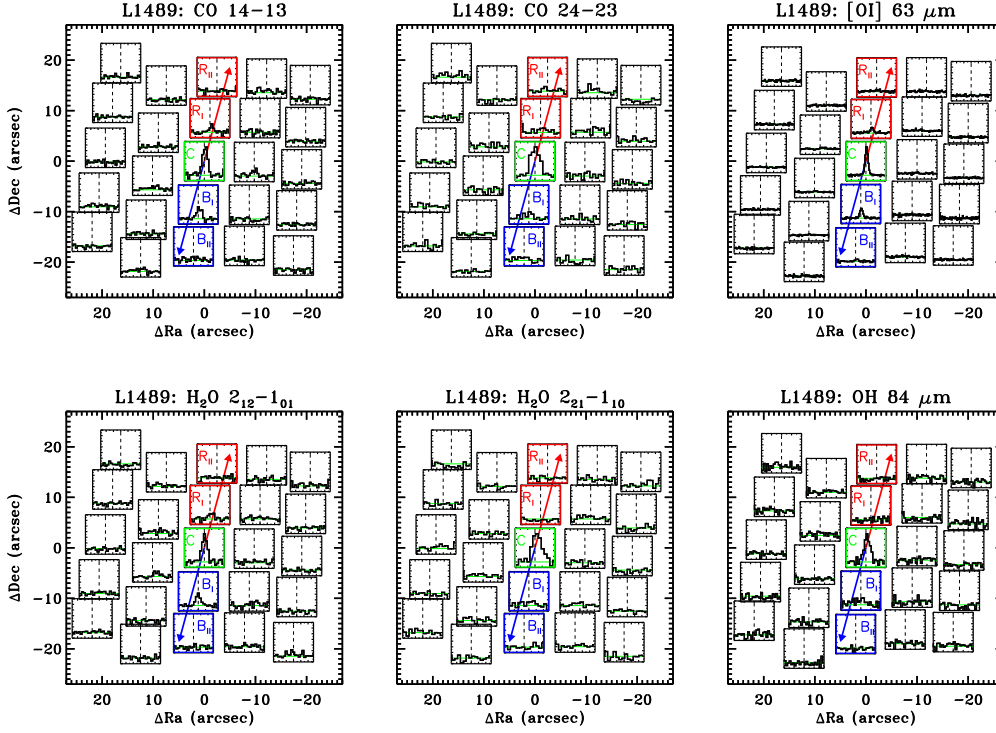
Figure 2.4 – The same as Figure 2.3 but for the Class I source L1489.

discussed in §3.3.

2.3.2 Spatial extent of line emission

PACS maps of the line emission in the detected species show a variety of patterns and thus allow us to spatially resolve the emission from different components of a young stellar object.

The Class 0 source NGC1333-IRAS4A and the Class I source L1489 are used here to demonstrate the differences in spatial distributions of the emission from the objects in our sample. Figures 2.3 and 4.A.2 show PACS 5×5 maps for the two sources in the [O I] 63.2 μm, H_2O 2_{12}-1_{01}, H_2O 2_{21}-1_{10}, CO 14-13, CO 24-23, and OH $^2\Pi_{3/2}$ $J = {}^7\!/_2 - {}^5\!/_2$ lines. In each map the CO 6-5 blue and red outflow directions are overplotted for comparison (Yıldız et al. in prep.). The same figures for the rest of our objects are included in the Online Material.

The NGC1333-IRAS4A emission in [O I], CO, and H_2O cover the outflow direction over the entire map, corresponding to a radius of 25″ or 5900 AU from the protostar. The [O I] emission peaks at the red outflow position. The CO and H_2O maps also show
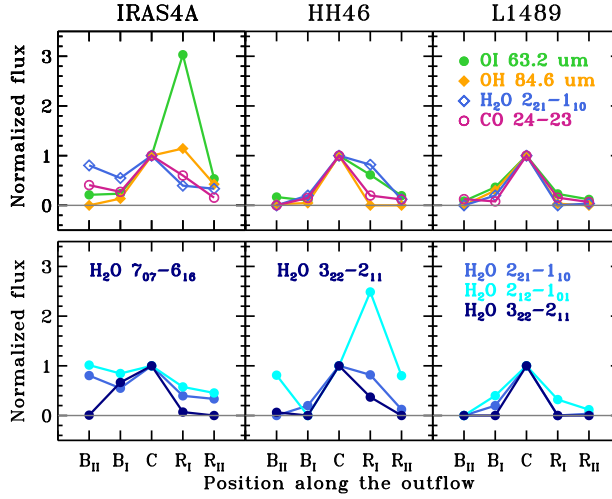
Figure 2.5 – Extent of line emission along the outflow direction for the selected molecular and atomic lines. Top panel: The [O I] 63.2 μm line (green filled circles), the OH 84.6 μm line (orange filled diamonds), the H$_2$O 2_{21}-1_{10} line at 108 μm (blue empty diamonds), and the CO 24-23 line (violet empty circles) are shown for each object. Bottom panel: The H$_2$O 2_{21}-1_{10} line at 108 μm (blue), the H$_2$O 2_{12}-1_{01} line at 179 μm (light blue) are shown for all objects. Additionally, the H$_2$O 7_{16}-6_{07} line at 71.9 μm is shown for IRAS4A and the H$_2$O 3_{22}-2_{11} at 89.9 μm line is shown for HH46 and L1489 (all in navy blue). The X-axis shows the selected spaxel names along the outflow direction (see Figure 2.3), whereas the Y-axis shows the flux normalized to the central spaxel (C) value.

a pattern of extended emission but are less concentrated than [O I], although some of this apparent extent can be attributed to the larger PSF at longer wavelengths. The CO emission, however, is rather symmetric and peaks in the center/red outflow position, whereas H$_2$O, contrary to [O I], is more pronounced in the blue outflow lobe, including the peak of the emission. The OH 84.6 μm line is detected both on-source and off-source, but with a pattern that is difficult to compare with other lines because of low signal-to-noise (as well as at the neigboring IRAS4B position in the SE corner of the map). OH follows the [O I] emission by peaking at the center/red outflow position. On the other hand, the maps of L1489 show that the emission from all species peaks strongly on-source, i.e. within a 5″ radius corresponding to 700 AU distance from the protostar. Weaker molecular and atomic emission is detected along the outflow direction and is more pronounced in the blue outflow position.

These differences are shown further in Figure 2.5, which illustrates the extent of line emission from various species and transitions in NGC1333-IRAS4A, HH46, and L1489, including higher excited H$_2$O lines. The distributions are normalized to the emission in the central spaxel. For HH46, [O I] and H$_2$O are strong in the red-outflow position R$_I$, whereas OH and CO 24-23 are observed only on-source. L1489 shows some extended emission in

the blue outflow (in particular in [O I] and OH), but clearly most of the emission originates in the central spaxel. Since L1489 is much closer to us than the other two sources (see Table 1), the extended emission in NGC1333-IRAS4A and HH46 indeed covers a much larger area on the sky.

NGC1333-IRAS4A and L1489 are thus the prototypes for the two morphologically different groups of objects: sources with *extended* emission and sources with *compact* emission. Figures 2.D.1 and 2.D.2 show the spectra in the four discussed species in the blue outflow, on-source and red outflow positions for those two groups. The adopted selection rule is based on the ratio of the on-source and the outflow [O I]: the sources where the outflow [O I] emission (in a selected position) accounts for more than the half of the on-source emission form the *extended* group, whereas the sources for which the off-source emission is 50% compared with the on-source emission form the *compact* group.

Table 2.2 summarizes the results of using the same criterion for the [O I] 63.2 μm, CO 14-13, H_2O 2_{12}-1_{01}, and OH $^2\Pi_{3/2}$ $J = 7/2 − 5/2$ lines in all objects[3]. The general trends are: (1) in the *compact* group, [O I] and OH emission dominate the central spaxel, whereas CO and H_2O either follow the same pattern or are off-source–dominated; (2) in the *extended* group OH is often strong off-source (except L1527 and HH46 where it dominates on-source), similar to CO and H_2O; (3) Most objects in the *extended* group are Class 0 objects, with the exception of TMC1A and HH46.; (4) Class 0 and I sources are almost equally represented in the *compact* group.

In a few cases both H_2O and CO are extended but in a different manner. For example, L1527 and NGC1333-IRAS4A show a brighter CO line and a weaker H_2O line in the red outflow position and the opposite in the blue outflow position (Figure 2.5). L483 shows similar differences, but with the brighter CO and weaker H_2O line in the blue outflow position. In those three cases the [O I] line is stronger at the position of weak H_2O; the same holds for the OH in case of NGC1333-IRAS4A (OH is not detected off-source in L483 and L1527). These differences are further discussed in §5.2.

For all objects, the [O I] emission is seen from the young stellar object and associated outflows rather than extended cloud emission. In the NGC1333-IRAS4A, 4B, Ser SMM3 and SMM4 regions, spaxels where the emission originates from the nearby sources are omitted. When detected, the [C II] emission is usually spread across the entire detector and seen in different strengths in the two nods, which both indicate that the emission is primarily produced by the parent cloud. TMC1 is the only source with [C II] detected from the central source (maps in both nods are shown in the Online Material). In Ser SMM1, [C II] emission follows the pattern of other species along the outflow direction (Goicoechea et al. 2012). The [C II] emission is not discussed further in this paper.

---

[3] No correction for PSF is performed. As a result, the calculated ratio of the on-source and off-source emission is lowered. The effect is the strongest for the CO 14-13 and H_2O 2_{12}-1_{01} lines. Also, no correction for different distances is made, but since our sources are located at a similar (mean) distance of 190±50 pc (excluding HH46), this does not change our conclusions.

Table 2.2 – Patterns of emission in atomic and molecular species.

Source	[O I]	CO 14-13	H$_2$O 2$_{12}$-1$_{01}$	OH 84.6
Compact emission				
NGC1333-IRAS2A	…	x	x	…
Ced110-IRS4	x	b	x	x
BHR71	x	r	…	…
L483	x	x	x	x
L723	x	b	b	x
L1489	x	x	x	x
TMR1	x	x	r	x
TMC1	x	b	b	x
RNO91	x	x	r	x
Extended emission				
NGC1333-IRAS4A	r	rb	rb	r
NGC1333-IRAS4B	b	b	b	b
L1527	r	b	x	x
Ser SMM1	rb	x	b	b
Ser SMM4	b	b	…	…
Ser SMM3	rb	rb	rb	b
TMC1A	b	b	rb	b
HH46	r	x	rb	x
IRAS15398	rb	rb	rb	rb

Notes. Compact emission (see text) is denoted with 'x'. Red and blue extended (outflow) emission that accounts for 50% of the on-source flux is denoted with 'r' and 'b'. BHR71 and Ser SMM4 were not observed in the H$_2$O 2$_{12}$-1$_{01}$ and OH 84.6 μm lines. NGC1333-IRAS2A shows non-detections of the above lines; the CO 15-14 line is used instead of CO 14-13 and the H$_2$O 3$_{03}$-2$_{12}$ line instead of H$_2$O 2$_{12}$-1$_{01}$ line.

2.3.3 Velocity shifts in [O I] and OH lines

Figure 2.6 shows the [O I] line at 63.2 μm towards the Class 0 sources NGC1333-IRAS4A, L1527, Ser SMM1, and SMM4 as well as the Class I sources TMC1A and HH46 (for comparison between PACS and ISO fluxes of the [O I] lines see Appendix E). The blue and red outflow profiles show significant line velocity shifts and, in particular in the case of HH46 and Ser SMM4, high-velocity line wings.[4]

Early results by van Kempen et al. (2010b) showed that the bulk of the [O I] emission in HH46 comes from low-velocity gas. On top of this 'quiescent' profile, high-velocity gas was detected in the blueshifted jet with a centroid velocity of about -170 km s^{-1} and in the redshifted jet with a centroid velocity of $+100$ km s^{-1}. Such velocity shifts, indicative of an optically invisible 'hidden' atomic jet, are seen towards at least a third of our objects (shown in Figure 2.6). High-velocity tails are detectable in a few [O I]-bright sources, but have a minor contribution to the total line emission.

The [O I] 63.2 μm velocity shifts and profile wings may be associated with similar features of the OH line at 84.6 μm. For NGC1333-IRAS4A, the OH 84.6 μm line from the source spaxel is redshifted by 90 km s^{-1}, compared with 50 km s^{-1} for the [O I] profile shift (see also Figure 2.D.3). HH46 also shows a tentative detection of blue-shifted high-velocity OH material that resembles the [O I] pattern. Within our sample, no other molecular lines have significant centroid velocity shifts, with typical limits of $\sim$ 40 km s^{-1} at < 100 μm and $\sim$ 100 km s^{-1} at > 100 μm. Such velocity shifts are at the velocity calibration limit and may be introduced by emission that is spatially offset within the slit(s). Inclination affects the projected velocity of the jet but is not likely to be the explanation for why a majority of sources do not show a velocity shift.

2.4 Analysis

2.4.1 Rotational diagrams

Boltzmann (or rotational) diagrams are used to determine the rotational temperatures T_{rot} from level populations for the Class 0/I objects from our sample (see Goldsmith & Langer 1978, for Boltzmann diagrams). For optically thin thermalized lines, the natural logarithm of the column density of the upper level N_u of a given transition over its degeneracy g_u is related linearly to the energy E_u of that level:

$$\ln \frac{N_u}{g_u} = \ln \frac{N_T}{Q(T_{rot})} - \frac{E_u}{k_B T_{rot}} \tag{2.1}$$

where $Q(T_{rot})$ denotes the rotational partition function at a temperature T_{rot} for a given molecule, N_T is the total column density and k_B is the Boltzmann constant.

---

[4] The velocity resolution of PACS is $\sim$ 90 km s^{-1} at 63 μm (or 0.02 μm). In principle, apparent velocity shifts can result from the location of the emission in the dispersion direction within each spaxel. This type of spatial offset is ruled out for the velocity shifts presented here because the velocity shifts are large and because we would expect to see stronger emission in neighboring spaxels than is observed.
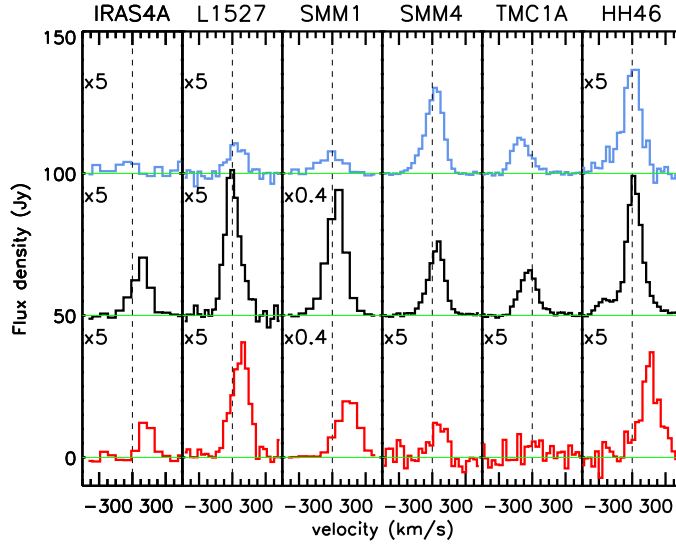
Figure 2.6 – Velocity shifts and high-velocity line wings in the [O I] line at 63.2 μm for NGC1333-IRAS4A, L1527, Ser SMM1, SMM4, TMC1A, and HH46. Selected blue outflow, on-source and red outflow positions are shown for each object from top to bottom in velocity range from -300 to 300 km s^{-1}. The black dashed line shows the laboratory wavelength of [O I].

The emitting region is unresolved in the PACS data due to the low spatial resolution, thus the number of emitting molecules, $\mathcal{N}_{\mathrm{u}}$, is calculated for each transition, defined as:

$$\mathcal{N}_{\mathrm{u}} = \frac{4\pi d^2 F_\lambda \lambda}{hcA} \tag{2.2}$$

F_λ denotes the flux of the line at wavelength λ, d is the distance to the source, A is the Einstein coefficient, c is the speed of light and h is Planck's constant.

Figure 2.7 shows CO and H$_2$O rotational diagrams calculated using the fluxes measured over the entire 5×5 PACS array for the Class 0 source Ser SMM3 and the Class I source L1489. Diagrams for all objects are included in the Appendix (Figures 2.F.1, 2.F.2, and 2.F.3).

Full range scan observations cover many more CO transitions than our targeted line scans (van Kempen et al. 2010a, Herczeg et al. 2012, Goicoechea et al. 2012, Manoj et al. 2013, Green et al. 2013, Dionatos et al. subm.). In those observations, two excitation temperature components are clearly present. The lower-T_{rot} component of $\sim 250 - 300$ K dominates mid-J transitions with $E_{\mathrm{u}}/k_{\mathrm{B}}$ below $\sim 1000-2000$ K. A higher-T_{rot} component of $\sim 500 - 1000$ K dominates high-J transitions with $E_{\mathrm{u}}/k_{\mathrm{B}}$ above ~ 2000 K. We call these components *warm* and *hot*, respectively, in order to distinguish them from the *cool* component, $T_{\mathrm{rot}} \sim 100$ K, observed in the $J < 14$ lines (van Kempen et al. 2009a, Yıldız
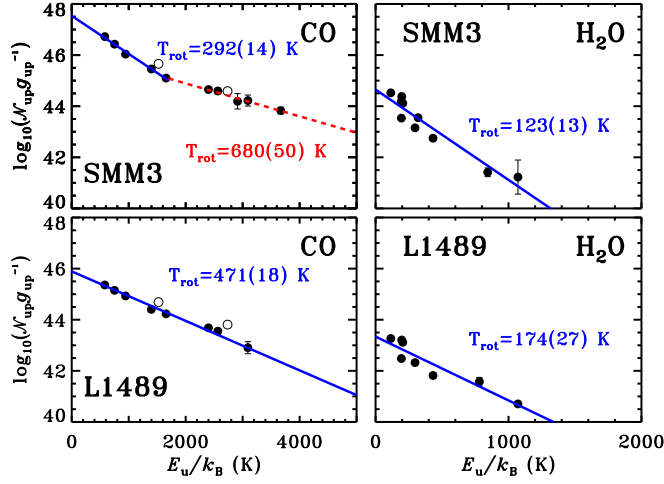
Figure 2.7 – CO (left panel) and H_2O (right panel) rotational diagrams for Ser SMM3 (Class 0) and L1489 (Class I) calculated using the total flux in lines measured in the PACS field-of-view. The base 10 logarithm of the number of emitting molecules from a level u, $\mathcal{N}_u$, divided by the degeneracy of the level, g_u, are written on the Y-axis. Two-component fits in the CO diagrams cover the transitions below and above $E_u/k_B \sim 1700$ K (CO 24-23) for the 'warm' and 'hot component' (see text). Each data point corresponds to one observed transition of a molecule. The limited number of lines observed in the line spectroscopy mode is responsible for the gaps in the otherwise linearly spaced CO diagrams. The error bars reflect the uncertainties in the fit

.

et al. 2012, Goicoechea et al. 2012). Motivated by these observations of complete CO ladders, we fit two linear components to our more limited set of CO data. The exceptions are L723, L1489, TMR1, and TMC1A, where there is no indication of the hot component in our dataset. The physical interpretation of these two components is discussed in §5.

As an example, the CO diagram of the Class 0 object Ser SMM3 in Figure 2.7 show a break around $E_u/k_B \sim 1200 - 2000$ K, with a rotational temperature for the warm component, T_{rot}(warm), of 292 ± 14 K and a rotational temperature for the hot component, T_{rot}(hot), of 670 ± 50 K. The error bars reflect the uncertainties given by the fit and include the uncertainties in individual line fluxes as given in Table A.2. The temperature fits include only relative flux uncertainties between lines and not the absolute flux uncertainty, which would shift the total luminosity up and down but would not change the temperature. The corresponding values for the Class I object L1489 are 405 ± 20 K and 480 ± 55 K for the warm and hot components, respectively. However, since a single temperature fit to these latter data is valid within the errors, one component fit is used to derive the temperature of 471 ± 20 K. As a result, the ratio of the number of emitting molecules of the hot CO over the warm CO is ~ 0.1 for Ser SMM3, whereas no value for hot CO can be given for L1489.

The rotational temperatures of warm and hot CO and H_2O, the numbers of emitting

Table 2.3 – CO and H_2O rotational excitation and number of emitting molecules $\mathcal{N}_u$ based on the full array data.

Source	Warm CO		Hot CO		H_2O	$\mathcal{N}_{CO}^{hot}/\mathcal{N}_{CO}^{warm}$
	$T_{rot}(K)$	$\log_{10}\mathcal{N}$	$T_{rot}(K)$	$\log_{10}\mathcal{N}$	$T_{rot}(K)$	
NGC1333-IRAS2A	310	49.1	. . .	. . .	(210)	. . .
NGC1333-IRAS4A	300	49.7	(390)	(49.4)	90	(0.5)
NGC1333-IRAS4B	340	49.6	820	48.7	200	0.1
L1527	(297)	(48.0)	(600)	(47.2)	70	(0.2)
Ced110-IRS4	(490)	(47.2)	(800)	(46.9)	90	(0.4)
BHR71	(370)	(49.4)	(550)	(49.0)	(140)	(0.4)
IRAS15398	280	48.9	(530)	(47.8)	50	(0.1)
L483	360	48.6	620	48.1	150	0.3
Serpens SMM1	350	49.9	690	49.0	150	0.1
Serpens SMM4	(260)	(49.5)	(690)	(48.3)	. . .	(0.1)
Serpens SMM3	290	49.6	660	48.6	130	0.1
L723	431	48.5	. . .	. . .	130	(0.4)
L1489	471	48.1	. . .	. . .	170	(0.8)
TMR1	470	48.3	. . .	. . .	170	(0.4)
TMC1A	420	47.9	. . .	. . .	. . .	. . .
TMC1	350	48.1	510	47.7	160	0.4
HH46	310	49.2	(630)	(48.3)	50	(0.1)
RNO91	(250)	(47.8)	. . .	. . .	(100)	. . .

Notes. Rotational temperatures and corresponding numbers of emitting molecules measured using less than 5 points are written in brackets (see Figures 2.F.1, 2.F.2, and 2.F.3). Non-detections are marked with ellipsis dots (. . .). In case of L723, L1489, TMR1, and TMC1A one component fit is used.

CO molecules and the ratio of hot over warm CO for all sources are tabulated in Table 3.2. The uncertainties due to the limited number of observed lines, associated with the fits and the selection of the break point are discussed in Appendix 2.H.

Median rotational temperatures of the CO warm component are 325 and 420 K for Class 0 and Class I sources, respectively (calculated using the unbracketed values from Table 3.2). The hot CO average temperature is ~700 K for the Class 0 sources; for the Class I sources the temperatures seem to be 100–200 K lower, but in general they are poorly constrained due to the limited detections. The median logarithm of the number of emitting CO molecules for the warm and hot components of Class 0 sources is 49.4 and 48.7, respectively. Therefore, about 16% of the CO molecules observed by PACS in Class 0 sources are hot.

The H_2O rotational diagrams of Class 0/I sources in Figure 2.7 show scatter in the single-temperature fits that significantly exceeds the measurement errors and is due to subthermal excitation and optical depth effects (Herczeg et al. 2012, see also Johnstone et al. 2003 for the case of CH_3OH). We refrain from calculating of the number of emitting
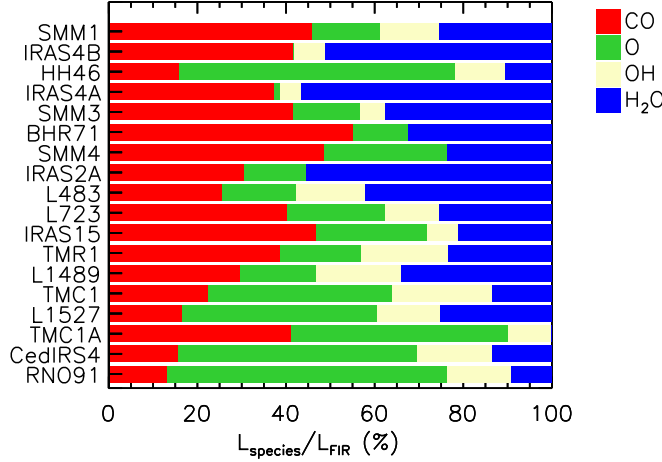
Figure 2.8 – Relative contributions of CO (red), [O I] (green), OH (yellow) and H_2O (blue) to the total far-IR gas cooling integrated over the entire PACS array are shown from left to right horizontally for each source. The objects are in the sequence of decreasing total gas far-IR cooling, L_{FIR}. Note that OH cooling is not available for BHR71 and Ser SMM4 and not measured in NGC1333-I2A. Water cooling is not calculated for TMC1A.

H_2O molecules because the high optical depths require orders of magnitude correction factors. Highly excited H_2O emission from at least some Class 0 and Class I sources is seen in the H_2O 8_{18}-7_{07} line at 63.3 μm (E_u/k_B=1071 K). The single rotational temperatures obtained from the fit to the H_2O diagrams in Figure 2.7 are ~120 K for the Class 0 source and ~170 K for the Class I source. Similarly low values of H_2O rotational temperatures are also obtained from full spectroscopy observations (Herczeg et al. 2012, Goicoechea et al. 2012). The fact that the H_2O rotational temperature is 100 K or higher already indicates that H_2O cannot be in the entrained outflow gas seen in ^{12}CO low$-J$ lines.

2.4.2   Far-infrared line cooling

The CO rotational temperatures of Class 0/I sources presented in §4.1 are used to estimate the flux in non-observed lines and to calculate the total far-infrared CO cooling. The extrapolation of the fluxes is limited to the transitions in the PACS range, from J=14-13 to J=49-48. This accounts for $\sim$ 80 % of the CO cooling calculated for the first 60 rotational transitions of CO (J 60, E_u/k_B 10006 K), used in CO cooling calculations by Nisini et al. (2002b) (see Appendix I). Additional line emission arising from the T_{rot} $\sim$ 100 K component seen in the CO J 13 with SPIRE (Goicoechea et al. 2012) and ground-based data (Yıldız et al. 2012) is not included in this estimation, because these lines probe a different physical component, the entrained outflow gas.

The far-IR cooling in H_2O lines is calculated by scaling the total H_2O flux observed

over the full PACS range towards NGC1333-IRAS4B and Serpens SMM1 (Herczeg et al. 2012, Goicoechea et al. 2012) to the limited number of lines observed here in the line spectroscopy mode. These two sources, even though both classified as Class 0, have very different water spectra, with IRAS4B showing numerous high-excitation water lines that are absent in Ser SMM1.

In the water rich source NGC1333-IRAS4B, the total luminosity of the water lines equals $2.6 \ 10^{-4} \ L_{\odot}$, whereas the luminosity calculated from the selected lines equals $1.0 \ 10^{-4} \ L_{\odot}$. For Serpens SMM1, where H_2O lines are much weaker as compared to CO, the total water luminosity observed in the PACS range equals $2.4 \ 10^{-4} \ L_{\odot}$, of which $1.1 \ 10^{-4} \ L_{\odot}$ is detected in the small set of lines observed in the line scan observations. Thus, the scaling factor from the line scan observations to the total far-IR water cooling, based on these two sources, is ~ 2.4[5].

Despite the obvious limitations of the method, which assumes similar gas properties for all the sources, it provides more reasonable values of the cooling than the extrapolation using the H_2O rotational temperature (see Appendix 2.H and 2.I). Indeed, as argued in Appendix I, the adopted scaling of the H_2O luminosity should be robust for a broad range of objects within the quoted uncertainties of ~30 %. As a further validation of our approach, the values derived for Class I sources in Taurus agree within 30% with the full range spectroscopy observations obtained in the DIGIT program (Lee et al., in prep.). H_2O cooling in the PACS range accounts for ~ 86 % of the total cooling in this molecule (from non-LTE large velocity gradient model of Serpens SMM1, Goicoechea et al. 2012).

For OH, a scaling factor of ~ 1.5 is derived based on the full scan observations of Ser SMM1 and IRAS4B, calculated in the same way as for H_2O. Fluxes of OH for all our sources are from (Wampfler et al. 2013).

The cooling in the [O I] lines is calculated as the sum of the observed fluxes in the 63 μm and 145 μm lines. Cooling in [C II] is omitted because the line emission is a minor contributor to the cooling budget (Goicoechea et al. 2012) and usually originates from extended cloud emission.

We use the definition of the total far-IR line cooling, L_{FIR}, adopted by Nisini et al. (2002b): $L_{FIR} = L_{O\,I} + L_{CO} + L_{H_2O} + L_{OH}$. The results of the calculations are summarized in Table 3.1 and illustrated in Figure 2.8, which shows the relative contributions to the total far-IR gas cooling, L_{FIR}, by different atomic and molecular species, individually for each object from our sample. Note that this definition does not include the contribution of H_2 near- and mid-infrared lines to the cooling. At off-source shock positions, H_2 can be a significant, and even dominant, gas coolant (Neufeld et al. 2009, Nisini et al. 2002a). However, at the much more obscured central source position, data on H_2 are generally not available. In case where they are, the H_2 mid-infrared emission (after extinction correction) is found to have a negligible contribution to the total cooling for Class 0 sources (Herczeg et al. 2012, Goicoechea et al. 2012).

H_2O, CO and [O I] are the most important gas cooling channels among the considered species. For the sources with the largest L_{FIR} in our sample (most of them are young Class

---

[5] For Ser SMM4 and BHR71, a scaling factor of ~ 10 is used. These two objects were observed in a limited number of settings and therefore the correction for the missing lines, so uncertainty, is larger with respect to other sources, with many more lines observed. The two sources are excluded from the analysis in §5.4.

Table 2.4 – Atomic and molecular far-IR line luminosities based on the full array data.

Source	L_{CO}	L_{H2O}	L_{OH}	L_{OI}	L_{FIR}
NGC1333-I2A	3.9	7.1	. . .	1.6	12.6
NGC1333-I4A	13.2	20.0	1.7	0.5	35.4
NGC1333-I4B	22.5	27.6	5	0.3	54.1
L1527	0.3	0.5	0.3	0.8	1.9
Ced110-IRS4	0.1	0.1	0.2	0.5	0.9
BHR71	12.1	7.1	. . .	2.8	22.0
IRAS15398	2.0	0.9	0.3	1.1	4.3
L483	1.7	2.8	1.0	1.1	6.7
Ser SMM1	42.8	23.6	11.5	14.3	93.1
Ser SMM4	7.4	3.6	. . .	4.2	15.2
Ser SMM3	10.5	9.5	1.4	3.9	25.3
L723	1.9	1.2	0.6	1.0	4.7
L1489	0.7	0.8	0.5	0.4	2.4
TMR1	1.0	0.6	0.5	0.5	2.6
TMC1A	0.5	. . .	0.1	0.6	1.2
TMC1	0.5	0.3	0.5	0.9	2.2
HH46	5.8	3.8	4.1	22.8	36.5
RNO91	0.1	0.1	0.1	0.5	0.8

Notes. All luminosities are in 10^{-3} $L_{\odot}$. Typical uncertainties are better than 30% of the quoted values. BHR71 and Ser SMM4 were not observed in the OH lines in our program, thus their OH luminosities are not available. OH is not detected in NGC1333-I2A and H_2O is not detected in TMC1A.

0 sources, except HH46), H_2O and CO clearly dominate the far-IR emission. [O I] is the most important coolant for those objects with relatively low L_{FIR} (and more evolved, except Ced110-IRS4). The relative contribution of H_2O is the highest for NGC1333-IRAS4A and IRAS4B, where it accounts for $\sim 50\%$ of L_{FIR}. The relative contribution of CO is the largest for Ser SMM1 and SMM3, where $\sim 40\%$ of L_{FIR} is emitted in this channel. [O I] dominates the far-IR emission in HH46 and RNO91 (both are Class I sources) with a relative contribution of $\sim 60\%$. The OH contribution to the total cooling is the highest for the Class I Taurus sources, in particular L1489, TMR1 and TMC1, where $\sim 20\%$ of the total cooling is done by OH. For the rest of the sources the typical OH contribution is $\sim 5 - 10\%$.

The Class I source HH46 was studied by van Kempen et al. (2010b), who used the central spaxel emission to determine relative contributions of 28, 22, 40, and 10% for CO, H_2O, [O I], and OH. Our results for this object, but using the full PACS array and correcting for the missing lines, yield: 16, 10, 63, and 11% for those species. This example illustrates that depending on the extent of emission in different molecular and atomic species, the derived values of the relative cooling can vary significantly, both between species and across the protostellar envelope. In HH46, a significant amount of the [O I] emission is found off-source and therefore in our calculations it is an even more significant cooling channel as compared to van Kempen et al. results (see Table 2.2 and Figure 2.D.1 in Appendix).

2.4.3 Flux correlations

To gain further insight into the origin of the emission of the various species, the correlation of various line fluxes is investigated. In addition, correlations between the far-infrared line cooling and other source parameters are studied. The strength of the correlations is quantified using the Pearson coefficient, r. The 3σ correlation corresponds to the Pearson coefficient of $r = 3/\sqrt{N-1}$, where N is the number of sources used for the calculation. For our sample of N=18 sources, $|r| < 0.7$ denotes a lack of correlation, $0.7 < |r| < 0.8$ a weak (3σ) correlation and $|r| > 0.8$ a strong correlation.

Figure 2.9 compares the luminosities in the H_2O 2_{12}-1_{01} line as a function of the CO 14-13, CO 24-23, [O I] 63.2 μm, and OH 84.6 μm line fluxes. Both the integrated luminosities over the 5×5 array and the central spaxels corrected for the missing flux according to standard PSF corrections are presented. Data for BHR71 and Ser SMM4 are not included since some lines are missing for these two sources.

A very tight correlation is found between the H_2O 2_{12}-1_{01} and the CO lines, both on large and on small scales ($r \sim 0.95$ for 5×5 fluxes and $r = 0.90$ for central spaxel luminosities). Thus, H_2O and CO – both in CO 14-13 and CO 24-23 – most likely arise in the same gas. OH also strongly correlates with H_2O, in particular on the larger scales ($r = 0.87$), where it very likely probes the same gas as CO and H_2O. However, on the central spaxel, the correlation between H_2O and OH weakens. The same results are found when the H_2O 3_{03}-2_{12} line is used ($E_u/k_B \sim 200$ K).

On the other hand, the [O I] 63 μm line luminosities do not correlate with the H_2O line luminosity, either on large or on small scales ($r = 0.42$ and $r = 0.21$, respectively).
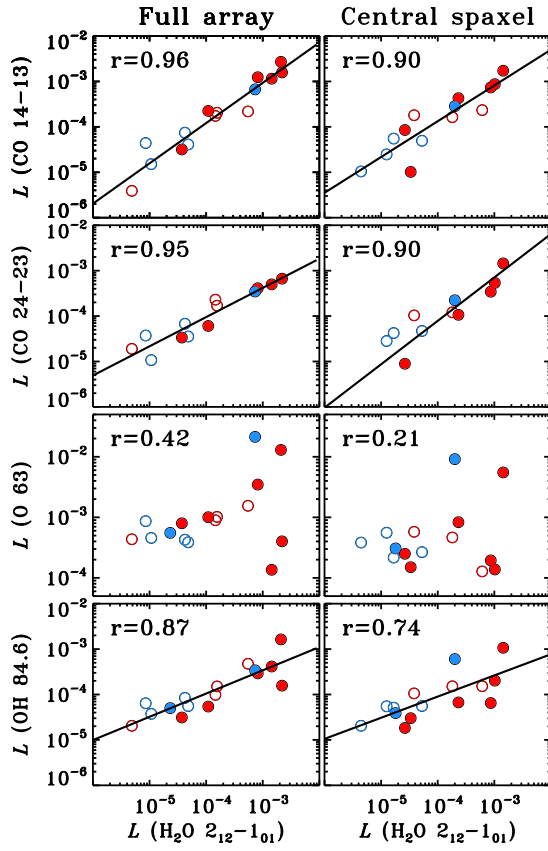
Figure 2.9 – Luminosity correlations between the H_2O 2_{12}-1_{01} line at 179.527 μm and (from top to bottom) CO 14-13, CO 24-23, [O I] at 63.18 μm, and OH at 84.6 μm, for 16 out of 18 objects (all luminosities in units of $L_\odot$). Full array and central spaxel luminosities are shown in the left and right columns, respectively. Red circles correspond to Class 0 sources and blue circles to Class I sources. Empty symbols show the *compact* sources, whereas filled symbols denote the *extended* sources. The Pearson coefficient of the correlation (r) is shown.
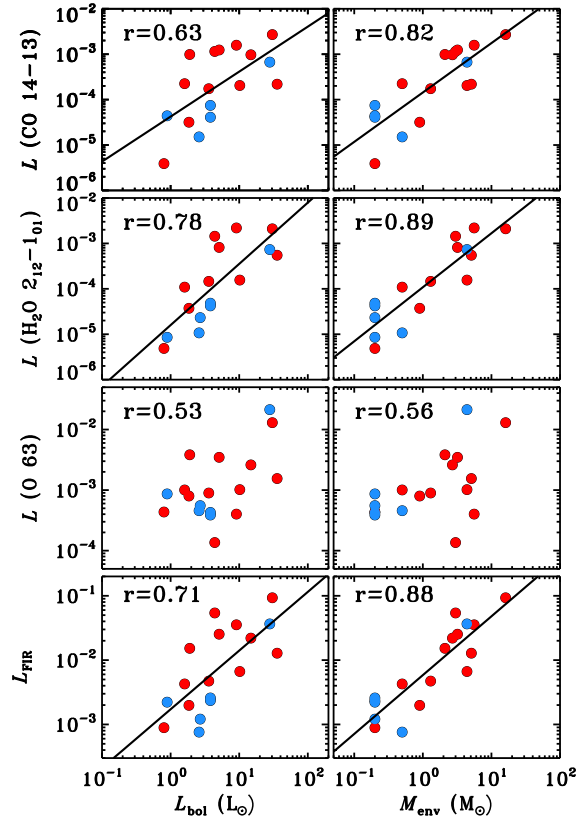
Figure 2.10 – Correlations of full array line emission with bolometric luminosity (left column) and envelope mass (right column) from top to bottom: CO 14-13, H_2O 2_{12}-1_{01}, [O I] at 63.2 μm line luminosities, and total far-IR gas cooling L_{FIR}.

Significant variations in the [O I] luminosities are found in particular for the H_2O-bright Class 0 sources. Similar results are obtained for the [O I] 145 μm line.

A strong correlation is also found between the two [O I] lines, at 63.2 and 145.5 μm ($r = 0.96$, see Figure 2.11). The observed ratios of the [O I] 63 μm / 145 μm lines vary from ~6 to ~26 with a median value of ~13 (see Table 2.5). Such a median line ratio corresponds to $n_H > 10^3$ cm^{-3} for optically thin lines excited by collisions with H_2 (see Figure 4 in Liseau et al. 2006). Line ratios of ~20, as observed for example in IRAS15398, L1489 and RNO91, are indicative of J-type shocks (Hollenbach & McKee 1989).

The median [O I] 63.2 to 145.5 flux ratio of ~10 for the Class 0 sources and ~16 for the Class I sources could imply stronger shocks for the more evolved sources. However, the
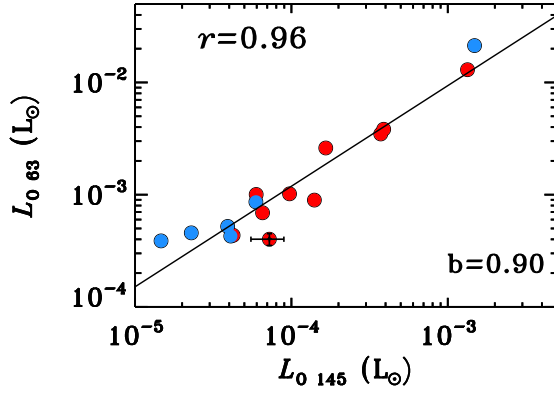
Figure 2.11 – Full array correlation between the [O I] line luminosities at 145 and 63 μm for 16 out of 18 objects (the [O I] 145 line is not detected in NGC1333-IRAS2A and 4B). Class 0 sources are shown in red and Class I sources in blue. A typical error is shown on the NGC1333-IRAS4A observation.

[O I] 63.2 flux may be suppressed for Class 0 sources because they have higher envelope masses and therefore higher extinctions than Class I sources (see also Herczeg et al. 2012, Goicoechea et al. 2012).

Mass loss rates can be derived directly from the luminosity of [O I] at 63 μm using the Hollenbach (1985) equation, $dM/dt = 10 \, L(\text{O I } 63)$, in units of 10^{-5} M$_\odot$ yr^{-1}. This formula assumes that the [O I] line traces the primary wind shock and that the shock is a major coolant, which is valid for pre-shock densities of 10^5 cm^{-3}. Mass loss rates calculated from this simple formula for our sources vary from 10^{-8} to 10^{-6} M$_\odot$ yr^{-1} and are the highest for Serpens SMM1 and HH46. Median values of the mass loss rate are 1 10^{-7} M$_\odot$ yr^{-1} and 0.5 10^{-7} M$_\odot$ yr^{-1} for Class 0 and Class I sources, respectively, which reflects the lower [O I] 63 μm line luminosities for the more evolved sources in Figure 2.11. In general, these values are in the same range as those of the entrained outflow material derived from low-J CO observations (Yıldız et al. in prep.). However, for some deeply-embedded and heavily extincted sources, e.g. NGC1333-IRAS4A, the low-J CO mass-loss rates are up to 2 orders of magnitude higher than those determined from the [O I] 63.2 line (see Yıldız et al. 2012 for low-J CO spectroscopy of NGC1333-IRAS4A).

Figure 2.10 shows the line luminosities of the CO 14-13, H$_2$O 2_{12}-1_{01}, and [O I] lines and the total far-IR line cooling L_{FIR} as functions of physical parameters: bolometric luminosity, L_{bol}, and envelope mass, M_{env} (for correlations with bolometric temperature and density at 1000 AU see Appendix G). Values for these parameters are taken from the physical models of Kristensen et al. (2012) and the results of this paper. The values of L_{bol} and M_{env} are not fully independent in our sample (a weak correlation exists, see Kristensen et al. 2012).

The CO and H$_2$O luminosities, as well as L_{FIR}, correlate with both L_{bol} and M_{env}.

Table 2.5 – Flux ratios of oxygen lines and inferred mass loss rates.

Object	F(O 63)/F(O 145)	dM/dt $(10^{-7}$ M$_\odot$ yr$^{-1})$
NGC1333-I2A	> 45.0	1.6
NGC1333-I4A	5.5	0.5
NGC1333-I4B	>15.8	0.1
L1527	10.6	0.8
Ced110-IRS4	10.3	0.5
BHR71	15.7	2.8
I15398	16.9	1.1
L483	10.5	1.1
Ser SMM1	9.7	14.3
Ser SMM4	9.8	4.2
Ser SMM3	9.3	3.9
L723	6.4	1.0
L1489	26.4	0.4
TMR1	10.4	0.5
TMC1A	13.3	0.6
TMC1	14.6	0.9
HH46	14.4	22.8
RNO91	20.0	0.5

The correlations are particularly strong when the envelope mass is used. However, no correlation is found for the [O I] fluxes and the [O I] line ratios with physical parameters.

2.5 Origin of far-IR line emission

The protostellar environment contains many physical components that can give rise to far-infrared line emission. As illustrated in Figure 5 of van Dishoeck et al. (2011), these include (i) the warm quiescent inner part of the envelope passively heated by the luminosity of the source (the 'hot core'); (ii) the entrained outflow gas; (iii) UV-heated gas along the cavity walls; (iv) shocks along the outflow cavity walls where the wind from the young star directly hits the envelope; (v) bow shocks at the tip of the jet where it impacts the surrounding cloud; (vi) internal working surfaces within the jet; and (vii) a disk embedded in the envelope. In the case of shocks, both C- and J-type shocks are possible. Spatially disentangling all of these components is not possible with the resolution of Herschel, but our data combined with velocity information from HIFI and physical-chemical models of the molecular excitation provide some insight into which components most likely dominate the emission (Visser et al. 2012, Herczeg et al. 2012).

Velocity-resolved spectra of ^{12}CO up to J_u=10 (Yıldız et al. 2010, 2012, Bjerkeli et al. 2011, Benedettini et al. 2012) and of several H$_2$O (Kristensen et al. 2010, Codella et al. 2010, Kristensen et al. 2011, 2012, Santangelo et al. 2012, Vasta et al. 2012) and OH (Wampfler et al. 2011) lines indicate that the bulk of the far-infrared emission has broad

51

line wings with $\Delta v > 15$ km s^{-1}. The quiescent warm inner envelope is primarily seen in the narrow ($\Delta v \lesssim 5$ km s^{-1}) ^{13}CO and C^{18}O isotopolog mid-J spectra centered at the source position but this component does not contribute to H$_2$O emission. The broad line wings combined with the spatial extent of both CO and H$_2$O beyond the central spaxel (i.e., beyond 1000 AU) argue against the hot core (option (i)) and the disk (option (vii)) being the main contributors, at least for the *extended* sources. Internal jet shocks (option (vi)) have high-velocity shifts of 50 km s^{-1} or more. While such fast-moving gas is seen in some [O I] (van Kempen et al. 2010b, and §3.3) and HIFI H$_2$O spectra (Kristensen et al. 2011), it is only a minor fraction of the total emission for our sources (based on a lack of extremely-high velocity (EHV)/ bullet emission in HIFI spectra) and is ignored here. Our maps are generally not large enough to cover the bow shocks at the tip of the outflow, ruling out option (v).

For these reasons, the far-infrared line emission seen here most likely originates in the *currently* shocked and UV-heated gas along the cavity walls in the protostellar environment (options (iii) and (iv)). This warm and hot gas should be distinguished from the cooler entrained outflow gas with rotational temperatures of ~100 K traced by ^{12}CO line wings up to $J_u \approx 10$ (Yıldız et al. 2012, option (ii)). Visser et al. (2012) developed a physical model that includes a passively heated envelope, UV-heated outflow cavity walls and heating by small-scale C-shocks. The model successfully reproduces emission from the central spaxel in three sources (emission from other spaxels was not included in the models). The cavity walls, carved by the outflows, are illuminated by the UV from the protostellar accretion shocks at the star-disk boundary although UV produced by shocks inside the cavity itself can also contribute (Spaans et al. 1995, van Kempen et al. 2009a). The small-scale C-type shocks are produced when the protostellar wind hits the outflow cavity walls and locally increases the gas temperature to more than 1000 K, driving much of the oxygen into water (Kaufman & Neufeld 1996). The UV-heated gas can provide ^{12}CO emission up to $J_u \sim 20$ depending on source parameters. Evidence for UV-heated gas also comes from strong extended ^{13}CO mid$-J$ emission along the cavity walls (van Kempen et al. 2009a, Yıldız et al. 2012). In contrast, shocks are predicted to produce the bulk of high-J CO (J 20) and all of the H$_2$O in the PACS range (Visser et al. 2012). The importance of the UV-heating was suggested to increase with evolutionary stage in the three sources studied by Visser et al. (2012), whereas the shock emission weakens for the more evolved sources. Qualitative analysis of the [O I] and OH distribution in one case, HH46, argued for a separate dissociative J-type shock centered on the source to explain the detected emission (van Kempen et al. 2010b).

In the following subsections, we seek to test these model predictions qualitatively against the new observations and for a larger sample. As we will see, the UV-heated component contributes less to the observed PACS lines than thought before. Also, evolutionary trends will be explored and compared to previous ISO observations (Giannini et al. 2001, Nisini et al. 2002b).

2.5.1 Spatial extent of line emission and correlations

The molecular and atomic far-IR emission is commonly observed to be extended along the outflow direction which is consistent with the above picture of the emission being associated with the cavity walls. The physical scales of the extent are $\sim 10^4$ and $\sim 10^3$ AU for the *extended* and *compact* groups, respectively.

Most of the extended sources are well-known Class 0 objects primarily known for their large-scale outflows. The extended emission seen in high$-J$ CO and H_2O transitions is therefore most likely associated directly with shocks that are currently taking place in the outflows. A few Class 0 sources famous for their large-scale outflows, e.g., BHR71 and NGC1333-IRAS2A, are found in the compact group. Those outflows extend well beyond the PACS field of view mapped here and their active outflow hot spots are not covered in our data. The excitation conditions for high$-J$ CO and H_2O emission in the outflow shocks have been determined recently in several studies based on PACS and HIFI observations (e.g., Tafalla et al. 2013, Santangelo et al. 2012, Vasta et al. 2012, Benedettini et al. 2012, Bjerkeli et al. 2012, Lefloch et al. 2012a, Codella et al. 2012a). All studies conclude that only a combination of high density and temperature can account for the observed intensities. In that respect, the dense, extended envelopes surrounding the Class 0 objects provide the ideal excitation conditions for extended sources (Kristensen et al. 2012).

The compact group contains most Class I objects in our sample and objects with outflows seen nearly face-on (e.g. Ced110-IRS4). The envelopes surrounding Class I objects are less dense than around Class 0 objects (Jørgensen et al. 2002, Kristensen et al. 2012), and thus less conducive to high$-J$ CO and H_2O excitation except close to the source itself. Their outflows are generally compact.

The fact that both the CO 14-13 and 24-23 fluxes as well as the H_2O 2_{12}-1_{01} and CO 14-13 fluxes correlate very strongly with each other, both in the 5×5 and central spaxels (Figure 2.9), and also show a similar spatial distribution, strengthens the conclusion that the H_2O and mid/high-J CO emission originate in the same physical component. Such strong H_2O emission can only originate in non-dissociative shocks (Neufeld & Dalgarno 1989). Thus, the observed correlation suggests that most of the H_2O and CO emission arises in shocks and that only a minor fraction of the CO 14-13 emission originates in the UV-heated gas. Velocity-resolved line profiles of the CO 14-13 (or neighboring CO lines such as CO 16-15) are needed to quantify the relative contributions of UV heating and shocks to the mid-J CO line profiles. For the single case for which such HIFI data are available in the WISH program, Ser SMM1, the line profile decomposition indicates that $\sim$25±4% of the flux comes from UV heated gas, but this number may vary from source to source (Kristensen et al. in prep.).

The fact that H_2O and CO emission is sometimes extended in a different manner (L1527, L483 and NGC1333-IRAS4A) (see §3.2) could be due to a variety of reasons, including asymmetric densities and UV fields across the core. Different densities on the two sides could be caused by irregularities or gradients of the surrounding cloud material distribution (Liu et al. 2012, Tobin et al. 2011) and can lead to different excitation of the molecules. The density also affects the penetration of the UV field, which in turn

53
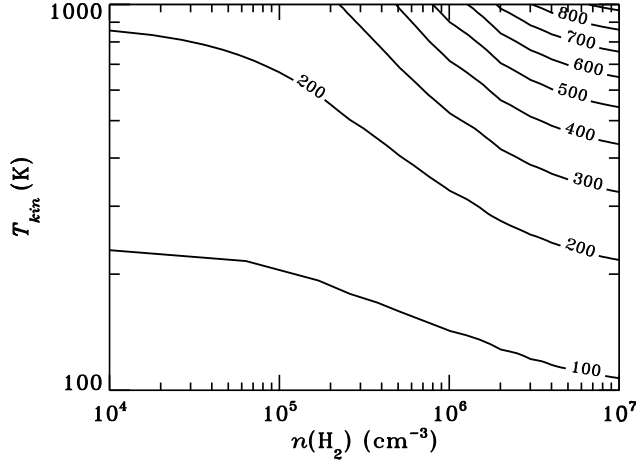
Figure 2.12 – CO rotational temperature $T_{\rm rot}$ from J=15–14 to 25–24 as a function of density $n_{\rm H}$ and temperature of the emitting gas derived from non-LTE excitation calculations.

results in abundance variations. For example, the UV field from the star-disk boundary can readily photodissociate the H_2O molecule but is not hard enough to dissociate CO. Higher extinction towards the red outflow lobe, as found for NGC1333-IRAS4B (Herczeg et al. 2012), can also result in different fluxes towards the two outflow lobes, but this should affect all species similarly as long as lines at similar wavelengths are compared.

The [O I] emission is usually extended along the outflow direction and resembles the pattern of the OH extent. In the two exceptions, L1527 and HH46, the [O I] is extended but the OH emission is seen only at the source position (see Table 2.2). For the *compact* sources, both [O I] and OH consistently peak together at the central position. Together with a weaker correlation of OH with H_2O and no correlation of [O I] with H_2O (Figure 2.9) as well as a strong correlation between [O I] and OH (Wampfler et al. 2013), this confirms the early conclusion that [O I] and at least part of the OH have a common origin. The [O I] and OH emission is most likely produced by dissociative shocks, in contrast to the non-dissociative shocks which explain the CO and H_2O emission (see Section 5.3).

2.5.2 Excitation

A remarkable observational finding is the rather constant CO rotational temperature of ~300 K for the warm component, as well as the common presence of a hotter component (see also Manoj et al. 2012, Green et al. subm.). In order to assess the physical conditions that could reproduce the observed $T_{\rm rot}$ of the warm component, non-LTE molecular excitation models were run for hydrogen densities of $n(H_2)$=$10^4 - 10^7$ cm^{-3} and kinetic temperatures of $T_{\rm kin} = 10^2 - 10^3$ K using RADEX (van der Tak et al. 2007) (see Figure 2.12). The ratio of column density and the line width N(CO)/ΔV, which enters the escape

probability calculation, is chosen such that the emission is optically thin. CO transitions from $J = 15 - 14$ to $J = 25 - 24$ are modeled using the high$-T$ collisional rate coefficients from Yang et al. (2010), extended by Neufeld (2012). The transitions are plotted as rotational diagrams and fitted with one rotational temperature, corresponding to the warm component.

The inferred physical conditions cover a broad range of T_{kin} and $n(H_2)$ (Figure 2.12). The range of possible scenarios can be described by two limiting solutions: (i) CO is subthermally excited in hot (T_{kin} 10^3 K), low-density ($n(H_2)$ 10^5 cm^{-3}) gas (Neufeld 2012, Manoj et al. 2012); or (ii) CO is close to LTE in warm ($T_{kin} \sim T_{rot}$) and dense ($n(H_2) > n_{crit} \sim 10^6$ cm^{-3}) gas. We favor the latter interpretation based on the strong association with H_2O emission and the high densities needed to excite H_2O (see §5.1 and Herczeg et al. 2012).

If H_2O and CO indeed co-exist, the low rotational temperatures of H_2O ($T_{rot} \sim 100 - 200$ K) as compared to those of CO ($T_{rot} \sim 300 - 750$ K) indicate sub-thermal excitation of H_2O, because the critical density of H_2O is higher than that of high$-J$ CO by 1–2 orders of magnitude (depending on J level; e.g. $n_{crit} \sim 10^6$ for CO 14-13 and $\sim 10^8$ cm^{-3} for H_2O 2_{12}-1_{01}). RADEX simulations of optically thick H_2O (see Herczeg et al. 2012 and Figure B.1 in Kristensen et al. 2011) indicate densities $n_H > 10^6$ cm^{-3} to reproduce our observed H_2O rotational temperatures. This clearly favors the high-density, moderately high-temperature solution (ii) for the CO excitation. The actual gas density very likely lies between the CO and H_2O critical densities if CO is assumed to be close to thermally excited, i.e., between a few 10^6 cm^{-3} to $10^8 - 10^9$ cm^{-3}. Such high densities are only found within a few hundred AU of the protostar or at shock positions where the gas is strongly compressed (Tafalla et al. 2013, Santangelo et al. 2012, Vasta et al. 2012). The hot CO component is not modeled in this work because it is less well defined than in other studies, which have larger samples of sources with complete 55-200 μm PACS spectra (see Manoj et al. 2012). However, as is clear from Fig. 2.12, $T_{rot} \sim 450 - 800$ K requires even warmer and higher density gas in our scenario (ii).

In the alternative solution (i) in which the entire CO far-infrared ladder comes from low-density, very high-temperature, high column density material (Neufeld 2012), the question arises where this gas is located in the protostellar environment. The only region close to the protostar (within the PACS central spaxel) where gas densities are lower than $\sim 10^5$ cm^{-3} is *inside* the outflow cavities. If the CO and H_2O emission were to originate from the jet itself, velocity shifts of the high$-J$ CO and H_2O lines would be expected in the short-wavelength parts of PACS spectra, where the spectral resolution is the highest. As discussed in §3.3, we do not see clear evidence for velocity shifts of 100 km s^{-1} or more in short-wavelength H_2O and CO lines. Low velocity emission from inside the cavity can originate from dusty disk winds (Panoglou et al. 2012), but more modeling is required to determine whether the line fluxes and profiles can be reproduced in this scenario. Moreover, this explanation would raise the question why there is no contribution from shocks along the higher density cavity walls, which surely must be present as well.

55
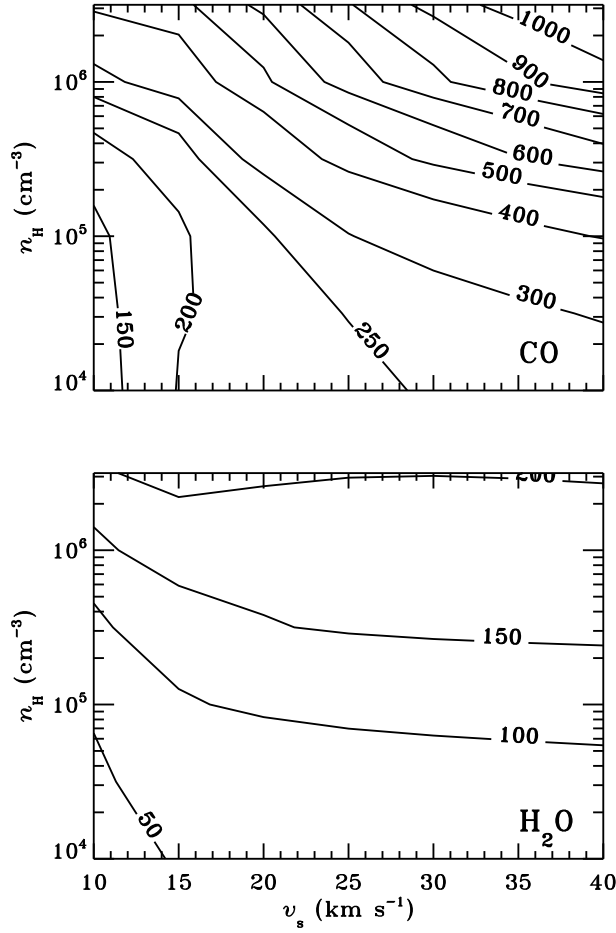
Figure 2.13 – Rotational temperature of CO (top) and H_2O (bottom) as a function of different shock velocities and pre-shock densities from the shock model results of Kaufman & Neufeld (1996). The rotational temperature is calculated from J=15-14 to 25-24 for CO and for the eight H_2O lines commonly observed in this sample.

2.5.3 Comparison with shock models

The association of the CO and H_2O emission with warm dense shocked gas can be further strengthened by comparison with shock models. H_2O and CO are efficiently excited in non-dissociative C-type shocks (Kaufman & Neufeld 1996, Bergin et al. 1998, Flower & Pineau des Forêts 2010). The models by Visser et al. (2012) used the output of the Kaufman & Neufeld (1996) models to compute line fluxes along the cavity walls. To test our full data set against these models and further explore parameter space, rotational temperatures were computed from the grid of Kaufman & Neufeld (1996) model fluxes and presented in Figure 2.13. The results show that CO excitation temperatures $T_{rot} \approx$ 300 K for J=15–25 are readily found for pre-shock densities of $\sim 3 \cdot 10^4 - 10^6$ cm^{-3} and a wide range of shock velocities. Similar results are obtained for the H_2O excitation temperatures: the observed values of 100–200 K correspond to the pre-shock densities of $\sim 10^5 - 10^6$ cm^{-3} and do not constrain the shock velocities.

The density probed by the CO and H_2O lines is not the pre-shock density; by the time CO and H_2O cooling becomes important, the gas has been compressed by the shock front and a more relevant density is the post-shock density (Flower & Pineau des Forêts 2010). The compression factor, n_{post} / n_{pre}, is $\sqrt{2} \times M_A$, where M_A is the Alfven Mach number, v_{shock} / v_A, and v_A is the Alfven velocity (Draine & McKee 1993). The Alfven velocity is $v_A = B / \sqrt{4\pi\rho} = 2.18$ km s^{-1} $b / \sqrt{\mu_H}$ where ρ is the pre-shock density, $\rho = \mu_H \, m_H \, n_{pre}$; the latter relation comes from the assumption that the magnetic field is frozen into the pre-shock gas and is $B = b \sqrt{n_{pre} \, [\text{cm}^{-3}]}$ μGauss. For a mean atomic weight, μ_H, of 1.4, the compression factor is

$$\frac{n_{post}}{n_{pre}} = \sqrt{2} M_A = \sqrt{2} \frac{v_{shock}}{v_A} \qquad (2.3)$$

$$= \sqrt{2} \frac{v_{shock}}{2.18 \, b / \sqrt{\mu_H}} = 0.78 \times v_{shock}/b \,. \qquad (2.4)$$

For a standard value of $b = 1$, the compression factor is thus $\gtrsim 10$ for all the shock velocities considered here, implying that the relevant post-shock densities are all $\gtrsim 10^6$ cm^{-3} as also shown by the RADEX results (Figure 13). At high velocities, ~ 50 km s^{-1}, the post-shock densities are greater than 10^7 cm^{-3} and the emission is in LTE.

Density is clearly the critical parameter: higher T_{rot} require higher pre-shock densities which in turn lead to higher post-shock densities. Thus, this shock model analysis is consistent with that presented in §5.2 and with the typical pre-shock densities found in the inner envelope. The presence of UV radiation in the outflow cavity may affect the shock structure, however, and new irradiated models are required to fully test this scenario (Kaufman et al., in prep.). With the addition of UV, some OH emission is very likely also produced by photodissociation of H_2O.

A large fraction of the [O I] and some OH emission must originate in a different physical component. Because the emission from these species does not correlate with that of CO and H_2O, especially in the central spaxel, their origin is most likely in dissociative shocks rather than non-dissociative C- or J-type shocks. In particular, the absolute flux
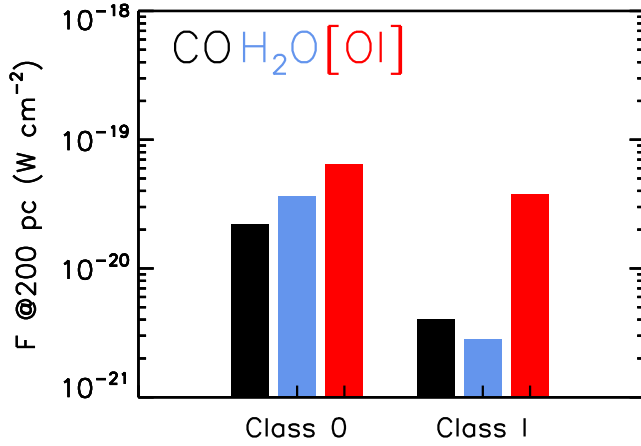
Figure 2.14 – Median line flux of the CO 14-13, H_2O 2_{12}-1_{01}, and [O I] $^3P_1 - ^3P_2$ lines for Class 0 and I objects from our sample are shown from left to right for each class in black, blue and red, respectively.

of [O I] is generally too high to be produced in non-dissociative, C-type shocks (Flower & Pineau des Forêts 2010). Dissociative shocks are typically found at the terminal bow shock where the >100 km s^{-1} jet rams into the surrounding cloud, but they can also be located closer to the protostar where the protostellar wind impacts directly on the dense inner envelope near the base of the wind (van Kempen et al. 2010b). In dissociative shocks, [O I] and OH emission greatly dominate over that of H_2O as molecules are gradually reformed in the dense post-shock gas (Neufeld & Dalgarno 1989). Some emission may also arise in the jet itself, as evidenced by the velocity shifts of ~100 km s^{-1} of the [O I] line in a few sources (Figure 2.6), but this is usually a minor component according to our data.

2.5.4 Evolution from Class 0 to Class I

Class 0 and Class I objects are relatively short phases of protostellar evolution (0.16 and 0.54 Myr, respectively, see Evans et al. 2009), yet our far-IR observations reveal a significant change in their spectral line characteristics. In the following, evolutionary trends of line fluxes, spatial extent, excitation and far-infrared gas cooling are discussed.

Figure 5.3 shows the median fluxes of the CO 14-13, H_2O 2_{12}-1_{01}, and [O I] $^3P_1 - ^3P_2$ lines for the 12 Class 0 and 6 Class I sources. Although the Class I sample is small, a factor of 5 decrease is observed in the CO and H_2O fluxes for the more evolved sources. These trends indicate that the molecular emission decreases quickly with evolution, whereas atomic emission remains similar. One explanation could be that molecular abundances are lower due to enhanced photodissociation as the envelope becomes more dilute. When the average density of the envelope drops (see Kristensen et al. 2012 for our sources), UV
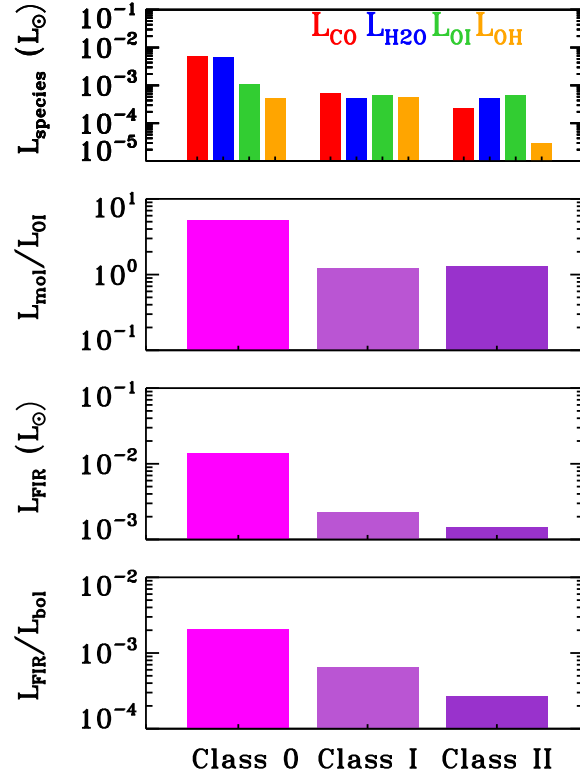
Figure 2.15 – *Panel 1:* Median cooling in CO, H$_2$O, OH, and [O I] lines for Class 0, I, and II objects are shown from left to right for each class in red, blue, orange and green colors, respectively. (Class II data from Podio et al. 2012.). *Panel 2:* Evolution of the ratio of molecular and atomic cooling. *Panel 3:* Evolution of the median total far-IR gas cooling. *Panel 4:* Evolution of the median total far-IR gas cooling over bolometric luminosity.

Table 2.6 – Median molecular and atomic luminosities for Class 0, I, and II sources.

Species	Class 0	Class I	Class II
L_{CO}	5.7	0.6	0.25
L_{H2O}	5.3	0.5	0.45
L_{OH}	0.4	0.5	0.03
L_{OI}	1.1	0.5	0.55
L_{mol}	11.0	1.6	0.73
L_{FIR}	14.0	2.3	1.45
L_{mol}/L_{OI}	5.2	1.2	1.3
L_{FIR}/L_{bol}	2.1	0.6	0.27

Notes. Luminosities are expressed in 10^{-3} $L_{\odot}$. Percent of the total FIR cooling is given for each species and total molecular cooling in brackets. Class II data are taken from Podio et al. (2012).

photons penetrate more readily and on larger spatial scales, thus dissociating more H_2O and OH to form O. This scenario was originally put forward by Nisini et al. (2002b).

An alternative explanation could be that the molecules are less excited because of the lower densities. The strong correlation of the line fluxes with M_{env} would be consistent with this option. Also, comparison of CO rotational temperatures for Class 0 and I sources shows that the former are characterized by higher temperatures of the hot component, possibly due to the higher densities. The warm component rotational temperatures of CO are remarkably constant for all sources, however. The rotational temperature of H_2O tends to increase for the Class I sources and is mainly due to the hot water detections in the Taurus objects. Since there are only 6 Class I sources in this sample it is difficult to examine how robust the high H_2O rotational temperatures are for the Class I sources, although these lines are now also seen in some Class II sources (Riviere-Marichalar et al. 2012). Dust extinction could hide the highly-excited H_2O lines at shorter wavelengths in the more embedded Class 0 sources (Herczeg et al. 2012). Disks may also contribute to the far-IR emission seen from some Class I sources but are most likely entirely obscured at short wavelengths by the more massive envelopes around Class 0 sources.

The evolution of the far-infrared gas cooling in CO, H_2O, OH, and [O I] is presented in Figure 2.15. Our calculations for Class 0 and I sources are supplemented by results from Podio et al. (2012) for the Class II sources (average cooling of DG Tau A and RW Aur) that drive prominent jets. Similar to the selected line flux trends, a factor of 10 decrease in the CO and H_2O cooling is detected for the Class I sources as compared to the Class 0 objects. Further decrease, although much less, is seen for the Class II objects. The absolute values of the OH cooling are similar in the Class 0 and I objects, but they decrease by a factor of 10 for the Class II objects. Cooling in [O I] does not change that dramatically in the three classes: a factor of 2 lower for Class I and II sources with respect to the Class 0 sources.

As a result, the relative contribution to the total cooling by different species changes significantly in the course of the embedded phase of evolution. In the earliest phase, CO

and H_2O dominate the total gas cooling with only a minor contribution from OH and [O I]. In the more evolved Class I phase, all species considered here contribute almost equally to the total gas cooling. The evolution of the total molecular cooling, L_{mol}, where $L_{mol} = L_{CO} + L_{H_2O} + L_{OH}$ with respect to atomic cooling, L_{OI}, shows a significant decrease by a factor of ~ 5 between Class 0 and I sources. In the Class II sources, [O I] is the main coolant among the considered species, followed by CO and H_2O. These conclusions are robust within the uncertainties of our calculations of the total luminosities. As discussed in §4.2, this discussion excludes any potential contribution from H_2 cooling.

Similarly, the total far-infrared gas cooling and the total cooling over the bolometric luminosity decrease with evolutionary stage, most drastically between the Class 0 and Class I phases. These results agree with the *ISO* observations of 17 Class 0 and 11 Class I sources (Giannini et al. 2001, Nisini et al. 2002b). The decrease in molecular emission was attributed to the less powerful jet impacting the lower-density envelope of the more evolved sources (Nisini et al. 2002b). Our results show that density may be more important than shock velocity in controlling the emission (see Figure 2.13).

2.6 Conclusions

We have characterized the *Herschel*/PACS spectra of 18 deeply embedded low-mass protostars. The spatially resolved information allows us to link the emission in different species with the physical components of a young stellar object and study the spatial scales over which the object interacts with its surroundings. The conclusions are as follows:

1. Emission from the H_2O $2_{12} - 1_{01}$ line at 179.5 μm ($E_u/k_B = 114$ K) is detected towards all Class 0 and I YSOs from our sample. The highly excited H_2O 8_{18}-7_{07} line ($E_u/k_B = 1071$ K) at 63.3 μm is detected in 7 out of 18 sources, in both Class 0 and I objects. CO lines are detected from $J = 14 - 13$ up to $J = 48 - 47$.

2. Emission in the H_2O, CO, OH and [O I] lines is extended along the outflow directions mapped in lower-J CO emission. The extent of emission covers the PACS array in the outflow direction for half of our sources (*extended* sample), which accounts for a region of $\sim 10^4$ AU. The rest of the sources show compact emission limited mostly to the central spaxel (a region of $\sim 10^3$ AU) (*compact* sample). The *extended* sample is dominated by Class 0 sources with evidence for active shocks ('hot spots') currently taking place along the outflow.

3. Fluxes of the H_2O $2_{12} - 1_{01}$ line and the CO $14 - 13$ and $24 - 23$ lines are strongly correlated with each other as well as with the physical source parameters L_{bol} and M_{env} suggesting they arise in the same physical component. In contrast, H_2O and CO fluxes correlate less strongly with the OH, in particular on small scales, and not at all with the [O I] line fluxes.

4. Rotational diagrams of CO show two distinct components – the *warm component* with T_{rot1} ~350 K and the *hot component* with $T_{rot2} \sim 700$ K. The hot component is weaker for Class I sources. Rotational diagrams of H_2O show scatter due to

61

subthermal excitation and optical depth effects and are characterized by $T_{\mathrm{rot1}} \sim 150$ K for all sources, with a tendency for higher temperatures for Class I sources.

5. CO and H_2O are argued to arise in non-dissociative shocks along the outflow walls with a range of pre-shock densities. UV heating appears to play a minor role in the excitation of these PACS lines but affects the shock structure and chemistry by dissociating H_2O to OH. These shocks are most likely responsible for the warm CO component. The origin of the hot CO component requires further data and analysis.

6. [O I] and part of the OH originate largely in dissociative shocks at the point of direct impact of the wind on the dense envelope. Only a few sources show high-velocity [O I] emission tracing a hidden atomic jet.

7. H_2O is a major coolant among the observed far-IR lines and accounts for 25 to 50% of the total far-IR gas cooling, L_{FIR}. CO is the other important coolant with a contribution of 5 to 50 % to L_{FIR}. The [O I] contribution to the total cooling accounts for 5-30% and increases for the more evolved sources, whereas 1-15% is radiated in the OH lines.

8. Weaker emission in the molecular lines for the more evolved sources can result either from lower envelope densities resulting in less excitation or from lower abundances of the molecules due to enhanced photodissociation. Both aspects very likely play a role, but density is plausibly the critical factor in controlling the line emission.

Acknowledgements

Appendix

2.A   Targeted lines and measurements

Table 2.A.1 lists the species and transitions observed in the PACS range with the line spectroscopy mode in the decreasing wavelength order. Information about the upper level energies, E_u/k_B, the Einstein coefficients, A, the weights, g_{up}, and frequencies, ν, are obtained from the Cologne Database for Molecular Spectroscopy (Müller et al. 2001, 2005), the Leiden Atomic and Molecular Database (Schöier et al. 2005) and the JPL Catalog (Pickett et al. 1998).

Tables 2.A.2 and 2.A.3 list line fluxes for all our sources in units of 10^{-20} W cm^{-2}. The uncertainties are 1σ measured in the continuum on both sides of each line; calibration uncertainty of 30% of the flux should be included for comparisons with other modes of observations or instruments.

Table 2.A.1 – Lines observed in the line spectroscopy mode.

Species	λ_{lab} (μm)	E_u/k_B (K)	A (s^{-1})	g_{up}	ν (GHz)
CO 14-13	185.999	580.49	2.739(-4)	29	1611.7935
o-H$_2$O 2_{21}-2_{12}	180.488	194.093	3.065(-2)	15	1661.0076
o-H$_2$O 2_{12}-1_{01}	179.527	114.377	5.599(-2)	15	1669.9048
o-H$_2$O 3_{03}-2_{12}	174.626	196.769	5.059(-2)	21	1716.7697
OH $\frac{3}{2},\frac{1}{2}$-$\frac{1}{2},\frac{1}{2}$	163.398	269.761	2.121(-2)	4	1834.7355
OH $\frac{3}{2},\frac{1}{2}$-$\frac{1}{2},\frac{1}{2}$	163.131	270.134	2.133(-2)	4	1837.7466
CO 16-15	162.812	751.72	4.050(-4)	33	1841.3455
[O I] $^3P_0$ $-^3$ P_1	145.525	326.630	1.750(-5)	1	2060.0691
CO 18-17	144.784	944.97	5.695(-4)	37	2070.6160
p-H$_2$O 8_{44}-7_{53}	138.641	1628.371	1.188(-2)	17	2162.3701
p-H$_2$O 3_{13}-2_{02}	138.528	204.707	1.253(-1)	7	2164.1321
p-H$_2$O 4_{04}-3_{13}	125.354	319.484	1.730(-1)	9	2391.5728
OH $\frac{5}{2},\frac{3}{2}$-$\frac{3}{2},\frac{3}{2}$	119.442	120.460	1.361(-2)	6	2509.9355
OH $\frac{5}{2},\frac{3}{2}$-$\frac{3}{2},\frac{3}{2}$	119.235	120.750	1.368(-2)	6	2514.2988
CO 22-21	118.581	1397.39	1.006(-3)	45	2528.1721
p-H$_2$O 5_{33}-5_{24}	113.948	725.097	1.644(-1)	11	2630.9595
o-H$_2$O 4_{14}-3_{03}	113.537	323.492	2.468(-1)	27	2640.4736
CO 23-22	113.458	1524.20	1.139(-3)	47	2642.3303
CO 24-23	108.763	1656.48	1.281(-3)	49	2756.3875
o-H$_2$O 2_{21}-1_{10}	108.073	194.093	2.574(-1)	15	2773.9766
CO 29-28	90.163	2399.84	2.127(-3)	59	3325.0054
p-H$_2$O 7_{44}-7_{35}	90.050	1334.815	3.549(-1)	15	3329.1853
p-H$_2$O 3_{22}-2_{11}	89.988	296.821	3.539(-1)	7	3331.4585
CO 30-29	87.190	2564.85	2.322(-3)	61	3438.3645
o-H$_2$O 7_{16}-7_{07}	84.767	1013.206	2.131(-1)	45	3536.6667
OH $\frac{7}{2},\frac{3}{2}$-$\frac{5}{2},\frac{3}{2}$	84.596	290.536	4.883(-1)	8	3543.8008
OH $\frac{7}{2},\frac{3}{2}$-$\frac{5}{2},\frac{3}{2}$	84.420	291.181	2.457(-2)	8	3551.1860
CO 31-30	84.411	2735.30	2.525(-3)	63	3551.5923
o-H$_2$O 6_{16}-5_{05}	82.032	643.496	7.517(-1)	39	3654.6033
CO 32-31	81.806	2911.18	2.735(-3)	65	3664.6843
CO 33-32	79.360	3092.47	2.952(-3)	67	3777.6357
OH $\frac{1}{2},\frac{1}{2}$-$\frac{3}{2},\frac{3}{2}$	79.182	181.708	2.933(-2)	4	3786.1318
OH $\frac{1}{2},\frac{1}{2}$-$\frac{3}{2},\frac{3}{2}$	79.116	181.936	5.818(-3)	4	3789.2703
p-H$_2$O 6_{15}-5_{24}	78.928	781.120	4.555(-1)	13	3798.2817
o-H$_2$O 4_{23}-3_{12}	78.7423	432.154	4.865e-01	27	3807.2585
CO 36-35	72.843	3668.82	3.639(-3)	73	4115.6055
p-H$_2$O 8_{17}-8_{08}	72.032	1270.28	3.050(1)	17	4161.9189
o-H$_2$O 7_{07}-6_{16}	71.947	843.47	1.161(0)	45	4166.8511
CO 38-37	69.074	4080.03	4.120(-3)	77	4340.1382
o-H$_2$O 8_{18}-7_{07}	63.324	1070.683	1.759	51	4734.2959
[O I] $^3P_1$ $-^3$ P_2	63.184	227.713	8.914(-5)	3	4744.7773
p-H$_2$O 4_{31}-4_{04}	61.809	552.263	2.383(2)	9	4850.3345
p-H$_2$O 7_{26}-6_{15}	59.987	1020.967	1.350	15	4997.6133
CO 44-43	59.843	5442.39	5.606(-3)	89	5009.6079
CO 46-45	57.308	5939.20	6.090(-3)	93	5231.2744
p-H$_2$O 4_{31}-3_{22}	56.325	552.263	1.463	9	5322.5459
o-H$_2$O 5_{32}-5_{05}	54.507	732.066	3.700(-2)	33	5500.1006
CO 49-48	53.898	6724.17	6.777(-3)	99	5562.2583

Table 2.A.2 – Line fluxes of Class 0 and I sources in 10^{-20} W cm^{-2}.

Species	Trans.	$\lambda_{\rm lab}$ (μm)	Full array flux (10^{-20} W cm^{-2})							
			IRAS2A	IRAS4A	L1527	CedIRS4	BHR71	IRAS15398	L483	SerSMM4
CO	14-13	185.999	1.65±0.28	9.42±0.08	0.52±0.14	0.14±0.01	7.79±0.15	4.19±0.10	1.31±0.02	5.75±0.10
CO	16-15	162.812	2.11±0.38	8.00±0.09	0.57±0.07	0.16±0.01	...	4.24±0.12	1.10±0.02	...
CO	18-17	144.784^a	2.76±0.29	6.74±0.09	0.51±0.08	0.24±0.02	8.54±0.16	3.11±0.09	1.16±0.05	3.68±0.12
CO	22-21	118.581	...	3.12±0.27	0.31±0.11	<0.20	...	2.21±0.20	0.61±0.02	...
CO	23-22	113.458^b	3.16±0.37	...	0.95±0.12	0.59±0.02	...	3.56±0.14	2.55±0.07	...
CO	24-23	108.763	...	3.92±0.28	<0.26	0.20±0.03	5.65±0.33	1.13±0.11	0.97±0.04	1.17±0.18
CO	29-28	90.163^c	<0.30	...	0.10±0.02	...	...	0.42±0.04	0.59±0.04	...
CO	30-29	87.190	<0.67	0.97±0.12	<0.33	<0.35	...	0.36±0.03	0.41±0.05	...
CO	32-31	81.806	<0.37	0.45±0.05	<0.21	0.16±0.04	...	0.26±0.04	0.43±0.05	...
CO	33-32	79.360	<0.54	0.47±0.09	0.13±0.03	0.14±0.05	...	0.40±0.05	0.60±0.07	...
CO	36-35	72.843^d	<0.42	<0.09	<0.36	<0.08	0.89±0.08	<0.16	0.19±0.04	0.40±0.09
o-H$_2$O	2_{21}–2_{12}	180.488^d	2.72±0.32	...	0.11±0.04	...	...	...	0.50±0.02	...
o-H$_2$O	2_{12}–1_{01}	179.527	3.13±0.34	13.03±0.08	0.77±0.06	<0.13	...	2.18±0.06	1.45±0.02	...
o-H$_2$O	3_{03}–2_{12}	174.626	4.88±0.47	10.54±0.11	0.61±0.07	0.24±0.01	...	1.93±0.09	1.30±0.02	...
p-H$_2$O	3_{13}–2_{02}	138.528	2.60±0.33	6.91±0.08	0.39±0.07	0.12±0.02	...	1.10±0.08	1.00±0.02	...
p-H$_2$O	4_{04}–3_{13}	125.354^d	<0.31	...	0.17±0.06	...	...	...	0.59±0.03	...
o-H$_2$O	2_{21}–1_{10}	108.073	3.84±0.51	10.23±0.21	0.78±0.17	0.26±0.04	4.88±0.22	1.82±0.19	1.33±0.05	2.16±0.17
p-H$_2$O	3_{22}–2_{11}	89.988	<0.30	2.37±0.12	0.10±0.03	0.13±0.04	...	0.30±0.02	0.61±0.04	...
o-H$_2$O	7_{16}–7_{07}	84.767	<0.44	<0.14	<0.36	<0.28	...	<0.10	0.14±0.05	...
p-H$_2$O	6_{15}–5_{24}	78.928	<0.65	<0.30	<0.41	<0.48	...	<0.13	<0.54	...
o-H$_2$O	4_{23}–3_{12}	78.742^c	<0.65	2.03±0.19	0.33±0.03	0.24±0.06	...	...	1.34±0.08	...
o-H$_2$O	7_{07}–6_{16}	71.947^e	<0.62	0.78±0.08	<0.26	...	0.32±0.04	...	0.60±0.05	<0.26
o-H$_2$O	8_{18}–7_{07}	63.324	<0.77	<0.16	<0.47	<0.57	0.50±0.11	<0.19	0.41±0.05	<0.44
O I	$^3P_0$ –$^3P_1$	145.525	<0.2	0.42±0.10	1.07±0.10	0.87±0.10	1.33±0.12	1.13±0.11	0.78±0.10	2.36±0.06
O I	$^3P_1$ –$^3P_2$	63.184	9.01±1.83	2.33±0.28	11.29±0.30	8.92±0.46	20.91±0.53	19.07±0.47	8.16±0.62	23.21±0.41

Notes. NGC1333-IRAS4B and Serpens SMM1 fluxes are published separately in Herczeg et al. (2012) and Goicoechea et al. (2012), respectively. CO 31-30 and OH 84.6 μm fluxes are presented in Wampfler et al. (2013). NGC1333-IRAS2A and NGC1333-IRAS4A full PACS range fluxes will appear in Karska et al. (in prep.), but IRAS2A central spaxel only fluxes were listed in Visser et al. (2012). Non-observed lines are marked with ellipsis dots (. . .). The uncertainties are 1σ measured in the continuum on both sides of each line; calibration uncertainty of 30% of the flux should be included for comparisons with other modes of observations or instruments. 1σ upper limits calculated using wavelength dependent values of full-width high maximum for a point source observed with PACS are listed for non-detections. $^{(a)}$ The baseline from one side is affected by p-H$_2$O 4_{13}-3_{22} line at 144.518 μm, which falls in the edge of the scan. $^{(b)}$ A blend with the o-H$_2$O 4_{14}-3_{03} line at 113.537 μm. $^{(c)}$ Lines at the edges of the scans, for many cases not possible to measure. Selected objects were observed in dedicated scan for the CO 29-28 line. $^{(d)}$ Lines observed in dedicated scans only for selected objects. $^{(e)}$ The line falls in the leakage region of PACS and therefore the flux is less reliable.

Table 2.A.3 – Line fluxes of Class 0 and I sources in 10^{-20} W cm^{-2}.

Species	Trans.	λ_{lab} (μm)	Full array flux (10^{-20} W cm^{-2})							
			SerSMM3	L723	L1489	TMR1	TMC1A	TMC1	HH46	RNO91
CO	14–13	185.999	7.06±0.11	0.64±0.02	0.83±0.03	1.22±0.11	0.54±0.08	0.78±0.10	1.06±0.08	0.24±0.02
CO	16–15	162.812	6.86±0.09	0.61±0.01	0.98±0.02	1.58±0.06	0.59±0.02	0.92±0.05	0.86±0.06	0.27±0.01
CO	18–17	144.784[a]	4.98±0.18	0.62±0.03	1.05±0.01	1.50±0.07	0.44±0.08	0.73±0.06	0.65±0.08	0.25±0.01
CO	22–21	118.581	3.42±0.13	0.35±0.03	0.82±0.02	0.81±0.12	0.60±0.11	0.41±0.08	0.72±0.14	0.08±0.02
CO	23–22	113.458[b]	6.75±0.19	0.67±0.03	1.95±0.02	2.30±0.15	0.69±0.09	1.24±0.09	0.68±0.11	0.33±0.03
CO	24–23	108.763	2.28±0.20	0.46±0.04	0.83±0.03	1.35±0.10	0.39±0.01	0.60±0.11	0.34±0.04	<0.18
CO	29–28	90.163[c]	1.96±0.10	0.14±0.03	0.57±0.04	0.37±0.07	<0.12	0.25±0.05	0.17±0.04	<0.08
CO	30–29	87.190	2.00±0.21	0.32±0.06	0.49±0.05	0.42±0.08	<0.11	0.24±0.04	0.28±0.04	0.07±0.03
CO	32–31	81.806	1.06±0.32	<0.27	<0.32	<0.20	<0.12	0.14±0.03	<0.20	<0.04
CO	33–32	79.360	1.30±0.28	<0.28	0.17±0.04	0.14±0.04	<0.11	0.16±0.03	<0.26	<0.07
CO	36–35	72.843	0.77±0.10	<0.10	<0.10	0.26±0.04	<0.03	0.07±0.02	<0.07	<0.02
o-H$_2$O	2_{21}–2_{12}	180.488[d]	1.23±0.11	0.14±0.02	…	…	…	…	…	…
o-H$_2$O	2_{12}–1_{01}	179.527	4.90±0.09	0.14±0.01	0.73±0.02	0.69±0.12	<0.13	0.29±0.04	1.16±0.10	<0.15
o-H$_2$O	3_{03}–2_{12}	174.626	4.59±0.08	0.30±0.02	0.83±0.03	0.50±0.09	<0.12	0.24±0.07	0.57±0.09	0.20±0.02
p-H$_2$O	3_{13}–2_{02}	138.528	2.59±0.07	0.36±0.02	0.70±0.02	0.53±0.07	0.11±0.06	0.33±0.06	0.38±0.07	0.11±0.01
p-H$_2$O	4_{04}–3_{13}	125.354[d]	1.38±0.08	0.10±0.02	…	…	…	…	…	…
o-H$_2$O	2_{21}–1_{10}	108.073	3.84±0.21	0.23±0.04	0.92±0.04	0.79±0.07	<0.31	0.41±0.14	0.21±0.04	0.09±0.02
p-H$_2$O	3_{22}–2_{11}	89.988	1.23±0.11	0.13±0.04	0.49±0.04	0.46±0.07	<0.09	0.15±0.04	0.16±0.03	<0.05
o-H$_2$O	7_{16}–7_{07}	84.767	<0.27	<0.21	<0.29	<0.15	<0.09	<0.10	<0.17	<0.04
p-H$_2$O	6_{15}–5_{24}	78.928	<0.42	<0.44	0.24±0.04	<0.19	<0.14	<0.12	<0.18	<0.06
o-H$_2$O	4_{23}–3_{12}	78.742[c]	2.93±0.25	0.24±0.07	0.93±0.10	0.55±0.04	…	0.30±0.05	…	0.19±0.06
o-H$_2$O	7_{07}–6_{16}	71.947[e]	0.59±0.10	0.14±0.04	…	…	…	…	…	…
o-H$_2$O	8_{18}–7_{07}	63.324	0.75±0.50	<0.35	0.61±0.04	0.59±0.07	<0.13	0.17±0.05	<0.23	<0.05
O I	$^3P_0$ –$^3P_1$	145.525	2.26±0.08	0.50±0.11	0.24±0.08	0.67±0.13	0.64±0.09	0.97±0.13	2.35±0.13	0.47±0.08
O I	$^3P_1$ –$^3P_2$	63.184	21.08±0.56	3.19±0.45	6.34±0.47	7.00±0.39	8.53±0.56	14.12±0.41	33.76±0.63	9.38±0.47

Notes. NGC1333-IRAS4B and Serpens SMM1 fluxes are published separately in Herczeg et al. (2012) and Goicoechea et al. (2012), respectively. CO 31-30 and OH 84.6 μm fluxes are presented in Wampfler et al. (2013). NGC1333-IRAS2A and NGC1333-IRAS4A full PACS range fluxes will appear in Karska et al. (in prep.), but IRAS2A central spaxel only fluxes were listed in Visser et al. (2012). Non-observed lines are marked with ellipsis dots (. . .). The uncertainties are 1σ measured in the continuum on both sides of each line; calibration uncertainty of 30% of the flux should be included for comparisons with other modes of observations or instruments. 1σ upper limits calculated using wavelength dependent values of full-width high maximum for a point source observed with PACS are listed for non-detections. [a] The baseline from one side is affected by p-H$_2$O 4_{13}-3_{22} line at 144.518 μm, which falls in the edge of the scan. [b] A blend with the o-H$_2$O 4_{14}-3_{03} line at 113.537 μm. [c] Lines at the edges of the scans, for many cases not possible to measure. Selected objects were observed in dedicated scan for the CO 29-28 line. [d] Lines observed in dedicated scans only for selected objects. [e] The line falls in the leakage region of PACS and therefore the flux is less reliable.

Figure 2.B.1 – Illustration of the correction curve method. *Top:* CO fluxes of Serpens SMM1 measured over 5×5 array divided by the central spaxel fluxes are plotted versus wavelengths. PACS PSF for a point source is shown in green. CO emission is clearly extended for this sources. *Middle:* Best signal-to-noise measurements are used to make a fit to the data and derive the wavelength-dependent correction factors. *Bottom:* CO fluxes measured over 5×5 array are divided by central spaxel measurements corrected for the extended emission using calculated correction factors are plotted versus wavelength. Accuracy longward ~100 μm is better than 10%, whereas the accuracy is ~30% for short-wavelength lines (100 μm).

2.B Extended source correction method

To account for the combination of real spatial extent in the emission and the wavelength-dependent PSF, we developed an 'extended source correction' method. We first inspected the 5×5 spectral (or contour) maps. Contributions from NGC1333-IRAS4A, Ser SMM6, and an unlabeled object were subtracted from the observations of NGC1333-IRAS4B, Ser SMM3, and SMM4 (e.g. Yıldız et al. 2012, Dionatos et al. subm.). In the next step, we used two long-wavelength lines of CO and H_2O (CO 14-13 at 185.999 μm and H_2O

67

$2_{12} - 1_{01}$ at 179.527 μm) to visualize the spatial extent of the line emission attributed to each object and summed all the spaxels that contained emission. Since all of our lines, except the [O I] line at 63.2 μm, are spectrally unresolved by PACS, single or double (for OH doublets, closeby and blended lines) Gaussian fits to the resulting spectra are used to calculate the line fluxes of the detected lines.

Summing the spectra from all 25 spaxels increases the noise and often prevents detecting weak lines. Using only those spaxels that contain most of the emission results in a much higher signal-to-noise and ultimately a higher detection rate for lines but fails to include emission that leaks out of those spaxels because of real spatial extent in the line and the instrumental PSF. Therefore, our 'extended source correction' method provides a wavelength-dependent correction factor to account for the missing flux. The main idea of the method is to use the brightest spaxels, which contain most of the emission, to measure the line fluxes and then correct the value for the missing flux, contained in the omitted spaxels. This method assumes that weak lines are similarly distributed to the strong ones, with observed differences in spatial distributions caused only by the wavelength dependence in the PSF.

The correction factors are derived using the strongest lines, i.e. those that can be measured in the brightest spaxels as well as in all spaxels that contain emission from the object (usually 25 of them). The ratio of flux in the small, bright extraction region and the large extraction region yields a wavelength-dependent *correction curve* (see Figure 2.B.1). A 0th-order fit (horizontal line) is used for the short-λ part of the spectrum, whereas a 1st- or 2nd-order polynomial is used for the long-λ part of the spectrum (100-110 μm). All line fluxes are then measured in only the brightest spaxels and multiplied by this correction factor. This method was used primarily for the full spectral scans.

2.C   Spectral energy distributions

Figure 2.C.1 shows the spectral energy distributions for all of our sources obtained from our PACS spectroscopy and literature measurements from *Spitzer*-IRAC and MIPS (Evans et al. 2009), 2MASS (Skrutskie et al. 2006), SCUBA (Shirley et al. 2000, Di Francesco et al. 2008), as well as APEX/LABOCA, Bolocam, SEST, ISO and IRAS telescopes. The PACS measurements cover the peak of dust emission and are in good agreement with the previous observations (for more details, see Kristensen et al. 2012).

For PACS, the overlap regions of different orders cause the regions of 70-73 μm, 98-105 μm and 190-220 μm to be less reliable in terms of continuum shapes and flux densities. These regions were thus excluded from our spectral energy distribution analysis. New values of $L_{\rm bol}$ and $T_{\rm bol}$ are calculated following the standard definitions of the two physical quantities (e.g., Dunham et al. 2010). Several methods of interpolation were tested for consistency of the results including linear interpolation, midpoint, prismodial method and trapezoidal summation. Among them the trapezoidal summation offered the most stable values and is used in this study.
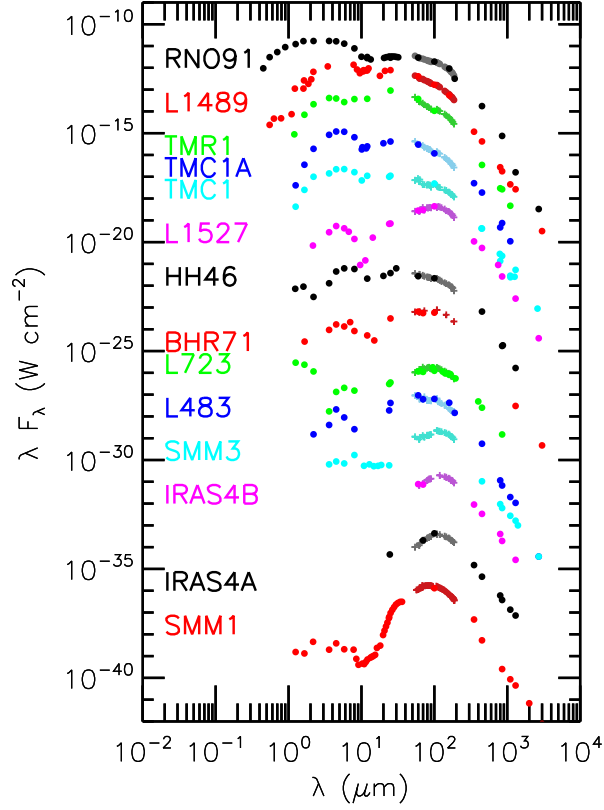
Figure 2.C.1 – Spectral energy distribution shapes for most of our sources. Literature observations are shown as filled circles, whereas our PACS observations are marked with crosses and drawn in a different hue (see Table 3.B.1). The maxima of the SEDs lie between 10^{-16} and 10^{-19} W cm^{-2} for all objects and thus, for better shape vizualisation, the SEDs are offset by several orders of magnitude. Objects are shown in the sequence of decreasing evolutionary parameter $L_{\mathrm{bol}}^{0.6}/M_{\mathrm{env}}$.

Table 2.C.1 – Continuum measurements for Class 0 and I sources.

λ (μm)	Continuum (Jy)																	
	I2A	I4A	I4B	L1527	CedIRS4	BHR71	I15398	L483	SMM1	SMM4	SMM3	L723	L1489	TMR1	TMC1A	TMC1	HH46	RNO91
62.050	289	16	9	17	15	79	12	85	153	…	11	9	43	37	38	8	34	37
62.700	235	…	…	…	…	…	…	66	159	…	…	…	…	…	…	10	…	…
63.184	243	20	…	18	14	85	12	85	166	…	14	9	42	37	41	10	35	36
69.300	303	34	13	31	17	…	21	76	224	…	21	15	49	38	43	7	39	42
72.843	349	38	15	27	18	125	…	113	245	2	20	14	48	36	41	8	39	43
79.160	394	54	24	40	21	…	24	93	325	…	29	17	51	35	42	9	42	47
81.806	412	61	28	41	21	…	26	98	346	…	31	20	52	37	43	10	44	47
84.600	436	68	32	46	23	…	27	102	373	…	33	22	52	36	43	10	47	49
87.190	457	78	34	50	24	…	28	110	399	…	37	21	53	…	45	10	48	52
89.990	460	83	37	51	24	…	27	113	417	…	40	21	51	35	42	9	48	50
108.070	427	157	…	78	45	302	54	206	551	22	88	34	63	49	56	15	67	69
108.760	426	156	…	79	45	304	54	206	552	22	88	34	62	48	54	15	67	69
113.458	417	…	…	93	47	…	56	162	558	…	92	35	61	48	53	15	67	70
118.581	410	178	93	97	50	…	59	165	561	…	98	36	61	49	53	15	68	71
125.354	416	…	…	100	…	…	…	165	571	…	105	37	…	…	…	…	68	…
138.528	402	206	110	106	57	…	66	168	570	…	117	38	55	48	50	16	70	71
145.525	412	211	115	98	58	326	68	201	587	45	122	39	54	47	48	17	71	70
157.700	397	220	121	107	60	…	71	163	558	…	128	40	52	46	46	17	74	70
162.812	387	216	121	103	59	…	69	157	536	…	124	40	50	43	43	16	72	68
169.100	364	201	113	95	53	…	65	145	510	…	117	36	45	39	38	15	68	62
174.626	357	206	119	98	57	…	69	149	468	…	121	37	46	39	40	16	72	63
179.527	325	198	116	88	51	…	64	139	441	…	115	36	42	35	35	15	67	58
185.999	287	191	103	79	46	263	60	156	401	56	103	31	38	31	31	14	…	51

Notes. Non-observed spectral regions are marked with ellipsis dots (…). The calibration uncertainty of 30% of the flux should be included for comparisons with other modes of observations or instruments.

Table 2.E.1 – Comparison between ISO and Herschel line emission in 10^{-20} W cm^{-2}.

Object	[O I] 63 um		[O I] 145 um	
	LWS	PACS	LWS	PACS
IRAS2	29.0 ± 2.9	9.01 ± 1.83	< 4.5	< 0.2
IRAS4 (A+B)	24.3 ± 1.6	4.2 ± 0.4	< 3.6	0.4 ± 0.1
L1527	13.4 ± 2.0	11.3 ± 0.3	4.8 ± 0.7	1.1 ± 0.1
L483	18.8 ± 2.0	8.2 ± 0.6	3.7 ± 1.0	0.8 ± 0.1
L723	14.5 ± 3.6	3.19 ± 0.5	3.1 ± 0.4	0.5 ± 0.1

2.D Spatial extent of line emission

Figures 2.D.1 and 2.D.2 show the spectra in the on-source and outflow positions for objects with *extended* emission and objects with *compact* emission, respectively (see §3.2).

Figure 2.D.3 presents the spectra of the [O I] 63.2 μm line, the OH 84.6 μm line, the H_2O 7_{16}-6_{07} line, and the CO $30 - 29$ line for the central target, two spaxels in the red-shifted outflow, and two spaxels in the blue-shifted outflow of NGC1333-IRAS4A.

2.E Comparing PACS and ISO far-IR spectra

Higher sensitivity of Herschel/PACS compared to ISO-LWS allows us to improve the detection rate of H_2O (15 out of 16 Class 0/I sources) and higher$-J$ CO transitions (14 out of 16 sources detected in CO 24-23). In particular, water detections in Class I sources are now possible for the majority of the sources. Detection of the more highly excited CO transitions allows to distinguish the *hot component* on the rotational diagram, which was not possible with ISO (Nisini et al. 2010a).

The chopping capabilities and the spatial resolution of *Herschel* at the distances of our objects allow us to distinguish the YSO–related atomic emission from the emission from the nearby objects or the surrounding cloud. Herschel observations show that only two objects (Ser SMM1 and TMC1) show [C II] emission associated with the YSO. The [O I] emission, on the other hand, is clearly extended in the outflow direction and most probably traces the hidden jet. For some of the outflow-dominated emission sources, the Herschel beam does not cover the full extent of the [O I] emission, whereas the ISO beam can suffer from the cloud or nearby sources emission. Table 2.E.1 shows the comparison between the [O I] emission for the sources observed with both instruments.

2.F Rotational diagrams

Figures 2.F.1, 2.F.2, and 2.F.3 show CO and H_2O rotational diagrams for all sources from our sample. Two-component fits are used for the CO diagrams and one-component fits for the H_2O diagrams. These fits are used to determine the total cooling budget in the two molecules for each objects, as discussed in §4. The errors in the temperatures reflect the

statistical error of the fit taking the uncertainties in individual line fluxes as listed in Table A.2 into account. They do not include the absolute flux uncertainties since the relative fluxes between lines within a single spectrum have much lower uncertainties.

2.G   Correlations

Figure 2.G.1 shows correlations between selected line luminosities and bolometric temperature (T_{bol}) and density at 1000 AU (n_{H2}). Strong correlations are found with the latter quantity.

2.H   Rotational temperature uncertainties

Figure 2.H.1 shows the CO and H_2O rotational diagrams for the NGC1333-IRAS4B and Serpens SMM1, using the data published in Herczeg et al. (2012) and Goicoechea et al. (2012). The full spectroscopy data is shown, with the full line coverage in the PACS range, as well as the selected lines only, typically observed in our line spectroscopy mode for 16 sources in our sample.

Rotational temperatures calculated from the rotational diagrams constructed using the full and limited line configurations are in good agreement for the CO. For the assumed ranges of the two components, the warm component T_{rot} error of the fit is ± 15 K and the hot component T_{rot} error is $\pm 50 - 100$ K.

The change of the energy break in a wide range of transitions results in ± 20 K error for the T_{rot}(warm) and ± 40 K for the T_{rot}(hot) for the full spectroscopy data. Those ranges are not well determined by line spectroscopy data only and thus in this work we always use 1700 K for this kind of observations.

H_2O rotational temperatures, on the other hand, are less accurately determined for the line spectroscopy observations than the formal error of the fit would imply. The scatter due to the subthermal excitation and very likely high opacities of the water lines result in significant differences in T_{rot} calculation, depending on the choice of observed lines. The fit to the water lines chosen in our program underestimates the resulting temperature by about 50-80 K for the NGC1333-IRAS4B and Serpens SMM1.

2.I   Cooling budget calculations

Since different methods of cooling budget calculation exist in the literature and will appear due to the availability of new Herschel observations, we perform here a comparison between the methods and estimate the differences between the resulting budgets.

Carbon monoxide

In order to calculate the CO cooling, Nisini et al. (2002b) calculated LVG models that reproduced the detected transitions and used them to determine the fluxes for the first 60

transitions of CO. Due to the limited *ISO* sensitivity, CO transitions from J =14-13 to J =22-21 (Class I) and J =29-28 (Class 0) were available for the brightest sources only which did not allow them to distinguish the *hot* component. Their method corresponds to a single-component fit to the excitation diagrams.

We use the entire PACS array line fluxes of NGC1333-IRAS4B and Ser SMM1 from Herczeg et al. (2012) and Goicoechea et al. (2012) to compare the observed CO total luminosities with those calculated using fits to the excitation diagrams (see Table 2.I.1). In particular, we show the results of the two-components fits for PACS data and three-components fits for PACS and SPIRE data, available for Ser SMM1. Three wavelength ranges are included: (i) the PACS range from 54-60 to 190 μm; (ii) the Nisini et al. 2002 range, namely 44-2601 μm; (iii) the PACS + SPIRE range, from 60 to 650 μm (for SMM1 only). Additionally, we include the fitting results to the observed lines only, in order to check how good our two/three-component linear fits reproduce the observations.

The calculations in Table 2.I.1 show that multi-component linear fits to the excitation diagrams agree well with the observed values of the total CO luminosity from the detected lines (rows 1+2 and 5+6). The uncertainties correspond to different choice of the break energy for the two components. The fits are then used to extrapolate the fluxes of the lines which are either blends or fall in the region of $\sim$100 μm, where the measured line fluxes are less reliable (row 3 for PACS range and row 7 for PACS+SPIRE range). The resultant total CO luminosities are a good measure of the far-IR CO cooling (for the PACS range) and total CO cooling (for PACS+SPIRE range).

The example of SMM1 shows that the additional CO emission from the entrained outflow gas increases the CO luminosity by a factor of 1.3 with respect to the extrapolated values from the warm CO component ($5.23 \cdot 10^{-2}$ L$_\odot$ versus $6.93 \cdot 10^{-2}$ L$_\odot$).

The relative CO luminosity in different spectral regions (A: J=4-3 to J=13-12 B: J=14-13 to J=24-23 and C: J=25-24 to J=44-43) for SMM1 is $\sim$2:2:1 (A:B:C) and for IRAS4B is $\sim$2:1 (B:C), when the additional cold CO component is included. Thus, approximately 80% of the CO luminosity comes from transitions lower than CO 24-23, roughly equally in both SPIRE and PACS ranges. The poorer determination of the hot component rotational temperature does not affect significantly the total cooling determination.

Water

Nisini et al. (2002) have calculated H$_2$O luminosities based on the assumption that H$_2$O emission arises from the same gas as CO, for which large velocity gradient (LVG) models determined the gas temperature and density. The model prediction were used to extrapolate H$_2$O line fluxes for rotational transitions with $J < 10$ and $E_u/k_B < 2031$ K.

Total H$_2$O cooling in this work (see §4.2) is calculated based on the full spectroscopy data for the NGC1333-IRAS4A and Serpens SMM1 (Herczeg et al. 2012 and Goicoechea et al. 2012). The average scaling factor than transfers the luminosity observed in the selected lines in the line spectroscopy mode to the total water luminosities (as observed in the range spectroscopy) is 2.4±0.3.

Table 2.I.1 – CO total luminosities for IRAS4B and SMM1 in 10^{-4} $L_{\odot}$.

Method	Range (μm)	IRAS4B	SMM1
Obs. line fluxes[a]	54-190	212	396
2-comp. fit for obs. lines only	54-190	210±2	394±5
2-comp. fit, PACS range[b]	**54-190**	**225±3**	**428±8**
2-comp. fit, Nisini+2002 range[c]	44-2601	271±6	523±4
Obs.PACS+SPIRE line fluxes	60-650	–	650
3-comp. fit for obs. lines only	60-650	–	648
3-comp. fit, PACS range[d]	60-650	–	690
3-comp. fit, Nisini+2002 range	44-2601	–	693

Notes. Errors correspond to standard deviation of the total CO cooling calculated using the break-point upper energies from 1000 to 2200 K. [a] From full PACS range, excluding CO 23-22 and CO 31-30 which are blended with the H_2O $4_{14} - 3_{03}$ and OH $^2\Pi_{3/2}$ $J = 7/2 - 5/2$, respectively. [b] Includes CO transitions from J =14-13 to J =48-47 (IRAS4B) or J =44-43 (SMM1). This is the method used to determine cooling budget in Table 4. [c] Includes CO transitions from J =1-0 to J =60-59, used in Nisini et al. (2002). [d] Includes CO transitions from J =4-3 to J =44-43.

An alternative method considered for the water cooling calculation is the extrapolation of the non-observed line fluxes based on the H_2O rotational temperature. Table 2.I.2 compares the results of this method with the values obtained when the scaling factor was used. The extrapolation is done for (i) the 328 lowest rotational transitions of water ($J < 10$, $E_u/k_B < 2031$ K, so called 'Nisini et al. range'); (ii) the same transitions but only for PACS range. Molecular information is obtained from the JPL and CDMS catalogs (Pickett et al. 1998, Müller et al. 2001, 2005).

Calculations for Serpens SMM3 show that the extrapolation of the fluxes based on the fitted rotational temperature results in a factor of ~ 2 higher total water luminosities than the value calculated using the scaling factor of 2.4. Even higher values are obtained when we extend the range used in Nisini et al. (2002). Additionally, the rotational temperature of H_2O derived from the line scan data is very likely underestimated by a factor of $\sim 1.3-1.6$ (see Appendix 2.H). This uncertainty has an effect on the derived, extrapolated, H_2O total cooling.

In summary, from the comparisons it is concluded that the total luminosity of both CO and H_2O in the PACS range is accurate to 30% or better.

Table 2.I.2 – Different methods of H_2O luminosities calculation (luminosities in 10^{-3} $L_\odot$).

Method	Ser SMM3
Observed line fluxes (line spec mode)	4.0
Scaling to the total PACS range scan flux (factor: 2.4)	9.6
T_{rot}=125 K	
Extrapolation for PACS range	18.3
Extrapolation for Nisini et al. range	23.5
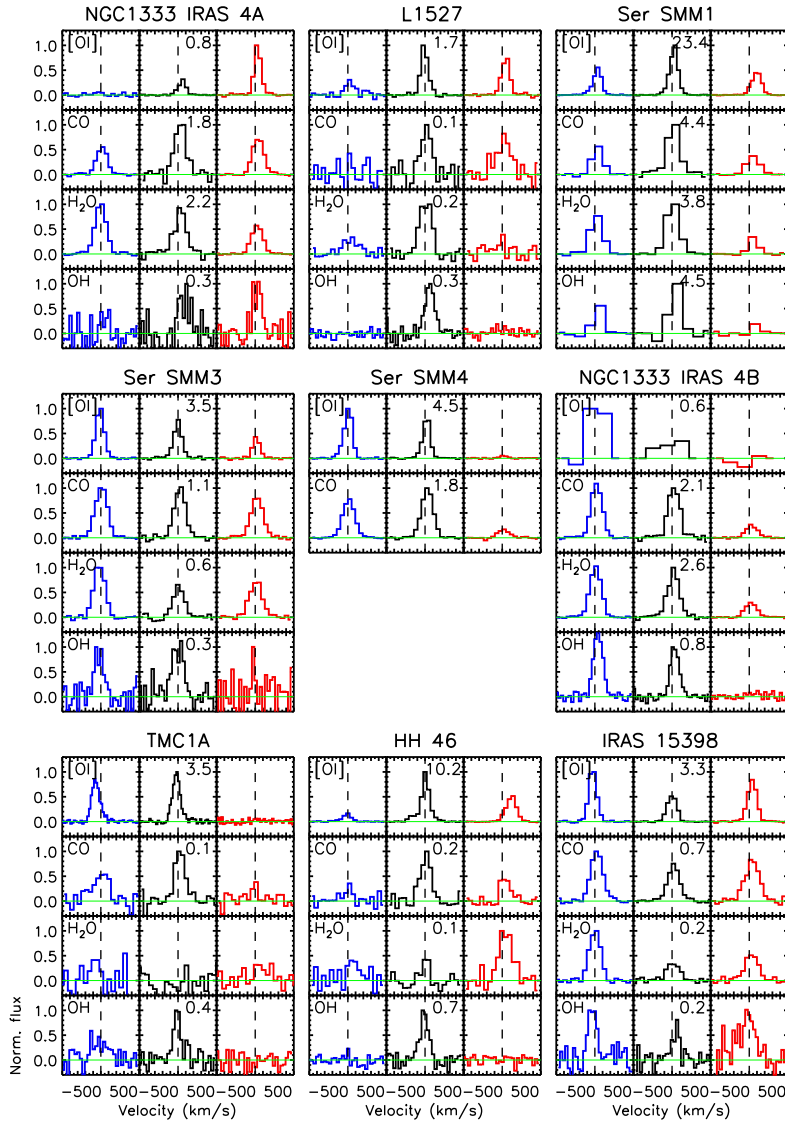
Figure 2.D.1 – Spectra of the [O I] 63.2 μm, CO $14 - 13$ 186.0 μm, H_2O 2_{12}-1_{01} 179.5 μm, and OH 84.6 μm lines in the selected blue outflow, on-source and red outflow positions (marked with blue, green and red frames around the spaxels e.g. in Figure 2.3) for the *extended* sources (see §3.2). The figure shows relative emission at different positions for each species separately. Measured line fluxes at central spaxel position in units of 10^{-20} W cm^{-2} are written next to the corresponding spectra.
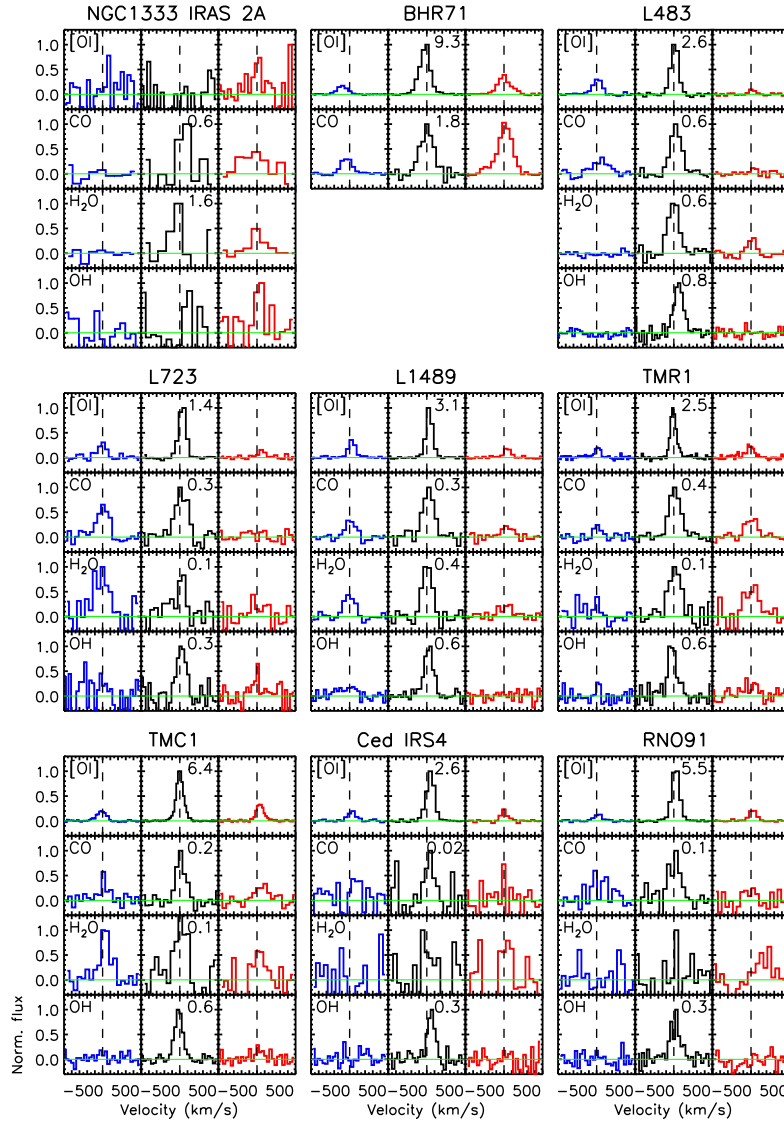
Figure 2.D.2 – The same as Figure 2.D.1 but for the *compact* sources.
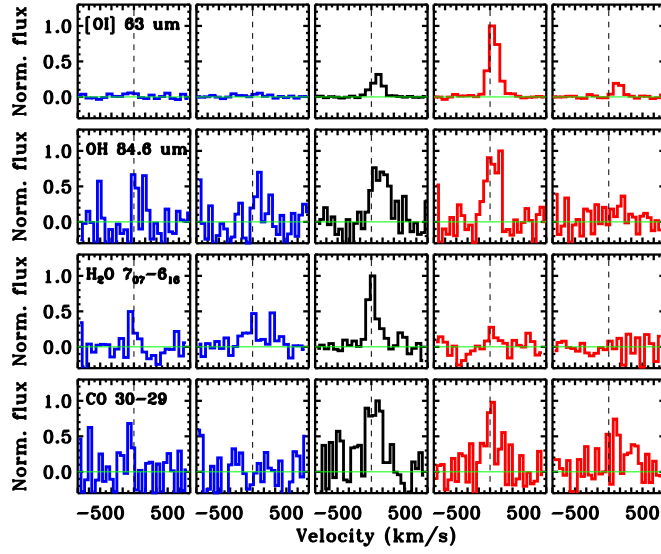
Figure 2.D.3 – NGC1333-IRAS4A spectra in the [O I] 63.2 μm line, the OH 84.6 μm line, the H_2O 7_{07}-6_{16} line, and the CO $30 - 29$ line. Two blue outflow, on-source and two red outflow positions are shown, corresponding to the the colored spaxels in Figure 2.3.
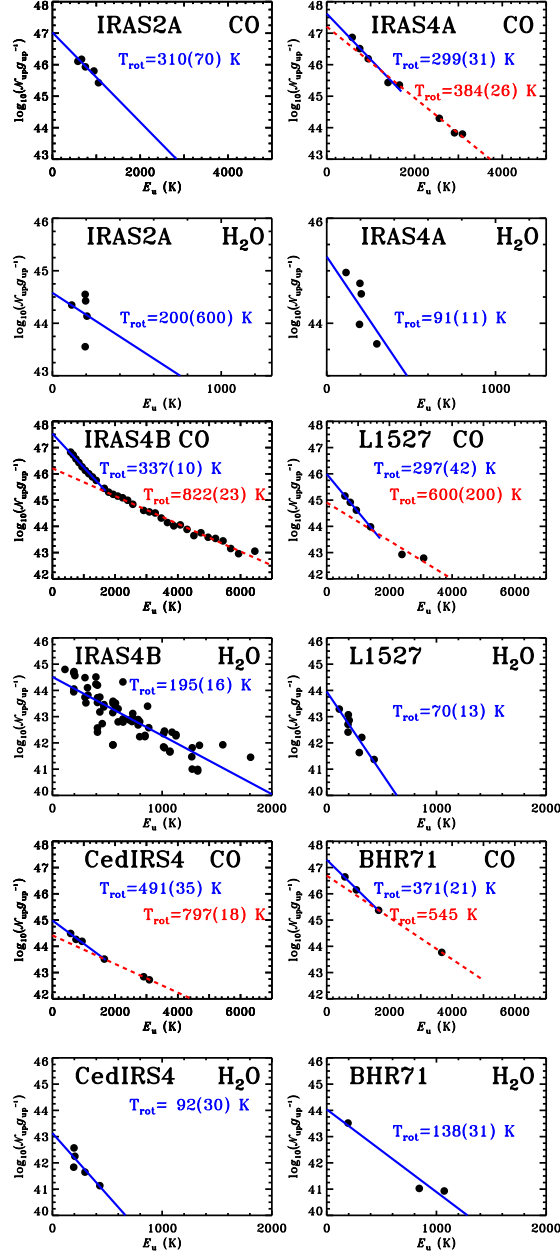
Figure 2.F.1 – Rotational diagrams of CO and H$_2$O for Class 0 sources. Blue and red lines show linear fits to warm and hot components, respectively. The corresponding rotational temperatures are written in the same colors. Errors associated with the fit are shown in the brackets.
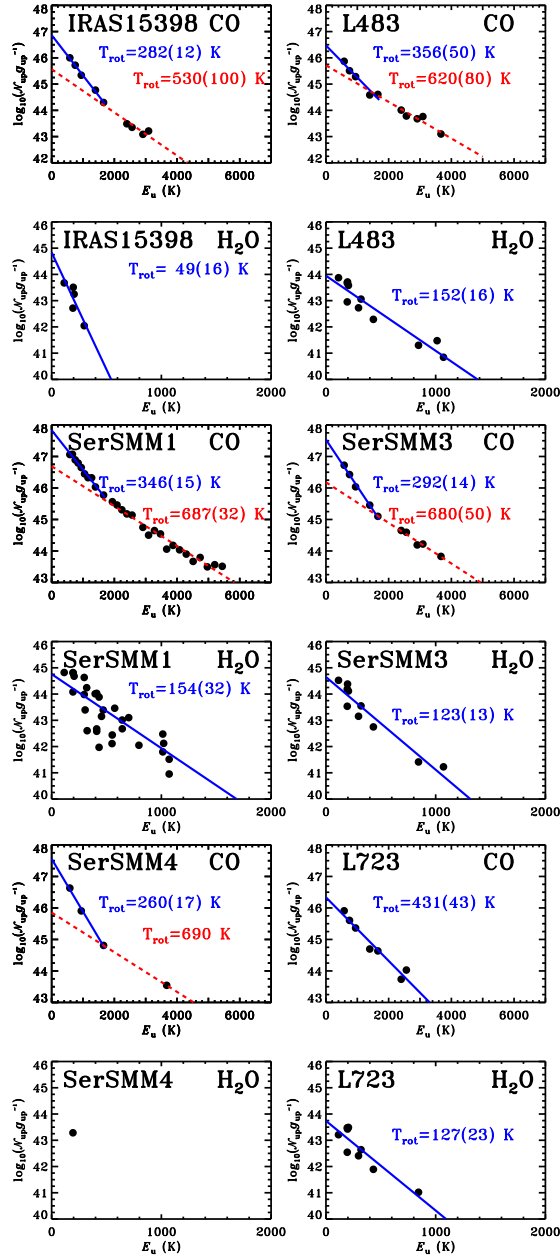
Figure 2.F.2 – The same as Figure 2.F.1, but for the remaining Class 0 sources. Warm component only is seen towards L723 in our diagram.
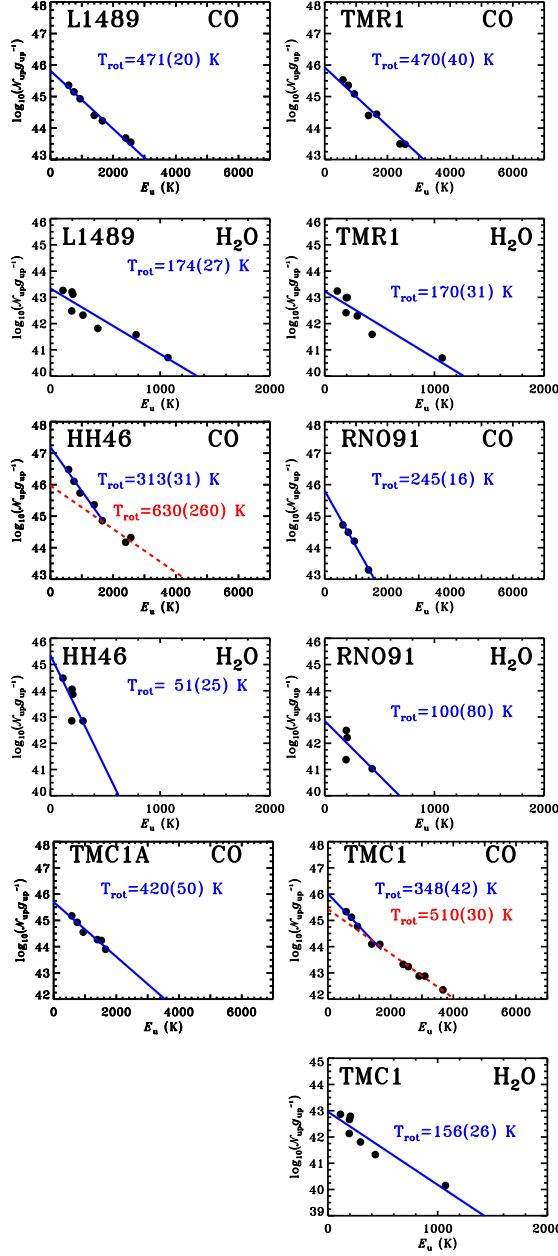
Figure 2.F.3 – Rotational diagrams of CO H$_2$O for Class I sources. Blue lines show linear fits to the data. The corresponding rotational temperatures are given. Errors associated with the fit are shown in the brackets. Warm components only are seen towards L1489, TMR1 and TMC1A in our diagrams.
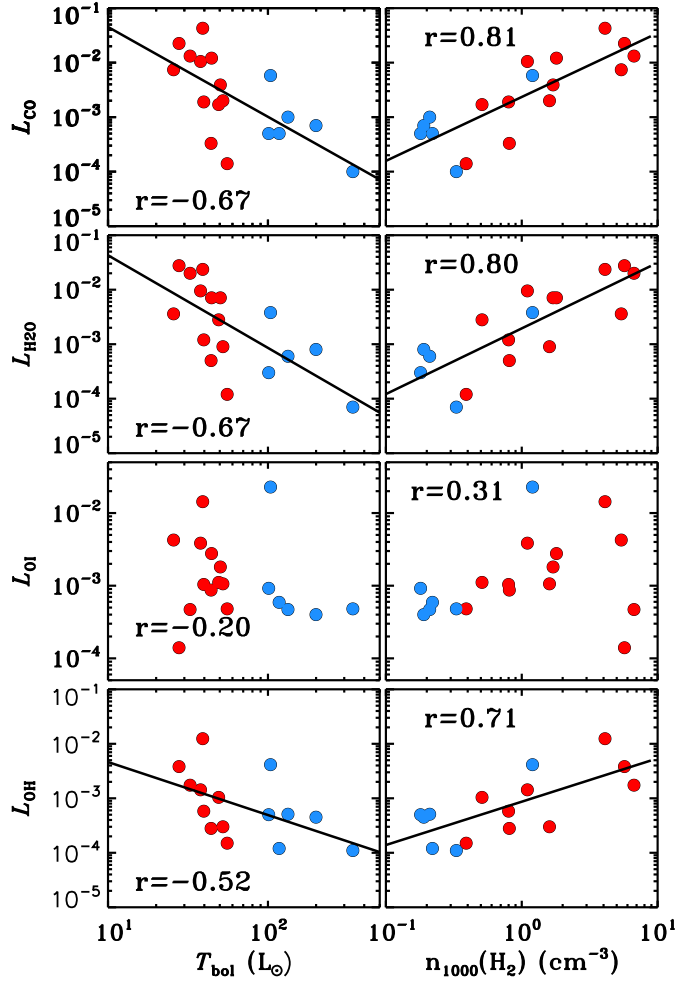
Figure 2.G.1 – Correlations between bolometric temperature (left column) and envelope density at 1000 AU (right column) and (from top to bottom): CO 14-13, H_2O 2_{12}-1_{01}, [O I] at 63.18 μm, and OH 84.6 μm line luminosities.
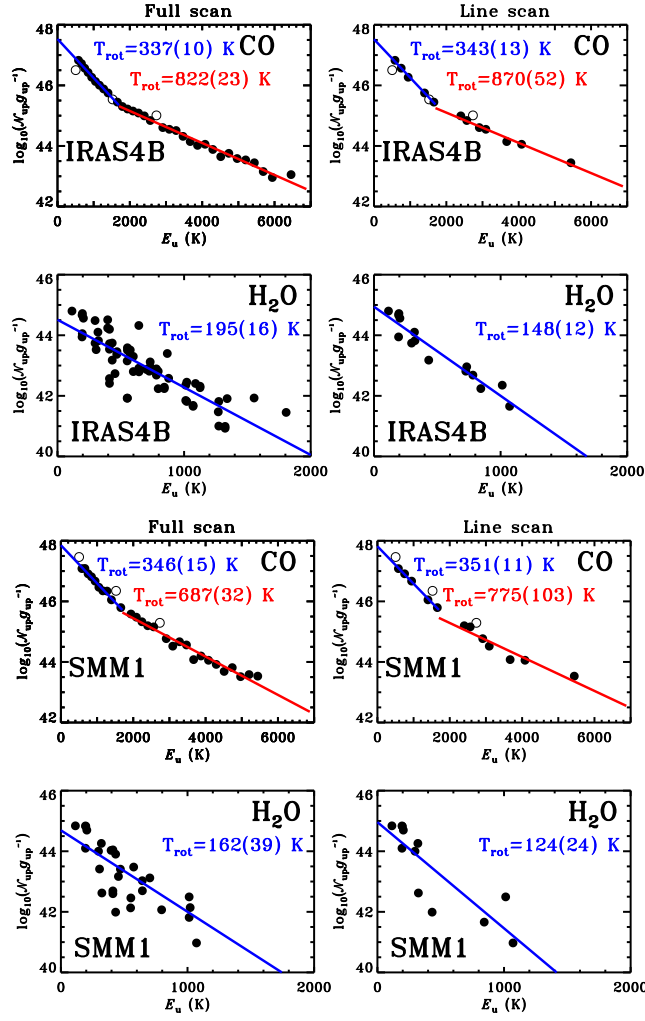
Figure 2.H.1 – The CO and H_2O rotational diagrams for NGC1333-IRAS4B and Serpens SMM1. Both the full spectroscopy line and the selected lines observed in the line scan mode are shown. Two component fit is done to the CO diagram with the break at 1700 K (i.e. transitions J 24 correspond to the warm component) and a single component fit to the H_2O diagram. Errors associated with the fit are shown in the brackets.

Far-infrared molecular lines from low- to high-mass star forming regions observed with *Herschel*

A. Karska, F. Herpin, S. Bruderer, J. R. Goicoechea, G. J. Herczeg, E. F. van Dishoeck,
I. San José-García, A. Contursi, H. Feuchtgruber, D. Fedele, A. Baudry, J. Braine,
L. Chavarría, J. Cernicharo, F. F. S. van der Tak, and F. Wyrowski

85

Abstract

Aims. Our aim is to study the response of the gas-to-energetic processes associated with high-mass star formation and compare it with previously published studies on low- and intermediate-mass young stellar objects (YSOs) using the same methods. The quantified far-infrared line emission and absorption of CO, H_2O, OH, and [O I] reveals the excitation and the relative contribution of different atomic and molecular species to the gas cooling budget.

Methods. Herschel-PACS spectra covering 55–190 μm are analyzed for ten high-mass star forming regions of luminosities $L_{bol} \sim 10^4 - 10^6 \, L_\odot$ and various evolutionary stages on spatial scales of $\sim 10^4$ AU. Radiative transfer models are used to determine the contribution of the quiescent envelope to the far-IR CO emission.

Results. The close environments of high-mass protostars show strong far-infrared emission from molecules, atoms, and ions. Water is detected in all 10 objects even up to high excitation lines, often in absorption at the shorter wavelengths and in emission at the longer wavelengths. CO transitions from $J = 14 - 13$ up to typically $29 - 28$ ($E_u/k_B \sim 580 - 2400$ K) show a single temperature component with a rotational temperature of $T_{rot} \sim 300$ K. Typical H_2O excitation temperatures are $T_{rot} \sim 250$ K, while OH has $T_{rot} \sim 80$ K. Far-IR line cooling is dominated by CO ($\sim 75\%$) and, to a smaller extent, by [O I] ($\sim 20 \%$), which becomes more important for the most evolved sources. H_2O is less important as a coolant for high-mass sources because many lines are in absorption.

Conclusions. Emission from the quiescent envelope is responsible for $\sim 45 - 85 \%$ of the total CO luminosity in high-mass sources compared with only $\sim 10\%$ for low-mass YSOs. The highest$-J$ lines (J_{up} 20) originate most likely in shocks, based on the strong correlation of CO and H_2O with physical parameters (L_{bol}, M_{env}) of the sources from low- to high-mass YSOs. The excitation of warm CO described by $T_{rot} \sim 300$ K is very similar for all mass regimes, whereas H_2O temperatures are ~ 100 K high for high-mass sources compared with low-mass YSOs. The total far-IR cooling in lines correlates strongly with bolometric luminosity, consistent with previous studies restricted to low-mass YSOs. Molecular cooling (CO, H_2O, and OH) is ~ 4 times greater than cooling by oxygen atoms for all mass regimes. The total far-IR line luminosity is about 10^{-3} and 10^{-5} times lower than the dust luminosity for the low- and high-mass star forming regions, respectively.

3.1 Introduction

High-mass stars ($M > 8$ M$_\odot$) play a central role in the energy budget, the shaping, and the evolution of galaxies (see review by Zinnecker & Yorke 2007). They are the main source of UV radiation in galaxy disks. Massive outflows and H II regions are powered by massive stars and are responsible for generating turbulence and heating the interstellar medium (ISM). At the end of their lives, they inject heavy elements into the ISM that form the next generation of molecules and dust grains. These atoms and molecules are the main cooling channels of the ISM. The models of high-mass star formation are still strongly debated: these two competing scenarios are turbulent core accretion and 'competitive accretion' (e.g. Cesaroni 2005). Molecular line observations are crucial to determining the impact of UV radiation, outflows, infall, and turbulence on the formation and evolution of the high-mass protostars and ultimately distinguish between those models.

Based on observations, the 'embedded phase' of high-mass star formation may empirically be divided into several stages (e.g. Helmich & van Dishoeck 1997, van der Tak et al. 2000, Beuther et al. 2007): (i) massive prestellar cores (PSC); (ii) high-mass protostellar objects (HMPOs); (iii) hot molecular cores (HMC); and (iv) ultra-compact H II regions (UCH II). The prestellar core stage represents initial conditions of high-mass star formation, with no signatures of outflow / infall or maser activity. During the high-mass protostellar objects stage, infall of a massive envelope onto the central star and strong outflows indicate the presence of an active protostar. In the hot molecular core stage, large amounts of warm and dense gas and dust are seen. The temperature of $T > 100$ K in subregions < 0.1 pc in size is high enough to evaporate molecules off the grains. In the final, ultra-compact H II regions stage, a considerable amount of ionized gas is detected surrounding the central protostar.

The above scenario is still debated (Beuther et al. 2007), in particular whether stages (ii) and (iii) are indeed intrinsically different. The equivalent sequence for the low-mass Young Stellar Objects (hereafter YSO) is better established (Shu et al. 1987, André et al. 1993, 2000). The 'embedded phase' of low-mass protostars consists of (i) the prestellar core, (ii) Class 0, and (iii) Class I phases. The Class 0 YSOs are surrounded by a massive envelope and drive collimated jets/ outflows. In the more evolved Class I objects, the envelope is mostly dispersed and more transparent for UV radiation. The outflows are less powerful and have larger opening angles.

Low-mass sources can be probed at high spatial resolution due to a factor of 10 shorter distances, which allow us to study well-isolated sources and avoid much of the confusion due to clouds along the line of sight. The line emission is less affected by foreground extinction and therefore provides a good tool for studying the gas's physical conditions and chemistry in the region. The slower evolutionary timescale results in a large number of low-mass YSOs compared to their high-mass counterparts, which is also consistent with observed stellar/core mass functions.

While low-mass YSOs are extensively studied in the far-infrared, first with the Infrared Space Observatory (ISO, Kessler et al. 1996) and now with *Herschel* (Pilbratt

et al. 2010b)[1], the same is not the case for high-mass sources (see e.g. Helmich & van Dishoeck 1997, Vastel et al. 2001, Boonman & van Dishoeck 2003). For those, the best-studied case is the relatively nearby Orion BN-KL region observed with ISO's Long- and Short-Wavelength Spectrometers (Clegg et al. 1996, de Graauw et al. 1996). Spectroscopy at long wavelengths (45-197 μm) shows numerous and often highly excited H_2O lines in emission (Harwit et al. 1998), high-J CO lines (e.g., up to J=43-42 in OMC-1 core, Sempere et al. 2000), and several OH doublets (Goicoechea et al. 2006), while the shorter wavelength surveys reveal the CO and H_2O vibration-rotation bands and H_2 pure rotational lines (van Dishoeck et al. 1998, Rosenthal et al. 2000). Fabry-Perot (FP) spectroscopy ($\lambda/\Delta\lambda \sim$10,000, 30 km s^{-1}) data show resolved P-Cygni profiles for selected H_2O transitions at $\lambda < 100\,\mu$m, with velocities extending up to 100 km s^{-1} (Wright et al. 2000, Cernicharo et al. 2006). At the shortest wavelengths ($< 45\,\mu$m) all pure rotational H_2O lines show absorption (Wright et al. 2000). ISO spectra towards other high-mass star forming regions are dominated by atomic and ionic lines (see review by van Dishoeck 2004), similar to far-IR spectra of extragalactic sources (Fischer et al. 1999, Sturm et al. 2002).

The increased sensitivity and spectral and spatial resolution of the Photodetector Array Camera and Spectrometer (PACS) (Poglitsch et al. 2010) onboard *Herschel* now allow detailed study of the molecular content of a larger sample of high-mass star forming regions. In particular, the more than an order of magnitude improvement in the spectral resolution over the ISO-LWS grating observing mode allows routine detections of weak lines against the very strong continuum of high-mass sources with *Herschel*, with line-to-continuum ratios below 1%.

The diagnostic capabilities of far-infrared lines have been demonstrated by the recent results on low- and intermediate-mass YSOs and their outflows (Fich et al. 2010, Herczeg et al. 2012, Goicoechea et al. 2012, Manoj et al. 2013, Wampfler et al. 2013, Karska et al. 2013, Green et al. 2013). The CO ladder from J=14-13 up to 49-48 and a few tens of H_2O lines with a range of excitation energies are detected towards the Class 0 sources, NGC1333 IRAS4B and Serpens SMM1 (Herczeg et al. 2012, Goicoechea et al. 2012). The highly-excited H_2O 8_{18}–7_{07} line at 63.3 μm ($E_u/k_B = 1071$ K) is seen towards almost half of the Class 0 and I sources in the Karska et al. (2013) sample, even for bolometric luminosities as low as ~ 1 L$_\odot$. Non-dissociative shocks and, to a lesser extent, UV-heating are suggested as the dominant physical processes responsible for the observed line emission (van Kempen et al. 2010b, Visser et al. 2012, Karska et al. 2013). The contribution from the bulk of the quiescent warm protostellar envelope to the PACS lines is negligible for low-mass sources. Even for the intermediate-mass source NGC7129 FIRS2, where the envelope contribution is higher, the other processes dominate (Fich et al. 2010).

In this paper, we present Herschel-PACS spectroscopy of ten sources that cover numerous lines of CO, H_2O, OH, and [O I] lines obtained as part of the 'Water in star forming regions with Herschel' (WISH) key program (van Dishoeck et al. 2011). WISH observed in total about 80 protostars at different evolutionary stages (from prestellar cores to cir-

---

[1] Herschel is an ESA space observatory with science instruments provided by European-led Principal Investigator consortia and with important participation from NASA.

cumstellar disks) and masses (low-, intermediate-, and high-mass) with both the Hetero-dyne Instrument for the Far-Infrared (HIFI; de Graauw et al. 2010) and PACS (Poglitsch et al. 2010). This paper focuses only on PACS observations of high-mass YSOs. It complements the work by van der Tak et al. (2013), which describes our source sample and uses HIFI to study spectrally resolved ground-state H_2O lines towards all our objects. That paper also provides updated physical models of their envelopes.

The results for high-mass YSOs will be compared with those for low- and intermediate-mass young stellar objects, analyzed in a similar manner (Karska et al. 2013, Wampfler et al. 2013, Fich et al. 2010) in order to answer the following questions: How does far-IR line emission/absorption differ for high-mass protostars at different evolutionary stages? What are the dominant gas cooling channels for those sources? What physical components do we trace and what gas conditions cause the excitation of the observed lines? Are there any similarities with the low- and intermediate-mass protostars?

The paper is organized as follows. Section 2 introduces the source sample and explains the observations and reduction methods, §3 presents results that are derived directly from the observations, §4 focuses on the analysis of the data, §5 discusses our results in the context of the available models, and §6 summarizes the conclusions.

3.2 Observations and data reduction

We present spectroscopy observations of ten high-mass star forming regions collected with the PACS instrument on board *Herschel* in the framework of the 'WISH' program. The sources have an average distance of $\langle D \rangle$=2.7 kpc and represent various stages of evolution, from the classical high-mass protostellar objects (HMPOs) to hot molecular cores (HMCs) and ultra-compact H II regions (UC H II). The list of sources and their basic properties are given in Table 4.1. Objects are shown in the sequence of increasing value of an evolutionary tracer, $L^{0.6}M_{\mathrm{env}}^{-1}$, introduced in Bontemps et al. (1996). The sequence does not always correspond well with the evolutionary stages most commonly assigned to the sources in the literature (last column of Table 2), perhaps because multiple objects in different evolutionary stages are probed within our spatial resolution element (see e.g. Wyrowski et al. 2006, Leurini et al. 2013, for the case of G327-0.6).

PACS is an integral field unit with a 5×5 array of spatial pixels (hereafter *spaxels*). Each spaxel covers $9\rlap{.}''4 \times 9\rlap{.}''4$, providing a total field of view of $\sim 47'' \times 47''$. The focus of this work is on the central spaxel. The central spaxel probes similar physical scales as the full 5×5 array in the ten times closer low-mass sources. Full 5×5 maps for the high-mass sources, both in lines and continuum, will be discussed in future papers.

The range spectroscopy mode on PACS uses large grating steps to quickly scan the full 50-210 μm wavelength range with Nyquist sampling of the spectral elements. The wavelength coverage consists of three grating orders (1st: 102-210 μm; 2nd: 71-105 μm; or 3rd: 51-73 μm), two of which are always observed simultanously (one in the blue, $\lambda < 105$ μm, and one in the red, $\lambda > 102$ μm, parts of the spectrum). The spectral resolving power is $R = \lambda/\Delta\lambda \approx$ 1000-1500 for the first order, 1500-2500 for the second order, and 2500-5500

Table 3.1 – Catalog information and source properties.

Object	D	L_{bol}	M_{env}	$L^{0.6}M_{\mathrm{env}}^{-1}$	Class
	(kpc)	($L_\odot$)	($M_\odot$)	($L_\odot^{0.6}M_\odot^{-1}$)	
G327-0.6	3.3	$7.3\ 10^4$	2044	0.41	HMC
W51N-e1	5.1	$5.2\ 10^5$	4530	0.59	UCH II
DR21(OH)	1.5	$1.3\ 10^4$	472	0.62	HMPO
W33A	2.4	$3.0\ 10^4$	698	0.70	HMPO
G34.26+0.15	3.3	$1.9\ 10^5$	1792	0.82	UCH II
NGC6334-I	1.7	$1.1\ 10^5$	750	1.41	HMC
NGC7538-I1	2.7	$1.1\ 10^5$	433	2.45	UCH II
AFGL2591	3.3	$1.2\ 10^5$	373	2.99	HMPO
W3-IRS5	2.0	$2.1\ 10^5$	424	3.68	HMPO
G5.89-0.39	1.3	$4.1\ 10^4$	140	4.18	UCH II

Notes. Source coordinates with references and their physical parameters are taken from van der Tak et al. (2013).

for the third order (corresponding to velocity resolution from ~75 to 300 km s^{-1}).

Two nod positions were used for chopping 3′ on each side of the source. The comparison of the two positions was made to assess the influence of the off-source flux of observed species from the off-source positions, in particular for atoms and ions. The [C II] fluxes are strongly affected by the off-position flux and saturated for most sources – we therefore limit our analysis of this species to the two sources with comparable results for both nods, AFGL2591 and NGC7538-IRS1 (see Table 2).

Typical pointing accuracy is better than 2″. However, two sources (G327-0.6 and W33A) were mispointed by a larger amount as indicated by the location of the peak continuum emission on maps at different wavelengths (for the observing log see Table 4.A.2 in the Appendix). To account for the non-centric flux distribution on the integral field unit due to mispointing and to improve the continuum smoothness, for these sources two spaxels with maximum continuum levels are used (spaxel 11 and 21 for G327 and 23 and 33 for W33A). Summing a larger number of spaxels was not possible owing to a shift of line profiles from absorption to emission. The spatial extent of line emission / absorption will be analyzed in future papers.

We performed the basic data reduction with the Herschel Interactive Processing Environment v.10 (HIPE, Ott 2010). The flux was normalized to the telescopic background and calibrated using Neptune observations. Spectral flatfielding within HIPE was used to increase the S/N (for details, see Herczeg et al. 2012, Green et al. 2013). The overall flux calibration is accurate to ~ 20%, based on the flux repeatability for multiple observations of the same target in different programs, cross-calibrations with HIFI and ISO, and continuum photometry.

Custom IDL routines were used to process the datacubes further. The line fluxes were extracted from the central spaxel (except G327-0.6 and W33A, see above) using Gaussian fits with fixed line width (for details, see Herczeg et al. 2012). Next, they were corrected

for the wavelength-dependent loss of radiation for a point source (see PACS Observer's Manual[2]). That approach is not optimal for the cases where emission is extended beyond the central spaxel, but that is mostly the case for atomic lines, which will be presented in a companion paper by Kwon et al. (in preparation, hereafter Paper II). The uncertainty introduced by using the point-source correction factors for extended sources depends on the amount of emission in the surrounding ring of spaxels. The continuum fluxes are calculated using all 25 spaxels, except G327-0.6 where one spaxel was excluded due to saturation. In most cases, the tabulated values are at wavelengths near bright lines. They are calculated using spectral regions on both sides of the lines (but masking any features) and interpolated linearly to the wavelength of the lines. The fluxes are presented in Table 3.B.1 in the Appendix. Our continuum fluxes are included in the spectral energy distribution fits presented in van der Tak et al. (2013), who used them to derive physical models for all our sources. Those models and associated envelope masses are used in this work in Sections 5.1 and 5.3. [tb]

3.3 Results

Figure 4.2 shows the full normalized PACS spectrum with line identifications for W3 IRS5, a high-mass protostellar object with the richest molecular emission among our sources. Carbon monoxide (CO) transitions from J=14-13 to J=30-29 are detected, all in emission (see blow-ups of high-J CO lines in Figures 3.C.1 and 3.C.2). Water-vapor (H_2O) transitions up to $E_{up} \sim 1000$ K are detected (e.g. $7_{16} - 6_{25}$ at 66.1 μm, see blow-ups in Figure 3.C.1). At wavelengths shortwards of $\sim$90 μm, many H_2O lines are seen in absorption, but those at longer wavelengths are primarily in emission.

Seven hydroxyl (OH) doublets up to $E_{up} \approx 618$ K are seen[3]. All lines within the $^2\Pi_{3/2}$ ladder (119, 84, and 65 μm doublets; see Figure 1 in Wampfler et al. 2013) are strong absorption lines. The $^2\Pi_{1/2}$ ladder lines (163 and 71 μm) are seen in emission. The cross-ladder transitions at 79 μm (OH $1/2,1/2$-$3/2,3/2$, $E_{up} \approx 180$ K) and 96 μm (OH $3/2,1/2$-$5/2,3/2$, $E_{up} \approx 270$ K) are absorption and emission lines, respectively. Only the ground-rotational lines of methylidyne (CH) are detected at 149 μm in absorption. The [O I] transitions at 63 μm and 145 μm are both strong emission lines in W3 IRS5. That is not always the case for other sources in our sample. The [O I] line at 63 μm, where the velocity resolution of PACS is at its highest ($\sim$90 km s^{-1}), shows a variety of profiles (see Figure 3.1): pure absorption (G327-0.6, W51Ne1, G34.26, W33A), regular P-Cygni profiles (AFGL2591, NGC6334-I), hints of inverse P-Cygni profiles in DR21(OH) and pure emission (W3 IRS5, NGC7538-I1, G5.89). The [O I] line at 145 μm, however, is always detected in emission. The P-Cygni profiles resolved on velocity scales of $\sim$ 100 km s^{-1} resemble the high-velocity line wings observed in ro-vibrational transitions of CO in some of the same sources (Mitchell et al. 1990, Herczeg et al. 2011), suggested to originate in the wind impacting the outflow cavities. Not all absorption needs to be associated with the source,

---

[2] http://herschel.esac.esa.int/Docs/PACS/html/pacs_om.html

[3] The highest-excited OH doublet at 71 μm is not considered further in the analysis, because the 70-73 μm region observed with PACS is affected by spectral leakage and thus is badly flux-calibrated.

however: it can also be due to foreground absorption (e.g. outflow lobe or the ISM). For example, ISO Fabry Perot and new Herschel/ HIFI observations of H_2O and OH in Orion also show line wings in absorption / emission extending to velocities up to ~ 100 km s^{-1} (Cernicharo et al. 2006, Goicoechea et al. 2006, Choi et al. in prep.), but the ISO-LWS Fabry-Perot observations of Orion did not reveal any P-Cygni profiles in the [O I] 63 μm line.

A comparison of selected line-rich parts of the spectra for all our sources is presented in Figure 3.2. The spectra are normalized by the continuum emission to better visualize the line absorption depths. However, the unresolved profiles of PACS underestimate the true absorption depths and cannot be used to estimate the optical depths. The 64-68 μm segment covers the highly-excited H_2O lines at 66.4, 67.1, and 67.3 μm ($E_{up} \approx 410$ K); high-J CO lines at 65.7 ($J =$40-39) and 67.3 ($J =$39-38); and the OH $^2\Pi_{3/2}$ $J = 9/2 - 7/2$ ($E_{up} \approx 510$ K) doublet at 65 μm. The low-lying H_2O lines are detected for all sources. The high-J CO lines are not detected in this spectral region. The OH doublet is detected for six out of ten sources (see also Figure 3.C.3 in the Appendix).

The main lines seen in the 148-157 μm region are CH $^2\Pi_{3/2}$ $J = 3/2 - ^2\Pi_{1/2}$ $J = 1/2$ transition at 149 μm (in absorption), CO 17-16, and H_2O $3_{22} - 3_{13}$ line at 156.2 μm ($E_{up} \approx 300$ K). Weak absorption lines at $\sim 155 - 156$ μm seen towards the hot core G327-0.6 are most likely C_3 ro-vibrational transitions (Cernicharo et al. 2000, Paper II).

The most commonly detected lines in the 170-182 μm spectral region include the CO 15-14 line and the H_2O lines at 174.6, 179.5, and 180.5 μm ($E_{up} \approx$100-200 K). The profiles of H_2O lines change from object to object: the H_2O $2_{12} - 1_{01}$ line at 179.5 μm is in absorption for all sources except W3 IRS5; the H_2O $2_{21} - 1_{12}$ at 180.5 μm is in emission for the three most evolved sources (top 3 spectra in Figure 3.2). The ammonia line at ~ 170 μm, NH_3 (3,2)a-(2,2)s, is detected toward four sources (G327-0.6, W51N-e1, G34.26, and NGC6334-I). An absorption line at ~ 181 μm corresponds to $H_2^{18}O$ $2_{12} - 1_{01}$ and/ or H_3O^+ $1_1^- - 1_1^+$ lines (Goicoechea & Cernicharo 2001). Extended discussion of ions and molecules other than CO, H_2O, and OH will appear in Paper II.

Line profiles of H_2O observed with HIFI show a variety of emission and absorption components that are not resolved by PACS (Chavarría et al. 2010, Kristensen et al. 2012, van der Tak et al. 2013). The only H_2O lines observed in common by the two instruments within the WISH program are the ground-state transitions: $2_{12} - 1_{01}$ at 179.5 μm (1670 GHz) and $2_{21} - 1_{12}$ at 180.5 μm (1661 GHz), both dominated by absorptions and therefore not optimal for estimating to what extent a complex water profile is diluted at the PACS spectral resolution. However, HIFI observations of the lines between excited rotational states, which dominate our detected PACS lines, are generally in emission at the longer wavelengths probed by HIFI. In the case of ^{12}CO 10–9, the line profiles of YSOs observed with HIFI consist of a broad outflow and a narrow quiescent component with the relative fraction of the integrated intensity of the narrow to broad components being typically 30-70% for low-mass sources (Yıldız et al. 2013). For the single case of a high-mass YSO, W3 IRS5, this fraction is about 50% (San José-García et al. 2013).

To summarize, PACS spectra of high-mass sources from our sample show detections of many molecular lines up to high excitation energies. CO, H_2O, OH, and CH lines are seen toward all objects, whereas weaker lines of other molecules are detected toward

fewer than half of the sources. CO lines are always seen in emission, CH in absorption, and other species show different profiles depending on the transition and the object. Table 3.C.1 shows the CO line fluxes for all lines in the PACS range.

3.4 Analysis

3.4.1 Far-IR line cooling

Emission lines observed in the PACS wavelength range are used to calculate the contribution of different species to the total line cooling from high-mass protostars. Our goal is to compare the cooling of warm gas by molecules and atoms with the cooling by dust and connect them with the evolutionary stages of the objects. Relative contributions to the cooling between different molecules are also determined, which can be an indicator of the physical processes in the environments of young protostars (e.g. Nisini et al. 2002b, Karska et al. 2013).

We define the total far-IR line cooling (L_{FIRL}) as the sum of all emission line luminosities from the fine-structure [O I] lines (at 63 and 145 μm) and the detected molecules, following Nisini et al. (2002b) and Karska et al. (2013). [C II], the most important line coolant of diffuse interstellar gas, is also expected to be a significant cooling agent in high-mass star forming regions and extragalactic sources. It is not explicitly included in our analysis, however, because the calculated fluxes are strongly affected by off-source emission and often saturated (see also Section 2). The emitted [C II] luminosity is shown below for only two sources, where reliable fluxes were obtained. Cooling in other ionic lines such as [O III], [N II], and [N III] is also excluded, due to the off-position contamination and the fact that those lines trace a different physical component than the molecules and [O I]. Since the only molecules with emission lines are CO, H_2O, and OH, the equation for the total far-IR line cooling can be written as $L_{FIRL} = L_{OI} + L_{CO} + L_{H_2O} + L_{OH}$.

Table 3.1 summarizes our measurements. The amount of cooling by dust is described by the bolometric luminosity and equals $\sim 10^4$-10^5 L$_\odot$ for our sources (van der Tak et al. 2013). The total far-IR line cooling ranges from ~ 1 to ~ 40 L$_\odot$, several orders of magnitude less than the dust cooling. Relative contributions of oxygen atoms and molecules to the gas cooling are illustrated in Figure 3.1. Atomic cooling is largest for the more evolved sources in our sample (see Table 1), in particular for NGC7538 IRS1 and AFGL2591, where it is the dominant line-cooling channel. For those two sources, additional cooling by [C II] is determined and amounts to $\sim$10-25% of L_{FIRL} (Table 3.1). Typically, atomic cooling accounts for $\sim$20 % of the total line far-IR line cooling. Molecular line cooling is dominated by CO, which is responsible for ~ 15 up to 85% of L_{FIRL}, with a median contribution of 74%. H_2O and OH median contributions to the far-IR cooling are less than 1%, because many of their transitions are detected in absorption. Assuming that the absorptions arise in the same gas, as found for the case of Orion (Cernicharo et al. 2006), they therefore do not contribute to the cooling, but to heating the gas. Still, the contribution of H_2O to the total FIR cooling increases slightly for more evolved sources, from $\sim$5% (DR21(OH)) to 30% (W3IRS5), whereas no such trend is seen for OH.
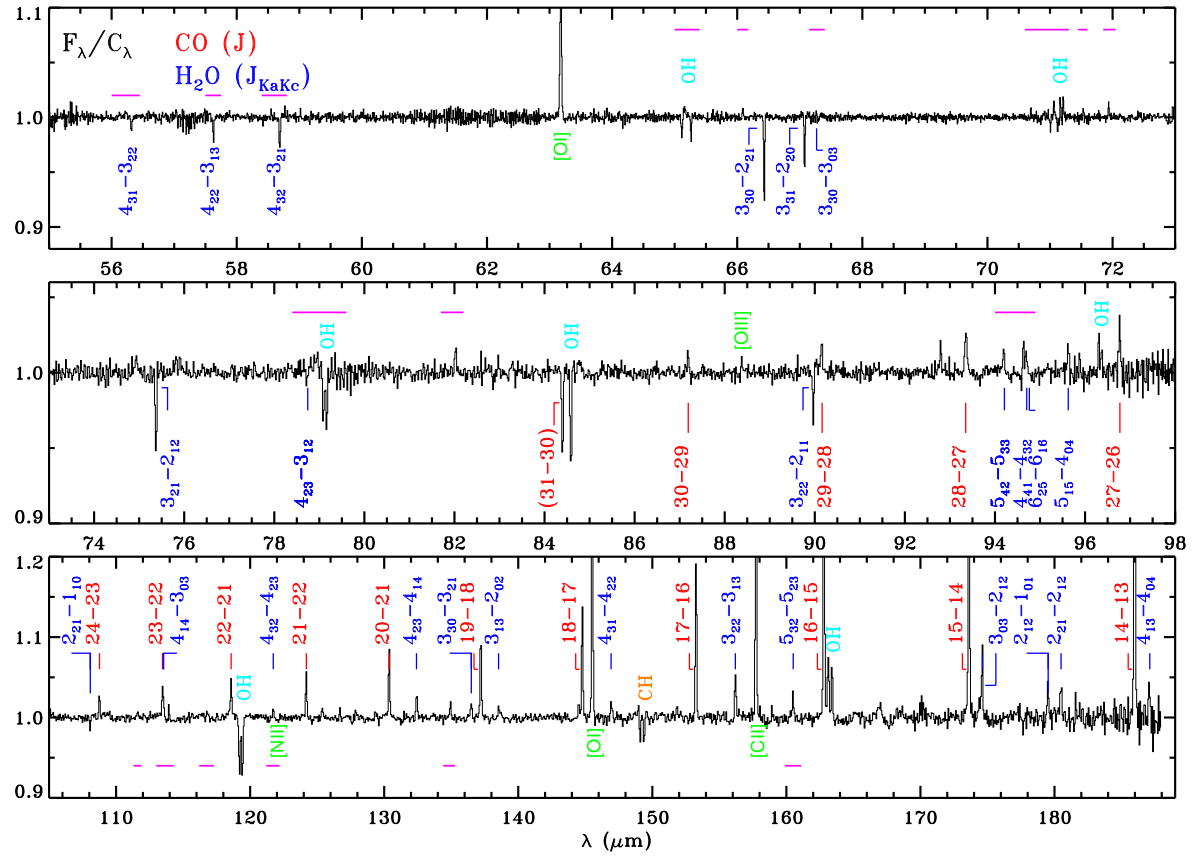
Figure 3.1 – Herschel-PACS continuum-normalized spectrum of W3 IRS5 at the central position. Lines of CO are shown in red, H$_2$O in blue, OH in light blue, CH in orange, and atoms and ions in green. Horizontal magenta lines show spectral regions zoomed in Figure 3.C.1.
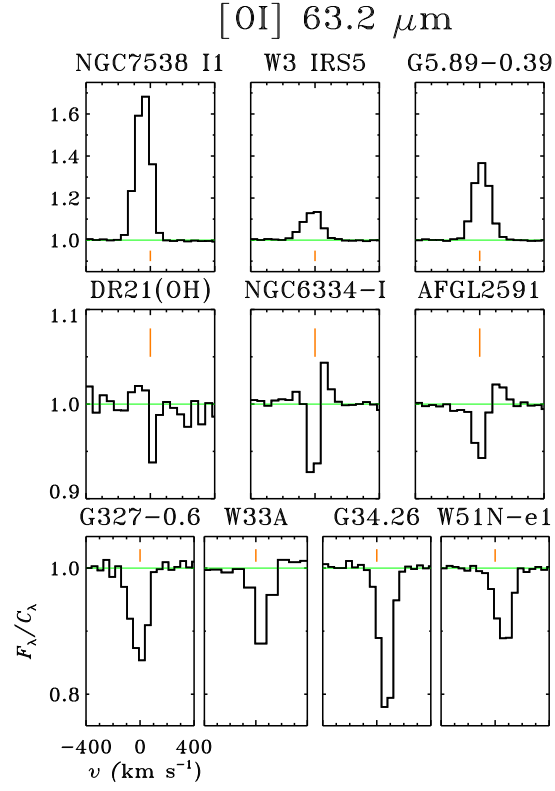
Figure 3.1 – Herschel-PACS profiles of the [O I] 63.2 μm line at central position.
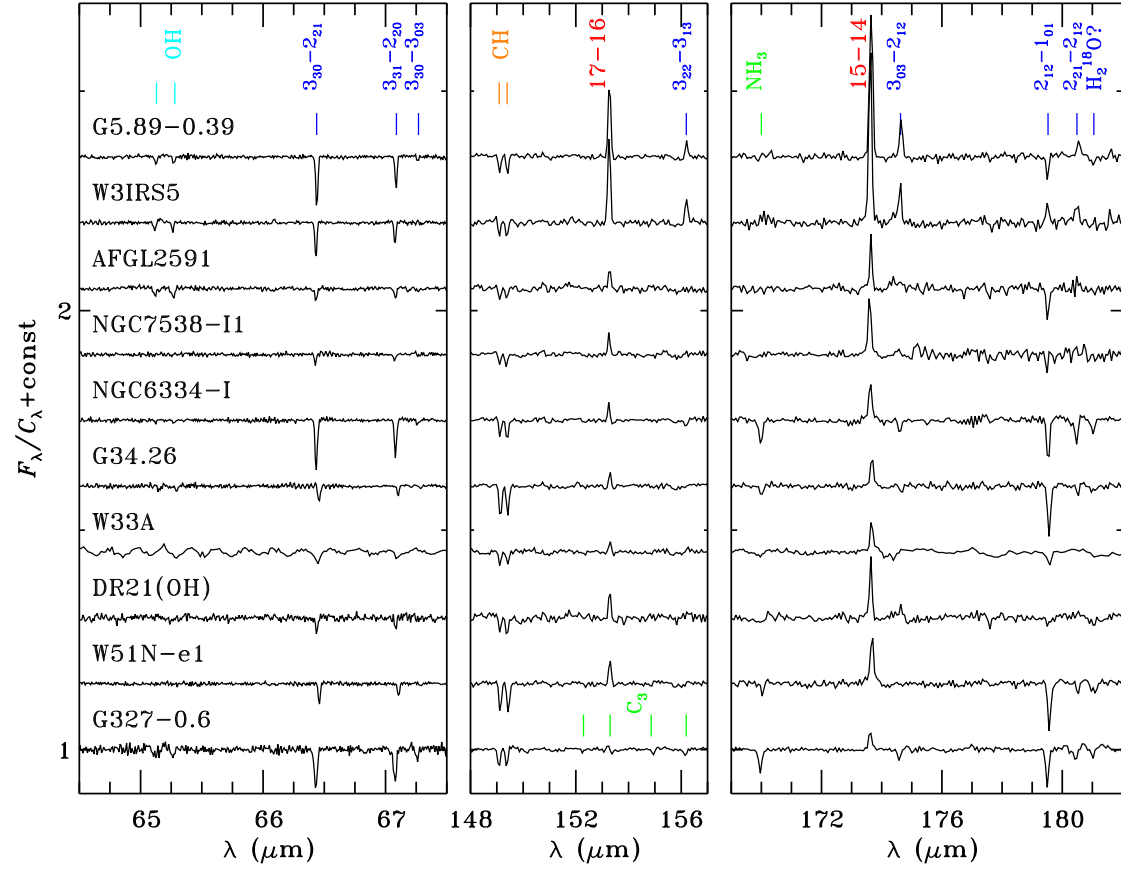
Figure 3.2 – Normalized spectral regions of all our sources at the central position at 64-68, 148-157, and 169-182 μm. Objects are shown in the evolutionary sequence, with the most evolved ones on top. Lines of CO are shown in red, H_2O in blue, OH in light blue, CH in orange, and NH_3 and C_3 in green. Spectra are shifted vertically to improve the clarity of the figure.
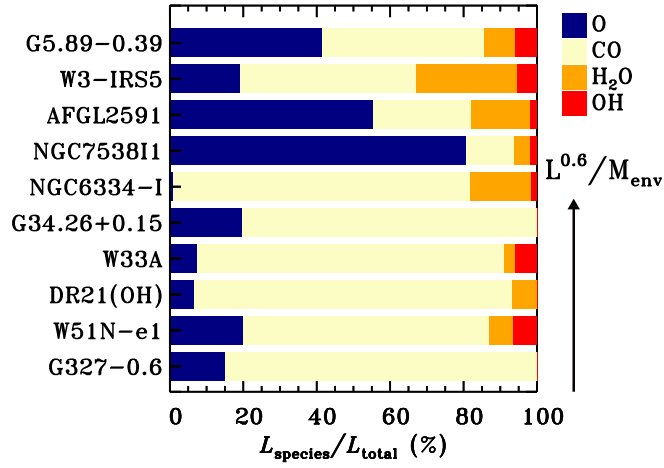
Figure 3.1 – Relative contributions of [O I] (dark blue), CO (yellow), H₂O (orange), and OH (red) cooling to the total far-IR gas cooling at central position are shown from left to right horizontally for each source. The objects follow the evolutionary sequence with the most evolved sources on top.

Table 3.1 – Far-IR line cooling by molecules and atoms in units of $L_\odot$.

Source	L_{bol} ($L_\odot$)	L_{FIRL}	L_{mol} ($L_\odot$)	L_{OI}	L_{CO}	L_{H2O} ($L_\odot$)	L_{OH}	L_{CII} ($L_\odot$)
G327-0.6	$7.3\ 10^4$	2.1(0.7)	1.8(0.6)	0.3(0.1)	1.8(0.6)	–	–	–
W51N-e1	$5.2\ 10^5$	37.8(10.8)	30.2(8.9)	7.6(1.8)	25.3(6.8)	2.5(1.1)	2.4(1.0)	–
DR21(OH)	$1.3\ 10^4$	1.4(0.4)	1.3(0.4)	0.09(0.03)	1.2(0.3)	0.09(0.04)	–	–
W33A	$3.0\ 10^4$	0.7(0.2)	0.6(0.2)	0.05(0.02)	0.6(0.2)	0.02(0.01)	0.04(0.01)	–
G34.26+0.15	$1.9\ 10^5$	9.6(2.9)	7.7(2.4)	1.9(0.5)	7.7(2.4)	–	–	–
NGC6334-I	$1.1\ 10^5$	4.2(1.3)	4.2(1.2)	0.04(0.03)	3.4(1.0)	0.7(0.2)	0.06(0.03)	–
NGC7538-IRS1	$1.1\ 10^5$	13.6(3.3)	2.6(0.8)	11.0(2.5)	1.8(0.5)	0.6(0.2)	0.2(0.1)	2.0(0.4)
AFGL2591	$1.2\ 10^5$	6.1(1.8)	2.7(0.8)	3.4(0.9)	1.6(0.5)	1.0(0.4)	0.11(0.04)	1.9(0.4)
W3-IRS5	$2.1\ 10^5$	22.0(6.0)	17.8(5.0)	4.2(1.0)	10.5(2.5)	6.1(2.2)	1.2(0.4)	–
G5.89-0.39	$4.1\ 10^4$	8.8(2.2)	5.1(1.3)	3.7(0.9)	3.9(0.9)	0.8(0.3)	0.5(0.2)	–

Notes. Columns show: (1) bolometric luminosity, L_{bol}, (2) total FIR line cooling, L_{FIRL} ($L_{\mathrm{mol}}+L_{\mathrm{OI}}$), (3) molecular cooling, L_{mol}, and (4) cooling by oxygen atoms, L_{OI}. Cooling by individual molecules is shown in column (5) CO, (6) H_2O, and (7) OH. Absence of emission lines that would contribute to the cooling are shown with "–" (absorption lines are detected for H_2O and OH). Errors are written in brackets and include 20% calibration error on individual line fluxes.

3.4.2 Molecular excitation

Detections of multiple rotational transitions of CO, H_2O, and OH allow us to determine the rotational temperatures of the emitting or absorbing gas using Boltzmann diagrams (e.g. Goldsmith & Langer 1999). For H_2O and OH, the densities are probably not high enough to approach a Boltzmann distribution and therefore the diagrams presented below are less meaningful.

Emission line fluxes are used to calculate the number of emitting molecules, $\mathcal{N}_u$, for each molecular transition using Equation (3.1), assuming that the lines are optically thin. Here, F_λ denotes the flux of the line at wavelength λ, d is the distance to the source, A the Einstein coefficient, c the speed of light, and h Planck's constant:

$$\mathcal{N}_u = \frac{4\pi d^2 F_\lambda \lambda}{hcA} \qquad (3.1)$$

The base-10 logarithm of $\mathcal{N}_u$ over degeneracy of the upper level g_u is shown as a function of the upper level energy, E_u, in Boltzmann diagrams (Figures 3.2 and 3.3). The rotational temperature is calculated in a standard way, from the slope b of the linear fit to the data in the natural logarithm units, $T_{rot} = -1/b$.

Because the size of the emitting region is not resolved by our instrument, the calculation of column densities requires additional assumptions and therefore only the total numbers of emitting molecules is determined. The formula for the total number of emitting molecules, $\mathcal{N}_{tot}$, is derived from the expression for total column density, $N_{tot} = Q \cdot \exp(a)$, where Q is the partition function for the temperature and a the y-intercept. Correcting for a viewing angle, $\Omega = d^2/\pi R^2$, and multiplying by the gas emitting area of radius R, yields

$$\mathcal{N}_{tot} = Q \cdot \exp(a) \cdot d^2. \qquad (3.2)$$

For details, see e.g. Karska et al. (2013) and Green et al. (2013).

For absorption lines, column densities, N_l, are calculated from line equivalent widths, W_λ, using Equation 3.3 (e.g. Wright et al. 2000).

$$N_l = \frac{8\pi c W_\lambda g_l}{\lambda^4 A g_u}. \qquad (3.3)$$

This relation assumes that the lines are optically thin, the covering factor is unity, and the excitation temperature $T_{ex} \ll hc/k\lambda$ for all lines. Some of the emission / absorption lines are likely P-Cygni profiles (Cernicharo et al. 2006) that are not resolved with PACS and which we assume to be pure emission / absorbing lines.

The natural logarithm of N_l over the degeneracy of the lower level, g_l, is shown in the Boltzmann diagrams as a function of the lower level energy, E_l (Figures 3.3, 3.4, and 3.6). Rotational temperatures and total column densities are calculated in the same way as for the emission lines (see above).

In the following sections, the excitation of CO, H_2O, and OH are discussed separately. Table 3.2 summarizes the values of rotational temperatures, T_{rot}, and total numbers of emitting molecules or column densities, for those species.
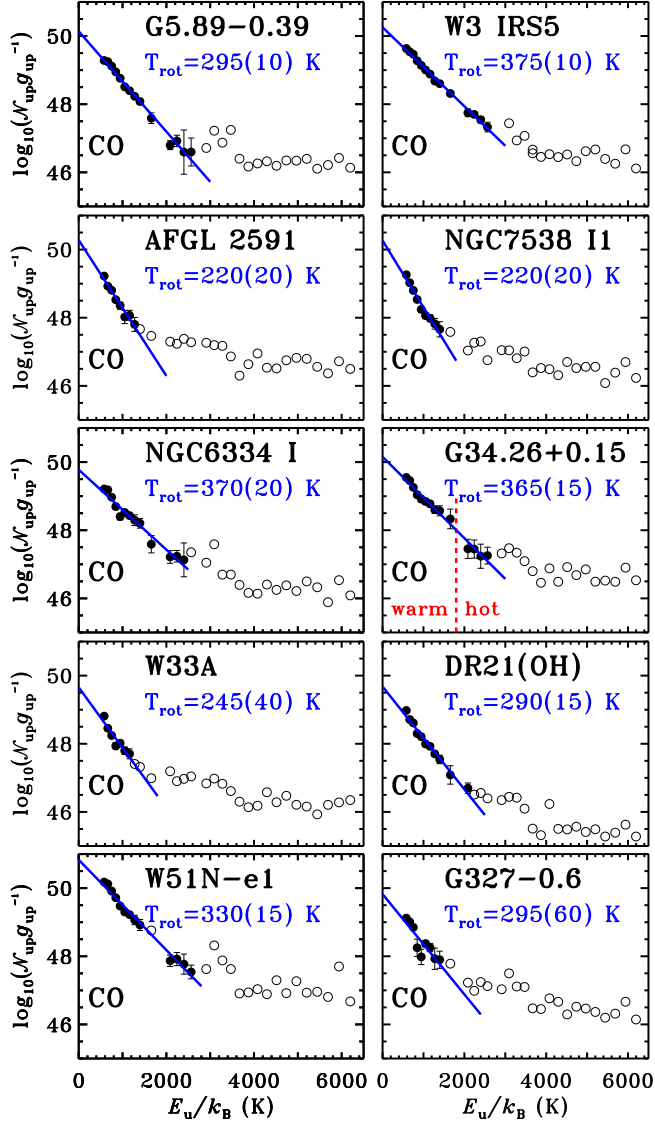
Figure 3.2 – Rotational diagrams of CO for all objects in our sample. The base-10 logarithm of the number of emitting molecules from a level u, N_u, divided by the degeneracy of the level, g_u, is shown as a function of energy of the upper level in kelvins, E_{up}. Detections are shown as filled circles, whereas three-sigma upper limits are shown as empty circles. Blue lines show linear fits to the data and the corresponding rotational temperatures. The vertical red line in the G34.26+0.15 panel shows the dividing line between the warm and hot components as seen in rotational diagrams of low-mass YSOs. Errors associated with the fit are shown in brackets.
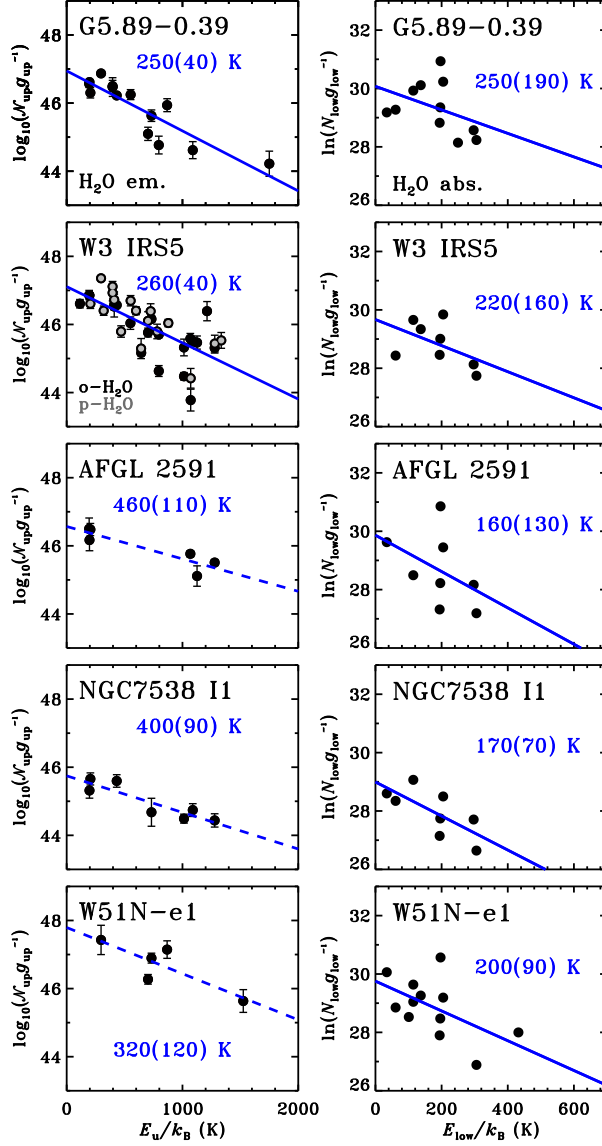
Figure 3.3 – Rotational diagrams of H_2O calculated using emission lines (left column) and absorption lines (right column), respectively. For emission line diagrams, the logarithm with base 10 of total number of molecules in a level u, $\mathcal{N}$, divided by the degeneracy of the level, g_u, is shown as a function of energy of the upper level in Kelvins, E_{low}. For absorptions lines, the natural logarithm of the column density in a level l, N_l, divided by the degeneracy of the level, g_l, is shown in y-axis. A one-component linear fit is shown with the corresponding value of rotational temperature and error of the fit in brackets. A solid line is used for the cases where at least 10 lines are detected. In the W3 IRS5 emission panel, para-H_2O lines are shown in gray and ortho-H_2O lines in black, respectively.

Table 3.2 – CO, H_2O, and OH rotational excitation

Source	Warm CO		H_2O (em.)		H_2O (abs.)		R^a	OH $^2\Pi_{3/2}$ ^{b}	OH^c
	$T_{rot}(K)$	$\log_{10}\mathcal{N}$	$T_{rot}(K)$	$\log_{10}\mathcal{N}$	$T_{rot}(K)$	$\ln N_{low}$	(arc sec)	$T_{rot}(K)$	$T_{rot}(K)$
G327-0.6	295(60)	51.9(0.3)	…	…	**210(80)**	34.5(0.5)	…	**105(12)**	77(29)
W51N-e1	330(15)	52.9(0.1)	320(120)	50.1(0.5)	**200(90)**	34.0(0.5)	3.4	66(-)	54(29)
DR21(OH)	290(15)	51.7(0.1)	…	…	…	…	…	**98(27)**	79(30)
W33A	245(40)	51.6(0.2)	…	…	…	…	…	…	…
G34.26+0.15	365(15)	52.3(0.1)	…	…	**270(210)**	34.0(0.6)	…	**89(5)**	71(15)
NGC6334-I	370(20)	51.9(0.1)	…	…	**180(40)**	34.6(0.3)	…	93(-)	71(50)
NGC7538-IRS1	220(20)	51.7(0.2)	400(90)	48.2(0.2)	170(70)	33.1(0.5)	1.1	52(-)	54(37)
AFGL2591	220(20)	51.7(0.2)	460(110)	49.1(0.2)	160(130)	33.9(1.1)	1.6	**105(29)**	89(21)
W3-IRS5	375(10)	52.4(0.1)	**260(40)**	49.3(0.2)	220(160)	34.1(0.6)	3.2	**109(3)**	83(22)
G5.89-0.39	295(10)	52.2(0.1)	**250(40)**	49.1(0.2)	**250(190)**	34.6(0.6)	3.0	**96(1)**	77(16)

Notes. Rotational temperatures of H_2O and OH within the $^2\Pi_{3/2}$ ladder are calculated using at least 10 and 3 lines / doublets, respectively, and are shown in boldface. Non-detections are marked with dots. For OH temperatures determined using only 2 transitions, the associated error is not given and marked with "-".
$^{(a)}$ Size of the H_2O emitting region assuming that all H_2O lines trace the same physical component (see Section 4.2.2.). $^{(b)}$ Rotational temperature of OH calculated using only the OH $^2\Pi_{3/2}$ ladder transitions, see Figure 9 and Section 4.2.3. $^{(c)}$ Rotational temperature of OH calculated using all lines detected in absorption.

3.4.2.1 CO

Figure 3.2 shows CO rotational diagrams for all our sources. CO detections, up to $J = 30$-29 ($E_u = 2565$ K), are described well by single rotational temperatures in the range from 220 K (AFGL2591 and NGC7538 IRS1) to ~370 K (W3IRS5 and G34.26+0.15) and the average of $T_{rot,CO}$ ~300(23)±60 K.[4] The highest temperatures are seen for objects where high-J CO transitions with $E_u > 2000$ K are detected.

Temperatures of ~300 K are attributed to the 'warm' component in low-mass YSOs (e.g. Goicoechea et al. 2012, Karska et al. 2013, Green et al. 2013), where they are calculated using transitions from $J_{up} = 14$ ($E_u = 580$ K) to 24 ($E_u = 1660$ K). In those sources, a break around $E_u \sim 1800$ K in the rotational diagram is noticeble (see vertical line in Figure 3.2) and J_{up} 25 transitions are attributed to the 'hot' component. Such a turning point is not seen in the diagrams of our high-mass sources with detections extending beyond the $J = 24 - 23$ transition.

In NGC7538 IRS1, a possible break is seen around $E_u \sim 1000$ K. A two-component fit to the data results in rotational temperatures T_{rot1} ~160±10 K and T_{rot2} ~370±35 K. The latter temperature is consistent within errors with the 'warm' component seen towards low-mass sources. The colder temperature resembles the $\sim 70 - 100$ K 'cool' component seen in J_{up} 14 transitions (e.g. Goicoechea et al. 2012, Karska et al. 2013, van der Wiel et al. 2013), detected at longer wavelengths than the PACS range.

The absence of the hot component toward all our sources is not significant according to the calculated upper limits. In addition to limited S/N and line-to-continuum ratio, there are other effects that may prevent the hot component from being detected. These include the fact that the continuum becomes more optically thick at the shorter wavelengths (see also below) and/or a smaller filling factor of the hot component in the PACS beam compared with low-mass sources. More generally, both the 'warm' and 'hot' components could still be part of a single physical structure as proposed in Neufeld (2012).

The average logarithm of the number of emitting (warm) CO molecules, $\log_{10}\mathcal{N}$, is similar for all objects, and equals 52.4(0.1)±0.5. Values of $\log_{10}\mathcal{N}$ in the range from 51.6 to 53.1 are derived. DR21(OH), one of the lowest bolometric luminosity sources in our sample, exhibits one of the lowest $\mathcal{N}$(CO) contents, whereas the highest CO content is found for W51N-e1, the most luminous source.

3.4.2.2 H$_2$O

Figure 3.3 shows rotational diagrams of H_2O calculated for five sources with H_2O lines detected both in emission and in absorption. Because the emitting region is not resolved by our observations, the diagrams calculated using the emission and absorption lines are shown separately. Figure 3.4 shows H_2O diagrams for the three sources where all H_2O lines are seen in absorption.

The rotational diagrams show substantial scatter, greater than the errors of individual data points, caused by large opacities, subthermal excitation (see Herczeg et al. 2012

---

[4] The value in the brackets (23) shows the average error of rotational temperatures for different sources, whereas ±60 is the standard deviation of rotational temperatures.
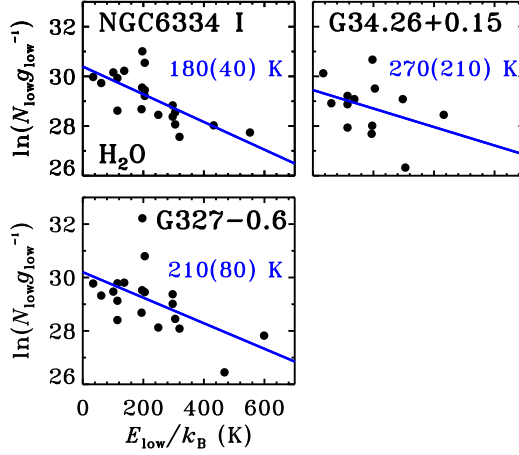
Figure 3.4 – Rotational diagrams of H_2O calculated using absorption lines. A single-component fit is used to calculate the temperature shown in the panels.

and below), and possible radiation excitation by far-IR dust emission pumping. The determination of rotational temperatures is therefore subject to significant errors when only a limited number of lines is detected. In Table 3.2 H_2O temperatures calculated using at least ten lines are indicated in boldface. Ro-vibrational spectra of H_2O from ISO-SWS towards massive protostars (four of them in common with our sample) show rotational temperatures of H_2O as high as 500 K, in agreement with the errors with our measurements (Boonman & van Dishoeck 2003).

The largest number of H_2O lines is detected in the two most evolved sources – G5.89-0.39 and W3 IRS5. Single component fits to 12 and 37 water emission lines, respectively, give similar rotational temperatures of $\sim$ 250 K (see Figure 3.3), with no systematic differences between o-H_2O and p-H_2O lines. Rotational temperatures determined for the remaining sources, with at least five detections of H_2O in emission, are higher, $T_{rot} \sim 300 - 450$ K, but are less accurate.

Rotational temperatures calculated from a single component fit to the absorption line diagrams are $\sim$ 200 K for all sources. They are in good agreement with the values obtained from the emission diagrams for G5.89-0.39 and W3 IRS5, suggesting that all H_2O lines originate in the same physical component (see e.g. Cernicharo et al. 2006). In such a scenario, the column densities should also agree, and the comparison of the total number of molecules calculated from emission lines and columns determined from the absorption lines yields the size of the emitting region, R. The radius of the H_2O emitting area under that condition equals $\sim$3 arcsec for G5.89-0.39 and W3 IRS5 (see Table 3.2).

To assess the effects of optical depth and subthermal excitation on the derived temperatures from the absorption lines, equivalent widths of lines are calculated using the radiative transfer code Radex (van der Tak et al. 2007) and translated to column densities
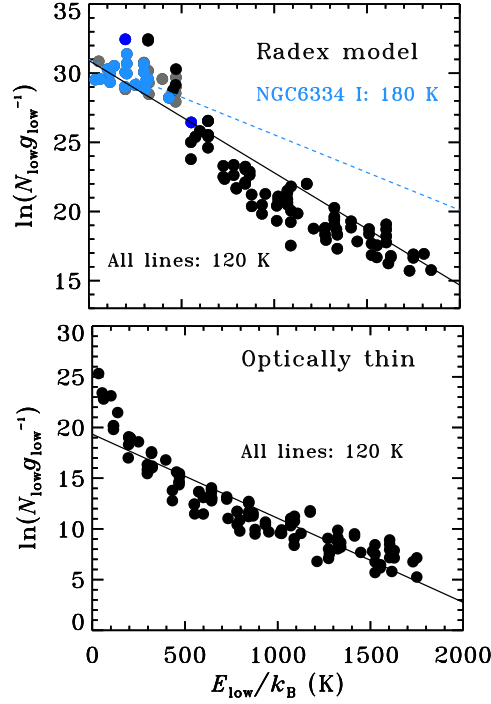
Figure 3.5 – *Top*: Rotational diagram of H_2O calculated assuming a kinetic temperature $T = 1000$ K, H_2 density $n = 10^6$ cm^{-3}, H_2O column density $2 \cdot 10^{16}$ cm^{-2}, and line width $\Delta V = 5$ km s^{-1}. Lines observed in absorption in NGC6334-I are shown in blue. Fits are done to all lines in the PACS range included in the LAMDA database (Schöier et al. 2005) (in black) and to the NGC6334-I lines (in blue). Darker shades denote optically thin lines. *Bottom*: The same as above, but assuming an H_2O column density 10^{12} cm^{-2}, such that all lines are optically thin.

using Equation (2). The adopted physical conditions of $T_{kin} = 1000$ K and $n = 10^6$ cm^{-3} are typical of warm, shocked region where water is excited (Goicoechea et al. 2012). The models were calculated using all H_2O lines in the PACS range included in the LAMDA database (Schöier et al. 2005). The latest available H_2O collisional coefficients are used (Daniel et al. 2011, and references therein).

Figure 3.5 shows the 'theoretical' rotational diagrams calculated for low and high column densities. A single component fit to *all* lines in the high column density model gives a temperature of ~ 120 K, consistent with subthermal excitation, and a total column density of $1.2 \cdot 10^{15}$ cm^{-2} ($\ln N_{low} \sim 34.7$), an order of magnitude lower than the input column. A separate fit to the lines detected in NGC6334-I gives a temperature of ~ 180 K and a slightly higher column density ($1.9 \cdot 10^{15}$ cm^{-2}). These observed lines are typically highly optically thick with $\tau \sim$ few tens, up to 100.

In the low column density model all lines are optically thin. A fit to all lines gives a
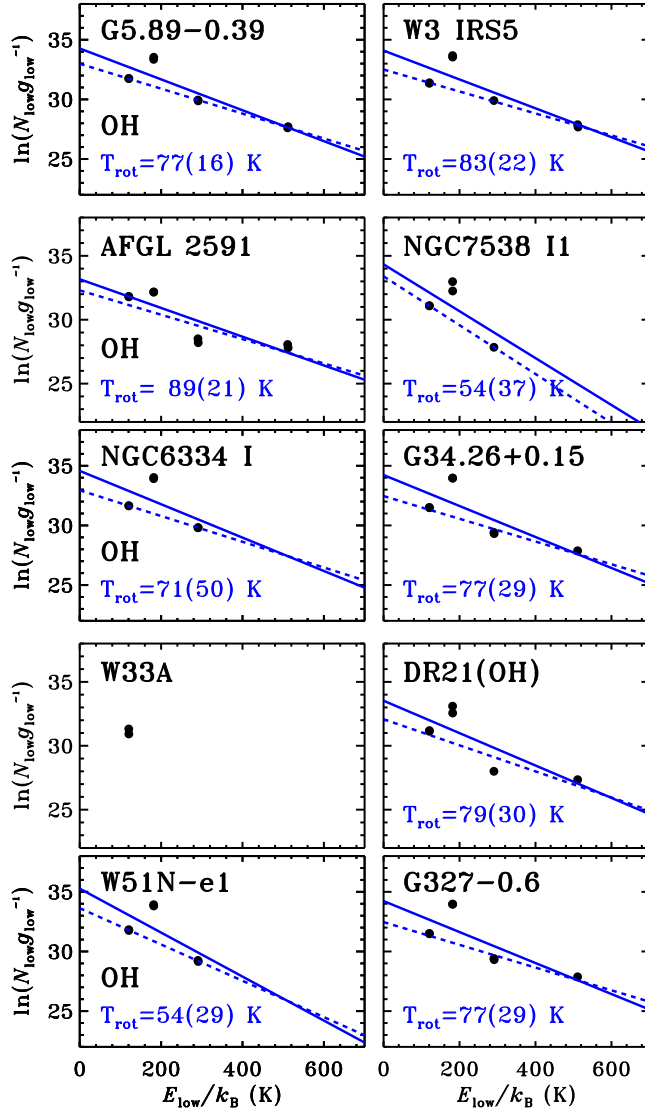
Figure 3.6 – Rotational diagrams of OH calculated using absorption lines, similar to Figure 3.4 for H_2O. The single component fit to all OH transitions detected in absorption is shown with a solid line with the corresponding temperature. A separate single component fit is done for the OH $^2\Pi_{3/2}$ ladder transitions and drawn in a dashed line. The respective rotational temperatures are tabulated in Table 3.2.

temperature of ∼ 120 K, similar to the high column density model. The level populations are clearly subthermal ($T_{\mathrm{rot}} \ll T_{\mathrm{kin}}$), resulting in the scatter in the diagram. These examples illustrate the difficulty in using the inferred rotational temperatures to characterize a complex environment of high-mass star forming regions.

The continuum opacity at PACS wavelengths is typically of the order of a few in the observed sources, as indicated by the source structures derived by van der Tak et al. (2013), and becomes higher at shorter wavelengths. This implies that the absorbing H_2O is on the frontside of the source. Also, any emission at short wavelengths must originate outside the region where the dust is optically thick.

3.4.2.3 OH

Figure 3.6 presents rotational diagrams of OH calculated using absorption lines. A single component is fitted to all detected lines. A separate fit is done for the lines originating in the $^2\Pi_{3/2}$ ladder, which are mostly collisionally excited. This fit excludes the intra-ladder 79 μm doublet, connecting with the ground state, which readily gets optically thick (Wampfler et al. 2013). A possible line-of-sight contribution by unrelated foreground is expected in the ground-state 119 μm line, which is included in the fit. The resulting rotational temperatures for each source are shown in Table 3.2, separately for those two fits.

The average rotational temperature for the $^2\Pi_{3/2}$ ladder is very similar for all objects and equals 100(12)±7 K. The inclusion of all OH doublets results in lower temperatures, $T_{\mathrm{rot,OH}}$ ∼79(22)±6 K.

3.5 Discussion: from low to high mass

3.5.1 Origin of CO emission

Several physical components have been proposed as a source of far-IR CO emission in isolated low-mass young stellar objects: (i) the inner parts of the quiescent envelope, passively heated by a central source (Ceccarelli et al. 1996, Doty & Neufeld 1997); (ii) gas in cavity walls heated by UV photons (van Kempen et al. 2009a, 2010b, Visser et al. 2012); (iii) currently shocked gas along the outflow walls produced by the protostellar wind-envelope interaction (van Kempen et al. 2010b, Visser et al. 2012, Karska et al. 2013).

The quiescent envelope of high-mass protostars is warmer and denser than for low-mass YSOs, and therefore its contribution to the far-IR CO emission is expected to be greater. In this section, we determine this contribution for a subsample of our sources using the density and temperature structure of each envelope obtained by van der Tak et al. (2013).

In this work, the continuum emission for all our objects is modeled using a modified 3D Whitney-Robitaille continuum radiative transfer code (Robitaille 2011, Whitney et al. 2013). For simplicity, the van der Tak et al. models do not contain any cavity or disk,

Table 3.1 – Input parameters for the $C^{18}O$ envelope emission model[a]

Object	X_0	X_{in}[b]	T_{ev} (K)	FWHM (km s^{-1})	$^{16}O/^{18}O$[c]
G327-0.6	$3.8\ 10^{-7}$	–	–	5.0	387
W51N-e1	$3.0\ 10^{-7}$	–	–	4.7	417
DR21(OH)	$1.3\ 10^{-6}$	–	–	2.4	531
NGC6334-I	$0.5\ 10^{-7}$	$2.0\ 10^{-7}$	35	4.2	437
G5.89-0.39	$0.1\ 10^{-7}$	$5.0\ 10^{-7}$	40	4.5	460
NGC7538-I1	$2.1\ 10^{-8}$	$7.5\ 10^{-7}$	35	2.1	614

Notes. [a] Parameters for the remaining sources will be presented in San José-García et al. (in prep.). [b] A jump abundance profile is used to model NGC6334-I, G5.89-0.39, and NGC7538 IRS1. [c] The ratio depends on the source's distance from the Galaxy center (Wilson & Rood 1994).

and assume a spherically symmetric power law density structure of the envelope, $n \propto r^{-p}$, where p is a free parameter. The size and mass of the envelope and the power law exponent, p, are calculated by best-fit comparison to the spectral energy distributions and radial emission profiles at 450 and 850 μm (Shirley et al. 2000). The models solve for the dust temperature as function of radius and assume that the gas temperature is equal to the dust temperature. For more detailed discussion, see van der Tak et al. (2013).

The envelope temperature and density structure from van der Tak et al. (2013) is used as input to the 1D radiative transfer code RATRAN (Hogerheijde & van der Tak 2000) in order to simultaneously reproduce the strengths of optically thin $C^{18}O$ lines from J =2-1 to 9-8 (following the procedure in Yıldız et al. 2010, 2012). The free parameters include $C^{18}O$ constant abundance X_0 and the line width, FWHM. For three sources, a 'jump' abundance profile structure is needed, described by the evaporation temperature T_{ev} and inner abundance X_{in}. The parameters derived from the fits are summarized in Table 3.1; the $C^{18}O$ observations are taken from San José-García et al. (2013), while the modeling details and results for all our objects will be presented in I. San José-García (in prep.).

The parameters from Table 3.1 are used as input for the RATRAN models of ^{12}CO. The integrated ^{12}CO line emission obtained from RATRAN is convolved with the telescope beam and compared with observed line fluxes.

Figure 3.1 compares the envelope model for NGC7538 IRS1 with the ^{12}CO J_{up} = 14 to 22 observations from Herschel/PACS, CO 3-2 (in 14" beam, San José-García et al. 2013), and CO 7-6 (in 8" beam, Boonman et al. 2003) from the James Clerk Maxwell Telescope. By design, the model fits the line profile of $C^{18}O$ 9-8 (San José-García et al. 2013, from Herschel/HIFI) shown in the bottom of Figure 3.1. The pure envelope model slightly underproduces the ^{13}CO 10-9 line, because it does not include any broad entrained outflow component ($T_{ex} \sim 70$ K, Yıldız et al. 2013). Adding such an outflow to the model (see Mottram et al. 2013) provides an excellent fit to the total line profile. For the case of ^{12}CO, the pure envelope model reproduces the 3-2 and 7-6 lines within a factor of two, with the discrepancy again caused by the missing outflow in the model. This envelope

Table 3.2 – Far-IR CO emission: observations and envelope models

Object	L_{CO}(obs)	L_{CO}(env)	
	$(L_\odot)$	$(L_\odot)$	(%)
High-mass YSOs[a]			
G327-0.6	1.9	1.6	84
W51N-e1	25.8	14.6	56
DR21(OH)	1.2	0.7	58
NGC6334-I	3.4	2.4	71
G5.89-0.39	3.9	1.8	46
NGC7538-I1	2.1	1.6	77
Low-mass YSOs[b]			
NGC1333 I2A	$4.1\ 10^{-3}$	$0.3\ 10^{-3}$	7
HH46	$6.9\ 10^{-3}$	$0.5\ 10^{-3}$	7
DK Cha	$5.1\ 10^{-3}$	$0.1\ 10^{-3}$	2

Notes. [a] Observed CO luminosities are calculated using detected transitions only, from J =14-13 to 30-29, depending on the source (see Table 3.C.1). The corresponding envelope CO luminosities are calculated using the same transitions. [b] Results from Visser et al. (2012). The observed CO emission is taken to be the total CO emission from all modeled physical components.

model reproduces the CO-integrated intensities for transitions up to J_{up} = 18, but the larger J CO fluxes are underestimated by a large factor.

Comparison of the observed and modeled integrated ^{12}CO line emission for the remaining sources from Table 3.1 is shown in Figure 3.2. As found for the case of NGC7538 IRS1, the contribution of the quiescent envelope emission can be as high as 70-100% of that of the J=15-14 line but decreases sharply for the higher-J transitions. Only 3% to 22% of CO J=22-21 line emission is reproduced by the envelope models. In total ∼ 50% to 100% of observed total FIR CO luminosity can be explained by the envelope emission (see Table 3.2).

This contribution is much greater than for low-mass YSOs, where the quiescent envelope is responsible for only up to 7% of the total CO emission (Visser et al. 2012). Still, even for the high-mass sources, an additional physical component is needed to explain the excitation of the highest-J CO lines. The broad line profiles of high-J (J 10) CO lines (San José-García et al. 2013) argue in favor of a shock contribution to the far-IR emission in ^{12}CO. There may also be a contribution from UV-heating of the outflow cavities by the photons from the protostellar accretion shocks or produced by high velocity shocks inside the cavities as found for low-mass YSOs (Visser et al. 2012), but this component is distinguished best by high-J ^{13}CO lines (van Kempen et al. 2009a). Physical models similar to those developed for low-mass sources by Visser et al. (2012), which include the different physical components, are needed to compare the relative contribution of the envelope emission, shocks, and UV-heating in the high-mass sources, but this goes beyond the scope of this paper.
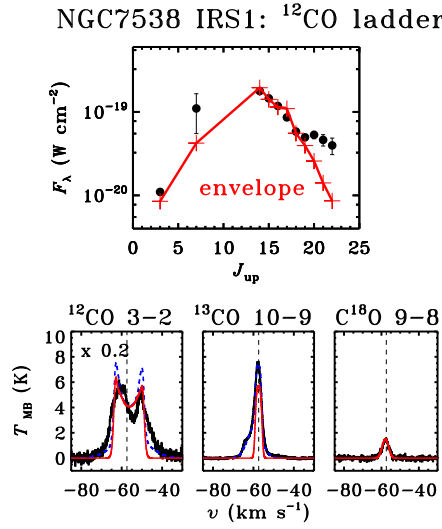
Figure 3.1 – *Top:* Comparison of integrated line fluxes of ^{12}CO observed by Herschel/PACS and from the ground (black dots with errorbars) and the predictions of the quiescent envelope passively heated by the luminosity of the source (red crosses) for NGC7538-IRS1. *Bottom:* The same model compared with the JCMT ^{12}CO 3-2 and Herschel/HIFI ^{13}CO 10-9 and C^{18}O 9-8 observed line profiles. An additional model including an outflow component is shown in blue dashed line.

3.5.2 Molecular excitation

The basic excitation analysis using Boltzmann diagrams in Section 4.2 shows remarkably similar rotational temperatures of each molecule for all our high-mass sources, irrespective of their luminosity or evolutionary stage. The average values of those temperatures are 300 K for CO, 220 K for H$_2$O, and 80 K for OH.

Figure 3.3 presents our results in the context of low- and intermediate-mass YSOs studies by Fich et al. (2010), Herczeg et al. (2012), Goicoechea et al. (2012), Manoj et al. (2013), Wampfler et al. (2013), Karska et al. (2013), Green et al. (2013), and Lee et al. (2013). Rotational temperatures from the Water In Star forming regions with Herschel (WISH), the Dust, Ice, and Gas In Time (DIGIT), and the Herschel Orion Protostar Survey (HOPS) programs are shown separately. OH rotational temperatures of NGC1333 I4B, Serpens SMM1, and L1448 are taken from the literature, whereas temperatures for the two additional low-mass YSOs and four intermediate-mass YSOs are calculated in Appendix B based on the line fluxes from Wampfler et al. (2013).

Rotational temperatures of CO are remarkably similar for most sources in the luminosity range from 10^{-1} to 10^6 L$_\odot$ and equal to $\sim 300 - 350$ K. For the high-mass sources, this refers to the shocked component, not the quiescent envelope component discussed in §5.1. To explain such temperatures in low-mass YSOs, two limiting solutions for the physical conditions of the gas have been proposed: (i) CO is subthermally excited in hot
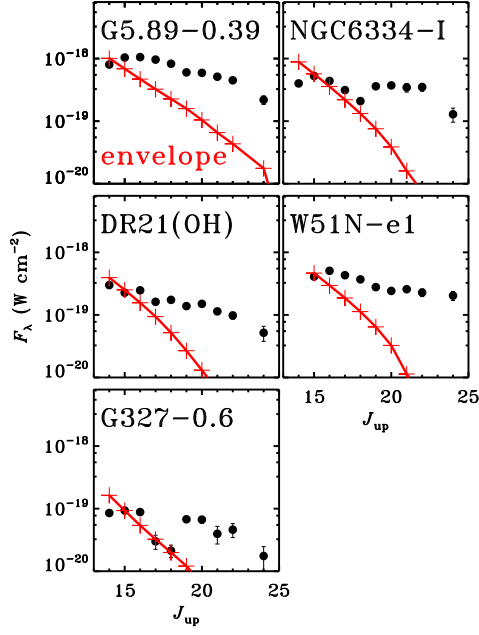
Figure 3.2 – Comparison of integrated line fluxes of CO observed by PACS only (black dots with error bars) and the predictions of the quiescent envelope passively heated by the luminosity of the source (red crosses).

(T_{kin} 10^3 K), low-density ($n(H_2)$ 10^5 cm^{-3}) gas (Neufeld 2012, Manoj et al. 2013); or (ii) CO is close to LTE in warm ($T_{kin} \sim T_{rot}$) and dense ($n(H_2)> n_{crit} \sim 10^6$ cm^{-3}) gas (Karska et al. 2013). The low-density scenario (i) in the case of even more massive protostars studied in this work is probably unlikely. Even though no ^{13}CO lines are detected in our PACS spectra, three of our high-mass protostars were observed in the fundamental $v = 1 - 0$ vibration-rotation bands of CO and ^{13}CO (Mitchell et al. 1990). The Boltzmann distribution of high-J populations of ^{13}CO, indicated by a single component on rotational diagrams, implies densities above 10^6 cm^{-3} for W33A and NGC7538-I1 and $> 10^7$ cm^{-3} for W3 IRS5.

Rotational temperatures of H$_2$O increase for the more massive and more luminous YSOs from about 120 K to 220 K (Figure 3.3). The similarity between the temperatures obtained from the absorption and emission lines argues that they arise in the same physical component in high-mass YSOs (see also Cernicharo et al. 2006). Owing to the high critical density, the water lines are most likely subthermally excited in both low- and high-mass YSOs (see discussion in Section 4.2.2), but in the denser environment of high-mass protostars, the gas is closer to LTE and therefore the rotational temperatures are higher. High optical depths of H$_2$O lines drive the rotational temperatures to higher values, both

111
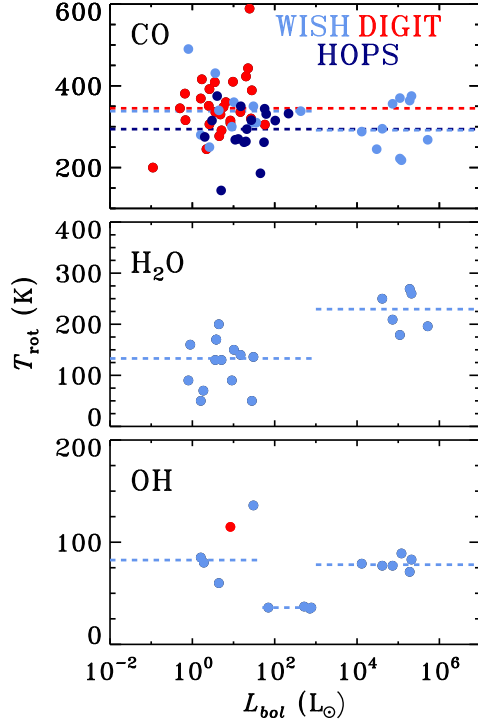
Figure 3.3 – Rotational temperatures of CO, H_2O, and OH for low- to high-mass star forming regions. WISH, DIGIT, and HOPS team's results with PACS are shown in blue, red, and navy blue, respectively. Dotted lines show the median values of the rotational temperature from each database; for the case of WISH, the median is calculated separately for objects with $L_{bol} < 10^3 \, L_{\odot}$ and $L_{bol} > 10^3 \, L_{\odot}$, except for OH where intermediate-mass YSOs covering $10^3 > L_{bol} > 50 \, L_{\odot}$ are also shown separately. The CO and H_2O excitation of intermediate-mass sources has not yet been surveyed with Herschel.

for the low- and high-mass YSOs. Lines are in emission, when the angular size of the emitting region ($\Delta\Omega_L$) multiplied by the blackbody at excitation temperature is larger than the continuum flux at the same wavelength,

$$\Delta\Omega_L \times B_\nu(T_{ex}) > F_{cont,\nu} \qquad (3.4)$$

and are in absorption in the opposite case.

Rotational temperatures of OH show a broad range of values for low-mass YSOs (from about 50 to 150 K), whereas they are remarkably constant for intermediate-mass YSOs (~ 35 K; see Appendix D) and high-mass YSOs (~ 80 K). The low temperatures found towards the intermediate-mass YSOs may be a result of the different lines detected towards those sources rather than a different excitation mechanism.

3.5.3 Correlations

Figure 3.4 shows relations between selected line luminosities of CO, H_2O, and [O I] transitions and the physical parameters of the young stellar objects. Our sample of objects is extended to the low-mass deeply embedded objects studied with PACS in Herczeg et al. (2012), Goicoechea et al. (2012), Wampfler et al. (2013), and Karska et al. (2013) and intermediate-mass objects from Fich et al. (2010) and Wampfler et al. (2013). This allows us to study a broad range of luminosities from ~ 1 to 10^6 $L_\odot$, and envelope masses, from 0.1 to 10^4 $M_\odot$.

The typical distance to low-mass sources is 200 pc and 3 kpc to high-mass sources. For this comparison, the full PACS array maps of low-mass regions are taken ($\sim 50''$), which corresponds to spatial scales of 10^4 AU, hence only a factor of 3 smaller than the central spaxel ($\sim 10''$) observation of high-mass objects. On the other hand, the physical sizes of the low-mass sources are smaller than those of high-mass sources by a factor that is comparable to the difference in average distance of low- and high-mass sources, so one could argue that one should compare just the central spaxels for both cases. Using only the central spaxel for the low-mass YSOs does not affect the results, however (see Figure 9 in Karska et al. 2013).

The choice of CO, H_2O, OH, and [O I] transitions is based on the number of detections of those lines in both samples and their emission profiles. The strengths of the correlations are quantified using the Pearson coefficient, r. For the number of sources studied here, the 3σ correlation corresponds to $r \approx 0.6$ and 5σ correlation to $r \approx 0.95$.

Figure 3.4 shows strong, 5σ correlations between the selected line luminosities and bolometric luminosities, as well as envelope masses. The more luminous the source, the higher is its luminosity in CO, H_2O, and [O I] lines. Similarly, the more massive is the envelope surrounding the growing protostar, the larger is the observed line luminosity in those species. The strength of the correlations over such broad luminosity ranges and envelope masses suggests that the physical processes responsible for the line emission are similar.

In the case of low-mass young stellar objects, Karska et al. (2013) link the CO and H_2O emission seen with PACS with the non-dissociative shocks along the outflow walls, most likely irradiated by the UV photons. The [O I] emission, on the other hand, was mainly attributed to the dissociative shocks at the point of direct impact of the wind on the dense envelope. In the high-mass sources, the envelope densities and the strength of radiation are higher, but all in all the origin of the emission can be similar.

3.5.4 Far-IR line cooling

Figure 3.5 compares the total far-IR cooling in lines, its molecular and atomic contributions, and the cooling by dust for the YSOs in the luminosity range from ~ 1 to 10^6 $L_\odot$. The far-IR line cooling, L_{FIRL}, correlates strongly (5σ) with the bolometric luminosity, L_{bol}, in agreement with studies on low-mass YSOs (Nisini et al. 2002b, Karska et al. 2013). Under the assumption that L_{FIRL} is proportional to the shock energy, the strong correlation between L_{bol} and L_{FIRL} has been interpreted by Nisini et al. (2002b) as a result

113
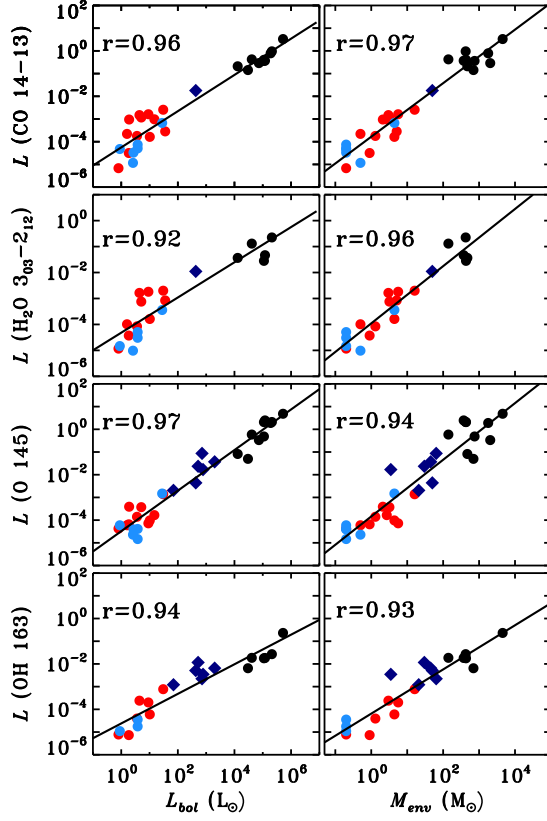
Figure 3.4 – Correlations of line emission with bolometric luminosity (left column) and envelope mass (right column) from top to bottom: CO 14-13, H_2O 3_{03}-2_{12}, [O I] at 145 μm and OH 163 μm line luminosities. Low- and intermediate-mass young stellar objects emission is measured over 5×5 PACS maps. Red and blue circles show Class 0 and Class I low-mass YSOs from Karska et al. (2013). Blue diamonds show intermediate-mass YSOs from Wampfler et al. (2013; O and OH lines) and from Fich et al. (2010; CO and H_2O line). High-mass YSOs fluxes are measured in the central position and shown in black. Pearson coefficient r is given for each correlation.
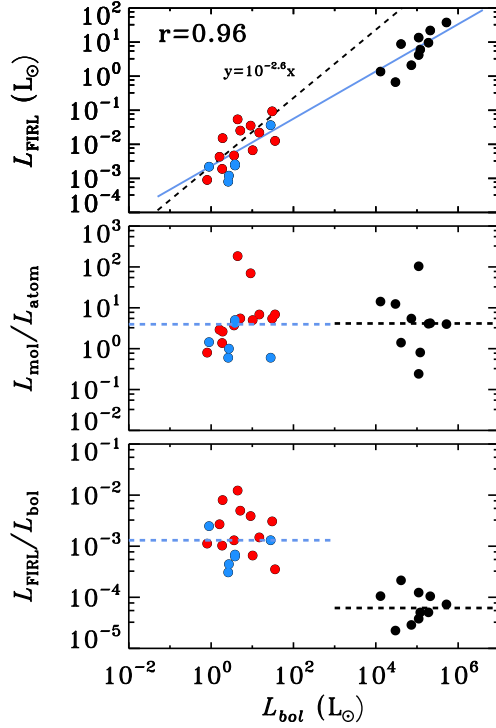
Figure 3.5 – From top to bottom: (1) Total far-IR line cooling; (2) Ratio of molecular to atomic cooling; (3) Gas-to-dust cooling ratio, L_{FIRL}/L_{bol}, where $L_{FIRL} = L_{mol} + L_{atom}$; as a function of bolometric luminosity. Low-mass YSOs are shown in red (Class 0) and blue (Class I), whereas high-mass ones are in black.

of the jet power/ velocity being correlated with the escape velocity from the protostellar surface or an initial increase in the accretion and ejection rate.

The ratio of molecular and atomic line cooling, L_{mol}/L_{atom}, is similar for YSOs of different luminosities, although a large scatter is present. Cooling in molecules is about four times higher than cooling in oxygen atoms. If cooling by [C II] was included in the atomic cooling, the L_{mol}/L_{atom} ratio would decrease for the high-mass sources. In low-mass YSOs, the [C II] emission accounts for less than 1% of the total cooling in lines (Goicoechea et al. 2012, for Ser SMM1). In the high-mass sources, this contribution is expected to be higher due to the carbon ionizing and CO dissociating FUV radiation. In Section 4.1 we estimate the [C II] cooling in two high-mass sources to 10-25% of L_{FIRL}.

The ratio of cooling by gas (molecular and atomic lines) and dust (L_{bol}) decreases from $1.3 \cdot 10^{-3}$ to $6.2 \cdot 10^{-5}$ from low to high-mass YSOs. It reflects that H_2O and, to a smaller extent, OH contribute less to the line luminosity in the high-mass sources, because many of its lines are detected in absorption. The detection of H_2O and OH lines in absorption

115

proves that IR pumping is at least partly responsible for the excitation of these molecules and the resulting emission lines (e.g. Goicoechea et al. 2006, Wampfler et al. 2013). When collisions play a marginal role, even the detected emission lines of those species do not necessarily cool the gas.

The above numbers do not include cooling from molecules outside the PACS wavelength range. This contribution can be significant for CO, where for low-mass sources the low-J lines are found to increase the total CO line luminosity by about 30% (Karska et al. 2013). Thus, the CO contribution to the total gas cooling is likely to be even larger than suggested by Table 3.1.

3.6 Conclusions

We have characterized the central position *Herschel*/PACS spectra of ten high-mass protostars and compared them with the results for low- and intermediate-mass protostars analyzed in a similar manner. The conclusions are as follows:

1. Far-IR gas cooling of high-mass YSOs is dominated by CO (from $\sim$ 15 to 85% of total far-IR line cooling, with a median contribution of 74%) and to a smaller extent by [O I] (with median value $\sim$20 %). H_2O and OH median contributions to the far-IR cooling are less than 1%. In contrast, for low-mass YSOs, the H_2O, CO, and [O I] contributions are comparable. The effective cooling by H_2O is reduced because many far-IR lines are in absorption. The [O I] cooling increases for more evolved sources in both mass regimes.

2. Rotational diagrams of CO in the PACS range show a single, *warm component*, corresponding to rotational temperature of $\sim$300 K, consistent with low-mass YSOs. Upper limits on high$-J$ CO do not exclude there being an additional, *hot component* in several sources of our sample.

3. Emission from the quiescent envelope accounts for $\sim$45-85 % of the total CO luminosity observed in the PACS range. The corresponding values for the cooler and less dense envelopes of low-mass YSOs are below 10%. Additional physical components, most likely shocks, are needed to explain the highest$-J$ CO lines.

4. Rotational diagrams of H_2O are characterized by $T_{rot} \sim 250$ K for all sources from both emission and absorption data. This temperature is about 100 K higher than for low-mass sources, probably due to the higher densities in high-mass sources. The diagrams show scatter due to subthermal excitation and optical depth effects.

5. OH rotational diagrams are described by a single rotational temperatures of $\sim$80 K, consistent with most low-mass YSOs, but higher by $\sim$45 K than for intermediate-mass objects. Similar to H_2O, lines are subthermally excited.

6. Fluxes of the H_2O $3_{03}-2_{12}$ line and the CO 14$-$13 line strongly correlate with bolometric luminosities and envelope masses over six and seven orders of magnitude,

respectively. This correlation suggests a common physical mechanism responsible for the line excitation, most likely the non-dissociative shocks based on the studies of low-mass protostars.

7. Across the wide luminosity range from $\sim$ 1 to 10^6 $L_\odot$, the far-IR line cooling strongly correlates with the bolometric luminosity, in agreement with studies of low-mass YSOs. The ratio of molecular and atomic line cooling is ~4, similar for all those YSOs.

8. Because several H_2O lines are in absorption, the gas-to-dust cooling ratio decreases from $1.3\cdot10^{-3}$ to $6.2\cdot10^{-5}$ from low to high-mass YSOs.

Acknowledgements

Appendix

3.A   Details of PACS observations

Table 4.A.2 shows the observing log of PACS observations used in this paper. The observations identifications (OBSID), observation day (OD), date of observation, total integration time, primary wavelength ranges, and pointed coordinates (RA, DEC) are listed. All spectra were obtained in pointed / chop-nod observing mode. Additional remarks are given for several sources. G327-0.6 and W33A observations were mispointed. NGC6334-I, W3IRS5, and NGC7538-IRS1 spectra were partly saturated and re-observed (re-obs). Two observations each of W51N-e1, G34.26, G5.89, and AFGL2591 were done using different pointing.

Table 3.A.1 – Log of PACS observations

Source	OBSID	OD	Date	Total time (s)	Wavelength ranges (μm)	RA ($^{\mathrm{h\ m\ s}}$)	DEC ($^{\mathrm{o\ '\ ''}}$)	Remarks
G327-0.6	1342216201	659	2011-03-04	6290	102-120	15 53 08.8	-54 37 01.0	mispointed
	1342216202	659	2011-03-04	4403	55-73	15 53 08.8	-54 37 01.0	mispointed
W51N-e1	1342193697	327	2010-04-06	4589	55-73	19 23 43.7	+14 30 28.8	diff. point.
	1342193698	327	2010-04-06	4969	102-120	19 23 43.7	+14 30 25.3	diff. point.
DR21(OH)	1342209400	551	2010-11-15	4401	55-73	20 39 00.8	+42 22 48.0	
	1342209401	551	2010-11-16	6280	102-120	20 39 00.8	+42 22 48.0	
W33A	1342239713	1018	2012-02-25	4403	55-73	18 14 39.1	-17 52 07.0	mispointed
	1342239714	1018	2012-02-25	3763	102-120	18 14 39.1	-17 52 07.0	mispointed
	1342239715	1018	2012-02-25	2548	174-210	18 14 39.1	-17 52 07.0	mispointed
G34.26+0.15	1342209733	542	2010-11-07	4589	55-73	18 53 18.8	+01 14 58.1	diff. point.
	1342209734	542	2010-11-07	4969	102-120	18 53 18.7	+01 15 01.5	diff. point.
NGC6334-I	1342239385	1013	2012-02-21	4403	55-73	17 20 53.3	-35 47 00.0	saturated
	1342239386	1013	2012-02-21	3763	102-120	17 20 53.3	-35 47 00.0	saturated
	1342239387	1013	2012-02-21	2548	174-210	17 20 53.3	-35 47 00.0	saturated
	1342252275	1240	2012-10-05	3771	102-120	17 20 53.3	-35 46 57.2	re-obs
NGC7538-I1	1342211544	589	2010-12-24	6290	102-120	23 13 45.3	+61 28 10.0	saturated
	1342211545	589	2010-12-24	4403	55-73	23 13 45.3	+61 28 10.0	saturated
	1342258102	1329	2013-01-02	3771	102-120	23 13 45.2	+61 28 10.4	re-obs
AFGL2591	1342208914	549	2010-11-14	6280	102-120	20 29 24.7	+40 11 19.0	diff. point.
	1342208938	550	2010-11-15	4403	55-73	20 29 24.9	+40 11 21.0	diff. point.
W3-IRS5	1342191146	286	2010-02-24	6345	102-120	2 25 40.6	+62 05 51.0	saturated
	1342191147	286	2010-02-24	4102	55-73	2 25 40.6	+62 05 51.0	saturated
	1342229091	860	2011-09-21	4403	55-73	2 25 40.6	+62 05 51.0	saturated
	1342229092	860	2011-09-21	4499	102-120	2 25 40.6	+62 05 51.0	re-obs
	1342229093	860	2011-09-21	2249	55-73	2 25 40.6	+62 05 51.0	re-obs
G5.89-0.39	1342217940	691	2011-04-05	4969	102-120	18 00 30.5	-24 04 00.4	diff. point.
	1342217941	691	2011-04-05	4589	55-73	18 00 30.5	-24 04 04.4	diff. point.

3.B   Continuum measurements

Table 3.B.1 shows the continuum fluxes for all our sources measured using the full PACS array. The fluxes were used in the spectral energy distributions presented by van der Tak et al. (2013).

121

Table 3.B.1 – Full-array continuum measurements in 10^3 Jy

λ (μm)	Continuum (10^3 Jy)									
	G327-0.6[a]	W51N-e1	DR21(OH)	W33A	G34.26	NGC6334I	NGC7538I1	AFGL2591	W3IRS5	G5.89
56.8	2.2	11.0	1.7	1.9	7.9	16.1	8.6	5.5	23.0	17.7
59.6	2.6	12.3	2.0	2.1	8.2	17.2	8.9	5.7	23.8	18.8
62.7	3.0	13.3	2.5	2.2	9.2	18.2	9.3	5.8	24.0	19.7
63.2	3.0	13.6	2.6	2.3	9.4	18.3	9.3	5.8	24.2	19.9
66.1	3.5	14.3	3.0	2.5	10.6	19.3	9.6	6.0	24.8	20.2
69.3	3.8	15.2	3.4	2.5	10.9	19.8	9.6	6.0	24.4	20.7
72.8	4.6	17.8	4.1	3.0	13.2	20.5	9.7	5.9	24.8	15.7
76.0	4.9	18.6	4.5	2.9	14.0	20.9	9.6	5.6	24.4	15.8
79.2	5.3	18.9	4.8	3.0	14.4	20.9	9.5	5.6	23.3	15.7
81.8	5.6	19.2	5.1	3.2	14.8	21.1	9.6	5.7	23.1	15.7
86.0	6.1	19.8	5.5	3.2	15.6	21.6	9.6	5.5	22.2	15.7
90.0	>3.2	20.1	5.9	3.4	16.0	21.8	9.9	5.5	21.8	15.3
93.3	>3.3	19.7	6.4	3.3	15.9	21.7	9.6	5.5	20.9	14.7
108.8	8.2	18.8	7.8	3.9	16.1	23.7	10.0	5.3	19.4	13.1
113.5	8.1	18.5	7.8	3.9	15.9	23.0	9.8	5.2	18.2	12.5
118.0	>7.1	18.1	7.9	3.8	15.6	22.2	9.5	5.0	17.3	11.9
125.4	>7.2	17.5	7.9	3.7	15.2	21.2	9.0	4.7	15.8	11.0
130.4	>7.2	16.7	7.8	3.6	14.6	20.2	8.5	4.4	14.6	10.2
136.0	8.1	16.1	7.7	3.5	14.1	19.2	8.1	4.2	13.4	9.6
145.5	8.0	14.7	7.6	3.3	13.0	17.4	7.3	3.8	11.7	8.4
158.5	7.7	12.6	6.9	3.0	11.1	15.1	6.3	3.3	9.5	6.8
164.0	7.5	11.7	6.6	2.9	10.3	14.1	5.8	3.0	8.6	6.1
169.1	7.2	11.0	6.0	2.7	9.7	13.6	5.4	2.8	7.9	5.7
175.8	6.9	10.0	5.9	2.7	8.9	12.3	5.0	2.6	7.0	5.0
179.5	6.6	9.5	5.6	2.4	8.5	11.6	4.7	2.4	6.5	4.7
186.0	5.6	8.7	4.8	2.4	7.8	10.2	4.0	2.0	5.5	4.2

Notes. The calibration uncertainty of 20% of the flux should be included for comparisons with other modes of observations or instruments. [a] One spaxel at N-W corner of the PACS map is saturated around 100 μm region due to the strong continuum; therefore the tabulated values are the lower limits to the total continuum flux from the whole map.

3.C   Tables with fluxes and additional figures

Table 3.C.1 shows line fluxes and 3 σ upper limits of CO lines toward all our objects in units of 10^{-20} W cm^{-2}. For details, see the table caption.

Figure 3.C.1 shows blow-ups of selected spectral regions of W3 IRS5 with high-J CO, H$_2$O, and OH lines. Figures 3.C.2 and 3.C.3 show blow-ups of selected CO and OH transitions towards all sources.

123

Table 3.C.1 – CO line fluxes in 10^{-20} W cm^{-2}

Trans.	λ_{lab} (μm)	Central position flux (10^{-20} W cm^{-2})									
		G327-0.6[a]	W51N-e1	DR21(OH)	W33A[a]	G34.26+0.15	NGC6334-I	NGC7538-I1	AFGL2591	W3IRS5	G5.89-0.39
CO 14-13	185.9990	8.52(0.48)	40.93(1.26)	29.93(0.67)	7.96(0.23)	23.05(1.14)	40.07(1.60)	17.79(0.52)	10.86(0.45)	76.67(1.38)	80.36(0.74)
CO 15-14	173.6310	9.34(0.36)	50.65(1.83)	22.65(1.07)	4.91(0.32)	26.30(1.07)	52.70(2.39)	14.54(0.33)	7.72(0.57)	86.13(1.76)	103.91(1.41)
CO 16-15	162.8120	8.82(0.51)	43.10(1.43)	24.71(0.92)	4.12(0.18)	22.71(1.06)	43.88(1.59)	11.78(0.39)	8.00(0.27)	99.73(1.08)	105.49(1.76)
CO 17-16	153.2670	3.00(0.76)	36.94(1.54)	16.19(1.21)	2.74(0.24)	18.52(1.63)	31.37(2.46)	8.60(0.56)	5.67(0.38)	86.40(1.31)	96.31(1.67)
CO 18-17	144.7840	2.13(0.48)	27.78(1.89)	17.40(1.13)	4.35(0.39)	18.27(1.53)	20.93(2.02)	5.82(0.47)	5.02(0.53)	83.05(1.69)	82.73(1.67)
CO 19-18	137.1960	6.76(0.64)	24.18(1.81)	13.82(1.07)	3.41(0.37)	20.16(1.68)	36.07(2.02)	4.96(0.42)	3.02(0.58)	79.39(1.54)	60.19(2.14)
CO 20-19	130.3690	6.68(0.81)	25.73(1.42)	15.02(0.93)	3.54(0.52)	21.93(1.93)	37.25(2.19)	5.31(0.54)	4.34(0.64)	77.08(2.27)	59.14(1.27)
CO 21-20	124.1930	3.96(1.24)	22.77(3.15)	11.38(0.87)	<0.75	18.69(2.02)	34.56(5.43)	4.62(0.72)	2.97(0.61)	60.64(2.13)	51.31(2.90)
CO 22-21	118.5810	4.61(1.16)	20.31(3.29)	9.79(1.23)	<0.77	21.66(3.21)	35.05(5.02)	3.97(0.89)	<0.90	63.44(2.81)	44.98(3.84)
CO 24-23	108.7630	<1.78	< 7.05	5.18(1.40)	<0.54	18.86(5.45)	12.89(3.28)	<1.68	<0.86	49.51(3.75)	21.89(3.45)
CO 27-26	96.7730	<0.86	4.71(0.79)	3.68(0.56)	<1.50	4.34(1.22)	9.46(1.76)	<2.49	<1.01	23.29(2.65)	6.16(0.81)
CO 28-27	93.3490	<1.75	6.28(1.21)	<0.94	<0.91	5.06(1.35)	11.75(1.99)	<4.97	<1.04	24.72(1.75)	9.71(1.63)
CO 29-28	90.1630	<1.24	5.23(1.54)	<1.23	<1.25	3.67(1.30)	10.80(5.36)	<6.35	<1.70	20.23(1.94)	5.38(3.49)
CO 30-29	87.1900	<1.10	3.59(0.72)	<1.00	<1.72	4.48(1.10)	<7.00	<2.10	<1.57	14.38(2.03)	6.32(2.59)
CO 32-31	81.8060	<1.19	<5.84	<1.19	<1.43	<2.31	<4.63	<1.84	<2.03	<9.49	<3.70
CO 33-32	79.3600	<3.99	<11.04	<1.70	<2.28	<3.76	<18.46	<2.09	<1.99	<3.40	<13.59
CO 34-33	77.0590	<1.88	<4.57	<1.83	<1.83	<3.17	<2.71	<1.40	<2.16	<5.27	<6.93
CO 35-34	74.8900	<2.06	<2.90	<0.99	<1.27	<2.03	<3.09	<2.50	<1.20	<1.83	<18.61
CO 36-35	72.8430	<0.55	<0.63	<0.29	<0.70	<1.17	<1.74	<0.69	<0.37	<7.03	<3.00
CO 38-37	69.0740	<1.36	<1.06	<1.93	<0.67	<1.77	<1.21	<3.23	<2.09	<2.16	<2.74
CO 39-38	67.3360	<1.20	<0.84	<0.40	<1.86	<0.80	<2.50	<2.40	<0.89	<1.99	<3.54
CO 40-39	65.6860	<0.57	<2.40	<0.43	<1.05	<2.40	<1.94	<2.17	<0.94	<2.63	<2.91
CO 41-40	64.1170	<1.06	<1.11	<0.57	<1.80	<1.54	<2.91	<1.59	<1.80	<5.56	<4.60
CO 42-41	62.6240	<1.03	<2.74	<0.44	<1.08	<2.50	<2.19	<1.91	<2.34	<4.01	<5.01
CO 43-42	61.2010	<0.90	<1.39	<0.58	<1.05	<1.20	<4.59	<2.10	<2.41	<4.94	<6.21
CO 44-43	59.8430	<0.67	<1.61	<0.39	<0.68	<1.41	<3.38	<2.30	<1.54	<2.85	<3.49
CO 45-44	58.5470	<0.96	<1.24	<0.55	<1.41	<1.42	<1.34	<1.69	<1.08	<6.77	<4.89
CO 46-45	57.3080	<2.33	<10.54	<1.03	<1.81	<4.01	<6.49	<3.75	<2.65	<6.46	<8.54
CO 47-46	56.1220	<0.76	<1.08	<0.50	<2.29	< 1.85	<2.51	<1.39	<1.71	<5.78	<4.79

Notes. The uncertainties are 1σ measured in the continuum on both sides of each line; calibration uncertainty of 20% of the flux should be included for comparisons with other modes of observations or instruments. 3σ upper limits calculated using wavelength-dependent values of full-width high maximum for a point source observed with PACS are listed for non-detections. CO 23-22 and CO 31-30 fluxes are not listed due to severe blending with the H$_2$O 4_{14}-3_{03} line at 113.537 μm and the OH $\frac{7}{2},\frac{3}{2}$-$\frac{5}{2},\frac{3}{2}$ line at 84.4 μm, which are often in absorption. CO 25-24, CO 26-25 and CO 37-36 transitions are located in the regions of overlapping orders, where the flux calibration is unreliable. [a] A mispointed observation. The fluxes are calculated from a sum of two spaxel closest to the true source position, see Section 2.

3.D   OH in low and intermediate mass sources

Figures 3.D.1 and 3.D.2 show rotational diagrams of OH for low- and intermediate-mass young stellar objects based on the fluxes presented in Wampfler et al. (2013). Only the sources with at least three detected doublets in emission (out of 4 targeted in total) are shown in diagrams. Rotational temperatures and total numbers of emitting molecules are summarized in Table 3.D.1. For low-mass YSOs, a single component fit is usually not a good approximation (with the exception of L1527 and IRAS15398). In the intermediate-mass YSOs, on the other hand, such an approximation holds and results in very similar rotational temperatures of OH $T_{rot} \sim 35$ K for all sources except NGC7129 FIRS2.

Table 3.D.1 – OH rotational excitation and number of emitting molecules $\mathcal{N}_u$ based on emission lines for low- and intermediate-mass sources

Source	T_{rot}(K)	$\log_{10}\mathcal{N}$
Low-mass YSOs		
NGC1333 I4A	270(700)	52.4(0.9)
L1527	**80(40)**	51.5(0.6)
Ced110 I4	380(1400)	51.4(0.9)
IRAS15398	**85(90)**	51.5(1.0)
L483	200(380)	52.0(0.9)
L1489	140(150)	51.6(0.7)
TMR1	490(2150)	52.0(0.8)
TMC1	170(290)	51.7(0.9)
HH46	160(350)	52.6(1.1)
Intermediate-mass YSOs		
NGC2071	37(10)	55.7(0.8)
Vela IRS17	35(10)	55.1(0.7)
Vela IRS19	36(15)	55.1(1.1)
NGC7129 FIRS2	170(270)	53.9(0.9)
L1641 S3MMS1	36(10)	54.7(0.8)

Notes. Rotational diagrams are shown in Figures 3.D.1 and 3.D.2. Objects with at least 3 detected doublets in Wampfler et al. (2013) are presented. Rotational temperatures of OH calculated with error less than 100 K are shown in boldface.
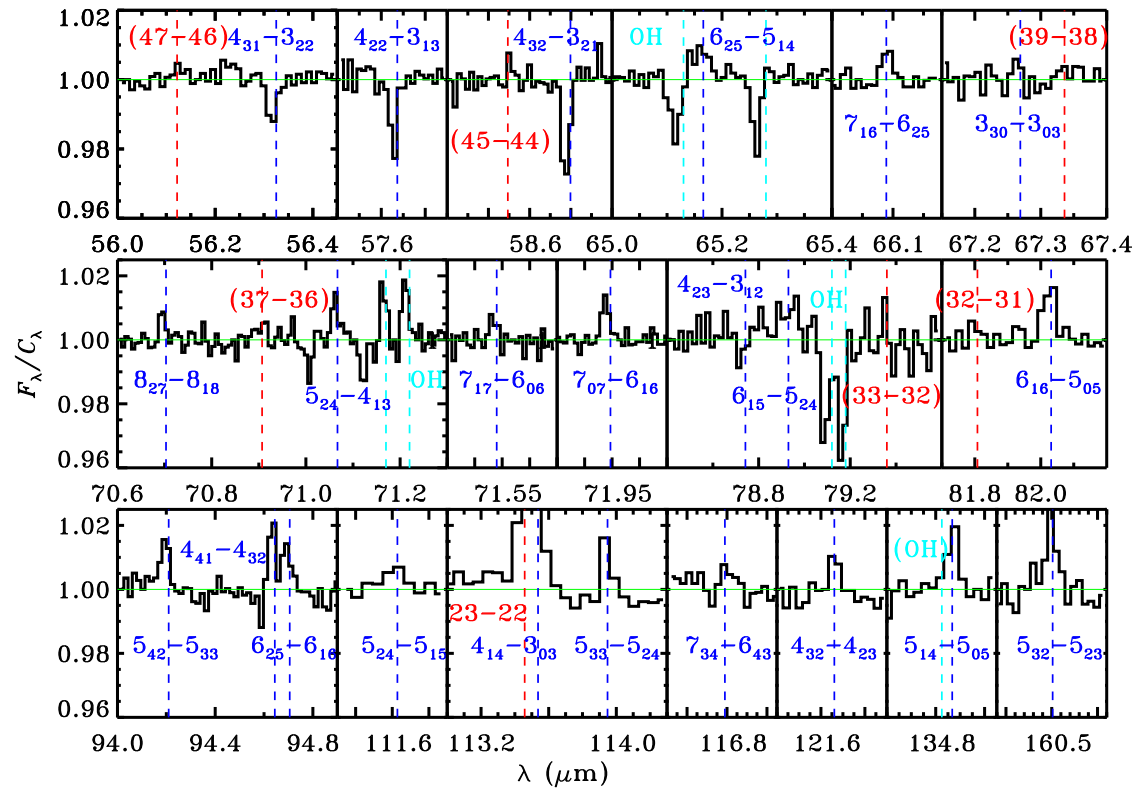
Figure 3.C.1 – Close-ups of several of the H_2O, CO and OH lines in W3IRS5 as shown in Figure 4.2. The rest wavelength of each line is indicated by dashed lines: blue for H_2O, red for CO, and light blue for OH. Identifications of the undetected lines in the presented spectral regions are shown in parenthesis.
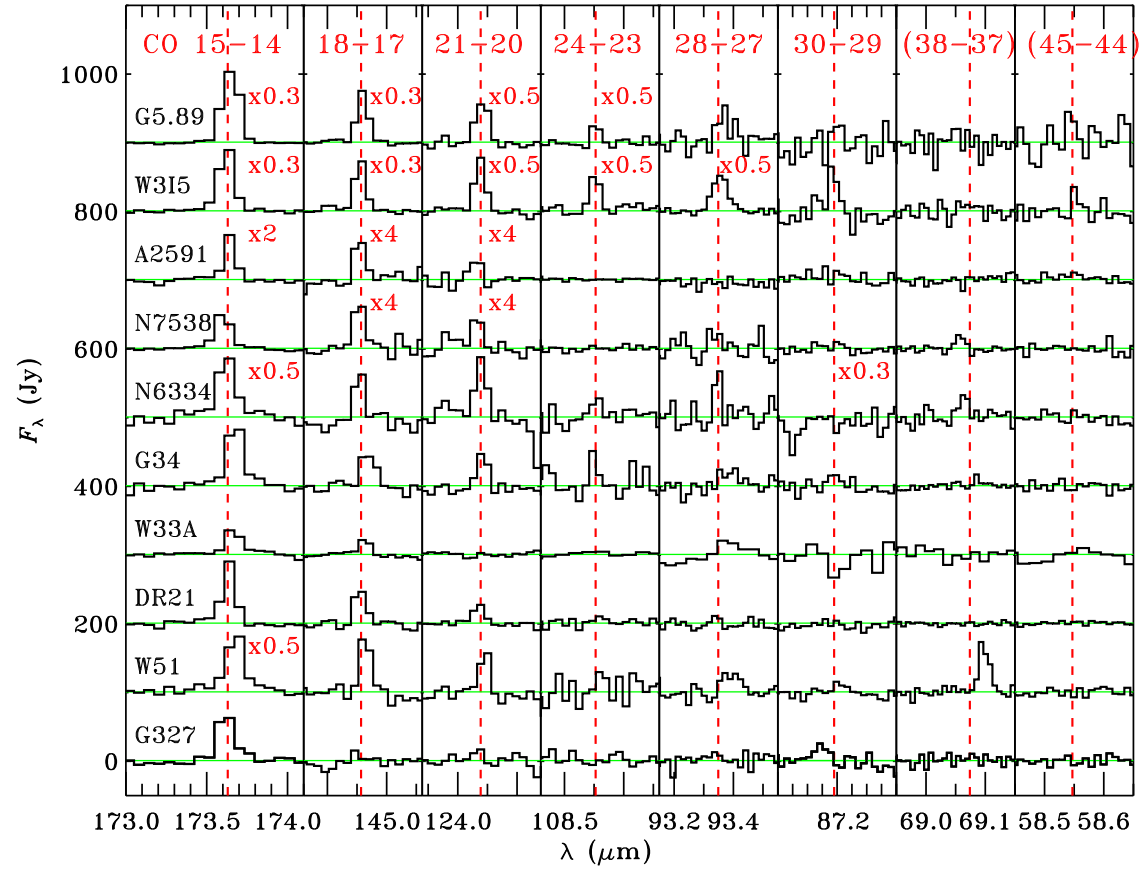
Figure 3.C.2 – Close-ups of several transitions of CO lines in the PACS wavelength range toward all sources. The spectra are continuum-subtracted and shifted vertically for better visualization.
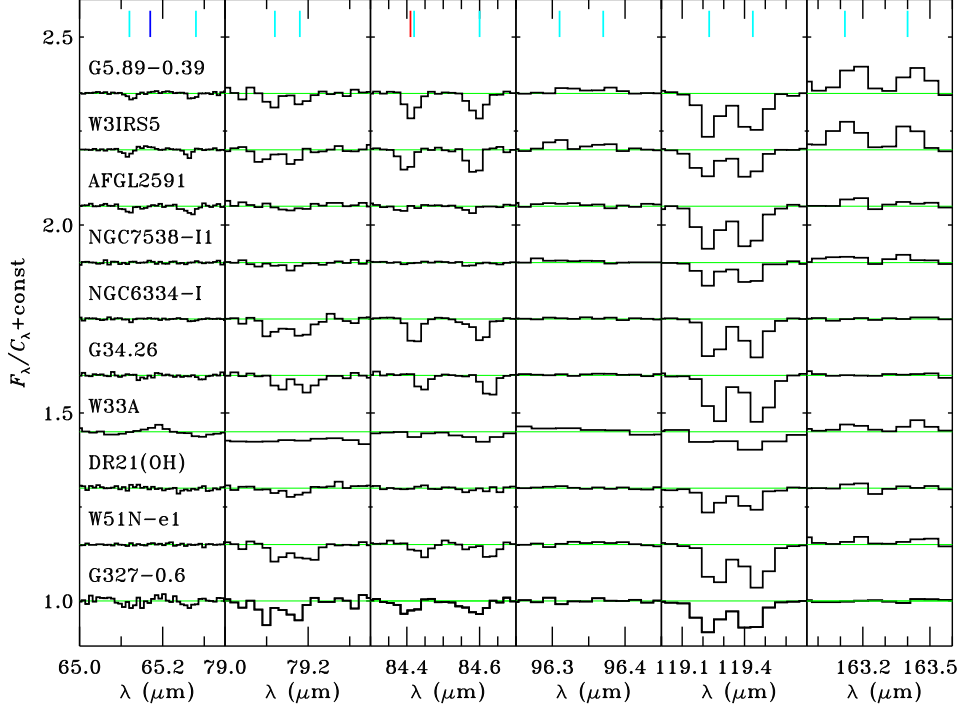
Figure 3.C.3 – Normalized spectra of OH doublets for all our sources at central position. Doublets at 71 and 98 μm are excluded because of poor calibration of those spectral regions observed with PACS. OH doublet at 84.4 μm is a blend with the CO 31-30 line, whereas OH at 65.13 μm can be affected by H_2O 6_{25}-5_{14} at 65.17 μm.
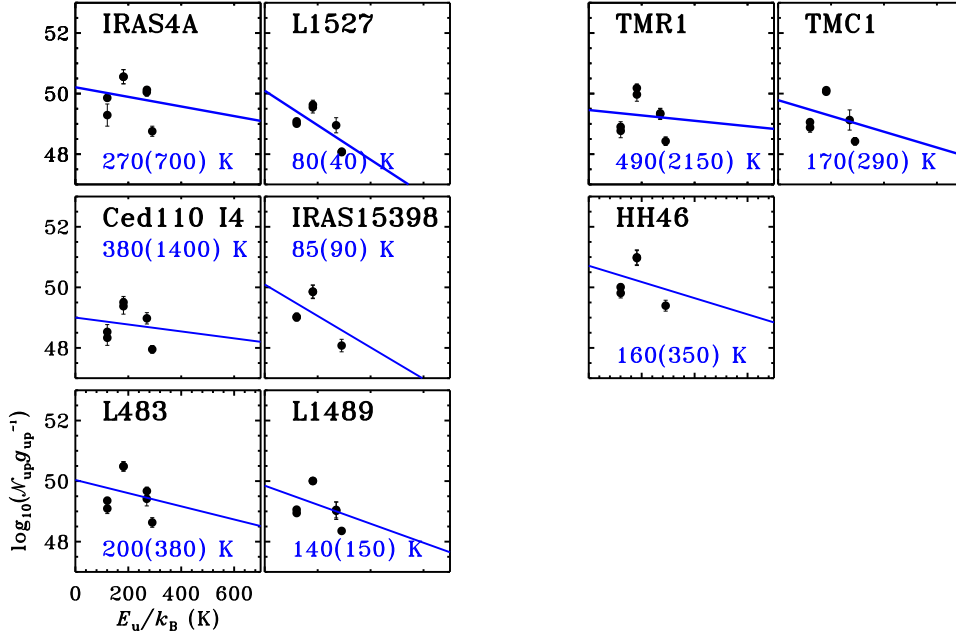
Figure 3.D.1 – OH rotational diagrams (from emission lines) for low-mass young stellar objects (fluxes from Wampfler et al. 2013).
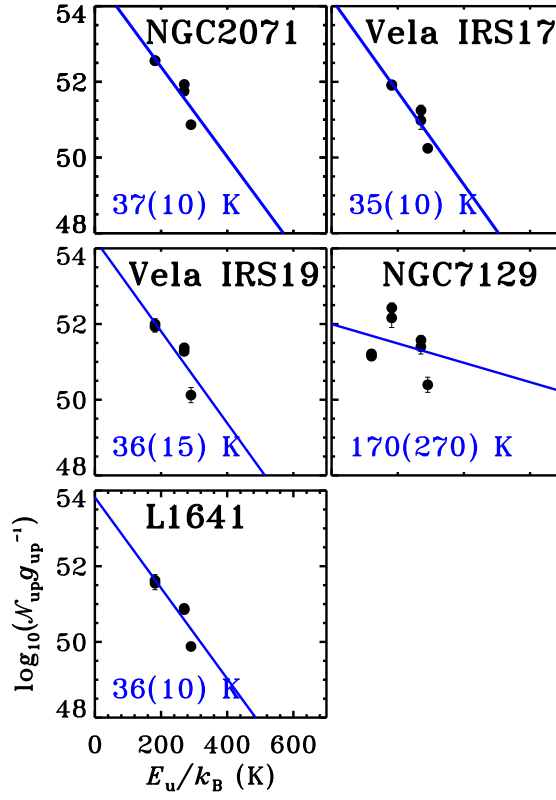
Figure 3.D.2 – OH rotational diagrams (from emission lines) for intermediate-mass young stellar objects (fluxes from Wampfler et al. 2013).

Shockingly low water abundances in *Herschel* / PACS observations of low-mass protostars in Perseus

A. Karska, L. E. Kristensen, E. F. van Dishoeck, M. N. Drozdovskaya, J. C. Mottram,
G. J. Herczeg, S. Bruderer, S. Cabrit, N. J. Evans II, D. Fedele, A. Gusdorf,
J. K. Jørgensen, M. J. Kaufman, G. J. Melnick, D. A. Neufeld, B. Nisini, G. Santangelo,
M. Tafalla, S. F. Wampfler

133

Abstract

Context. Protostars interact with their surroundings through jets and winds impacting on the envelope and creating shocks, but the nature of these shocks is still poorly understood.

Aims. Our aim is to survey far-infrared molecular line emission from a uniform and significant sample of deeply-embedded low-mass young stellar objects (YSOs) in order to characterize shocks and the possible role of ultraviolet radiation in the immediate protostellar environment.

Methods. Herschel/PACS spectral maps of 22 objects in the Perseus molecular cloud were obtained as part of the 'William Herschel Line Legacy' (WILL) survey. Line emission from H_2O, CO, and OH is tested against shock models from the literature.

Results. Observed line ratios are remarkably similar and do not show variations with source physical parameters (luminosity, envelope mass). Most ratios are also comparable to those found at off-source outflow positions. Observations show good agreement with the shock models when line ratios of the same species are compared. Ratios of various H_2O lines provide a particularly good diagnostic of pre-shock gas densities, $n_H \sim 10^5$ cm^{-3}, in agreement with typical densities obtained from observations of the post-shock gas when a compression factor of order 10 is applied (for non-dissociative shocks). The corresponding shock velocities, obtained from comparison with CO line ratios, are above 20 km s^{-1}. However, the observations consistently show one-to-two orders of magnitude lower H_2O-to-CO and H_2O-to-OH line ratios than predicted by the existing shock models.

Conclusions. The overestimated model H_2O fluxes are most likely caused by an overabundance of H_2O in the models since the excitation is well-reproduced. Illumination of the shocked material by ultraviolet photons produced either in the star-disk system or, more locally, in the shock, would decrease the H_2O abundances and reconcile the models with observations. Detections of hot H_2O and strong OH lines support this scenario.

4.1   Introduction

Shocks are ubiquitous phenomena where outflow-envelope interactions take place in young stellar objects (YSO). Large-scale shocks are caused by the bipolar jets and protostellar winds impacting the envelope along the 'cavity walls' carved by the passage of the jet (Arce et al. 2007, Frank et al. 2014). This important interaction needs to be characterized in order to understand and quantify the feedback from protostars onto their surroundings and, ultimately, to explain the origin of the initial mass function, disk fragmentation and the binary fraction.

Theoretically, shocks are divided into two main types based on a combination of magnetic field strength, shock velocity, density, and level of ionization (Draine 1980, Draine et al. 1983, Hollenbach et al. 1989, Hollenbach 1997). In 'continuous' ($C-$type) shocks, in the presence of a magnetic field and low ionization, the weak coupling between the ions and neutrals results in a continuous change in the gas parameters. Peak temperatures of a few 10^3 K allow the molecules to survive the passage of the shock, which is therefore referred to as non-dissociative. In 'jump' ($J-$type) shocks, physical conditions change in a discontinuous way, leading to higher peak temperatures than in C shocks of the same speed and for a given density. Depending on the shock velocity, J shocks are either non-dissociative (velocities below about $\sim 30\,\mathrm{km\,s^{-1}}$, peak temperatures of about a few 10^4 K) or dissociative (peak temperatures even exceeding 10^5 K), but the molecules efficiently reform in the post-shock gas.

Shocks reveal their presence most prominently in the infrared (IR) domain, where the post-shock gas is efficiently cooled by numerous atomic and molecular emission lines. Cooling from H_2 is dominant in outflow shocks (Nisini et al. 2010b, Giannini et al. 2011), but its mid-IR emission is strongly affected by extinction in the dense envelopes of young protostars (Giannini et al. 2001, Nisini et al. 2002b, Davis et al. 2008, Maret et al. 2009). In the far-IR, rotational transitions of water vapor (H_2O) and carbon monoxide (CO) are predicted to play an important role in the cooling process (Goldsmith & Langer 1978, Neufeld & Dalgarno 1989, Hollenbach 1997) and can serve as a diagnostic of the shock type, its velocity, and the pre-shock density of the medium (Hollenbach et al. 1989, Kaufman & Neufeld 1996, Flower & Pineau des Forêts 2010, 2012).

The first observations of the critical wavelength regime to test these models ($\lambda \sim 45 - 200\,\mu$m) were taken using the Long-Wavelength Spectrometer (LWS, Clegg et al. 1996) onboard the *Infrared Space Observatory* (ISO, Kessler et al. 1996). Far-IR atomic and molecular emission lines were detected toward several low-mass deeply-embedded protostars (Nisini et al. 2000, Giannini et al. 2001, van Dishoeck 2004), but its origin was unclear due to the poor spatial resolution of the telescope ($\sim 80''$, Nisini et al. 2002b, Ceccarelli et al. 2002).

The sensitivity and spectral resolution of the Photodetector Array Camera and Spectrometer (PACS, Poglitsch et al. 2010) onboard *Herschel* allowed a significant increase in the number of young protostars with far-IR line detections compared with the early ISO results and has revealed rich molecular and atomic line emission both at the protostellar (e.g. van Kempen et al. 2010b, Goicoechea et al. 2012, Herczeg et al. 2012, Visser et al. 2012, Green et al. 2013, Karska et al. 2013, Lindberg et al. 2013, Manoj et al. 2013,

135

Wampfler et al. 2013) and at pure outflow positions (Santangelo et al. 2012, 2013, Codella et al. 2012b, Lefloch et al. 2012b, Vasta et al. 2012, Nisini et al. 2013).

The unprecedented spatial resolution of PACS allowed detailed imaging of L1157 providing firm evidence that most of far-IR H_2O emission originates in the outflows (Nisini et al. 2010a). A mapping survey of about 20 protostars revealed similarities between the spatial extent of H_2O and high$-J$ CO (Karska et al. 2013). Additional strong flux correlations between those species and similarities in the velocity-resolved profiles (Kristensen et al. 2010, 2012, San José-García et al. 2013, Santangelo et al. 2014) suggest that the emission from the two molecules arises from the same regions. This is further confirmed by finely-spatially sampled PACS maps in CO 16-15 and various H_2O lines in shock positions of L1448 and L1157 (Santangelo et al. 2013, Tafalla et al. 2013). On the other hand, the spatial extent of OH resembles the extent of [O I] and, additionally, a strong flux correlation between the two species is found (Karska et al. 2013, Wampfler et al. 2013). Therefore, at least part of the OH emission most likely originates in a dissociative $J-$shock, together with [O I] (Wampfler et al. 2010, Benedettini et al. 2012, Wampfler et al. 2013).

To date, comparisons of the far-IR observations with shock models have been limited to a single source or its outflow positions (e.g. Nisini et al. 1999, Benedettini et al. 2012, Vasta et al. 2012, Santangelo et al. 2012, Dionatos et al. 2013, Lee et al. 2013, Flower & Pineau des Forêts 2013). Even in these studies, separate analysis of each species (or different pairs of species) often led to different sets of shock properties that needed to be reconciled. For example, Dionatos et al. (2013) show that CO and H_2 line emission in Serpens SMM3 originates from a 20 km s^{-1} J shock at low pre-shock densities ($\sim 10^4$ cm^{-3}), but the H_2O and OH emission is better explained by a 30-40 km s^{-1} C shock. In contrast, Lee et al. (2013) associate emission from both CO and H_2O in L1448-MM with a 40 km s^{-1} C shock at high pre-shock densities ($\sim 10^5$ cm^{-3}), consistent with the analysis of the L1448-R4 outflow position (Santangelo et al. 2013). Analysis restricted to H_2O lines alone often indicates an origin in non-dissociative J shocks (Santangelo et al. 2012, Vasta et al. 2012, Busquet et al. 2014), while separate analysis of CO, OH, and atomic species favors dissociative J shocks (Benedettini et al. 2012, Lefloch et al. 2012a). The question remains how to break degeneracies between these models and how typical the derived shock properties are for young protostars. Also, surveys of high-J CO lines with PACS have revealed two universal temperature components in the CO ladder toward all deeply-embedded low-mass protostars (Herczeg et al. 2012, Goicoechea et al. 2012, Green et al. 2013, Karska et al. 2013, Kristensen et al. 2013, Manoj et al. 2013, Lee et al. 2013). The question is how the different shock properties relate with the 'warm' ($T \sim 300$ K) and 'hot' ($T \gtrsim 700$ K) components seen in the CO rotational diagrams.

In this paper, far-IR spectra of 22 low-mass YSOs observed as part of the 'William Herschel Line Legacy' (WILL) survey (PI: E.F. van Dishoeck) are compared to the shock models from Kaufman & Neufeld (1996) and Flower & Pineau des Forêts (2010). All sources are confirmed deeply-embedded YSOs located in the well-studied Perseus molecular cloud spanning the Class 0 and I regime (Knee & Sandell 2000, Enoch et al. 2006, Jørgensen et al. 2006, 2007b, Hatchell et al. 2007a,b, Davis et al. 2008, Enoch et al. 2009, Arce et al. 2010). H_2O, CO, and OH lines are analyzed together for this uniform sam-

ple to answer the following questions: Do far-IR line observations agree with the shock models? How much variation in observational diagnostics of shock conditions is found between different sources? Can one set of shock parameters explain all molecular species and transitions? Are there systematic differences between shock characteristics inferred using the CO lines from the 'warm' and 'hot' components? How do shock conditions vary with the distance from the powering protostar?

This paper is organized as follows. Section 2 describes our source sample, instrument with adopted observing mode, and reduction methods. §3 presents the results of the observations: line and continuum maps, and the extracted spectra. §4 shows comparison between the observations and shock models. §5 discusses results obtained in §4 and §6 presents the conclusions.

4.2   Observations

All observations presented here were obtained as part of the 'William Herschel Line Legacy' (WILL) OT2 program on *Herschel* (Mottram et al. in prep.). The WILL survey is a study of H_2O lines and related species with PACS and the Heterodyne Instrument for the Far-Infrared (HIFI, de Graauw et al. 2010) toward an unbiased flux-limited sample of low-mass protostars newly discovered in the recent *Spitzer* (c2d, Gutermuth et al. 2009, 2010, Evans et al. 2009) and *Herschel* (André et al. 2010) Gould Belt imaging surveys. Its main aim is to study the physics and chemistry of star-forming regions in a statistically significant way by extending the sample of low-mass protostars observed in the 'Water in star-forming regions with Herschel' (WISH, van Dishoeck et al. 2011) and 'Dust, Ice, and Gas in Time' (DIGIT, Green et al. 2013) programs.

This paper presents the *Herschel*/PACS spectra of 22 low-mass deeply-embedded YSOs located exclusively in the Perseus molecular cloud (see Table 4.1) to ensure the homogeneity of the sample (similar ages, environment, and distance). The sources were selected from the combined SCUBA and *Spitzer*/IRAC and MIPS catalog of Jørgensen et al. (2007b) and Enoch et al. (2009), and all contain a confirmed embedded YSO (Stage 0 or I, Robitaille et al. 2006, 2007) in the center.

The WILL sources were observed using the line spectroscopy mode on PACS which offers deep integrations and finely sampled spectral resolution elements (minimum 3 samples per FWHM depending on the grating order, PACS Observer's Manual[1]) over short wavelength ranges (0.5–2 μm). The line selection was based on the prior experience with the PACS spectra obtained over the full far-infrared spectral range in the WISH and DIGIT programs and is summarized in Table 4.A.1. Details of the observations of the Perseus sources within the WILL survey are shown in Table 4.A.2.

---

[1] http://herschel.esac.esa.int/Docs/PACS/html/pacs_om.html

Table 4.1 – Catalog information and source properties

Object	R.A. (h m s)	Decl. (o ′ ″)	$T_{\rm bol}$ (K)	$L_{\rm bol}$ ($L_\odot$)	$M_{\rm env}$ ($M_\odot$)	Region	Other names
Per01	03:25:22.32	+30:45:13.9	44	4.5	1.14	L1448	Per-emb 22, L1448 IRS2, IRAS03222+3034, YSO 1
Per02	03:25:36.49	+30:45:22.2	50	10.6	3.17	L1448	Per-emb 33, L1448 N(A), L1448 IRS3, YSO 2
Per03[a]	03:25:39.12	+30:43:58.2	47	8.4	2.56	L1448	Per-emb 42, L1448 MMS, L1448 C(N), YSO 3
Per04	03:26:37.47	+30:15:28.1	61	1.2	0.29	L1451	Per-emb 25, IRAS03235+3004, YSO 4
Per05	03:28:37.09	+31:13:30.8	85	11.1	0.35	NGC1333	Per-emb 35, NGC1333 IRAS1, IRAS03255+3103, YSO 11
Per06	03:28:57.36	+31:14:15.9	85	6.9	0.30	NGC1333	Per-emb 36, NGC1333 IRAS2B, YSO 16
Per07	03:29:00.55	+31:12:00.8	37	0.7	0.32	NGC1333	Per-emb 3, HRF 65, YSO 18
Per08	03:29:01.56	+31:20:20.6	131	16.8	0.86	NGC1333	Per-emb 54, HH 12, YSO 19
Per09	03:29:07.78	+31:21:57.3	128	23.2	0.24	NGC1333	Per-emb 50
Per10	03:29:10.68	+31:18:20.6	45	6.9	1.37	NGC1333	Per-emb 21, HRF 46, YSO 23
Per11[b]	03:29:12.06	+31:13:01.7	28	4.4	5.42	NGC1333	Per-emb 13, NGC1333 IRAS4B', YSO 25
Per12	03:29:13.54	+31:13:58.2	31	1.1	1.30	NGC1333	Per-emb 14, NGC1333 IRAS4C, YSO 26
Per13	03:29:51.82	+31:39:06.0	40	0.7	0.51	NGC1333	Per-emb 9, IRAS03267+3128, YSO 31
Per14	03:30:15.14	+30:23:49.4	88	1.8	0.14	B1-ridge	Per-emb 34, IRAS03271+3013
Per15	03:31:20.98	+30:45:30.1	35	1.7	1.29	B1-ridge	Per-emb 5, IRAS03282+3035, YSO 32
Per16	03:32:17.96	+30:49:47.5	30	1.1	2.75	B1-ridge	Per-emb 2, IRAS03292+3039, YSO 33
Per17[c]	03:33:14.38	+31:07:10.9	43	0.7	1.20	B1	Per-emb 6, B1 SMM3, YSO 35
Per18[c]	03:33:16.44	+31:06:52.5	25	1.1	1.22	B1	Per-emb 10, B1 d, YSO 36
Per19	03:33:27.29	+31:07:10.2	93	1.1	0.23	B1	Per-emb 30, B1 SMM11, YSO 40
Per20	03:43:56.52	+32:00:52.8	27	2.3	2.05	IC 348	Per-emb 1, HH 211 MMS, YSO 44
Per21	03:43:56.84	+32:03:04.7	34	2.1	1.88	IC 348	Per-emb 11, IC348 MMS, IC348 SW, YSO 43
Per22	03:44:43.96	+32:01:36.2	43	2.6	0.64	IC 348	Per-emb 8, IC348 a, IRAS03415+3152, YSO 48

Notes. Bolometric temperatures and luminosities are determined including the PACS continuum values; the procedure will be discussed in Mottram et al. (in prep.). Numbered Per-emb names come from Enoch et al. (2009), whereas the numbered YSO names come from Jørgensen et al. (2006) and were subsequently used in Davis et al. (2008). Other source identifiers were compiled using Jørgensen et al. (2007b), Rebull et al. (2007), Davis et al. (2008), and Velusamy et al. (2013). Observations obtained in 2011 which overlap with Per03 and Per11 are presented in Lee et al. (2013) and Herczeg et al. (2012), respectively. [a] Tabulated values come from Green et al. (2013), where full PACS spectra are obtained. The WILL values for $T_{\rm bol}$ and $L_{\rm bol}$ are 48 K and 8.0 $L_\odot$, respectively, within 5% of those of Green et al. (2013). [b] Tabulated values come from Karska et al. (2013) and agree within 2% of the values 29 K and 4.3 $L_\odot$ obtained here. We prefer to use the previously published values because the pointing of that observation was better centered on the IRAS4B. [b] The off-positions of Per17 and Per18 were contaminated by other continuum sources, and therefore the $T_{\rm bol}$ and $L_{\rm bol}$ are calculated here without the Herschel / PACS points.

PACS is an integral field unit with a 5×5 array of spatial pixels (hereafter *spaxels*) covering a field of view of $\sim 47'' \times 47''$. Each spaxel measured $\sim 9.4'' \times 9.4''$, or 2×10^{-9} sr, and at the distance to Perseus ($d = 235$ pc, Hirota et al. 2008) resolves emission down to $\sim$2,300 AU. The total field of view is about 5.25×10^{-8} sr and $\sim$11,000 AU. The properly flux-calibrated wavelength ranges include: $\sim$55–70 μm, $\sim$72–94 μm, and $\sim$105–187 μm, corresponding to the second (< 100 μm) and first spectral orders (> 100 μm). Their respective spectral resolving power are R $\sim$2500–4500 (velocity resolution of Δv $\sim$70-120 km s^{-1}), 1500–2500 (Δv $\sim$120-200 km s^{-1}), and 1000–1500 (Δv $\sim$200-300 km s^{-1}). The standard chopping-nodding mode was used with a medium (3′) chopper throw. The telescope pointing accuracy is typically better than 2″ and can be evaluated to first order using the continuum maps.

The basic data reduction presented here was performed using the Herschel Interactive Processing Environment v.10 (HIPE, Ott 2010). The flux was normalized to the telescopic background and calibrated using observations of Neptune. Spectral flatfielding within HIPE was used to increase the signal-to-noise (for details, see Herczeg et al. 2012, Green et al. 2013). The overall flux calibration is accurate to $\sim$ 20%, based on the flux repeatability for multiple observations of the same target in different programs, cross-calibrations with HIFI and ISO, and continuum photometry.

Custom IDL routines were used to extract fluxes using Gaussian fits with fixed line width (for details, see Herczeg et al. 2012). The total, 5×5 line fluxes were calculated by co-adding spaxels with detected line emission, after excluding contamination from other nearby sources except Per 2, 3, 10, and 18, where spatial separation between different components is too small (see §3.1). For sources showing extended emission, the set of spaxels providing the maximum flux was chosen for each line separately. For point-like sources, the flux is calculated at the central position and then corrected for the PSF using wavelength-dependent correction factors (see PACS Observer's Manual). Table 4.A.3 shows the line detections toward each source, while the actual fluxes will be tabulated in the forthcoming paper for all the WILL sources (Karska et al. in prep.).

4.3 Results

In the following sections, PACS lines and maps of the Perseus YSOs are presented. Most sources in this sample show emission in just the central spaxel. Only a few sources show extended emission and those maps are compared to maps at other wavelengths to check for possible contamination by other sources and their outflows. In this way, the spaxels of the maps with emission originating from our objects are established and line fluxes determined over those spaxels. The emergent line spectra are then discussed.

4.3.1 Spatial extent of line emission

Table 4.1 provides a summary of the patterns of H_2O 2_{12}-1_{01} line and continuum emission at 179 μm for all WILL sources in Perseus (maps are shown in Figs. 4.A.1 and 4.A.2). The mid-infrared continuum and H_2 line maps from Jørgensen et al. (2006) and Davis

et al. (2008, including CO 3–2 observations from Hatchell et al. 2007a) are used to obtain complementary information on the sources and their outflows. For a few well-known outflow sources, large-scale CO 6-5 maps from Yıldız et al. (subm.) are also considered.

As shown in Table 4.1, the majority of the PACS maps toward Perseus YSOs do not show any extended line emission. The well-centered continuum and line emission originates from a single object and an associated bipolar outflow for 12 out of 22 sources. Among the sources with spatially-resolved extended emission on the maps, various reasons are identified for their origin as illustrated in Fig. 4.1. In the map of Per 2, contribution from three nearby protostars and a strong outflow from the more distant L1448-MM source cause the extended line and continuum pattern. Emission in the Per 12 map is detected away from the continuum peak, but the emission originates from a large-scale outflow from NGC1333-IRAS4A, not the targeted source. The H_2O emission in the Per 20 map is detected in the direction of the strong outflow and its extent is only slightly affected by the small mispointing revealed by the asymmetric continuum emission.

Extended emission beyond the well-centered continuum, as in the case of Per 20, is seen clearly only in Per 9 and Per 21-22. Additionally, the continuum peaks for Per 3, 8, and 11 are off-center, whereas the line emission peaks on-source, suggesting that some extended line emission is associated with the source itself and not only due to the mispointing. [2] Similar continuum patterns are seen in Per 6 and Per 10, but here the line emission peaks a few spaxels away from the map center. In both cases, contribution from additional outflows / sources is the cause of the dominant off-source line emission.

To summarize, when the contamination of other sources and their outflows can be excluded, Perseus YSOs show that the H_2O 2_{12}-1_{01} line emission is either well-confined to the central position on the map or shows at best weak extended line emission (those are marked with 'e' in Table 2). In total, 7 out of 22 sources show extended emission in the H_2O 2_{12}-1_{01} line associated with the targeted sources. Emission in CO, OH, and other H_2O lines follows the same pattern (see Figure 4.A.3). Similarly compact emission was seen in a sample of 30 protostars surveyed in the DIGIT program (Green et al. 2013). In contrast, the WISH PACS survey (Karska et al. 2013) revealed strong extended emission in about half of the 20 low-mass protostars. There, the analysis of patterns of molecular and atomic emission showed that H_2O and CO spatially co-exist within the PACS field-of-view, while OH and [O I] lines are typically less extended, but also follow each other spatially and not H_2O and CO.

---

[2] On-source observations that contained Per 3 and Per 11 in the same field-of-view are discussed in separate papers by Lee et al. (2013) and Herczeg et al. (2012), respectively.

Table 4.1 – Notes on mapped regions for individual sources

Object	Continuum		Line		Sources		Outflows		Remarks
	on	off	on	off	single	multiple	single	multiple	
Per01	X	-	X	-	X	-	X	-	
Per02	X	-	-	X	-	X	-	Xc	three sources (3), contam. by Per03 (1,2)
Per03	-	X	Xe		-	X	-	X	a binary (1,4)
Per04	X	-	nd	nd	X	-	X	-	
Per05	X	-	X	-	X	-	X	-	
Per06	-	X	-	X	-	X?	-	Xc	contam. by NGC1333 IRAS 2A in N-W (5)
Per07	X	-	nd	nd	X	-	Xc	-	contam. in lines in N-W
Per08	-	X	Xe	-	X	-	X	-	
Per09	X	-	Xe	-	X?	-	X?	-	
Per10	-	X	-	X	-	X	-	Xc	two sources (1,2), dominated by YSO 24 (1,2)
Per11	-	X	Xe	-	-	X	-	Xc	NGC1333 IRAS4A in N-W (5)
Per12	X	-	nd	nd	X	-	Xc	-	contam. in lines by NGC1333 IRAS4A in N-W (5)
Per13	X	-	nd	nd	X?	-	X?		
Per14	X	-	X	-	X?	-	X?		
Per15	X	-	X	-	X	-	X	-	
Per16	X	-	nd	nd	X	-	X	-	
Per17	-	X?	nd	nd	-	X	-	Xc?	Per18 in S-E, nodded on emission
Per18	X	-	X	-	X	-	-	Xc?	B1-b outflow? (2)
Per19	X	-	X	-	X	-	X	-	
Per20	X	-	Xe	-	X	-	X	-	
Per21	X	-	Xe	-	X?	-	X?	-	
Per22	X	-	Xe	-	X?	-	X?	-	

Notes. Columns 2-5 indicate the location of the continuum at 179 μm and line emission peak of the H_2O 2_{12}-1_{01} (179.527 μm) transition on the maps (whether on or off-center). Columns 6-9 provide information about the number of sources and their outflows in the mapped region. Contamination by the outflows driven by sources outside the PACS field-of-view is mentioned in the last column. Extended emission associated with the targeted sources is denoted by 'e'. Non-detections are abbreviated by 'nd', while 'c' marks the contamination of the targeted source map by outflows from other sources. References: (1) Jørgensen et al. (2006), (2) Davis et al. (2008), (3) Looney et al. (2000), (4) Hirano et al. (2010), Lee et al. (2013), (5) Yıldız et al. (subm).
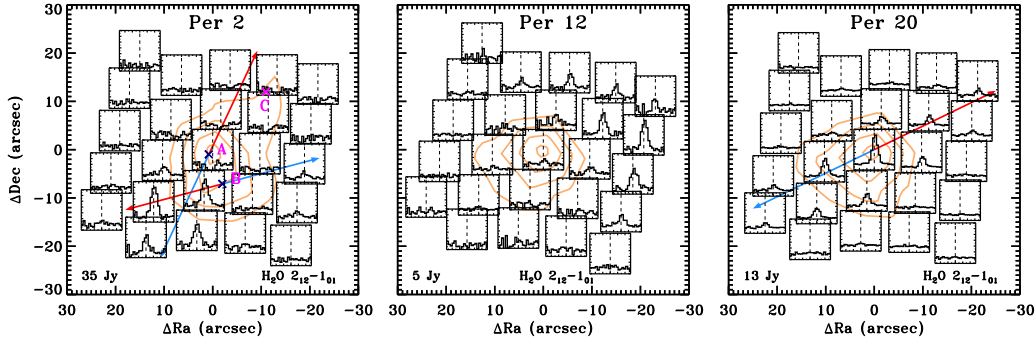
Figure 4.1 – PACS spectral maps in the H_2O 2_{12}-1_{01} line at 179 μm illustrating sources with extended emission due to multiple sources in one field (Per 2), contamination by the outflow driven by another source (Per 12), and associated with the targeted protostar (Per 20). Even though the emission on the maps seems to be extended in many sources in Perseus, the extended emission *associated with the targeted protostar itself* is detected only towards a few of them (see Table 2). The orange contours show continuum emission at 30%, 50%, 70%, and 90% of the peak value written in the bottom left corner of each map. L1448 IRS 3A, 3B, and 3C sources and their CO 2–1 outflow directions are shown on the map of Per 2 (Kwon et al. 2006, Looney et al. 2000); the blue outflow lobe of L1448-MM also covers much of the observed field. CO 2–1 outflow directions of Per 20 / HH211 are taken from Gueth & Guilloteau (1999). Wavelengths in microns are translated to the velocity scale on the X-axis using laboratory wavelengths (see Table 4.A.1) of the species and cover the range from -600 to 600 km s^{-1}. The Y-axis shows fluxes in Jy normalized to the spaxel with the brightest line on the map in a range -0.2 to 1.2.

4.3.2 Line detections

In the majority of our sources, all targeted rotational transitions of CO, H_2O, and OH are detected, see Fig. 4.2 and Tables 4.A.1 and 4.A.3. The [O I] line at 63 μm and the [C II] line at 158 μm will be discussed separately in a forthcoming paper including all WILL sources (Karska et al. in prep.) and are not included in the figure and further analysis.

The CO 16-15 line with an upper level energy (E_u/k_B) of about 750 K is seen in 17 ($\sim$80%), the CO 24-23 ($E_u/k_B \sim$ 1700 K) in 16 ($\sim$70%), and the CO 32-31 ($E_u/k_B \sim$ 3000 K) in 8 ($\sim$30%) sources. The most commonly detected ortho-H_2O lines are: the 2_{12}-1_{01} line at 179 μm ($E_u/k_B \sim$ 110 K) and the 4_{04}-3_{13} line at 125 μm ($E_u/k_B \sim$ 320 K), seen in 15 sources ($\sim$ 70 %), whereas the 6_{16}-5_{05} line at 82 μm ($E_u/k_B \sim$ 640 K) is detected in 13 sources ($\sim$ 60 %). The para-H_2O line 3_{22}-2_{11} at 90 μm ($E_u/k_B \sim$ 300 K) is seen toward 9 sources ($\sim$ 50 %).

Three OH doublets targeted as part of the WILL survey, the OH $^2\Pi_{1/2}, J = {}^1/2 - {}^2\Pi_{3/2}, J = {}^3/2$ at 79 μm, $^2\Pi_{3/2}$ $J = {}^7/2 - {}^5/2$ doublet at 84 μm ($E_u/k_B \sim$ 290 K), and $^2\Pi_{1/2}$ $J = {}^3/2 - {}^1/2$ doublet at 163 μm ($E_u/k_B \sim$ 270 K), are detected in 14, 15, and 13 objects, respectively ($\sim$ 60 − 70 %).
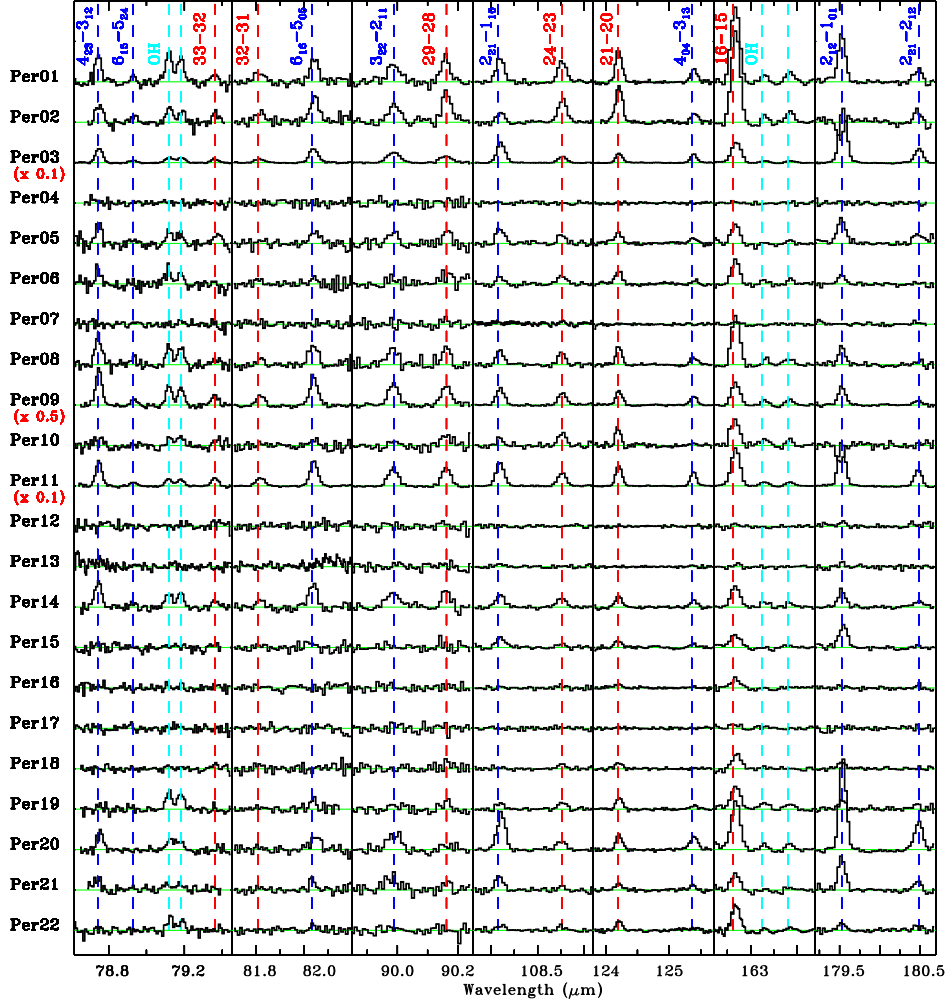
Figure 4.2 – Line survey of deeply-embedded young stellar objects in Perseus at the central position on the maps. Spectra are continuum subtracted and not corrected for the PSF. Line identification of CO (red), H_2O (blue), and OH (light blue), are shown. Each spectrum is on a scale from 0 to 5 Jy in the y-axis, with the brightest sources – Per 3, Per 9, and Per 11 – scaled down in flux density by a factor of 0.1, 0.5, and 0.1, respectively.

Sources without any detections of molecular lines associated with the targeted protostars are Per 4, 7, 12, and 17 (see Table 4.A.3). In Per 13 only two weak H_2O lines at 108 and 125 μm are seen, whereas in Per 16 only a few of the lowest-J CO lines are detected. A common characteristic of this weak-line group of objects, is a low bolometric temperature (all except Per 4) and a low bolometric luminosity (see Table 4.1), always
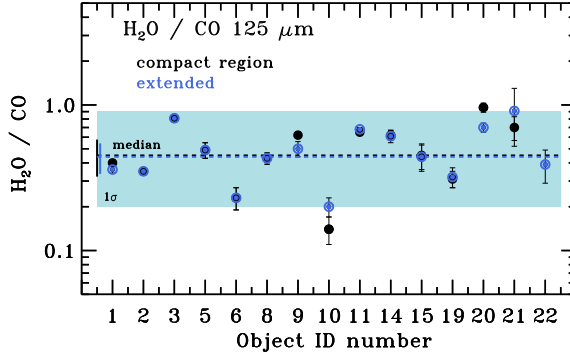
Figure 4.3 – Flux ratios of the H_2O 4_{04}-3_{13} and CO 21-20 lines at ~125 μm calculated using *compact* and *extended* flux extraction regions (see text) corrected for contamination from other sources / outflows. Median values for the two configurations are shown by the dashed line. The light blue rectangle shows the parameter space between the minimum and maximum values of line ratios in the more extended configuration. The error bars reflect the uncertainties in the measured fluxes of the two lines, excluding the calibration error, which is the same for those closely spaced lines.

below 1.3 $L_{\odot}$. However, our sample also includes a few objects with similarly low values of L_{bol}, that show many more molecular lines (in particular Per 3, but also Per 15 and 21), so low luminosity by itself is not a criterion for weak lines. On the other hand, low bolometric temperature and high luminosity is typically connected with strong line emission (Kristensen et al. 2012, Karska et al. 2013).

4.3.3 Observed line ratios

Observed line ratios are calculated using the fluxes obtained from the entire 5×5 PACS maps in cases of extended emission where contamination by a nearby source and / or outflows is excluded. For point sources, a wavelength-dependent PSF correction factor is applied to fluxes obtained from the central spaxel (for details, see §2). In principle, ratios using lines that are close in wavelength could be calculated using smaller flux extraction regions, and no PSF correction would be required. However, the transition wavelengths of H_2O are not proportional to the upper energy levels, as is the case for CO, and comparisons of lines tracing similar gas have to rely on lines that lie far apart in wavelength. We explore to what extent the size of the extraction region affects the inferred line ratios. Since our aim is to understand the influence of the extended emission associated with the source(s), the ratios of lines close in wavelength are studied to avoid the confusion due to the PSF variations.

Fluxes of the nearby H_2O 4_{04}-3_{13} and CO 21-20 lines located at 124–125 μm are cal-

culated first using only the central spaxel (*compact region*) and then using all the spaxels with detected line emission (*extended region*). Fig. 4.3 illustrates that the line ratios calculated in these two regions are fully consistent. Therefore, for the subsequent analysis the extended region is used for comparisons with models. Table 4.A.4 shows the minimum and maximum values of the observed line ratios, their mean values, and the standard deviations for all sources with detections.

Even taking into account the uncertainties in flux extraction, the line ratios span remarkably narrow ranges of values, see Table 4.2 for a selection of H_2O, CO, and OH line ratios. The largest range is seen in the H_2O 2_{12}-1_{01}/CO 16-15 line ratio, which spans an order of magnitude. In all the other cases the line ratios are similar up to a factor of a few. The most similar are the OH line ratios which differ only by a factor of two, consistent with previous studies based on a large sample of low-mass YSOs in Wampfler et al. (2013). The observed similarities also imply that the line ratios do not depend on protostellar luminosity, bolometric temperature, or envelope mass (see Fig. 4.B.1).

Our line ratios for Perseus sources are consistent with the previously reported values for other deeply-embedded protostars observed in the same way ('on source') as tabulated in Table 4.2. Some differences are found for PACS observations of shock positions away from the protostar ('off source'). Most notably, the ratios using the low excitation H_2O 2_{12}-1_{01} line at 179 μm are up to a factor of two larger than those observed in the protostellar vicinity. Such differences are not seen when more highly-excited H_2O lines are compared with each other, for example H_2O 2_{21}-1_{10} and 4_{04}-3_{13} lines, or with the high$-J$ CO lines, for example CO 24–23. The ratios of two CO lines observed away from the protostar, e.g. the CO 16–15 and CO 24–23 ratios, are at the low end of the range observed toward the protostellar position.

Spectrally-resolved profiles of the H_2O 2_{12}-1_{01} line observed with HIFI toward the protostar position reveal absorptions at source velocity removing about 10% of total line flux (e.g. Kristensen et al. 2010, Mottram et al. in press). Our unresolved PACS observations therefore provide a lower limit to the H_2O emission in the 2_{12}-1_{01} line. This effect, however, is too small to explain the differences in the line ratios at the 'on source' and 'off source' positions.

Table 4.2 – Comparison of observed H_2O, CO, and OH line ratios with literature values

Object	2_{12}-1_{01} / 16-15	4_{04}-3_{13} / 24-23	16-15 / 24-23	2_{12}-1_{01} / 4_{04}-3_{13}	2_{21}-1_{10} / 4_{04}-3_{13}	OH 84 / 79	Ref.
			Perseus (this work)				
Perseus	0.2–2.4	0.2–1.1	1.2–4.6	1.3–6.3	1.4–5.5	1.1–2.4	This work
			On–source (literature)				
SMM3 b	1.0±0.1	0.5± 0.2	3.3±0.8	7.1±1.0	3.7±1.0	1.4±0.7	(1)
c	0.9±0.2	0.9± 0.3	4.6±1.0	4.9±1.0	2.3±0.8	2.4±1.2	(1)
r	1.0±0.1	**2.0±0.7**	**9.4±2.3**	4.7±1.0	3.1±0.9	n.d.	(1)
SMM4 r	0.8±0.1	0.4± 0.1	3.6±0.6	7.8±1.6	3.0±1.3	1.1±0.5	(1)
L1448-MM	2.3±1.3	1.2±0.7	2.1±1.2	4.1±2.3	2.6±1.5	1.4±0.9	(2)
NGC1333 I4B	1.0±0.1	1.0±0.1	1.9±0.1	1.9±0.1	2.0±0.1	1.2±0.2	(3)
			Off–source (literature)				
L1157 B1	**4.0±0.5**	–	–	11.0	2.9±1.2	n.d.	(4,5)
B1’	2.1±0.2	–	–	**9.2±2.2**	2.8±1.0	0.9±0.5	(4,5)
B2	**17.0±8.4**	n.d.	>0.3	**>7.7**	n.d.	–	(6)
R	**5.3±2.4**	>0.26	>0.5	**10.6±4.7**	1.8±0.8	–	(6)
L1448 B2	2.3±0.4	0.4±0.3	2.8±0.9	**15.0±6.5**	3.7±1.6	–	(6)
R4	**8.2±3.0**	>0.3	>0.9	**23.2±9.7**	3.3±1.2	–	(6)

Notes. Sources in the upper part of the table refer to protostellar positions within the PACS maps, sources in the lower part refer to shock positions away from the protostar. Ranges of line ratios calculated for Perseus sources are listed at the top. Line ratios of sources that exceed the Perseus values are shown in boldface. The L1157 B1’ position refers to the high-excitation CO emission peak close to the nominal position of the B1 shock spot (Benedettini et al. 2012). Non-detections are abbreviated with n.d. OH 84 / 79 refers to the ratio of two OH doublets, at 84 and 79 μm respectively. The total flux of the 84 μm doublet is calculated by multiplying by two the 84.6 μm flux, due to the blending of the 84.4 μm line with the CO 31-30 line. References: (1) Dionatos et al. (2013), (2) Lee et al. (2013), (3) Herczeg et al. (2012), (4) Benedettini et al. (2012), (5) Busquet et al. (2014), (6) Santangelo et al. (2013).

4.4 Analysis

The fact that multiple molecular transitions over a wide range of excitation energies are detected, points to the presence of hot, dense gas and can be used to constrain the signatures of shocks created as a result of outflow-envelope interaction. In particular, the line ratios of H_2O, CO, and OH are useful probes of various shock types and parameters that do not suffer from distance uncertainties.

Similarities between the spatial extent of different molecules (§3.1) coupled with similarities in the velocity-resolved line profiles among these species (Kristensen et al. 2010, Yıldız et al. 2013, San José-García et al. 2013, Mottram et al. in press) strongly suggest that all highly-excited lines of CO and H_2O arise from the same gas. Some differences may occur for OH, which is also associated with dissociative shocks and can be affected by radiative excitation (see §5). Modeling of absolute line fluxes requires sophisticated two-dimensional (2D) physical source models for the proper treatment of the beam filling factor (Visser et al. 2012). Those models also show that UV heating alone is not sufficient to account for the high excitation lines. Hence, the focus in this analysis is on shocks. Since the absolute flux depends sensitively on the assumed emitting area, in the subsequent analysis only the line ratios are compared.

In the following sections, properties of shock models and the predicted line emission in various species are discussed (§4.1) and observations are compared with the models, using line ratios of the same species (§4.2), and different species (§4.3). Special focus will be given to $C-$type shocks where grids of model results are available in the literature. Observations suggest that most of the mass of hot gas is in $C-$type shocks toward the central protostellar positions, at least for H_2O and CO with $J < 30$ (Kristensen et al. 2013, Kristensen et al. in prep.); higher-J CO, OH and [O I] transitions, on the other hand, will primarily trace $J-$type shocks (e.g. Wampfler et al. 2013, Kristensen et al. 2013). The excitation of OH and [O I] will be analyzed in a forthcoming paper; the $J > 30$ CO emission is only detected toward ~ 30% of all sources and so is likely unimportant for the analysis and interpretation of the data presented here. Only limited discussion of $J-$ type shocks is therefore presented below.

4.4.1 Model line emission

Models of shocks occurring in a medium with physical conditions typical for the envelopes of deeply-embedded young stellar objects provide a valuable tool for investigating shock characteristics: shock type, velocity, and the pre-shock density of (envelope) material.

Model grids have been published using a simple 1D geometry either for steady-state C and J type shocks (Hollenbach et al. 1989, Kaufman & Neufeld 1996, Flower & Pineau des Forêts 2010) or time-dependent $C - J$ type shocks (Gusdorf et al. 2008, 2011, Flower & Pineau des Forêts 2012). The latter are non-stationary shocks, where a $J-$type front is embedded in a $C-$type shock (Chieze et al. 1998, Lesaffre et al. 2004a,b). These shocks are intermediate between pure $C-$ and $J-$type shocks and have temperatures and physical extents in between the two extremes.

147

C-J shocks may be required for the youngest outflows with ages less than 10^3 yrs, (Flower & Pineau des Forêts 2012, 2013, for the case of IRAS4B, Per 11). Here the dynamical age of the outflow is taken as an upper limit of that of the shock itself, which may be caused by a more recent impact of the wind on the envelope. The age of our sources is of the order of 10^5 yrs (Sadavoy et al. 2014, for Class 0 sources in Perseus) and they should have been driving winds and jets for the bulk of this period, so this timescale is long enough for any shocks close to the source position to have reached steady state. While we cannot exclude that a few individual shocks have been truncated, our primary goal is to examine trends across the sample. Invoking *C-J* type shocks with a single truncation age as an additional free parameter is therefore not a proper approach for this study. The focus is therefore placed on comparing $C-$type shock results from Kaufman & Neufeld (1996, KN96 from now on) and Flower & Pineau des Forêts (2010, F+PdF10 from now on) with the observations.

All models assume the same initial atomic abundances and similarly low degrees of ionization, $x_i \sim 10^{-7}$ for *C* shocks. The pre-shock transverse magnetic field strength is parametrized as $B_0 = b \times \sqrt{n_H(\text{cm}^{-3})} \, \mu$Gauss, where n_H is the pre-shock number density of atomic hydrogen and b is the magnetic scaling factor, which is typically 0.1-3 in the ISM (Draine 1980). The value of b in KN96 and F+PdF10 is fixed at a value of 1.

The main difference between the two shock models is the inclusion of grains in the F+PdF10 models (Flower & Pineau des Forêts 2003). As the electrons are accelerated in the magnetic precursor, they attach themselves to grains thereby charging the grains and thus increasing the density of the ionized fluid significantly. This increase in density has the effect of enhancing the ion-neutral coupling (Draine 1980), thereby effectively lowering the value of b compared to the KN96 models. As a consequence, the maximum kinetic temperature is higher in the F+PdF10 models for a given shock velocity, v. The stronger coupling between the ions and neutrals results in narrower shocks (Flower & Pineau des Forêts 2010), with shock widths scaling as $\propto b^2(x_i n_H v)^{-1}$ (Draine 1980). This proportionality does not capture the ion-neutral coupling exactly, as, for example, the grain size distribution influences the coupling (Guillet et al. 2007, 2011). The compression in *C* shocks also changes with the coupling since the post-shock density depends on the magnetic field, $n_{\text{post}} \sim 0.8 v n_H b^{-1}$ (e.g. Karska et al. 2013). The column density of emitting molecules is a function of both shock width and compression factor, and as a zeroth-order approximation the column density is $N \sim n_{\text{post}} \times L \sim b x_i^{-1}$. The ionization degree is not significantly different between the KN96 and F+PdF10 models because it is primarily set by the cosmic ray ionization rate, and thus the F+PdF10 models predict lower column densities than the KN96 models for a given velocity and density.

Another important difference is that the F+PdF10 models take into account that molecules frozen out onto grain mantles can be released through sputtering when the shock velocity exceeds $\sim 15 \text{ km s}^{-1}$ (Flower & Pineau des Forêts 2010, 2012, Van Loo et al. 2013). Therefore, the gas-phase column densities of molecules locked up in ices increase above this threshold shock velocity with respect to the KN96 models, an effect which applies to both CO and H_2O. Furthermore, H_2O forms more abundantly in the post-shock gas of F+PdF10 models, because H_2 reformation is included, unlike in the KN96 models

(Flower & Pineau des Forêts 2010).

Molecular emission is tabulated by KN96 for a wide range of shock velocities, from $v = 5$ to 45 km s^{-1} in steps of 5 km s^{-1}, and a wide range of pre-shock densities $n_{\rm H}$, from 10^4 to $10^{6.5}$ cm^{-3} in steps of $10^{0.5}$ cm^{-3}. The F+PdF10 grid is more limited in size, providing line intensities for only two values of pre-shock densities, namely 10^4 and 10^5 cm^{-3}, and a comparable range of shock velocities, but calculated in steps of 10 km s^{-1}. Calculations are provided for CO transitions from $J = 1 - 0$ to $J = 60 - 59$ in KN96 and only up to $J = 20 - 19$ in F+PdF10. The two sets of models use different collisional rate coefficients to calculate the CO excitation. F+PdF10 show line intensities for many more H$_2$O transitions (in total $\sim$120 lines in the PACS range, see §2) than in the older KN96 grid (18 lines in the same range), which was intended for comparisons with the Submillimeter Wave Astronomy Satellite (SWAS, Melnick et al. 2000) and ISO data. KN96 use collisional excitation rates for H$_2$O from Green et al. (1993) and F+PdF10 from Faure et al. (2007). Line intensities for OH are only computed by KN96, assuming only collisional excitation and using the oxygen chemical network of Wagner & Graff (1987). The reaction rate coefficients in that network are within a factor of 2 of the newer values by Baulch et al. (1992) and tabulated in the UMIST database (www.udfa.net, McElroy et al. 2013), see also a discussion in van Dishoeck et al. (2013).

We also use CO fluxes extracted from the grid of models presented by Kristensen et al. (2007), since high$-J$ CO lines are missing in F+PdF10. This grid is based on the shock model presented in Flower & Pineau des Forêts (2003) and covers densities from 10^4–10^7 cm^{-3} and velocities from 10–50 km s^{-1} (denoted as F+PdF* from now on). The main difference compared to the results from F+PdF10 is that CO and H$_2$O level populations are not calculated explicitly through the shock; instead analytical cooling functions are used to estimate the relevant line cooling and only afterwards line fluxes are extracted (Flower & Gusdorf 2009). Models with $b = 1$ are used. The CO line fluxes presented here are computed using the 3D non-LTE radiative transfer code LIME (Brinch & Hogerheijde 2010), for levels up to $J = 80$–79. The CO collisional rate coefficients from Yang et al. (2010) extended by Neufeld (2012) are used.

In the following sections, the model fluxes of selected CO, H$_2$O, and OH lines are discussed for a range of shock velocities and three values of pre-shock densities: 10^4, 10^5, and 10^6 cm^{-3}. Note that the post-shock densities traced by observations are related to the pre-shock densities via the compression factor dependent on the shock velocity and magnetic field. In C shocks, the compression factor is about 10 (e.g. Karska et al. 2013).

Figure 4.1 compares model fluxes of various CO, OH, and H$_2$O lines from the KN96 models (panels a and d) and, for a few selected CO and H$_2$O lines, compares the results with the F+PdF10 or F+PdF* models (panels b, c, e, and f).

4.4.1.1 CO

The KN96 model line fluxes for CO 16-15, CO 21-20, and CO 29-28 are shown in panel a of Fig. 4.1. The upper energy levels of these transitions lie at 750 K, 1280 K, and 2900 K, respectively, while with increasing shock velocity, the peak $C-$shock temperature increases from about 400 K to 3200 K (for 10 to 40 km s^{-1}) and is only weakly dependent

149
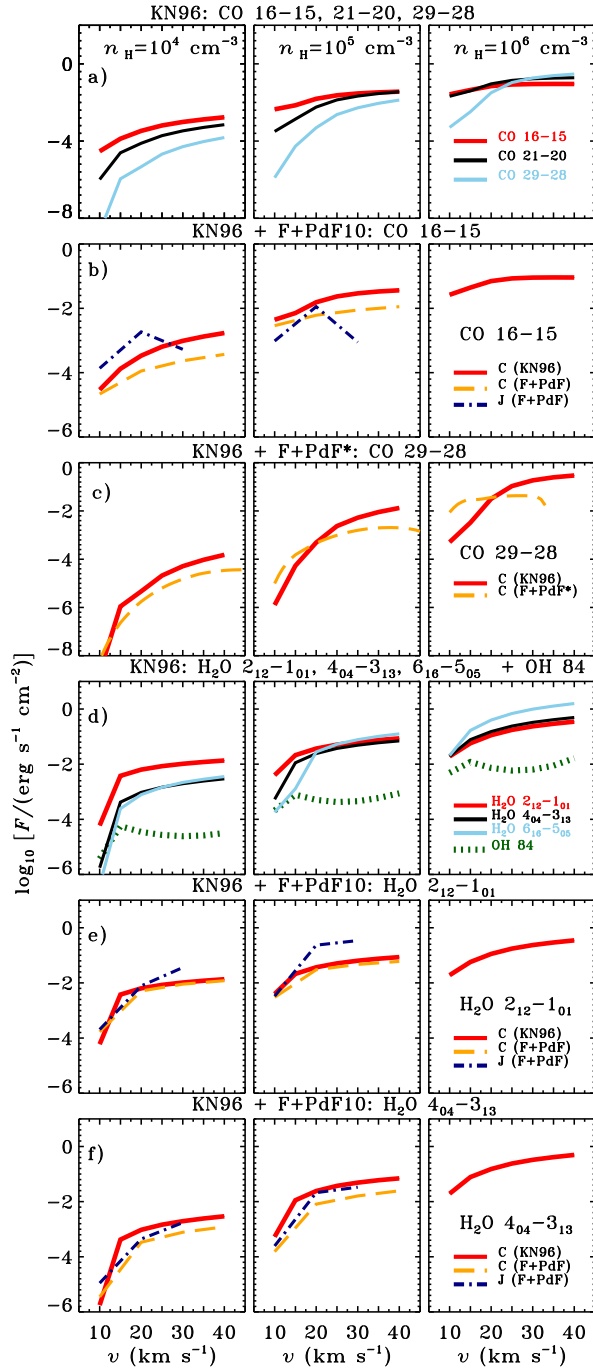
Figure 4.1 – Absolute fluxes of selected CO, H₂O, and OH lines predicted by Kaufman & Neufeld and Flower & Pineau des Forêts models and shown as a function of shock velocity. OH 84 refers to the OH $^2\Pi_{3/2}$ $J = ^{7}/_2 - ^{5}/_2$ doublet at 84 μm.

on the assumed density (see Fig. 3 of KN96). Therefore, the CO 16-15 line is already excited at relatively low shock velocities ($v \sim 10$ km s^{-1}, for $n_H = 10^4$ cm^{-3}), whereas the higher$-J$ levels become populated at higher velocities. At a given shock velocity, emission from the CO 16-15 line is the strongest due to its lower critical density, $n_{cr} \sim 9 \times 10^5$ cm^{-3} at $T = 1000$ K (Neufeld 2012). This situation only changes for the highest pre-shock densities, when the line becomes thermalized and the cooling in other lines dominates.

The CO 16-15 flux from the F+PdF10 $C-$type shock models is comparable to the KN96 flux for the $v \sim 10$ km s^{-1} shock, but increases less rapidly with shock velocity despite the sputtering from grain mantles (panel b of Fig. 4.1). As explained before, it is expected that the column density and the corresponding line fluxes are lower in the F+PdF10 models. For slow shocks the higher temperatures in the latter models compensate for the smaller column density resulting in a similar CO 16-15 flux.

In $J-$type shocks, the peak temperatures of the post-shock gas are 1400, 5500, 12000, and 22000 K for the shock velocities of 10, 20, 30, and 40 km s^{-1} respectively (Neufeld & Dalgarno 1989, Kaufman & Neufeld 1996). For 10-20 km s^{-1} shocks, these high temperatures more easily excite the CO 16-15 line with respect to $C-$type shock emission. For shock velocities above 20 km s^{-1}, such high temperatures can lead to the collisional dissociation of H$_2$ and subsequent destruction of CO and H$_2$O molecules, resulting in the decrease of CO fluxes. This effect requires high densities and therefore the CO flux decrease is particularly strong for the pre-shock densities 10^5 cm^{-3}.

4.4.1.2 H$_2$O

The H$_2$O fluxes show a strong increase with shock velocities above $v \sim 10 - 15$ km s^{-1} in both models, especially at low pre-shock densities (panels d-f of Fig. 4.1). At this velocity, the gas temperature exceeds ~ 400 K, so the high-temperature route of H$_2$O formation becomes efficient (Elitzur & Watson 1978, Elitzur & de Jong 1978, Bergin et al. 1998, KN96), which quickly transfers all gas-phase oxygen into H$_2$O via reactions with H$_2$ (KN96).

In contrast to CO, the upper level energies of the observed H$_2$O lines are low and cover a narrow range of values, $E_{up} \sim 200 - 600$ K. As a result, the effect of peak gas temperature on the H$_2$O excitation is less pronounced (Fig. 3 of KN96) and after the initial increase with shock velocity, the H$_2$O fluxes in the KN96 models stay constant for all lines. For high pre-shock densities, the higher lying levels are more easily excited and, as a consequence, the fluxes of the H$_2$O 6_{16}-5_{05} line become larger than those of the H$_2$O 2_{12}-1_{01} line. The critical densities of these transitions are about 2 orders of magnitude higher than for the CO 16-15 line and the levels are still sub-thermally excited at densities of 10^6-10^7 cm^{-3}.

The H$_2$O 2_{12}-1_{01} fluxes in the $C-$type F+PdF10 models are remarkably similar to those found by KN96 (panel e of Fig. 4.1), while the H$_2$O 4_{04}-3_{13} fluxes are lower by a factor of a few over the full range of shock velocities and pre-shock densities in the F+PdF10 models (panel f of Fig. 4.1). Lower H$_2$O fluxes are expected due to smaller column of H$_2$O in the models with grains (§4.1). For the lower$-J$ lines, the various factors (lower column density through a shock but inclusion of ice sputtering and H$_2$ reformation)

apparently conspire to give similar fluxes as for KN96.

In J−type shocks, the fluxes of H_2O 2_{12}-1_{01} and 4_{04}-3_{13} lines increase sharply for shock velocities 10–20 km s^{-1} (panels e and f of Fig. 4). The increase is less steep at 30 km s^{-1} shocks for n_H=10^5 cm^{-3}, when the collisional dissociation of H_2 and subsequent destruction of H_2O molecules occurs (fluxes for larger shock velocities are not computed in F+PdF10 and hence not shown). Below 30 km s^{-1}, line fluxes from J−type shocks are comparable to those from C−type shock predictions except for the H_2O 2_{12}-1_{01} fluxes at high pre-shock densities, which are an order of magnitude higher with respect to the C−type shock predictions. The difference could be due to smaller opacities for the low-excitation H_2O line in the J shocks.

4.4.1.3 OH

The fluxes of the $^2\Pi_{3/2}$ $J = ^7/_2 - ^5/_2$ doublet at 84 μm ($E_u/k_B \sim 290$ K) calculated with the KN96 models are shown with the H_2O lines in panel d of Fig. 4.1. Not much variation is seen as a function of shock velocity, in particular beyond the initial increase from 10 to 15 km s^{-1}, needed to drive oxygen to OH by the reaction with H_2. At about 15 km s^{-1}, the temperature is high enough to start further reactions with H_2 leading to H_2O production. The trend with increasing pre-shock density is more apparent, with OH fluxes increasing by two orders of magnitude between the 10^4 cm^{-3} to 10^6 cm^{-3}, as the density becomes closer to the critical density of the transition.

4.4.2 Models versus observations – line ratios of the same species

Comparison of observed and modeled line ratios of different pairs of CO, H_2O, and OH transitions is shown in Fig. 4.2. The line ratios are a useful probe of molecular excitation and therefore can be used to test whether the excitation in the models is reproduced correctly, which in turn depends on density and temperature, and thus shock velocity.

4.4.2.1 CO line ratios

Given the universal shape of the CO ladders observed toward deeply-embedded protostars (see §1 and the discussion on the origin of CO ladders in §5), three pairs of CO lines are compared with models: (i) CO 16-15 and 21-20 line ratio, corresponding to the 'warm', 300 K component (panel a); (ii) CO 16-15 and 29-28 line ratio, combining transitions located in the 'warm' and 'hot' (> 700 K) components (panel b); (iii) CO 24-23 and 29-28, both tracing the 'hot' component (panel c). All ratios are consistent with the C−type shock models from both KN96 and F+PdF10 for pre-shock densities above n_H=10^4 cm^{-3}. For the CO 16-15/21-20 ratio, a pre-shock density of n_H=10^5 cm^{-3} and shock velocities of 20-30 km s^{-1} best fit the observations. Shock velocities above $\sim$ 25 km s^{-1} are needed to reproduce the observations of the other two ratios at the same pre-shock density. Alternatively, higher pre-shock densities with velocities below 30 km s^{-1} are also possible.

The KN96 C−shock CO line ratios for lower-to-higher−J transitions (panel b of Fig. 4.2) decrease with velocity, due to the increase in peak temperature that allows ex-
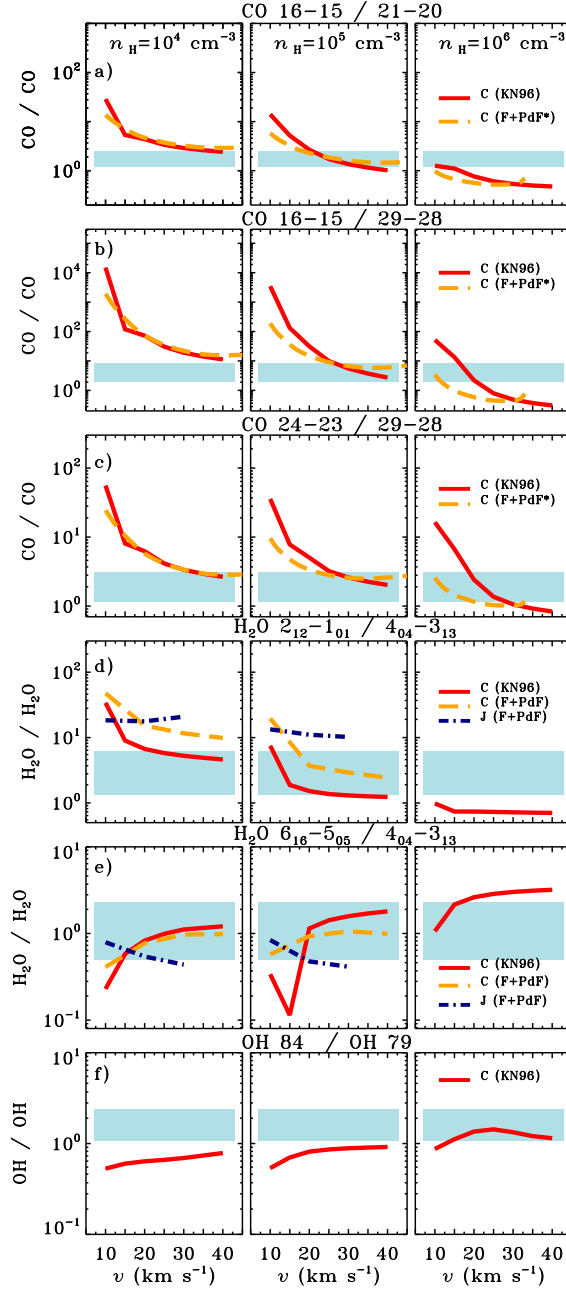
Figure 4.2 – Line ratios of the same species using Kaufman & Neufeld (1996) *C* shock models (KN96, solid line) and Flower & Pineau des Forêts (2010) *C* and *J* shock models (F+PdF, dashed and dashed-dotted lines, respectively). Ratios are shown as a function of shock velocity and for pre-shock densities of 10^4 cm^{-3} (left), 10^5 cm^{-3} (center), and 10^6 cm^{-3} (right). Observed ratios are shown as grey rectangles.

153

citation of the higher-J CO transitions. The effect is strongest at low pre-shock densities (see §4.1.1) and for the sets of transitions with the largest span in J numbers. The CO 16-15 / 29-28 line ratio (ΔJ_{up} = 13) decreases by almost three orders of magnitude between shock velocities of 10 and 40 km s^{-1} over the range of pre-shock densities. In contrast, the CO 16-15 / 21-20 and CO 24-23 / 29-28 line ratios show drops of about one order of magnitude with increasing velocity (panel a and c of Fig. 4.2). These model trends explain why the observed CO line ratios are good diagnostics of shock velocity.

In absolute terms, the line ratios calculated for a given velocity are inversely proportional to the pre-shock density. The largest ratios obtained for $n_H=10^4$ cm^{-3} result from the fact that the higher$-J$ levels are not yet populated at low shock-velocities, while the lower$-J$ transitions reach LTE at high shock-velocities and do not show an increase of flux with velocity. This effect is less prominent at higher pre-shock densities, where the higher$-J$ lines are more easily excited at low shock velocities.

The F+PdF* CO line ratios, extending the Flower & Pineau des Forêts (2003) grid to higher$-J$ CO lines, are almost identical to the KN96 predictions for pre-shock densities $n_H=10^4$ cm^{-3}. For higher densities, the low-velocity $C-$shock models from F+PdF* are systematically lower than the KN96 models, up to almost an order of magnitude for 10–15 km s^{-1} shocks at $n_H=10^6$ cm^{-3}. Therefore, the pre-shock density is less well constrained solely by CO lines.

For densities of 10^5 cm^{-3}, shock velocities of 20-30 km s^{-1} best reproduce the ratios using only transitions from the 'warm' component, while shock velocities above 25 km s^{-1} match the ratios using the transitions from the 'hot' component. Velocities of that order are observed in CO $J = 16 - 15$ HIFI line profiles (Kristensen et al. 2013, in prep.), but higher-J CO lines dominated by the hot component have not been obtained with sufficient velocity resolution.

4.4.2.2 H$_2$O line ratios

Two ratios of observed H$_2$O lines are compared with the $C-$ and $J-$type shock models: (i) the ratio of the low excitation H$_2$O 2_{12}-1_{01} and moderate excitation 4_{04}-3_{13} lines (panel d of Fig. 5) and (ii) the ratio of the highly-excited H$_2$O 6_{16}-5_{05} and 4_{04}-3_{13} lines (panel e). Similar to the CO ratios, $C-$type shocks with pre-shock densities of 10^5 cm^{-3} reproduce the observations well. Based on the observations of ratio (i), C shocks with a somewhat larger (F+PdF10) or smaller (KN96) pre-shock density are also possible for a broad range of shock velocities. On the other hand, no agreement with the $J-$type shocks is found for this low-excitation line ratio. Observations of ratio (ii) indicate a similar density range as ratio (i) for the KN96 models, but extend to 10^4 cm^{-3} for the F+PdF10 models, with agreement found for both $C-$ and $J-$type.

The model trends can be understood as follows. For 10-20 km s^{-1} shocks, increasing temperature in the C shock models from KN96 allows excitation of high-lying H$_2$O lines and causes the H$_2$O 2_{12}-1_{01}/4_{04}-3_{13} line ratio to decrease and the H$_2$O 6_{16}-5_{05}/4_{04}-3_{13} line ratio to increase. At higher shock velocities, the former ratio shows almost no dependence on shock velocity, while a gradual increase is seen in the ratio using two highly-excited lines in the KN96 models. At high pre-shock densities ($n_H=10^6$ cm^{-3}), the upper level

transitions are more easily excited and so the changes are even smaller.

The H_2O 2_{12}-1_{01}/4_{04}-3_{13} line ratios calculated using the $C-$type shock models from F+PdF10 are a factor of a few larger than the corresponding ratios from the KN96 models (see the discussion of absolute line fluxes in Sec. 4.1.2). As a result, when compared to observations, the F+PdF10 models require pre-shock densities of at least n_H=10^5 cm^{-3}, while the KN96 models suggest a factor of few lower densities. Overall, the best fit to both the CO and H_2O line ratios is for pre-shock densities around 10^5 cm^{-3}.

4.4.2.3 OH line ratios

Comparison of the observed OH 84 and 79 μm line ratio with the KN96 $C-$type models (panel f of Fig. 5) indicates an order of magnitude higher pre-shock densities, n_H=10^6 cm^{-3}, with respect to those found using the CO and H_2O ratios. However, the KN96 models do not include any far-infrared radiation, which affects the excitation of the OH lines, in particular the 79 μm (Wampfler et al. 2010, 2013). Additionally, part of OH most likely originates in a $J-$type shock, influencing our comparison (Wampfler et al. 2010, Benedettini et al. 2012, Karska et al. 2013, Kristensen et al. 2013).

Similar to the absolute fluxes of the 84 μm doublet discussed in §4.1.3, not much variation in the ratio is seen with shock velocity. The ratio increases by a factor of about two between the lowest and highest pre-shock densities.

4.4.3 Models and observations - line ratios of different species

Figure 4.3 compares observed line ratios of various H_2O and CO transitions with the C and $J-$type shock models. The line ratios of different species are sensitive both to the molecular excitation and their relative abundances.

4.4.3.1 Ratios of H_2O and CO

Comparison of observations to the KN96 and F+PdF10 models shows that the $C-$type shocks at pre-shock density $n_H = 10^5$ cm^{-3}, which best reproduces the line ratios of same species, fail to reproduce the observed line ratios of different species (Fig. 4.3). There are only a few cases where the observations seem to agree with the models at all. For $n_H = 10^5$ cm^{-3}, a few H_2O/CO line ratios fit at low velocities (< 20 km s^{-1}) (panels a, c and e) but this does not hold for all ratios. Moreover, such low shock velocities have been excluded in the previous section. Higher densities, $n_H = 10^6$ cm^{-3}, are needed to reconcile the observations of the H_2O 2_{12}-1_{01}/CO 29-28 line ratio. Observations of all the other ratios, using more highly-excited H_2O lines, are well below the model predictions.

The patterns seen in the panels in Fig. 4.3 can be understood as follows. The KN96 C type shock models show an initial rise in the H_2O 2_{12}-1_{01} and CO 16-15 line ratios from 10 to 15 km s^{-1} shocks (panel a), as the temperature reaches the 400 K and enables efficient H_2O formation. Beyond this velocity, the line ratios show no variations with velocity. The decrease in this line ratio for higher densities, from 10 at 10^4 cm^{-3} to 0.1 at

155
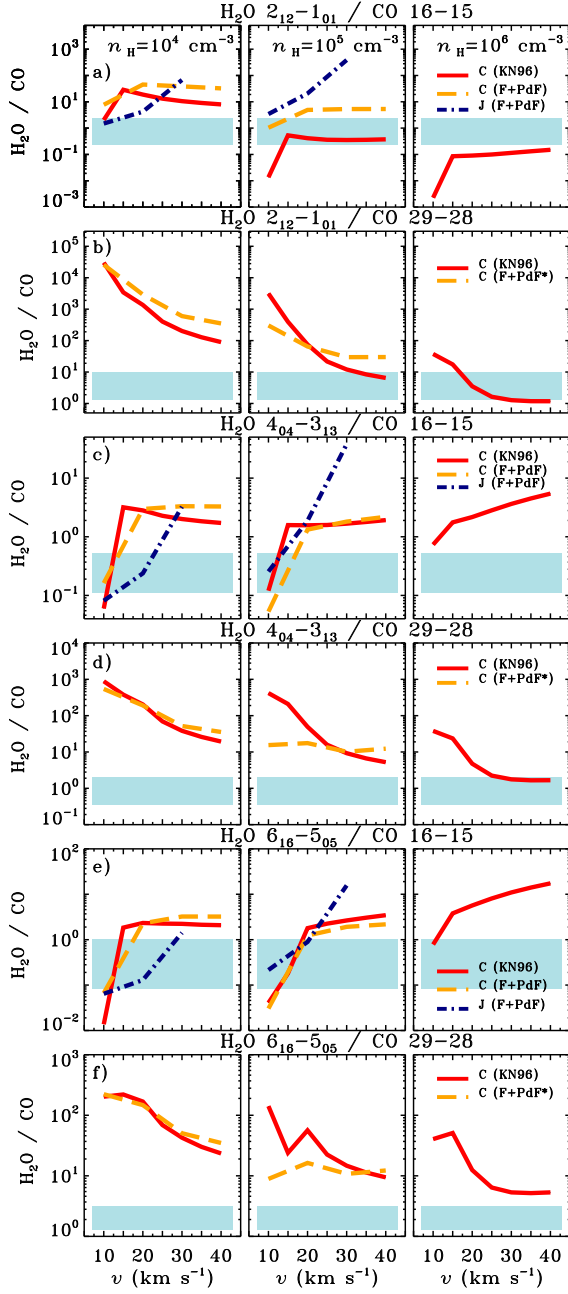
Figure 4.3 – H$_2$O to CO line ratios using Kaufman & Neufeld (1996) *C* shock models (KN96, solid line) and Flower & Pineau des Forêts (2010) *C* and *J* shock models (F+PdF, dashed and dashed-dotted lines, respectively). Ratios are shown as a function of shock velocity and for pre-shock densities of 10^4 cm^{-3} (left), 10^5 cm^{-3} (center), and 10^6 cm^{-3} (right). Observed ratios are shown as grey rectangles.

$n_H = 10^6$ cm^{-3} is due to the larger increase of the column of the population in the $J_u = 16$ level with density compared to the increase in the H_2O 2_{12} level (see Fig. 4.1 above).

Line ratios of H_2O 2_{12}-1_{01} and higher $-J$ CO lines (e.g. 29-28, panel b) show more variation with velocity. A strong decrease by about an order of magnitude and up to two orders of magnitude are seen for the ratios with CO 24-23 and CO 29-28, respectively (the ratio with CO 24-23 is not shown here). These lines, as discussed in §4.1.1 and 4.2.1, are more sensitive than H_2O to the increase in the maximum temperature attained in the shock that scales with shock velocities and therefore their flux is quickly rising for higher velocities (Fig. 4.1). The decrease is steeper for models with low pre-shock densities, since $n_H \sim 10^6$ cm^{-3} allows excitation of high$-J$ CO lines at lower temperatures. At this density, the H_2O/CO line ratios are the lowest and equal about unity.

Due to the lower CO 16-15 fluxes in the C−type shock models from F+PdF10 and similar H_2O 2_{12}-1_{01} fluxes (Fig. 4.1), the H_2O-to-CO ratios are generally larger than in the KN96 models. The exceptions are the ratios with higher$-J$ CO which are more easily excited, especially at low shock velocities, in the hotter C−type shocks from F+PdF*.

For the same reason, the increasing ratios seen in the J shock models are caused by the sharp decrease in CO 16-15 flux for shock velocity $v = 30$ km s^{-1}, rather than the change in the H_2O lines. At such high-velocities for J shocks, a significant amount of CO can be destroyed by reactions with hydrogen atoms (Flower & Pineau des Forêts 2010, Suutarinen et al. 2014). Since the activation barrier for the reaction of H_2O with H is about 10^4 K, the destruction of H_2O does not occur until higher velocities.

Similar trends to the line ratios with H_2O 2_{12}-1_{01} are seen when more highly-excited H_2O lines are used (panels c-f of Fig. 4.3), supporting the interpretations that variations are due to differences in CO rather than H_2O lines.

4.4.3.2   Ratios of CO and H_2O with OH

Fig. 4.4 shows line ratios of CO or H_2O with the most commonly detected OH doublet at 84 μm. The ratios are calculated for three values of pre-shock densities (10^4, 10^5, and 10^6 cm^{-3}) using exclusively the KN96 models, because the F+PdF10 grid does not present OH fluxes.

In general, the observed CO/OH, and H_2O/OH ratios are similar for all sources but much lower than those predicted by the models assuming that a significant fraction of the OH comes from the same shock as CO and H_2O (see Sec. 5.1.). The only exception is the CO 24-23/OH 84 μm ratio where models and observations agree for densities $10^4 - 10^5$ cm^{-3} and shock velocities below 20 km s^{-1}. For any other set of lines discussed here, the observations do not agree with these or any other models.

As discussed in previous sections, the trends with shock velocity are determined mostly by the changes in the CO lines, rather than the OH itself, as seen in Fig. 4.1 (panel d). At shock velocities below 20 km s^{-1} the OH model flux exceeds that of CO due to the abundance effect: not all OH has been transferred to H_2O yet at low temperatures. Due to the lower critical densities of the CO lines ($n_{cr} \sim 10^6 - 10^7$ cm^{-3}) compared with the OH line ($n_{cr} \sim 10^9$ cm^{-3}), the lines for various pre-shock densities often cross and change the order in the upper panels of Fig. 4.4. The corresponding trends in the H_2O/OH
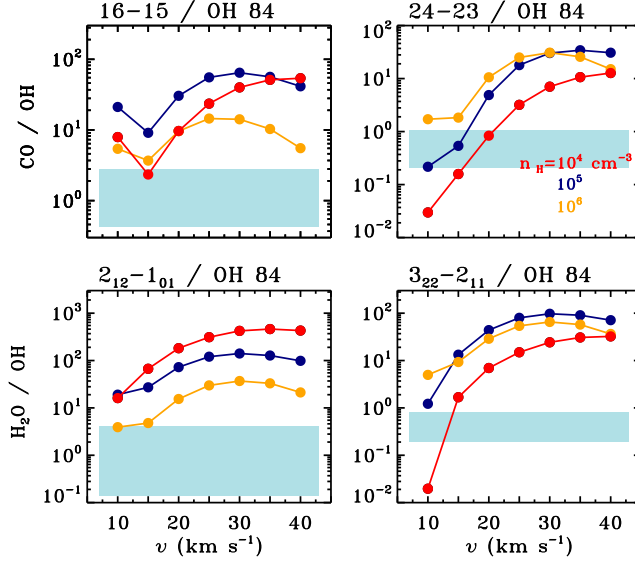
Figure 4.4 – CO to OH and H_2O to OH line ratios as a function of shock velocities using KN96. The range of line ratios from observations is shown as filled rectangles.

line ratios are similar to those of CO/OH, except that the variations with shock velocity are smaller and the critical densities are more similar.

4.5 Discussion

4.5.1 Shock parameters and physical conditions

Spectrally resolved HIFI observations of the CO 10–9 and 16–15 line profiles (Kristensen et al. 2013 and in prep., Yildiz et al. 2013) as well as various H_2O transitions (Kristensen et al. 2012, Mottram et al. in press) reveal at least two different kinematic shock components: non-dissociative C-type shocks in a thin layer along the cavity walls (so-called 'cavity shocks') and J-shocks at the base of the outflow (also called 'spot shocks'), both caused by interaction of the wind with the envelope. Both shocks are different from the much cooler entrained outflow gas that is observed in the low-J CO line profiles (Yıldız et al. 2013).

One possible physical explanation for our observed lack of variation is that although the outflow structure depends on the mass entrainment efficiency and the amount of mass available to entrain (the envelope mass), the wind causing the shocks does not depend on these parameters. Instead the cavity shock caused by the wind impinging on the inner envelope depends on the shock velocity and the density of the inner envelope (Kristensen

et al. 2013, Mottram et al. in press). Thus, the lack of significant variation in the line ratios suggests that the shock velocities by the oblique impact of the wind are always around 20–30 km s^{-1}.

In Section 4 the observed emission was compared primarily to models of $C-$type shock emission. Although $J-$type shocks play a role on small spatial scales in low-mass protostars (Kristensen et al. 2012, 2013, Mottram et al. in press) their contribution to CO emission originating in levels with $J_{up} \lesssim 30$ is typically less than $\sim 50\%$. Since higher$-J$ CO emission is only detected toward 30% of the sources, the $J-$type shock component is ignored for CO. For the case of H$_2$O, spectrally resolved line profiles observed with HIFI reveal that the profiles do not change significantly with excitation up to $E_{up} = 250$ K (Mottram et al. in press); $J-$type shock components typically contribute $< 10\%$ of the emission. It is unclear if the trend of line profiles not changing with excitation continues to higher upper-level energies, in particular all the way up to $E_{up} = 1070$ K ($J = 8_{18}$—7_{07} at 63.32 μm). OH and [O I], on the other hand, almost certainly trace dissociative $J-$type shocks (e.g., van Kempen et al. 2010b, Wampfler et al. 2013) but a full analysis of their emission will be presented in a forthcoming paper. Thus, in the following the focus remains on comparing emission to models of $C-$type shocks.

Figure 4.1 summarizes the different line ratios as a function of pre-shock density discussed in the previous sections. General agreement is found between the observations and models when line ratios of different transitions of *the same species* are used (see top row for H$_2$O, CO, and OH examples), indicating that the excitation of individual species is reproduced well by the models. The H$_2$O line ratios are a sensitive tracer of the pre-shock gas density since they vary less with shock velocity than those of CO. The C shock models from KN96 with pre-shock gas densities in the range of 10^4-10^5 cm^{-3} are a best match to the observed ratios, consistent with values of 10^5 cm^{-3} from the C shock models of F+PdF10. For the considered range of shock velocities, the compression factor in those shocks, defined as the ratio of the post-shock and pre-shock gas densities, varies from about 10 to 30 (Neufeld & Dalgarno 1989, Draine & McKee 1993, Karska et al. 2013). The resulting values of post-shock densities, traced by the observed molecules, are therefore expected to be 10^5-10^6 cm^{-3}.

The CO line ratios, on the other hand, are not only sensitive to density, but also to the shock velocities, due to their connection to the peak temperature attained in the shock. In the pre-shock density range of 10^4-10^5 cm^{-3}, indicated by the H$_2$O line ratios, shocks with velocities above 20 km s^{-1} best agree with the CO observations. Within this range of densities, the predictions from both the KN96 and F+PdF10 C shock models show a very good agreement with each other.

The ratio of two OH lines from the KN96 models compared with the observations suggest higher pre-shock densities above 10^5 cm^{-3}, but this ratio may be affected by infrared pumping (Wampfler et al. 2013). Also, some OH emission traces (dissociative) $J-$shocks, based on its spatial connection and flux correlations to [O I] emission (Wampfler et al. 2010, 2013, Karska et al. 2013). The single spectrally-resolved OH spectrum towards Ser SMM1 (Fig. 3, Kristensen et al. 2013) suggests that the contribution of the dissociative and non-dissociative shocks is comparable. Thus, observed CO/OH and H$_2$O/OH line ratios are only affected at the factor ~ 2 level and the discrepancy in the bottom row of
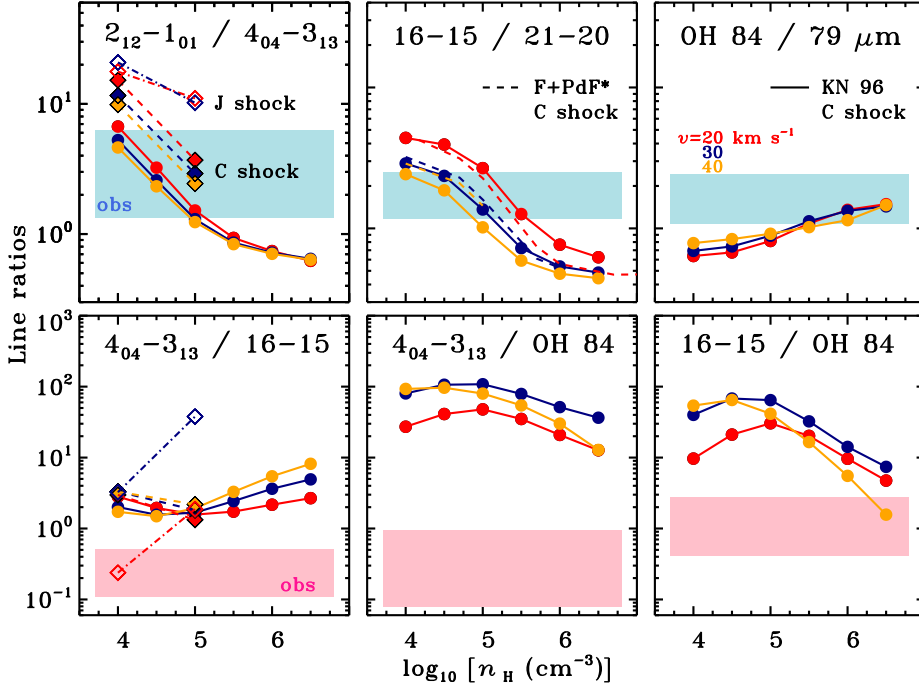
Figure 4.1 – Ratios of line fluxes in units of erg cm^{-2} s^{-1} as a function of logarithm of density of the pre-shock gas, n_H. Ratios of different transitions of the same molecules are shown at the top row and line ratios comparing different species are shown at the bottom. Filled symbols and full lines show models of C shocks (circles – from Kaufman & Neufeld, diamonds – from Flower & Pineau des Forêts), whereas the empty symbols and dash-dotted lines show models of J shocks (Flower & Pineau des Forêts 2010). Colors distinguish shock velocities – 20 km s^{-1} shocks are shown in red, 30 km s^{-1} in blue, and 40 km s^{-1} in orange.

Fig. 4.1 remains.

Overall, the observed CO and H$_2$O line ratios are best fit with C−shock models with pre-shock densities of ∼10^5 cm^{-3} and velocities ≳20 km s^{-1}, with higher velocities needed for the excitation of the highest−J CO lines.

The shock conditions inferred here can be compared to the temperatures and densities found from single-point non-LTE excitation and radiative-transfer models, e.g., RADEX (van der Tak et al. 2007) and from non-LTE radiative transfer analysis of line intensity ratios (Kristensen et al. 2013, Mottram et al., in prep.) toward various sources. Typically, densities ≳ 10^6 cm^{-3} and temperatures of ∼ 300 K and ≳ 700 K are required to account for the line emission (Herczeg et al. 2012, Goicoechea et al. 2012, Santangelo et al. 2012, Vasta et al. 2012, Karska et al. 2013, Santangelo et al. 2013). Within this range of densities, the predictions from both the KN96 and F+PdF10 C−shock models reproduce CO observations. However, the disconnect between predicted pre-shock conditions required

to reproduce H_2O and CO is puzzling (see below).

A small number of individual sources have been compared directly to shock models (Lee et al. 2013, Dionatos et al. 2013) and the conclusions are similar to what is reported here: pre-shock conditions of typically 10^4-10^5 cm^{-3}, and emission originating in C−type shocks. None of the sources analyzed previously were therefore special or atypical, rather these shock conditions appear to exist toward every embedded protostar.

At shock positions away from the protostar, dissociative or non-dissociative J−type shocks at the same pre-shock densities are typically invoked to explain the FIR line emission (Benedettini et al. 2012, Santangelo et al. 2012, Busquet et al. 2014). Differences between the protostar position and the distant shock positions are revealed primarily by our line ratios using the low-excitation H_2O 2_{12}-1_{01} (Table 3) and can be ascribed to the differences in the filling factors and column densities between the immediate surrounding of the protostar and the more distant shock positions (Mottram et al. in press).

4.5.2 Abundances and need for UV radiation

In contrast with the ratios of two H_2O or CO lines, the ratios calculated using *different* species do not agree with the shock models (Figure 4.1, bottom row). The ratios of H_2O-to-CO lines are overproduced by the C shock models from both the KN96 and F+PdF10 grids by at least an order of magnitude, irrespective of the assumed shock velocity. Although there are a few exceptions (e.g. the ratio of H_2O 2_{12}-1_{01} and CO 16-15), the majority of the investigated sets of H_2O and CO lines follow the same trend. Observations agree only with slow, <20 km s^{-1}, J shock models, but as shown above, those models do not seem to reproduce the excitation properly (Fig. 4.2).

The discrepancy between the models and observations is even larger in the case of the H_2O-to-OH line ratios, as illustrated in Fig. 4.1. The two orders of magnitude disagreement with the C shock models cannot be accounted by any excitation effects for any realistic shock parameters. Additional comparison to J shock models is not possible due to a lack of OH predictions for J shocks in the F+PdF10 models.

The CO-to-OH ratios are overproduced by about an order of magnitude in the C shock models, similar to the H_2O-to-CO ratios. The agreement improves for fast ($v = 40$ km s^{-1}) shocks in high density pre-shock medium ($\sim 10^{6.5}$ cm^{-3}), but those parameters are not consistent with the line ratios from the same species.

An additional test of the disagreement between models and observations is provided by calculating the fraction of each species with regard to the sum of CO, H_2O and OH emission. For that purpose, only the strongest lines observed in our program are used. As seen in Table 4.1, the observed percentage (median) of H_2O is about 30 % and OH is about 25 %. In contrast, KN96 models predict typically 70-90 % of flux in the chosen H_2O lines and only up to 2% in the OH lines.

The only possible way to reconcile the models with the observations, after concluding that the excitation is treated properly in the models, is to reconsider the assumed abundances. The fact that the H_2O-to-CO and CO-to-OH ratios are simultaneously overestimated suggests a problem with the abundances of H_2O and OH, rather than that of CO. The scenario with the overestimated H_2O abundances and underestimated OH abundances

161

Table 4.1 – Fraction of H_2O and OH emission with respect to total far-IR molecular emission

$\log n_H(cm^{-3})$	Obs. (%)	KN96 models (%)		
		v (km s^{-1}):		
		20	30	40
	H_2O / (CO+H_2O+OH)			
4	29	95.5	92.6	90.0
4.5	29	91.6	86.3	82.8
5	29	84.6	78.2	75.3
5.5	29	77.3	71.2	70.4
6	29	71.3	68.5	70.7
6.5	29	68.3	69.6	73.3
	OH / (CO+H_2O+OH)			
4	25	0.7	0.3	0.2
4.5	25	0.7	0.3	0.3
5	25	0.7	0.3	0.4
5.5	25	0.9	0.4	0.6
6	25	1.3	0.5	1.1
6.5	25	1.9	0.8	2.4

Notes. In this analysis, the following lines are used: H_2O lines at 179.5 μm, 125.4 μm, 108.1 μm, and 90.0 μm; CO lines at 162.8 μm, 124.2 μm, 108.7 μm, and 90.2 μm; OH lines at 79 μm and 84 μm. Median values of the fractions calculated from 18 sources with line detections are adopted in case of observations (column Obs.).

would translate into a too large H_2O-to-OH abundance ratio in the models. A possible and likely solution is photodissocation of H_2O to OH and subsequently to atomic oxygen. As noted above, some OH also comes from the dissociative shock seen in [O I].

A significant shortcoming of all these shock models lies in their inability to account for grain-grain interactions, which has been shown to significantly alter the structure of the shocks propagating in dense media ($n_H > 10^5$ cm^{-3}, Guillet et al. 2007, 2009, 2011). These grain-grain interactions mostly consist of coagulation, vaporization, and shattering effects affecting the grains. Their inclusion in shock models necessitates a sophisticated treatment of the grains, especially following their charge and size distribution (Guillet et al. 2007). Most remarkably, such interactions eventually result in the creation of small grain fragments in large numbers, which increases the total dust grain surface area and thereby changes the coupling between the neutral and the charged fluids within the shock layer. The net effect is that the shock layer is significantly hotter and thinner (Guillet et al. 2011), which in turn affects the chemistry and emission of molecules (Guillet et al. 2009).

Unfortunately, at the moment these models are computationally expensive and are not well-suited for a grid analysis; moreover, the solutions found by Guillet et al. do not converge for preshock densities of 10^6 cm^{-3} or higher. A recent study by Anderl et al. (2013) shows that it is possible to approximate these effects in a computationally efficient way, and subsequently evaluated the line intensities of CO, OH and H_2O on a small grid of models. When including grain-grain interactions, CO lines were found

to be significantly less emitting than in 'simpler' models, while a smaller decrease was found for H_2O lines, and a small increase for OH. These trends probably still need to be systematically investigated on larger grids of models before they can be applied to our present comparison efforts.

Regardless of the effect of grain-grain interactions, Snell et al. (2005) invoked several scenarios to reconcile high absolute H_2O fluxes with the shock models for the case of supernova remnants. These include (i) the high ratio of atomic to molecular hydrogen, which drives H_2O back to OH and O, (ii) freeze-out of H_2O in the post-shock gas, (iii) freeze-out of H_2O in the pre-shock gas, and (iv) photodissociation of H_2O in the pre- and post-shock gas. Due to the high activation barrier of the $H_2O + H \rightarrow OH + H_2$ reaction ($\sim 10^4$ K), the first scenario is not viable. The freeze-out in the post-shock gas (ii) is not effective in the low density regions considered in Snell et al. (2005), but can play a role in the vicinity of protostars, where densities above $\sim 10^6$ cm^{-3} are found (e.g. Kristensen et al. 2012, this work). However, this mechanism alone would not explain the bright OH and high$-J$ H_2O lines seen toward many deeply-embedded sources (e.g. Karska et al. 2013, Wampfler et al. 2013). A similar problem is related to the freeze-out in the pre-shock gas (iii), which decreases the amount of e.g. O, OH, and H_2O in the gas phase for shock velocities below 15 km s^{-1}.

Therefore, the most likely reason for the overproduction of H_2O in the current generation of shock models, at the expense of OH, is the omission of the effects of ultraviolet irradiation (scenario iv) of the shocked material. The presence of UV radiation is directly seen in Ly-α emission both in the outflow-envelope shocks (Curiel et al. 1995, Walter et al. 2003) and at the protostar position (Valenti et al. 2000, Yang et al. 2012). Additionally, UV radiation on scales of a few 1000 AU has been inferred from the narrow profiles of ^{13}CO 6-5 observed from the ground toward a few low-mass protostars (Spaans et al. 1995, van Kempen et al. 2009a, Yıldız et al. 2012). H_2O can be photodissociated into OH over a broad range of far-UV wavelengths, including by Ly-α, and this would provide an explanation for the disagreement between our observations and the models. Photodissociation of CO is less likely, given the fact that it cannot be dissociated by Ly-α and only by very hard UV photons with wavelengths < 1000 Å. The lack of CO photodissociation is consistent with weak [C I] and [C II] emission observed toward low-mass YSOs (Yıldız et al. 2012, Goicoechea et al. 2012, Karska et al. 2013). At the positions away from the protostars, on the other hand, the bow-shocks at the tip of the protostellar jets can produce significant emission in the [C I] (van Kempen et al. 2009a). Therefore, it is unlikely that lower line excitation at those positions is due to the weaker UV. The differences seen in the resolved line profiles (e.g. Santangelo et al. 2012, Vasta et al. 2012, Mottram et al. in prep.) indicate that the lower column densities involved are the more likely reason for differences in the excitation.

Visser et al. (2012) proposed a scenario in which the lower-lying CO transitions observed with PACS ($14 < J_u < 23$) originate in UV–heated gas and higher$-J$ transitions ($J_u > 24$) in shocked material. All water emission would be associated with the same shocks as responsible for the higher-J CO emission with less than 1% of the water emission coming from the PDR layer. Although not modeled explicitly, the UV irradiation from the star-disk boundary impinging on the shocks naturally accounts for the lower

H_2O abundance. The authors predict that while the dynamics of the hot layers where both shocks and UV irradiation play a role will be dominated by the shocks, only the UV photons penetrate further into the envelope, where the dynamics would resemble the quiescent envelope. The lower-temperature UV-heated gas has indeed been observed to be quiescent on the spatial scales of the outflow cavity through observations of medium-J ^{13}CO lines (Yıldız et al. 2012, subm.).

Flower & Pineau des Forêts (2013) proposed a model where all emission originates in a non-stationary shock wave, where a J−type shock is embedded in a C−type shock. Without a detailed modeling of individual sources based on different source parameters it is not possible to rule out any of these solutions. However, the trends reported here suggest that it is possible to find a pure shock solution, in agreement with Flower & Pineau des Forêts (2013), as long as UV photons are incorporated to provide dissociation of H_2O. Complementary observations, preferably at higher angular resolution, are required to break the solution degeneracy and determine the relative role the shocks and UV photons play on the spatial scales of the thickness of the cavity wall. Models whose results depend sensitively on a single parameter such as time, are ruled out by the fact that the observed line ratios are so similar across sources.

4.6   Conclusions

We have compared the line ratios of the main molecular cooling lines detected in 22 low-mass protostars using *Herschel*/PACS with publicly available one-dimensional shock models. Our conclusions are the following:

- Line ratios of various species and transitions are remarkably similar for all observed sources. No correlation is found with source physical parameters.

- Line ratios observed toward the protostellar position are consistent with the values reported for the positions away from the protostar, except for some ratios involving the low-excitation H_2O 2_{12}-1_{01} line. Coupled with the larger absolute fluxes of highly-excited H_2O and CO lines at the protostellar positions, this indicates that lines at distant off-source shock positions are less excited.

- General agreement is found between the observed line ratios of the same species (H_2O, CO, and OH) and the C shock models from Kaufman & Neufeld (1996) and Flower & Pineau des Forêts (2010). Ratios of H_2O are particularly good tracers of the density of the ambient material and indicate pre-shock densities of order 10^5 cm^{-3} and thus post-shock densities of order 10^6 cm^{-3}. Ratios of CO lines are more sensitive to the shock velocities and, for the derived range of pre-shock densities, indicate shock velocities above 20 km s^{-1}.

- Ratios of CO lines located in the 'warm' component of CO ladders (with $T_{rot} \sim 300$ K) are reproduced with shock velocities of 20-30 km s^{-1} and pre-shock densities of 10^5 cm^{-3}. The CO ratios using the lines from the 'hot' component ($T_{rot} \gtrsim 700$ K) are better reproduced by models with shock velocities above 25 km s^{-1}.

- A lack of agreement is found between models and the observed line ratios of different species. The H_2O-to-CO, H_2O-to-OH, and CO-to-OH line ratios are all overproduced by the models by 1-2 orders of magnitude for the majority of the considered sets of transitions.

- Since the observed molecular excitation is properly reproduced in the C shock models, the most likely reason for disagreement with observations is the abundances in the shock models, which are too high in case of H_2O and too low in case of OH. Invoking UV irradiation of the shocked material, together with a dissociative J shock contribution to OH and [O I], would lower the H_2O abundance and reconcile the models and observations.

New UV-irradiated shock models will allow us to constrain the UV field needed to reconcile the shock models with observations (M. Kaufman, priv. comm.) Those models should also account for the grain-grain processing, which affects significantly the shocks structure at densities $\sim 10^6$ cm^{-3} (Guillet et al. 2011). The effects of shock irradiation as a function of the distance from a protostar will help to understand the differences in the observed spectrally-resolved lines from HIFI at 'on source' and distant shock-spot positions.

Acknowledgements

Appendix

4.A Supplementary material

Table 4.A.1 provides molecular / atomic information about the lines observed in the WILL program.

Table 4.A.2 shows the observing log of PACS observations including observations identifications (OBSID), observation day (OD), date of observation, total integration time, and pointed coordinates (RA, DEC).

Table 4.A.3 informs about which lines are detected toward the Perseus sources. The full list of line fluxes for all WILL sources including Perseus will be tabulated in the forthcoming paper (Karska et al. in prep.).

Figures 4.A.1 and 4.A.2 show line and continuum maps around 179.5 μm for all the Perseus sources in the WILL program.

Figure 4.A.3 show maps in the H_2O 4_{23}-3_{12} line at 78.74 μm, OH 84.6 μm, and CO 29-28 at 90.16 μm for Per1, Per5, Per9, and Per20, all of which show bright line emission and centrally peaked continuum. The lines are chosen to be located close in the wavelength so that the variations in the PSF does not introduce significant changes in the emission extent.

Table 4.A.4 summarizes observed and modeled line ratios used in the Analysis section.

Table 4.A.1 – Atomic and molecular data[a] for lines observed in the WILL program

Species	Transition	Wave (μm)	Freq.[b] (GHz)	E_u/k_B (K)	A_{ul}[c] (s^{-1})
H_2O	2_{21}-2_{12}	180.488	1661.0	194.1	3.1(-2)
H_2O	2_{12}-1_{01}	179.527	1669.9	114.4	5.6(-2)
OH	$3/2,1/2$-$1/2,1/2$	163.398	1834.7	269.8	2.1(-2)
OH	$3/2,1/2$-$1/2,1/2$	163.131	1837.7	270.1	2.1(-2)
CO	16-15	162.812	1841.3	751.7	4.1(-4)
[C II]	$^2P_{3/2} - ^2P_{1/2}$	157.74	2060.0	326.6	1.8(-5)
H_2O	4_{04}-3_{13}	125.354	2391.6	319.5	1.7(-1)
CO	21-20	124.193	2413.9	1276.1	8.8(-4)
CO	24-23	108.763	2756.4	1656.5	1.3(-3)
H_2O	2_{21}-1_{10}	108.073	2774.0	194.1	2.6(-1)
CO	29-28	90.163	3325.0	2399.8	2.1(-3)
H_2O	3_{22}-2_{11}	89.988	3331.5	296.8	3.5(-1)
H_2O	7_{16}-7_{07}	84.767	3536.7	1013.2	2.1(-1)
OH	$7/2,3/2$-$5/2,3/2$	84.596	3543.8	290.5	4.9(-1)
OH	$7/2,3/2$-$5/2,3/2$	84.420	3551.2	291.2	2.5(-2)
CO	31-30	84.411	3551.6	2735.3	2.5(-3)
H_2O	6_{16}-5_{05}	82.032	3654.6	643.5	7.5(-1)
CO	32-31	81.806	3664.7	2911.2	2.7(-3)
CO	33-32	79.360	3777.6	3092.5	3.0(-3)
OH	$1/2,1/2$-$3/2,3/2$	79.182	3786.1	181.7	2.9(-2)
OH	$1/2,1/2$-$3/2,3/2$	79.116	3789.3	181.9	5.8(-3)
H_2O	6_{15}-5_{24}	78.928	3798.3	781.1	4.6(-1)
H_2O	4_{23}-3_{12}	78.742	3807.3	432.2	4.9(-1)
H_2O	8_{18}-7_{07}	63.324	4734.3	1070.7	1.8
[O I]	$^3P_1 - ^3P_2$	63.184	4744.8	227.7	8.9(-5)

Notes. [a] Compiled using the CDMS (Müller et al. 2001, 2005) and JPL (Pickett et al. 1998) databases. [b] Frequencies are rest frequencies. [c] $A(B) \equiv A \times 10^B$

Table 4.A.2 – Log of PACS observations

Source	OBSID	OD	Date	Total time (s)	RA (h m s)	DEC (o ′ ″)
Per01	1342263508	1370	2013-02-12	851	3 25 22.32	+30 45 13.9
	1342263509	1370	2013-02-12	1986	3 25 22.32	+30 45 13.9
Per02	1342263506	1370	2013-02-12	851	3 25 36.49	+30 45 22.2
	1342263507	1370	2013-02-12	1986	3 25 36.49	+30 45 22.2
Per03	1342263510	1370	2013-02-12	851	3 25 39.12	+30 43 58.2
	1342263511	1370	2013-02-12	1986	3 25 39.12	+30 43 58.2
Per04	1342264250	1383	2013-02-25	851	3 26 37.47	+30 15 28.1
	1342264251	1383	2013-02-25	1986	3 26 37.47	+30 15 28.1
Per05	1342264248	1383	2013-02-25	851	3 28 37.09	+31 13 30.8
	1342264249	1383	2013-02-25	1986	3 28 37.09	+31 13 30.8
Per06	1342264247	1383	2013-02-25	1986	3 28 57.36	+31 14 15.9
	1342264246	1383	2013-02-25	851	3 28 57.36	+31 14 15.9
Per07	1342264244	1383	2013-02-25	1986	3 29 00.55	+31 12 00.8
	1342264245	1383	2013-02-25	851	3 29 00.55	+31 12 00.8
Per08	1342264242	1383	2013-02-25	1986	3 29 01.56	+31 20 20.6
	1342264243	1383	2013-02-25	851	3 29 01.56	+31 20 20.6
Per09	1342267611	1401	2013-03-15	1986	3 29 07.78	+31 21 57.3
	1342267612	1401	2013-03-15	851	3 29 07.78	+31 21 57.3
Per10	1342267615	1401	2013-03-15	1986	3 29 10.68	+31 18 20.6
	1342267616	1401	2013-03-15	851	3 29 10.68	+31 18 20.6
Per11	1342267607	1401	2013-03-15	1986	3 29 12.06	+31 13 01.7
	1342267608	1401	2013-03-15	851	3 29 12.06	+31 13 01.7
Per12	1342267609	1401	2013-03-15	1986	3 29 13.54	+31 13 58.2
	1342267610	1401	2013-03-15	851	3 29 13.54	+31 13 58.2
Per13	1342267613	1401	2013-03-15	1986	3 29 51.82	+31 39 06.0
	1342267614	1401	2013-03-15	851	3 29 51.82	+31 39 06.0
Per14	1342263512	1370	2013-02-12	1986	3 30 15.14	+30 23 49.4
	1342263513	1370	2013-02-12	851	3 30 15.14	+30 23 49.4
Per15	1342263514	1370	2013-02-12	1986	3 31 20.98	+30 45 30.1
	1342263515	1370	2013-02-12	851	3 31 20.98	+30 45 30.1
Per16	1342265447	1374	2013-02-16	1986	3 32 17.96	+30 49 47.5
	1342265448	1374	2013-02-16	851	3 32 17.96	+30 49 47.5
Per17	1342263486	1369	2013-02-11	1986	3 33 14.38	+31 07 10.9
	1342263487	1369	2013-02-11	851	3 33 14.38	+31 07 10.9
Per18	1342265449	1374	2013-02-16	1986	3 33 16.44	+31 06 52.5
	1342265450	1374	2013-02-16	851	3 33 16.44	+31 06 52.5
Per19	1342265451	1374	2013-02-16	1986	3 33 27.29	+31 07 10.2
	1342265452	1374	2013-02-16	851	3 33 27.29	+31 07 10.2
Per20	1342265453	1374	2013-02-16	1986	3 43 56.52	+32 00 52.8
	1342265454	1374	2013-02-16	851	3 43 56.52	+32 00 52.8
Per21	1342265455	1374	2013-02-16	1986	3 43 56.84	+32 03 04.7
	1342265456	1374	2013-02-16	851	3 43 56.84	+32 03 04.7
Per22	1342265701	1381	2013-02-23	1986	3 44 43.96	+32 01 36.2
	1342265702	1381	2013-02-23	851	3 44 43.96	+32 01 36.2

169

Table 4.A.3 – Line detections toward our Perseus sources

Wave (μm)	Species	Per 1	2	3	4	5	6	7	8	9	10	11	12	13	14	15	16	17	18	19	20	21	22
63.184	[O I]	✓	✓	✓	✓	✓	✓	✓	✓	✓	✓	✓	✓	–	✓	✓	✓	✓	✓	✓	✓	✓	✓
63.324	H_2O	✓	✓	✓	–	–	✓	–	✓	✓	–	✓	–	–	✓	–	–	–	–	–	–	–	–
63.458	H_2O	–	–	✓	–	–	–	–	✓	✓	–	✓	–	–	–	–	–	–	–	–	–	–	–
78.742	H_2O	✓	✓	✓	–	✓	✓	–	✓	✓	–	✓	–	–	✓	–	–	–	–	–	✓	✓	✓
78.928	H_2O	✓	✓	✓	–	✓	–	–	–	✓	–	✓	–	–	–	–	–	–	–	–	–	–	–
79.120	OH	✓	✓	✓	–	✓	✓	–	✓	✓	✓	✓	–	–	✓	–	–	–	–	✓	✓	✓	✓
79.180	OH	✓	✓	✓	–	✓	✓	–	✓	✓	✓	✓	–	–	✓	–	–	–	–	✓	✓	✓	✓
79.360	CO	✓	✓	✓	–	✓	–	–	–	✓	–	✓	–	–	✓	–	–	–	–	–	–	–	–
81.806	CO	✓	✓	✓	–	–	✓	–	✓	✓	–	✓	–	–	✓	–	–	–	–	–	–	–	–
82.032	H_2O	✓	✓	✓	–	✓	✓	–	✓	✓	–	✓	–	–	✓	✓	–	–	–	✓	–	✓	✓
84.411	OH+CO	✓	✓	✓	–	✓	✓	–	✓	✓	✓	✓	–	–	✓	✓	–	–	–	✓	✓	✓	✓
84.600	OH	✓	✓	✓	–	✓	✓	–	✓	✓	✓	✓	–	–	✓	✓	–	–	–	✓	✓	✓	✓
84.767	H_2O	–	–	✓	–	–	–	–	–	–	–	–	–	–	–	–	–	–	–	–	–	–	–
89.988	H_2O	✓	✓	✓	–	✓	–	–	✓	✓	–	✓	–	–	✓	–	–	–	–	–	–	✓	–
90.163	CO	✓	✓	✓	–	✓	–	–	✓	✓	✓	✓	–	–	✓	–	–	–	–	–	–	✓	–
108.073	H_2O	✓	✓	✓	–	✓	✓	–	✓	✓	✓	✓	–	✓	✓	✓	–	–	✓	✓	✓	✓	✓
108.763	CO	✓	✓	✓	–	✓	✓	–	✓	✓	✓	✓	–	–	✓	✓	–	–	✓	✓	✓	✓	✓
124.193	CO	✓	✓	✓	–	✓	✓	–	✓	✓	✓	✓	–	–	✓	✓	✓	–	✓	✓	✓	✓	✓
125.354	H_2O	✓	✓	✓	–	✓	✓	–	✓	✓	✓	✓	–	✓	✓	✓	–	–	–	✓	✓	✓	✓
162.812	CO	✓	✓	✓	–	✓	✓	–	✓	✓	✓	✓	–	–	✓	✓	✓	–	✓	✓	✓	✓	✓
163.120	OH	✓	✓	✓	–	–	✓	–	✓	✓	✓	✓	–	–	✓	–	–	–	✓	✓	✓	–	✓
163.400	OH	✓	✓	✓	–	–	✓	–	✓	✓	✓	✓	–	–	✓	✓	–	–	✓	✓	✓	✓	–
179.527	H_2O	✓	✓	✓	–	✓	✓	–	✓	✓	✓	✓	–	–	✓	✓	–	–	✓	✓	✓	✓	✓
180.488	H_2O	✓	✓	✓	–	✓	–	–	–	✓	–	✓	–	–	✓	–	–	–	✓	✓	✓	✓	✓
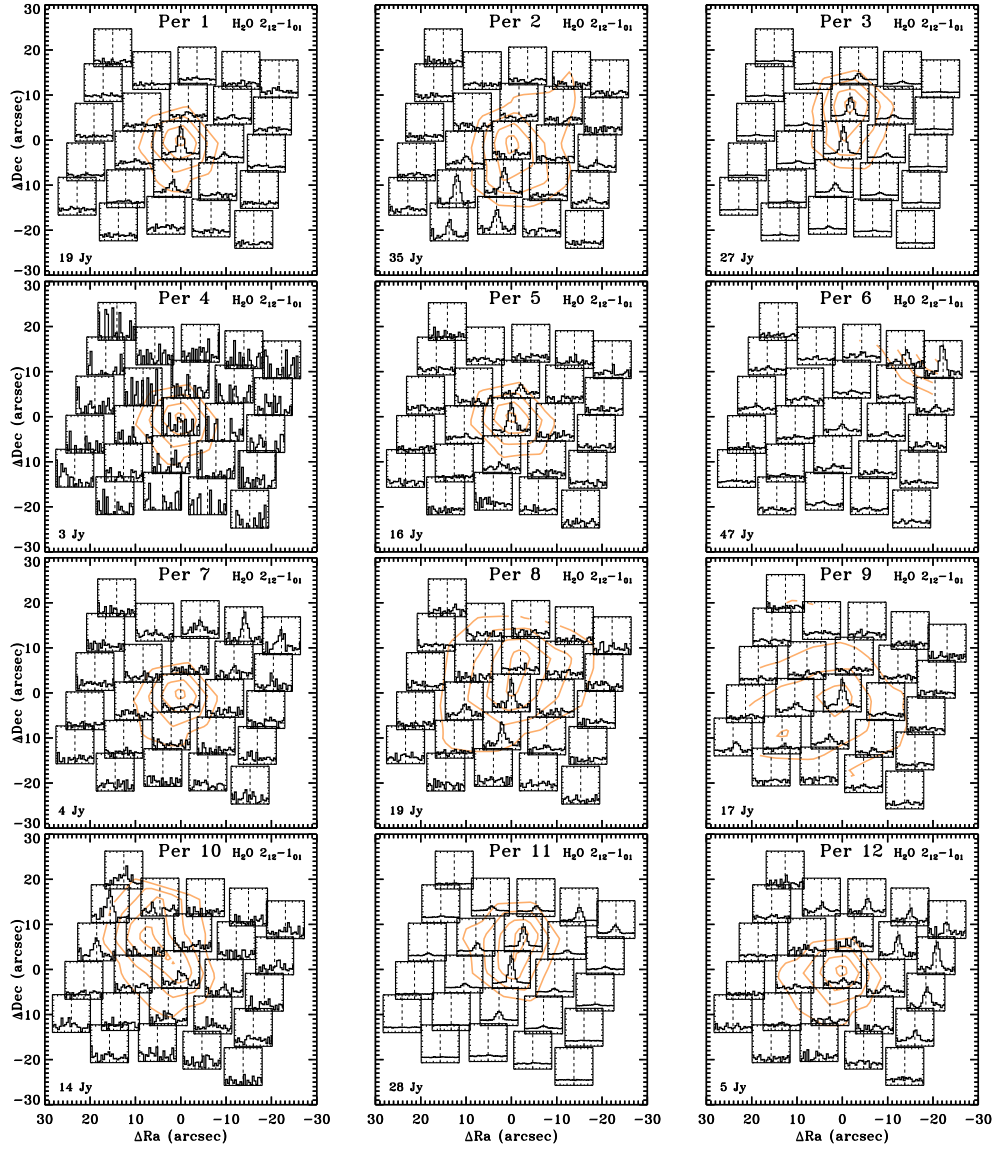
Figure 4.A.1 – PACS spectral maps in the H_2O 2_{12}-1_{01} line at 179.527 μm. Wavelengths in microns are translated to the velocity scale on the X-axis using laboratory wavelengths of the species and cover the range from -600 to 600 km s^{-1}. The Y-axis shows fluxes normalized to the spaxel with the brightest line on the map in a range -0.2 to 1.2. The orange contours show continuum emission at 30%, 50%, 70%, and 90% of the peak value written in the bottom left corner of each map.
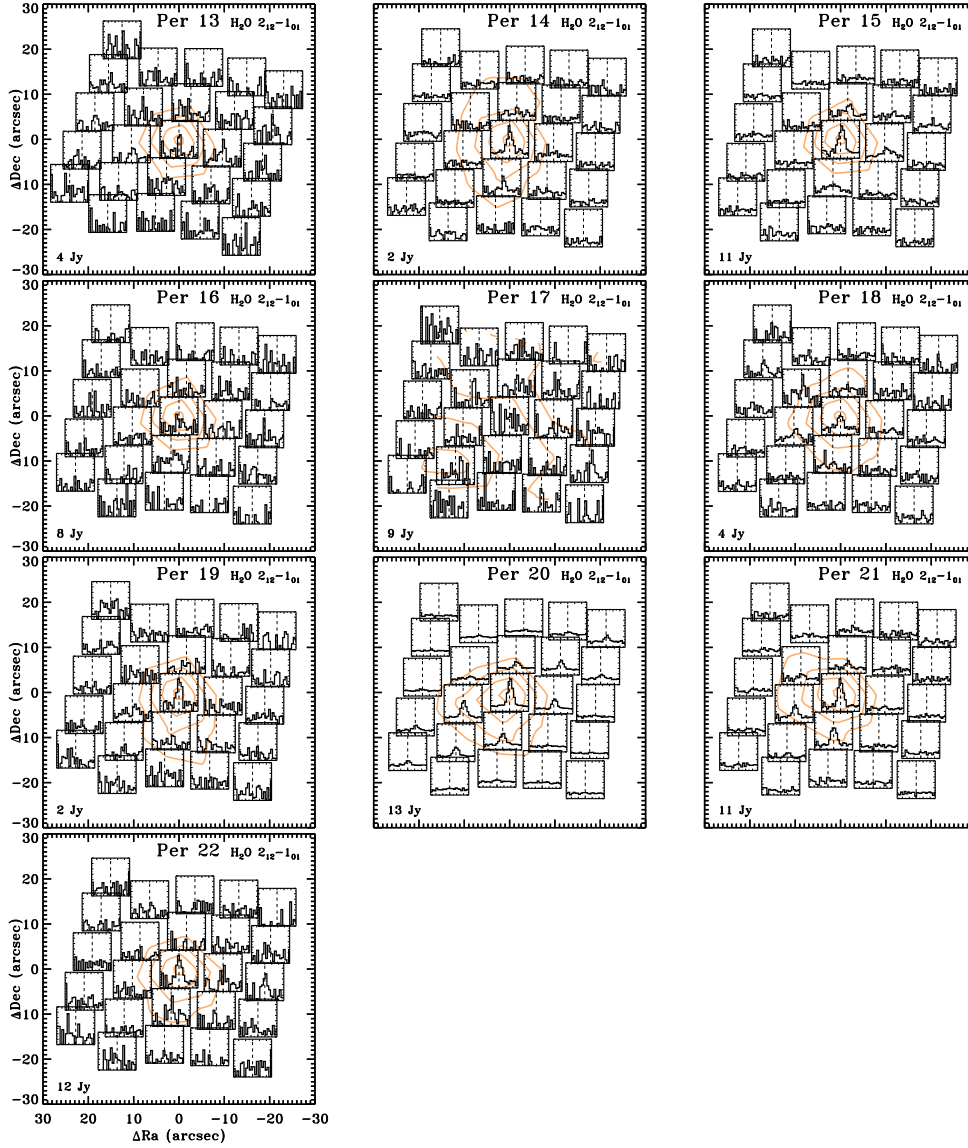
Figure 4.A.2 – The same as Fig. 4.A.1 but for the remaining sources.
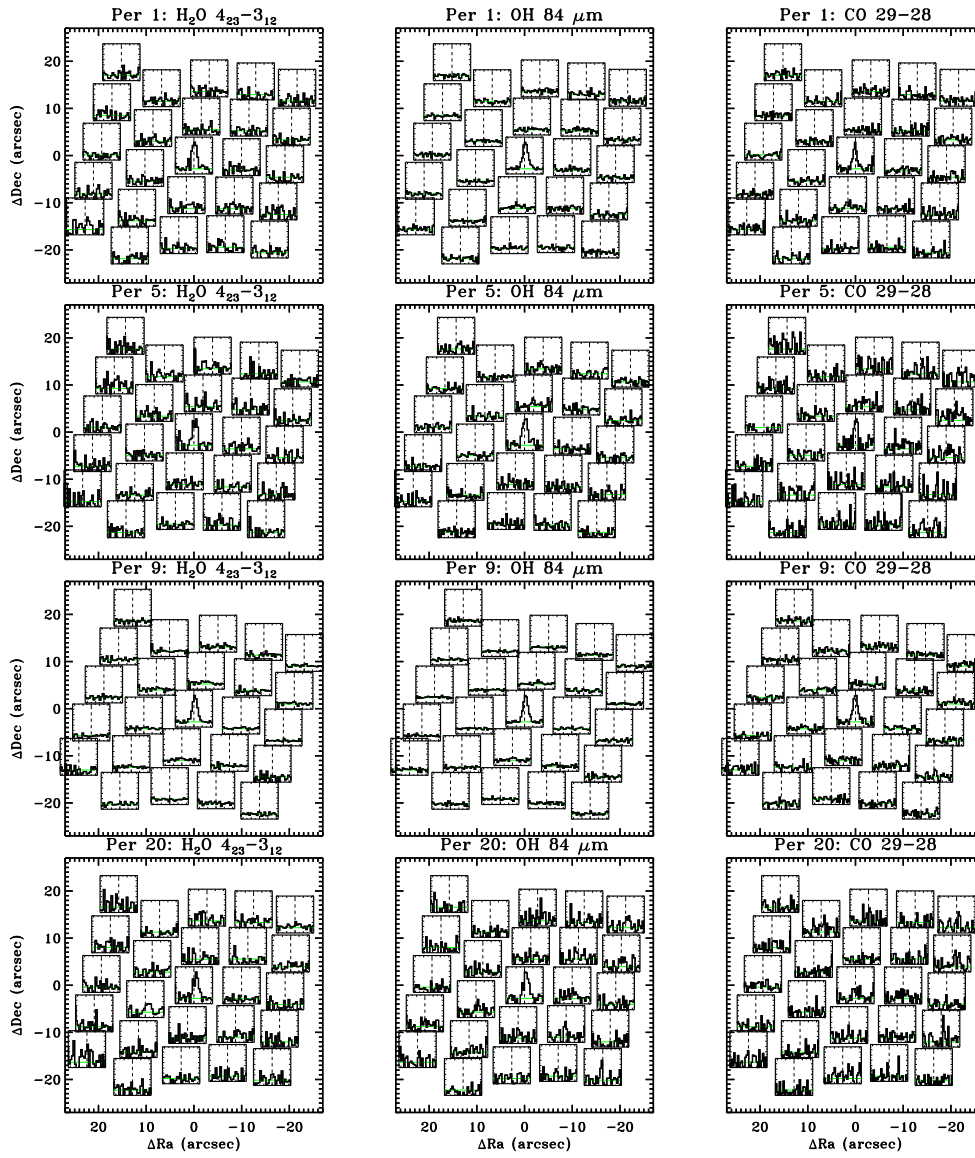
Figure 4.A.3 – PACS spectral maps in the H_2O 4_{23}-3_{12} line at 78.74 μm, the OH line at 84.6 μm, and the CO 29-28 line at 90.16 μm for a few sources with bright line emission and centrally peaked continuum. The x-axis range covers -450 to 450 km s^{-1} and the y-axis range covers -0.2 to 1.2, with line emission normalized to the emission in the brightest spaxel.

Table 4.A.4 – Observed and model line ratios based on Kaufman & Neufeld (1996)

Line 1	Line 2	Observed line ratios Line 1 / Line 2					Models - C shock (KN96) $\log n_H=4$			$\log n_H=5$			$\log n_H=6$		
		N	Min	Max	Mean	Std	v=20	30	40	20	30	40	20	30	40
CO 16-15	21-20	17	1.2	2.5	1.7	0.4	4.4	2.9	2.4	2.7	1.4	1.0	0.8	0.5	0.5
CO 16-15	24-23	16	1.2	4.6	2.3	0.9	11.6	5.7	4.2	6.2	2.1	1.3	0.9	0.5	0.4
CO 16-15	29-28	10	1.9	8.3	3.8	1.8	72.2	31.4	2.2	19.1	5.5	0.5	11.3	2.7	0.3
CO 21-20	29-28	10	1.4	4.1	2.2	0.8	16.5	11.7	2.9	6.6	4.1	0.9	4.6	2.7	0.6
$H_2O\ 2_{12}$-1_{01}	4_{04}-3_{13}	15	1.3	6.3	3.0	1.6	6.7	5.3	4.6	1.5	1.3	1.2	0.7	0.7	0.7
$H_2O\ 2_{12}$-1_{01}	6_{16}-5_{05}	13	0.7	5.9	2.4	1.8	8.1	4.7	3.8	1.3	0.8	0.7	0.3	0.2	0.2
$H_2O\ 2_{21}$-1_{10}	4_{04}-3_{13}	16	1.4	5.5	2.8	1.1	4.2	3.6	3.3	2.3	2.0	1.8	1.5	1.3	1.3
$H_2O\ 2_{21}$-1_{10}	6_{16}-5_{05}	13	0.9	5.5	2.1	1.3	5.0	3.2	2.7	2.0	1.2	1.0	0.6	0.4	0.4
OH 84	OH 79	14	1.1	2.4	1.7	0.3	0.6	0.7	0.8	0.8	0.9	0.9	1.4	1.3	1.1
$H_2O\ 2_{12}$-1_{01}	CO 16-15	16	0.2	2.4	0.9	0.8	18.8	10.6	8.0	0.4	0.4	0.4	0.1	0.1	0.1
$H_2O\ 2_{21}$-1_{10}	CO 24-23	16	0.6	3.8	1.7	1.0	135.7	41.1	24.2	22.5	7.0	4.8	3.0	2.2	2.5
$H_2O\ 3_{22}$-2_{11}	CO 29-28	9	0.7	2.1	1.2	0.4	51.9	11.6	6.7	45.3	8.3	4.7	6.6	2.2	2.0
$H_2O\ 4_{04}$-3_{13}	CO 16-15	15	0.1	0.5	0.3	0.1	2.8	2.0	1.7	1.6	1.7	1.9	2.2	3.6	5.4
$H_2O\ 4_{04}$-3_{13}	CO 21-20	15	0.2	0.9	0.5	0.2	12.3	5.8	4.2	4.2	2.3	2.0	1.7	2.0	2.6
$H_2O\ 6_{16}$-5_{05}	CO 16-15	13	0.1	1.0	0.5	0.3	2.3	2.2	2.1	0.05	0.07	0.1	0.01	0.02	0.04
$H_2O\ 6_{16}$-5_{05}	CO 21-20	13	0.2	1.4	0.7	0.4	10.2	6.5	5.1	0.1	0.1	0.1	0.01	0.01	0.02
$H_2O\ 6_{16}$-5_{05}	CO 24-23	13	0.4	1.6	0.9	0.5	27.0	12.7	8.8	11.2	5.7	4.7	5.2	5.0	6.4
$H_2O\ 6_{16}$-5_{05}	CO 32-31	8	1.2	4.6	3.0	1.1	576.3	91.6	43.3	165.4	28.1	15.6	28.6	6.6	5.5
$H_2O\ 2_{12}$-1_{01}	OH 84	15	0.1	4.2	1.2	1.3	182.2	422.8	429.4	72.5	140.7	98.6	15.4	37.0	21.2
$H_2O\ 3_{22}$-2_{11}	OH 84	9	0.2	0.8	0.4	0.2	7.0	24.2	32.4	43.9	97.3	71.2	28.8	65.3	36.5
CO 16-15	OH 84	15	0.4	2.8	1.1	0.7	9.7	40.0	54.0	30.4	64.6	41.5	9.6	14.2	5.5
CO 24-23	OH 84	15	0.2	1.1	0.5	0.3	0.8	7.0	12.7	4.9	30.3	30.8	10.6	30.8	15.1

Notes. Number of YSOs with detections of the two lines in the ratio (N), minimum (Min) and maximum (Max) value of the ratio, mean ratio value (Mean) and standard deviation (Std) is given for the observed line ratios. Model line ratios are calculated for three values of pre-shock densities, $n_H=10^4$, 10^5, and 10^6 cm^{-3}, and three values of shock velocities, v=20, 30, and 40 km s^{-1}. See Table 4.A.1 for the full identifiers of the lines.
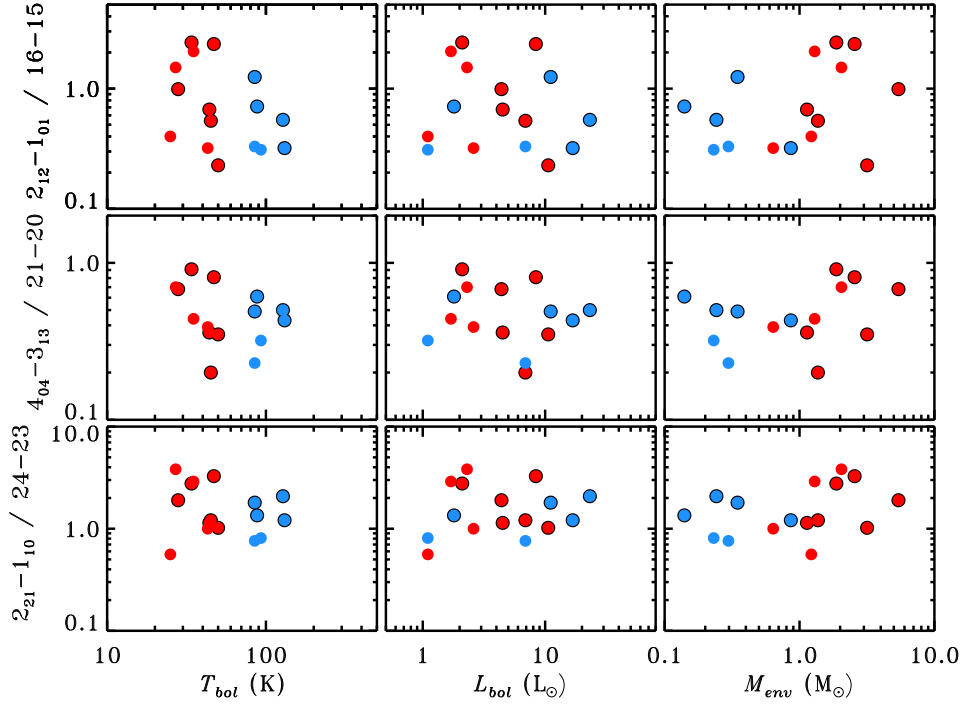
Figure 4.B.1 – H$_2$O-to-CO line ratios and, from left to right, bolometric temperature, bolometric luminosity, and envelope mass. The ratios are calculated using lines at nearby wavelengths for which the same, limited to the central spaxel, extraction region is considered. Shown are line ratios of the H$_2$O 2_{12}-1_{01} line at 179 μm and CO 16-15 at 163 μm (top), the H$_2$O 4_{04}-3_{13} and CO 21-20 lines at about 125 μm (middle), and the H$_2$O 2_{21}-1_{10} and CO 24-23 lines at about 108 μm (bottom). Red and blue symbols correspond to sources with T_{bol} 70 and > 70 K, respectively. Black rim is drawn for the sources with detections of CO 29-28 line.

4.B   Correlations with source parameters

Figure 4.B.1 shows selected H$_2$O-to-CO line ratios as a function of source physical parameters (bolometric luminosity, temperature, and envelope mass). Lack of correlation is seen in all cases.

Physics of deeply-embedded low-mass protostars: evolution of shocks, ultraviolet radiation, and mass flux rates

A. Karska, E. F. van Dishoeck, N. J. Evans II, L. E. Kristensen, J. C. Mottram,
J. D. Green, G. J. Herczeg, J. K. Jørgensen, and DIGIT, WISH, and WILL teams

Abstract

During the embedded phase of the protostellar evolution, the dense envelope is partly accreted onto the protostar and partly dispersed by the outflow. Far-infrared molecular and atomic lines are unique diagnostics of the physical conditions, outflow shocks and ultraviolet radiation needed to understand the physics of the accretion and dispersal process. We used *Herschel* / PACS to obtain spectral maps of 90 nearby ($D \lesssim 450$ pc) low-mass protostars at 55-210 μm as part of the 'Water in Star Forming Regions with Herschel' (WISH), 'William Herschel Line Legacy' (WILL), and 'Dust, Ice, and Gas in Time' (DIGIT) surveys. The maps show typically compact (~1000 AU scales) emission in CO, H_2O, and OH lines, and more extended (up to ~10,000 AU) emission in [O I] and [C II] lines.

Rich molecular spectra are detected towards 70 out of 90 sources, including 27 sources with the detection of the highly-excited H_2O 8_{18}-7_{07} line ($E_u/k_B = 1071$ K) and highly-excited CO ($J_{up} \gtrsim 30$) emission. Similar to previous studies, two components are found on CO rotational diagrams corresponding to median rotational temperatures of ~ 320 K and ~ 690 K. Detection of highly-excited CO and H_2O lines and analysis of CO rotational diagrams indicate an origin in hot ($T \gtrsim 300$ K) and dense ($n \gtrsim 10^4$ cm^{-3}) gas. Non-dissociative shocks can reproduce the observed molecular emission, but additional dissociative shocks and / or ultraviolet radiation (UV) are needed to account for the [O I] and some of the OH emission. The [C II] emission cannot be reproduced by any shock model and, when spatially associated with a young stellar object, characterizes the hard ultraviolet radiation ($\lambda < 1100$ Å) from the protostar. For the few sources where this line is detected, incident radiation fields $G \sim 10 - 100$ G$_0$ are found, in agreement with UV fields employed in recent models of UV irradiated cavities (Visser et al. 2012). Inferred densities of $n \sim 10^4 - 10^{5.5}$ cm^{-3} for the PDR layer are an order of magnitude lower than those obtained independently from shock models, suggesting the origin of [C II] emission is in the jet and not the outflow cavity walls.

The decrease of the H_2O / OH intensity ratio from Class 0 to Class I stages provides direct evidence for an increasing role of UV radiation as the protostar evolves. Such a trend is not found for the H_2O / [O I] ratio, most probably due to the larger contribution from the jet to the [O I] emission in the dense envelopes of Class 0 sources. Mass flux rates of dM_w/dt $\sim 10^{-8}$ M$_\odot$ yr^{-1} are determined from the [O I] line, on the assumption that most of the [O I] emission originates solely in the dissociative jet shock, which we argue is not the case so these values are in fact upper limits. Nevertheless, these rates are up to about an order of magnitude lower than those determined for the entrained outflow gas from the CO 3-2 and CO 6-5 maps, especially for the most deeply embedded sources. In contrast, Class I sources show lower CO / [O I] mass flux rates than the Class 0 sources, suggesting that the jet evolves from molecular to atomic form during the embedded phase.

5.1 Introduction

Complex physical processes are at play during the earliest, deeply-embedded stage of low-mass star formation. A fraction of the dense envelope material is accreted onto the protostar, but part of it is also removed in the form of collimated jets that entrain the surrounding material and produce wider-angle outflows. The envelope is partially emptied in the outflow cones allowing ultraviolet (UV) photons from a protostar to reach the 'cavity walls'. The 'bow shock', at the tip of the jet, is strong enough to produce additional UV that heats the cavities. The interplay of these processes makes it difficult to characterize them individually and track their evolution from the Class 0 to I stages.

The common signature of these processes is a presence of hot ($T \gtrsim 300$ K) and dense ($n \gtrsim 10^4$ cm^{-3}) gas that cools via emission lines of hydrogen (H_2), water vapor (H_2O), carbon monoxide (CO), hydroxyl (OH), atomic oxygen ([O I]), and ionized carbon ([C II]) at far-infrared wavelengths (Hollenbach et al. 1989). Observed intensities of those lines and their line ratios are therefore useful diagnostics of shocks and photodissociation regions (PDRs) produced in the young stellar object (YSO) environment. In particular, the type of shock, its velocity, and the pre-shock density of the ambient medium can be obtained from comparisons to detailed shock models (e.g. Kaufman & Neufeld 1996, Flower & Pineau des Forêts 2010, 2012). Independent measures of the gas density and the incident UV field in a YSO can be derived from the PDR models (e.g. Kaufman et al. 1999), but the shocks and large-scale cloud PDR contribution to the emission lines need to be first subtracted.

First far-infrared (IR) spectra of low-mass YSOs were obtained with Long-Wavelength Spectrometer onboard the *Infrared Space Observatory* (Kessler et al. 1996, Clegg et al. 1996). The main shortcoming of those early observations was the large telescope beam ($\sim 80''$) and thus the contamination from the cloud PDR emission and from multiple sources and / or outflows. Nevertheless, a few pointed observations of L1448 allowed to associate the far-IR line emission with the H_2 and low-J CO outflow (Nisini et al. 2000). A combination of a slow, non-dissociative shock and a fast, dissociative shock from the jet was then invoked to explain the observed molecular and [O I] emission, respectively (Giannini et al. 2001, Nisini et al. 2002b). A survey of 28 Class 0/I protostars revealed a gradual decrease in the molecular emission and an increase in the [O I] emission, attributed to the weakening of shocks and less-shielded UV for the less-massive envelopes of more evolved sources. For the Class 0 sources, however, the [O I] emission was linked only to jet shocks, and as such was used to derive mass loss rates (denoted here as mass flux rates). Giannini et al. (2001) found agreement between those rates and the CO mass flux tracing the entrained outflow activity over much longer periods and suggested that the mass flux rate, and thus the accretion, occur at a constant pace during the protostellar phase.

Far-IR spectral maps from the Photodetector Array Camera and Spectrometer (PACS) (Poglitsch et al. 2010) on board the *Herschel* Space Observatory (Pilbratt et al. 2010a)[1]

---

[1] Herschel is an ESA space observatory with science instruments provided by European-led Principal Investigator consortia and with important participation from NASA.

are well-suited to revisit the *ISO*/LWS results due to enhanced sensitivity, along with improved spatial and spectral resolution. The array of 5×5 elements covers a total field of view of $\sim 47''$ with $9.4''$ pixels, corresponding to the spatial resolution scales of order ~ 1000 AU at distances to the nearby protostars ($D \sim 200$ pc).

The PACS maps obtained as part of the 'Water in Star forming regions with Herschel' (WISH) survey show extended molecular and [O I] emission along the outflow direction in half of the 18 targeted sources and [C II] emission associated with a cloud PDR (van Dishoeck et al. 2011, Nisini et al. 2010a, Karska et al. 2013, Santangelo et al. 2013). In the 'Dust, Ice, and Gas in Time' survey of 30 protostars, much more compact emission was detected, implying that the extended emission is not a common characteristics of Class 0/I YSOs (Green et al. 2013). At the same time, CO rotational diagrams in all those sources show surprisingly similar two temperature components, with $T_{\rm rot} \sim 300$ K and $\gtrsim 700$ K, irrespective of the protostellar luminosity, envelope mass, and evolutionary stage (see also Goicoechea et al. 2012, Herczeg et al. 2012, Lindberg et al. 2013, van der Marel et al. 2013). CO ladders for small subsamples of sources have been modeled with a combination of non-dissociative shocks and UV heating along the cavity wall (van Kempen et al. 2010b, Visser et al. 2012), but an equally good solution was obtained by invoking two shocks alone (Flower & Pineau des Forêts 2013). The argument in favor of a hot component arising in the slow dissociative shock was put forward by Kristensen et al. (2013), who linked the hotter component with a kinematic component extracted from velocity-resolved H_2O profiles of the same protostars observed with the Heterodyne Instrument for the Far-Infrared (HIFI; de Graauw et al. 2010).

A systematic comparison of *Herschel* / PACS spectra of 22 protostars in Perseus with shock models from Kaufman & Neufeld (1996) and Flower & Pineau des Forêts (2010) was presented in Karska et al. (subm.). Line ratios of various CO, and separately H_2O lines, show good agreement with non-dissociative shock models with pre-shock densities of $\sim 10^5$ cm^{-3} and shock velocities of $\gtrsim 20$ km s^{-1}. However, the models used for those comparisons overproduced by 1-2 orders of magnitude the H_2O / CO and H_2O / OH line ratios, indicating that the inclusion of shock illumination by ultraviolet photons is needed. The presence of irradiated shocks is also invoked to explain the complex H_2O spectra from HIFI, with the 'broad' and 'offset' components linked to irradiated $C-$type and $J-$type shocks, respectively (Kristensen et al. 2013, Suutarinen et al. 2014, Mottram et al. subm.). Since the $J-$type dissociative shocks contribute only a small fraction of the flux to the CO lines with $J \lesssim 30$, a larger number of sources with even higher$-J$ CO lines is needed to study this component with PACS.

To address those issues, a consistent analysis of a large and uniform sample of protostars is clearly needed. In this paper, the WISH and DIGIT sources are re-analyzed together with an additional 50 sources observed as part of the 'William Herschel Line Legacy' survey (WILL, Mottram et al. in prep.) to answer the following questions: What determines the detection of highly-excited CO and spatially-extended line emission? What are the typical spatial scales of line emission? Do line fluxes of different species correlate with each other? What part of the [O I] and [C II] emission originates in the YSOs and can be attributed to the shock and / or PDR components? Do total molecular and atomic cooling rates change from the Class 0 to Class I stage? What are the implications for the

mass flux rates calculated from the [O I] line and how do they compare with the mass flux rates based on CO outflows?

This paper is organized as follows. Section 2 describes our sample selection, observations, and data reduction. §3 compiles results on detection statistics and cross-species line correlations. §4 shows analysis of CO excitation, molecular and atomic cooling, and mass loss rates, and how they evolve from Class 0 to I phase. Comparison of absolute line emission of [O I] and [C II] lines to shock and photodissociation regions models is presented. §5 discusses the results obtained in §3 and §4 and §6 presents the summary and conclusions.

5.2 Observations

5.2.1 Sample selection

The low-mass embedded protostars analyzed here were initially observed as part of the 'Water In Star forming regions with Herschel' (WISH, van Dishoeck et al. 2011) and 'Dust, Ice, and Gas In Time' (DIGIT, Green et al. 2013) surveys, comprised of 18 and 29 Class 0/I protostars targeted with PACS, respectively, including 8 overlap sources. This sample was subsequently enlarged by the 'William Herschel Line Legacy' survey (WILL, Mottram et al. in prep.), where an additional 50 Class 0/I sources were observed, including 2 sources in common with the WISH and DIGIT programs. Three more sources were further extracted from the PACS spectral maps of the primary targets (ID numbers 4, 82, 85), increasing the sample to 90 sources in total (for details, see Table 5.1). Most of our sources are located in Perseus (30 sources), Taurus (12 sources), Ophiuchus (9 sources), Aquila Rift complex (6 sources in Aquila, 7 sources in W40, and 2 sources in Serpens South), Corona Australis (5 sources), and Serpens (3 sources) molecular clouds, at distances $\lesssim$ 450 pc (for distance references see Kristensen et al. 2012, Green et al. 2013, Mottram et al. in prep.).

The selection procedure for the WISH and DIGIT sources are discussed in detail in van Dishoeck et al. (2011) and Green et al. (2013), with a general rule that all of them are well-known and extensively studied protostars. The WILL sources were selected based on unbiased mid-IR and millimeter continuum observations with *Spitzer* and various ground-based telescopes. Protostars in Perseus and Ophiuchus were selected from the 'Cores to Disk' program (c2d, Evans et al. 2009), and extensively discussed in Jørgensen et al. (2007a) and Rebull et al. (2007) (Perseus) and in Jørgensen et al. (2008) (Ophiuchus), with (sub-)millimeter follow-up in Enoch et al. (2009), van Kempen et al. (2009c), and van der Marel et al. (2013). Protostars in Taurus were observed as part of the 'Taurus Spitzer Survey' and catalogued in Rebull et al. (2010). Corona Australis (CrA 1) and Ophiuchus North / Scorpius (Sco1) protostars are from the 'Spitzer Gould Belt Survey' (Peterson et al. 2011, Hatchell et al. 2012). Sources located in the Aquila Rift complex (Gutermuth et al. 2008) are catalogued in Maury et al. (2011). The details will be discussed in Mottram et al. in prep.

The entire sample of protostars covers a broad range of bolometric temperatures and

181
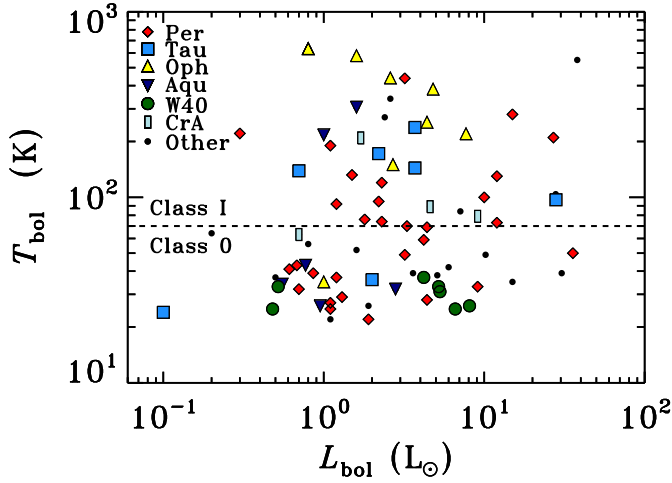
Figure 5.1 – $T_{bol} - L_{bol}$ diagram illustrating the variety of physical parameters determined for the protostars from our survey. Protostars in Perseus, Taurus, Ophiuchus, Aquila, W40, and CrA are showed in red diamonds, blue squares, yellow triangles, navy rotated triangles, green circles, and light blue rectangles, respectively.

luminosities (Table 5.1), with specific clouds often located at selected parts of the T_{bol} – L_{bol} diagram, as illustrated in Figure 5.1. The most luminous protostars are those in Perseus and Taurus, with average bolometric luminosities of $5-6 \, L_\odot$, whereas the sources in Aquila have on average the lowest luminosities, $\sim 1.3 \, L_\odot$. Bolometric temperatures are the lowest for the Serpens and W40 protostars (average T_{bol} of ~ 30 K) and the highest for Ophiuchus protostars (~ 370 K). The average bolometric temperature for the rest of the clouds is around 100 K. In total, 45 Class 0 (T_{bol} 70 K) and 45 Class I ($T_{bol} > 70$ K and 650 K) sources were observed.

Table 5.1 – Bolometric Temperatures, Luminosities, and Envelope Masses of Embedded Protostars

ID	Position	Cloud	Dist. (pc)	T_{bol} (K)	L_{bol} ($L_\odot$)	M_{env}[a] ($M_\odot$)	Region	Other names	Project[b]
1	03:25:22.33 +30:45:14.0	Per	235	74	2.3	1.1	L1448	Per-emb 22, YSO 1, L1448 IRS2, I03222+3034	WILL (Per01)
2	03:25:36.48 +30:45:22.3	Per	235	73	12	3.2	L1448	Per-emb 33, YSO 2, L1448 N(A), L1448 IRS3	WILL (Per02)
3	03:25:38.82 +30:44:06.3	Per	235	69	4.4	3.9	L1448	Per-emb 26, YSO 3, L1448 C(S)	DIGIT
4	03:25:39.10 +30:43:58.0	Per	235	190	1.1	2.6	L1448	Per-emb 42, YSO 3, L1448 MMS, L1448 C(N)	DIGIT (Per03)
5	03:26:37.46 +30:15:28.0	Per	235	92	1.2	0.3	L1451	Per-emb 25, YSO 4, I03235+3004	WILL (Per04)
6	03:27:39.09 +30:13:03.0	Per	235	59	4.2	–	L1455	Per-emb 17, YSO 6, I03245+3002, L1455-IRS1	DIGIT
7	03:28:00.40 +30:08:01.3	Per	235	221	0.3	–	L1455	Per-emb 46, L1455-IRS3, I03249+2957	DIGIT
8	03:28:37.09 +31:13:30.7	Per	235	130	12	0.4	NGC1333	Per-emb 35, YSO 11, NGC1333 I1, I03255+3103	WILL (Per05)
9	03:28:55.56 +31:14:36.6	Per	235	50	35.7	5.1	NGC1333	Per-emb 27, YSO 15, NGC1333 I2A	WISH
10	03:28:57.36 +31:14:15.7	Per	235	100	10	0.3	NGC1333	Per-emb 36, YSO 16, NGC1333 I2B	WILL (Per06)
11	03:29:00.52 +31:12:00.7	Per	235	32	0.7	0.3	NGC1333	Per-emb 3, YSO 18, HRF 65	WILL (Per07)
12	03:29:01.57 +31:20:20.7	Per	235	280	15	0.9	NGC1333	Per-emb 54, YSO 19, HH 12	WILL (Per08)
13	03:29:07.76 +31:21:57.2	Per	235	210	27	0.2	NGC1333	Per-emb 50	WILL (Per09)
14	03:29:10.50 +31:13:31.0	Per	235	33	9.1	5.6	NGC1333	Per-emb 12, YSO 22, NGC1333 I4A	WISH
15	03:29:10.68 +31:18:20.5	Per	235	70	3.3	1.4	NGC1333	Per-emb 21, YSO 23, HRF 46	WILL (Per10)
16	03:29:12.04 +31:13:01.5	Per	235	28	4.4	3.0	NGC1333	Per-emb 13, YSO 25, NGC1333 I4B	WISH (Per11)
17	03:29:13.52 +31:13:58.0	Per	235	39	0.9	1.3	NGC1333	Per-emb 14, YSO 26, NGC1333 I4C	WILL (Per12)
18	03:29:51.82 +31:39:06.1	Per	235	41	0.6	0.5	NGC1333	Per-emb 9, YSO 31, I03267+3128	WILL (Per13)
19	03:30:15.12 +30:23:49.2	Per	235	120	2.3	0.1	B1-ridge	Per-emb 34, I03271+3013	WILL (Per14)
20	03:31:20.96 +30:45:30.2	Per	235	37	1.2	1.3	B1-ridge	Per-emb 5, YSO 32, I03282+3035	WILL (Per15)
21	03:32:17.95 +30:49:47.6	Per	235	29	1.3	2.8	B1-ridge	Per-emb 2, YSO 33, I03292+3039	WILL (Per16)
22	03:33:12.85 +31:21:24.1	Per	235	438	3.2	–	B1	Per-emb 64, I03301+3111, Bolo76	DIGIT
23	03:33:14.40 +31:07:10.9	Per	235	43	0.7	1.2	B1	Per-emb 6, YSO 35, B1 SMM3	WILL (Per17)
24	03:33:16.45 +31:06:52.5	Per	235	25	1.1	1.2	B1	Per-emb 10, YSO 36, B1 d	WILL (Per18)
25	03:33:16.66 +31:07:55.2	Per	235	132	1.5	–	B1	Per-emb 40, YSO 37, B1 a, I03301+3057	DIGIT
26	03:33:17.85 +31:09:32.0	Per	235	76	1.8	–	B1	Per-emb 29, YSO 38, B1 c	DIGIT
27	03:33:27.28 +31:07:10.2	Per	235	95	2.2	0.2	B1	Per-emb 30, YSO 40, B1 SMM11	WILL (Per19)
28	03:43:56.53 +32:00:52.9	Per	235	22	1.9	2.1	IC 348	Per-emb 1, YSO 44, HH 211 MMS	WILL (Per20)
29	03:43:56.85 +32:03:04.6	Per	235	27	1.1	1.9	IC 348	Per-emb 11, YSO 43, IC348 MMS, IC348 SW	WILL (Per21)
30	03:44:43.94 +32:01:36.1	Per	235	49	3.2	0.6	IC 348	Per-emb 8, YSO 48, IC348 a, I03415+3152	WILL (Per22)
31	04:04:42.9 +26:18:56.3	Tau	140	238	3.7	0.2		L1489	DIGIT/WISH
32	04:19:58.4 +27:09:57.0	Tau	140	131	1.5	0.3		I04169+2702	WILL (Tau01)

Table 5.1 – continued from previous page

ID	Position	Cloud	Dist. (pc)	T_{bol} (K)	L_{bol} ($L_\odot$)	M_{env}[a] ($M_\odot$)	Region	Other names	Project[b]
33	04:21:11.4 +27:01:09.0	Tau	140	271	0.5	–		I04181+2654A	WILL (Tau02)
34	04:21:56.9 +15:29:45.9	Tau	140	24	0.1	–		IRAM 04191+1522	DIGIT
35	04:22:00.6 +26:57:32.0	Tau	140	178	0.4	–		FS Tau B	WILL (Tau03)
36	04:27:02.6 +26:05:30.0	Tau	140	159	1.4	0.6		DG Tau B	WILL (Tau04)
37	04:27:57.3 +26:19:18.0	Tau	140	52	0.5	0.1		I04248+2612 AB	WILL (Tau06)
38	04:29:30.0 +24:39:55.0	Tau	140	132	0.6	–		I04264+2433	WILL (Tau07)
39	04:31:34.1 +18:08:04.9	Tau	140	97	28	2.3		L1551 IRS5	DIGIT
40	04:35:35.3 +24:08:19.0	Tau	140	72	1.1	0.1		I04325+2402 A	WILL (Tau09)
41	04:39:53.9 +26:03:09.8	Tau	140	36	2.0	0.9		L1527, I04368+2557	DIGIT/WISH
42	04:39:13.9 +25:53:20.6	Tau	140	144	3.7	0.2		TMR 1, I04361+2547 AB	DIGIT/WISH
43	04:39:35.0 +25:41:45.5	Tau	140	172	2.2	0.2		TMC 1A, I04365+2535	DIGIT/WISH
44	04:41:12.7 +25:46:35.9	Tau	140	139	0.7	0.2		TMC 1, I04381+2540	DIGIT/WISH
45	08:25:43.9 -51:00:36.0	Core	450	104	27.9	4.4		HH 46	WISH
46	11:06:47.0 -77:22:32.4	Cha	178	56	0.8	0.2	Cham I	Ced110 IRS4	WISH
47	11:09:28.51 -76:33:28.4	Cha	178	–	2.9	–	Cham I	ISO192, CaINa2	WILL (Cha01)
48	12:01:36.3 -65:08:53.0	Core	178	84	7.1	2.7		BHR71	DIGIT/WISH
49	12:53:17.23 -77:07:10.7	Cha	178	550	38.0	0.8	Cham II	DK Cha, I12496-7650	DIGIT
50	12:59:06.58 -77:07:39.9	Cha	178	220	1.9	–	Cham II	ISO-CHAII 28	WILL (Cha02)
51	15:43:01.29 -34:09:15.4	Lup	130	52	1.6	0.5		I15398-3359	WISH
52	16:26:21.48 -24:23:04.2	Oph	125	254	4.4	0.1	L1688	Oph-emb 8, GSS30 IRS1, Elias 21	DIGIT
53	16:26:25.80 -24:24:28.8	Oph	125	35	1.0	0.8	L1688	Oph-emb 3, VLA 1623	DIGIT
54	16:26:44.2 -24:34:48.4	Oph	125	440	2.6	0.05	L1688	WL 12	DIGIT
55	16:26:59.1 -24:35:03.3	Oph	125	150	2.7	0.2	L1688	WL 22, ISO-Oph 90	WILL (Oph01)
56	16:27:09.36 -24:37:18.4	Oph	125	383	4.8	0.04	L1688	Oph-emb 16, Elias 29, WL 15	DIGIT
57	16:27:28.1 -24:39:33.4	Oph	125	633	0.8	0.3	L1688	Oph-emb 13, IRS 44	DIGIT
58	16:27:29.4 -24:39:16.1	Oph	125	633	0.8	0.3	L1688	IRS46	DIGIT
59	16:31:35.76 -24:01:29.2	Oph	125	580	1.6	0.3	L1709	Oph-emb 17, IRS 63	DIGIT
60	16:32:00.96 -24:56:42.7	Oph	125	150	7.7	0.1	L1689	Oph-emb 10	WILL (Oph02)
61	16:34:29.3 -15:47:01.4	Core	125	340	2.6	0.5		RNO 91	WISH
62	16:46:58.27 -09:35:19.8	Sco	125	–	1.0	0.1		L260 SMM1	WILL (Sco01)
63	18:17:29.9 -04:39:39.5	Core	200	49	10.2	4.4		L 483 MM	WISH
64	18:29:03.82 -01:39:01.5	Aqu	260	26	1.0	1.1		Aqu-MM2	WILL (Aqu01)
65	18:29:08.60 -01:30:42.8	Aqu	260	32	2.8	0.8		Aqu-MM4	WILL (Aqu02)

Table 5.1 – continued from previous page

ID	Position	Cloud	Dist. (pc)	T_{bol} (K)	L_{bol} ($L_\odot$)	M_{env}[a] ($M_\odot$)	Region	Other names	Project[b]
66	18:29:49.56 +01:15:21.9	Ser	429	39	30.4	16.1		Ser-emb 6, Ser SMM1, FIRS1	WISH
67	18:29:56.7 +01:13:17.2	Ser	429	26	1.9	2.1		Ser SMM4	DIGIT/WISH
68	18:29:59.3 +01:14:01.7	Ser	429	38	5.1	3.2		Ser SMM3	DIGIT/WISH
69	18:29:37.70 -01:50:57.8	SerS	260	22	1.1	0.4		SerpS-MM1	WILL (SerS01)
70	18:30:04.13 -02:03:02.1	SerS	260	35	15	3.0		SerpS-MM18	WILL (SerS02)
71	18:30:25.10 -01:54:13.4	Aqu	260	217	1.0	0.3		Aqu-MM6	WILL (Aqu03)
72	18:30:28.63 -01:56:47.7	Aqu	260	306	1.6	0.4		Aqu-MM7	WILL (Aqu04)
73	18:30:29.03 -01:56:05.4	Aqu	260	34	0.6	0.2		Aqu-MM8	WILL (Aqu05)
74	18:30:49.94 -01:56:06.1	Aqu	260	43	0.8	0.2		Aqu-MM14	WILL (Aqu06)
75	18:31:09.42 -02:06:24.5	W40	260	37	4.2	0.7		W40-MM3	WILL (W40-1)
76	18:31:10.36 -02:03:50.4	W40	260	33	5.2	0.8		W40-MM5	WILL (W40-2)
77	18:31:46.54 -02:04:22.5	W40	260	26	8.1	1.2		W40-MM26	WILL (W40-3)
78	18:31:46.78 -02:02:19.9	W40	260	31	5.3	0.6		W40-MM27	WILL (W40-4)
79	18:31:47.90 -02:01:37.2	W40	260	25	6.6	0.7		W40-MM28	WILL (W40-5)
80	18:31:57.24 -02:00:27.7	W40	260	25	0.5	0.1		W40-MM34	WILL (W40-6)
81	18:32:13.36 -01:57:29.6	W40	260	33	0.5	0.1		W40-MM36	WILL (W40-7)
82	19:01:48.03 -35:57:22.2	CrA	130	209	1.7	2.0		RCrA IRS 5A	DIGIT
83	19:01:48.47 -36:57:14.9	CrA	130	63	0.7	–		RCrA IRS 5N	DIGIT
84	19:01:55.33 -36:57:17.0	CrA	130	79	9.1	–		RCrA IRS 7A + SMM 1C	DIGIT
85	19:01:56.42 -36:57:28.3	CrA	130	89	4.6	–		RCrA IRS 7B	DIGIT
86	19:02:58.67 -37:07:35.9	CrA	130	–	0.9	0.7		CrA-44, IRAS 32c	WILL (CrA01)
87	19:17:53.7 +19:12:20.0	Core	300	39	3.6	1.3		L 723 MM	WISH
88	19:37:00.9 +07:34:09.6	Core	106	37	0.5	1.2		B335	DIGIT
89	20:39:06.3 +68:02:16.0	Core	325	42	6.0	1.5		L1157	DIGIT
90	21:24:07.5 +49:59:09.0	Core	200	64	0.2	–		L1014	DIGIT

Notes. Numbered Per-emb and Oph-emb names come from Enoch et al. (2009), the Perseus / YSO names come from Jørgensen et al. (2006) and were subsequently used in Davis et al. (2008). Aqu, SerpS, and W40 numbered names are from Maury et al. (2011). Other source identifiers were compiled using Jørgensen et al. (2007b), Rebull et al. (2007), Davis et al. (2008), and Velusamy et al. (2013) (for Perseus), and Rebull et al. (2010) for Taurus. Chamaeleon names come from Spezzi et al. 2013 (Cham II) and Winston et al. 2012 (Cham I). [a] Envelope masses are from Kristensen et al. (2012) for WISH / DIGIT and Mottram et al. (in prep.) for WILL sources. [b] Source names used in the WILL program and entered in the Herschel Archive are written in brackets.

5.2.2 Observations and data reduction

Single footprint spectral maps of all our sources were obtained with the PACS instrument onboard *Herschel*. Each map consists of 25 spatial pixels (*spaxels*) of $9''.4 \times 9''.4$ arranged in the 5×5 array with a total field of view of $\sim 47'' \times 47''$. Each spaxel contains a (sub-)spectrum observed in first (red) or second (blue) order, within the wavelength ranges of 102-210 μm and 51-105 μm, respectively. The spectral resolving power increases with wavelength from about 1000 to 2000 (corresponding to velocity resolutions of ~140 to 320 km s^{-1}) in the first order and from about 1500 to 3000 (~100 to 210 km s^{-1}) in the second order.

Two main observing schemes were used: line spectroscopy mode for the WISH and WILL sources and range spectroscopy mode for the DIGIT sources. The line spectroscopy mode allows observations of small spectral regions ($\Delta\lambda \sim$0.5-2 μm) around selected lines and is particularly suited for deep integrations. The range spectroscopy mode provides the full spectrum from $\sim$ 50 to 210 μm but the spectral sampling within a resolution element is about 3-4 times coarser than in the line spectroscopy mode. For both schemes, the chopping / nodding observing mode within $6'$ from the source was used to subtract the background emission.

Data reduction for both observing modes was performed with the Herschel Interactive Processing Environment (HIPE, Ott 2010). The flux was normalized to the telescopic background and calibrated using observations of Neptune. Spectral flatfielding within HIPE was used to increase the signal-to-noise ratio (for details, see Herczeg et al. 2012 Green et al. 2013). Overall flux uncertainty is about 20% from cross-comparisons of sources in common within our programs.

The 1D spectrum is obtained by summing a custom number of spaxels chosen after investigation of the 2D spectral maps (Karska et al. 2013). For sources with extended line emission, the co-addition of spaxels with detected emission increases the S / N, smooths the continuum, and enables correction for significant differences in beam sizes over the wide spectral range covered by PACS. For sources with the point-like emission in all lines, only the central spaxel spectrum is used, but the line fluxes are multiplied by the wavelength-dependent instrumental correction factors ($\sim$ 1.4 at 70 μm and $\sim$ 2.3 at 180 μm, see PACS Observer's Manual[2]).

Since lines are spectrally unresolved (except [O I], see below), the line fluxes are calculated by fitting Gaussians to the final 1D spectrum. Single Gaussians are used for well-isolated lines and double or triple Gaussians for closeby lines, including blends. The line width of the Gaussians is fixed to the instrumental value of unresolved lines, except the [O I] line at 63 μm which often shows high-velocity wings (van Kempen et al. 2010b, Karska et al. 2013). In this case, integration and / or broad Gaussian fitting are applied.

---

[2] http://herschel.esac.esa.int/Docs/PACS/html/pacs_om.html
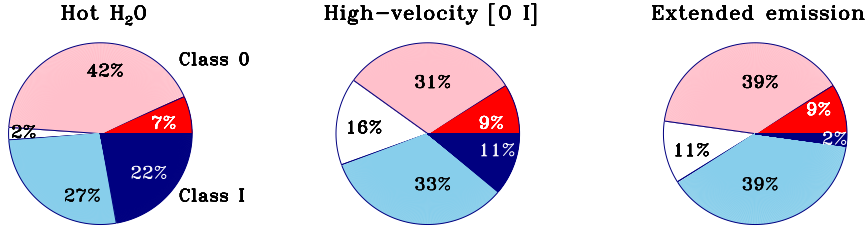
Figure 5.1 – Detection statistics for the hot H_2O 8_{18}-7_{07} line at 63 μm, high-velocity [O I] emission, and an extended pattern of line emission. Detections are shown in red (Class 0) and navy blue (Class I), non-detections for Class 0 sources are shown in pink and for Class I sources in light blue. The sources without T_{bol} determination (unknown Class) and contamination from nearby outflows and / or large-scale cloud emission in the [O I] line are shown in white.

5.3 Results

5.3.1 Detection statistics

PACS spectra of low-mass protostars show exclusively lines of CO, H_2O, OH, [O I], and [C II]. CO, H_2O and OH lines are seen in emission, with the exception of the H_2O 2_{12}-1_{01} line seen in absorption in a few fields with multiple outflows. The [O I] lines are seen in emission in the majority of cases, unless originating from large-scale photodissociation regions contaminating the off-position. The [C II] line at 158 μm is even more sensitive to the cloud emission and typically detected in the off-positions as well. In total, the CO 16-15 line targeted in the WISH, DIGIT, and WILL programs, is detected in 70 out of 90 sources, the H_2O 2_{12}-1_{01} line in 57 sources, and the OH doublet $^2\Pi_{3/2}$ $J = 7/2 - 5/2$ at 84 μm in 62 sources. Atomic emission associated with a YSO is detected in 71 sources in the [O I] 63 μm line and in 10 sources in the [C II] line.

Our large sample of sources also allows investigation of the detection statistics of interesting features found in PACS maps by previous studies. Figure 5.1 illustrates the percent of sources with the detections of hot H_2O, high-velocity [O I] emission, and an extended pattern of line emission.

A strong detection of the H_2O 6_{16}-5_{05} line at 63 μm ($E_{up} \sim 1000$ K) in the Class 0 protostar NGC1333 IRAS 4B was one of the first surprises revealed in the high-sensitivity *Herschel* / PACS data (Herczeg et al. 2012). The line flux of this H_2O transition in IRAS 4B exceeds the flux of the nearby [O I] line. Even though no other source in our sample shows such a bright H_2O 8_{18}-7_{07} line as found in IRAS 4B, the line is detected in about a quarter of our sources. The detections are non-evenly distributed for Class 0 and Class I sources – almost half of the Class I sources show the detection of the H_2O 8_{18}-7_{07} line in contrast to mere 14% of Class 0 sources. The line is also detected in Class II sources: in 4 out of 8 T Tauri stars in Fedele et al. (2013) and in 8 out of 33 gas-rich T Tauri disks (or 68 in total) in Riviere-Marichalar et al. (2012). Interestingly, the H_2O 8_{18}-7_{07} line is often detected in the absence of lower$-J$ H_2O lines for those more evolved sources and most likely originates from the disk (Fedele et al. 2012, 2013, Riviere-Marichalar et al. 2012).

187

PACS spectral maps of the [O I] and [C II] lines at 63 and 158 μm provide a means to disentangle the emission associated with a young protostar from the large-scale cloud emission and to fully explore the diagnostic potential of these forbidden lines. [C II] emission is very rarely associated with YSOs and primarily traces the photodissociated regions of molecular clouds (Karska et al. 2013). Since the [C II] emission is typically detected at the off-positions and subtracted by chopping, most of the maps show more or less uniformly distributed [C II] in absorption. Only 10 sources show [C II] in emission, related either to the central or outflow positions of YSOs.

Unlike maps in the [C II] line, the majority of our sources show [O I] emission related to YSOs with the pattern strongly indicating an origin in the jet / outflow (Green et al. 2013, Karska et al. 2013). The spectral resolution of PACS is about 90 km s^{-1} at these wavelengths, resolving only the highest-velocity, jet-related component of the [O I] line. The [O I] velocity shift is most clearly seen in the red outflow of HH 46 (van Kempen et al. 2010b), while for the other sources the best signature of high-velocity emission is a broad line width, exceeding the best-fit Gaussian profile reproducing the maximum intensity. In total, 20% of sources, evenly distributed among Class 0 and I sources, show high-velocity emission associated with the [O I] line.

Spatially-extended emission in molecular lines is not as common a feature as seen in the [O I] line. The H_2O 2_{12}-1_{01} line at 179 μm is clearly extended in several well-known Class 0 outflow sources, most notably in the cases of L1157 (Nisini et al. 2010a), L1448 (Nisini et al. 2013), and NGC1333 IRAS 4A (Karska et al. 2013, Santangelo et al. 2014). The statistical study of the line emission extent is only possible based on the single footprint 5×5 maps. Preliminary analysis showed significant variation, with almost half of the sources in the WISH sample having extended emission (Karska et al. 2013), but only a minor fraction in the DIGIT sample (Green et al. 2013). Extended molecular emission is only detected in 8 Class 0 and 2 Class I sources in our combined sample beyond the central 9.4″ spaxel, altogether only $\sim$ 10% of 90 sources. The large fraction of sources with extended emission in the WISH sample is due to the observational bias in the source sample, where sources with strong outflow emission were preferentially selected.

5.3.2   Cross-species line flux correlations

Correlations between line fluxes are a useful indicator of which groups of species are related to the same and / or different physical components in a YSO. Karska et al. (2013) found strong line flux correlations between H_2O and high$-J$ CO lines and, based also on the similarity in their spatial distribution, suggested a common origin in non-dissociative shocks. A lack of correlation was found with the [O I] line, which traces dissociative shocks and to a smaller extent the hidden atomic jet (Karska et al. 2013). Weak correlations of OH with H_2O and its similar spatial distribution to that of [O I] indicated that OH is also partly tracing the dissociative shocks.

Figure 5.2 revisits the above results using an extended sample of sources and most-commonly detected lines of CO, H_2O, OH, and [O I] observed in the WISH, DIGIT, and WILL programs. The correlations are quantified following the formulation of a correlation factor, r, in Marseille et al. (2010, Appendix A), that can be translated to the significance
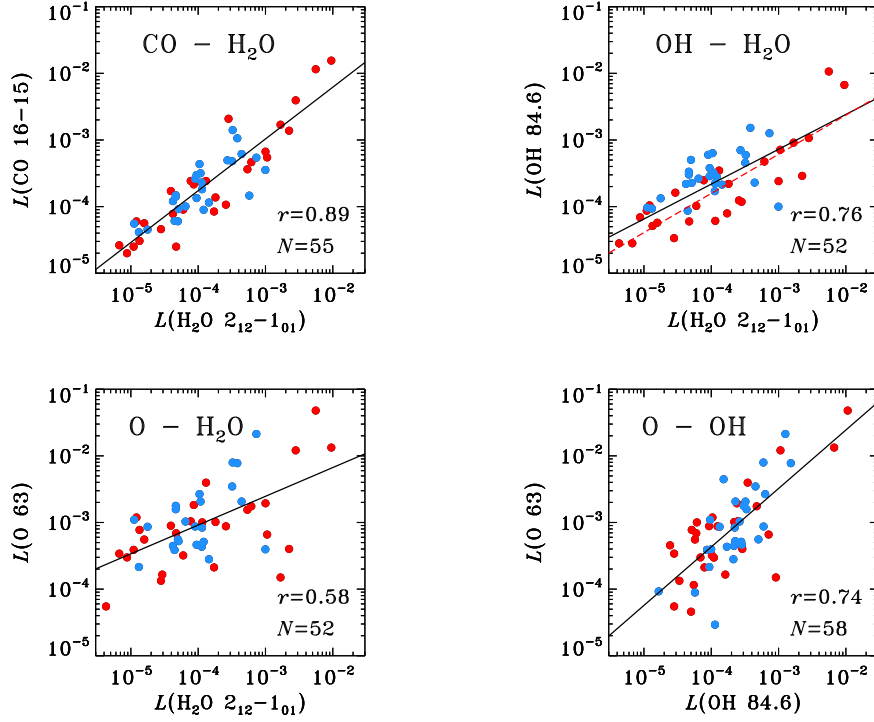
Figure 5.2 – Flux correlations between the H_2O 2_{12}-1_{01} line at 179 μm and the CO 16-15 and OH 84.6 μm lines (top) and the [O I] 63 μm line with the H_2O 2_{12}-1_{01} and OH 84.6 μm lines (bottom). Class 0 sources are shown in red and Class I sources in blue. Solid lines show the best linear fits obtained with a least-squares method. A separate fit to the Class 0 sources only is shown on the H_2O - OH plot as red dashed line. Correlation coefficients (r) and number of sources with line detections (N) are shown on the plots.

level of a correlation when multiplied by $\sqrt{N-1}$, where N is the sample size. Using this procedure, the strongest, 6.5σ correlation is found between the H_2O and CO lines and a somewhat weaker, 5.4σ correlation is seen between the H_2O and OH lines. The weakest, 4.1σ correlation is obtained between the H_2O and [O I] lines, while the [O I] and OH lines correlate at the 5.6σ level.

While these results are qualitatively consistent with the results from the WISH sample, the extended sample allows a further distinction between the Class 0 and I sources. The H_2O – CO line fluxes are correlated at a significance of 4.8σ for Class 0 sources and 4.0σ for the Class I sources. The H_2O and OH lines show correlations of 4.4σ for Class 0 sources and only 2.6σ for Class I sources.

Clearly, the correlations between the pairs of molecular lines are stronger for the less evolved Class 0 sources, while a comparable, 4σ correlation is found between the [O I] and OH line fluxes for both Class 0 and I sources. At the same time, the OH line luminosi-

ties are larger for the Class I sources with the same H_2O fluxes as the Class 0 sources (see the H_2O – OH panel), suggesting that the fraction of OH associated with the component traced by the [O I] line increases for more evolved sources.

The different origin of H_2O and [O I] emission, revealed by the weak correlation between the two species, is further supported by differences in the correlations with source physical parameters (see Figures 5.B.1 and 5.B.2 Appendix B). The [O I] line is tightly related to the source bolometric luminosity, L_{bol}, while the H_2O line luminosities are mostly influenced by the envelope mass, M_{env}. The trend for H_2O could be a pure excitation effect, since the lines are subthermally excited. However, a recent study of spectrally resolved HIFI line profiles of the same sources shows a decreasing line width of the H_2O lines from Class 0 to Class I (Mottram et al. submitted), showing that evolution also influences the H_2O - M_{env} relation.

5.4   Analysis

5.4.1   CO excitation

Rotational temperatures (T_{rot}) and number of molecules (N) of the emitting gas from low-mass YSOs are routinely calculated from PACS spectra using Boltzmann diagrams (e.g. Green et al. 2013, Karska et al. 2013, Manoj et al. 2013). The most meaningful results are obtained for CO, since its excitation is dominated by collisions and the lines are mostly optically thin (based on the upper limits on ^{13}CO line fluxes, Goicoechea et al. 2012, Lee et al. 2013). The CO rotational diagrams in the PACS range covering $J =14$-13 up to 49-48 show a break around the $J = 24 - 23$ transition and therefore are often fitted with two straight lines. The corresponding components are referred as the 'warm' and 'hot' (Karska et al. 2013), to distinguish them from the 'cold', 70-100 K component detected at $J \lesssim 10$ transitions (Goicoechea et al. 2012, Yıldız et al. 2013). Rotational temperatures obtained in this manner are surprisingly similar in all low-mass embedded YSOs, and equal to about 300-350 K (CO $J \sim 14 - 24$ lines) and $\gtrsim 700$ K (CO $J \gtrsim 24$ lines), respectively. Similar values of the warm component temperatures are even seen in much more massive protostars (Karska et al. 2014), further suggesting that an underlying universal physical mechanism is responsible for the excitation in all sources. The number of emitting molecules varies more strongly from source to source, increasing with source bolometric luminosity (Figure 25 of Green et al. 2013, see also Manoj et al. 2013).

In the following sections, rotational temperatures and number of emitting molecules are correlated with source physical parameters (bolometric luminosities and envelope masses) and compared on a cloud-to-cloud basis. The CO diagrams for the WISH sources are presented in Karska et al. (2013) and for the DIGIT sources in Green et al. (2013), Lee et al. (2013), Dionatos et al. (2013), Lindberg et al. (2014), and J.-E. Lee et al. (submitted). The procedures used to derive meaningful parameters from rotational diagrams with a limited number of targeted lines and associated errors are explained in Appendix B, where the remaining diagrams for the WILL sources are also shown (Figures 5.C.1 and 5.C.2).
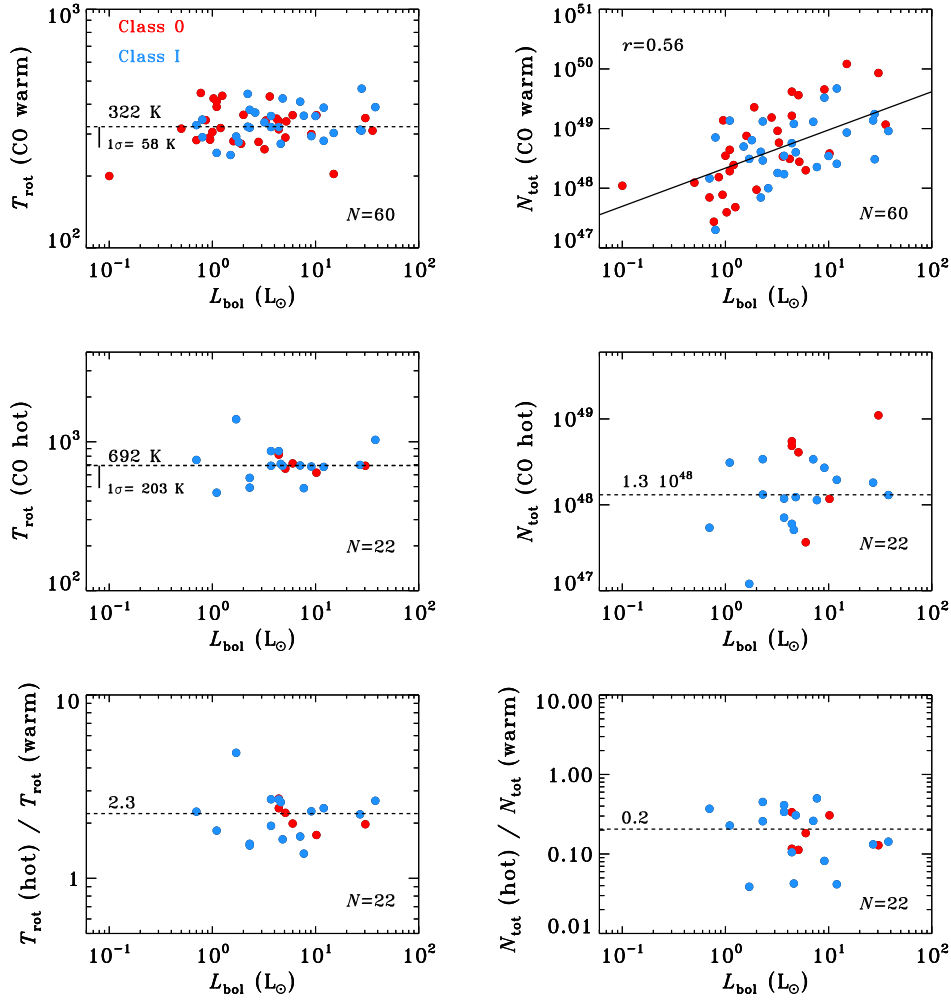
Figure 5.1 – CO rotational temperatures (left) and numbers of emitting molecules (right) for the 'warm component' (top), 'hot component' (middle), and their ratios in the 'hot' and 'warm' components as a function of bolometric luminosity. Solid lines show the best linear fits obtained with a least-squares method, only for the cases where the correlation coefficient r exceeds the 2σ threshold (see text). Otherwise, the median values are shown in dashed lines. Class 0 sources are shown in red and Class I sources in blue.

5.4.1.1 Correlations with source physical parameters

The left panel of Figure 5.1 shows the rotational temperatures of CO in the warm and hot components, and the ratio of the temperatures in the two components, as functions

Table 5.1 – Correlation coefficients for CO excitation and sources parameters relations

	L_{bol}		M_{env}	
	r	N	r	N
T_{rot} (warm)	0.17	60	-0.27	48
T_{rot} (hot)	0.09	22	0.06	20
T_{rot} (hot) / T_{rot} (warm)	-0.06	22	0.20	20
$\mathcal{N}$ (warm)	**0.56**	60	**0.65**	48
$\mathcal{N}$ (hot)	0.33	22	**0.79**[a]	18[a]
$\mathcal{N}$ (hot) / $\mathcal{N}$ (warm)	-0.24	22	-0.43	20

Notes. Correlation coefficients exceeding the 3σ threshold values are shown in boldface. Positive coefficients are indicators of correlations while negative – the anti-correlations. No correlations are found with bolometric temperature, T_{bol}. [a] R CrA IRS 5A and L1157 are excluded from the fit. The correlation coefficient when the two sources are included is 0.47, below the threshold.

of source bolometric luminosity. The warm component in the CO diagrams is detected in 60 sources with a median rotational temperature of ~320 K and standard deviation of ~60 K. The hot component is seen in only 22 sources with a corresponding median temperature of ~690 K and standard deviation of 200 K. The larger spread in the hot component temperatures is most likely due to the fewer lines detected in this component and their lower S/N; the intrinsic spread may be smaller. The ratio of the hot and warm rotational temperatures is of order 2.

The correlation coefficients between rotational temperatures or their ratio and source bolometric luminosities (Table 5.1) are in all cases below the 3σ threshold value, equal to $r_t = 0.39$ for $N = 60$ sources and 0.65 for $N = 22$ sources (Marseille et al. 2010). Therefore, in line with previous studies, CO rotational temperatures are not related to the source bolometric luminosities even in this much larger source sample.

On the other hand, the coefficient of $r = 0.56$, translating to the 4.3σ significance level, strongly suggests a correlation between the number of emitting warm CO molecules and the bolometric luminosity (right panel of Figure 5.1). No such correlation is found for the hot component numbers of molecules and their ratio with the number of warm molecules, likely due to the less accurate measurements and limited source sample with a detected hot component. The median of the number of molecules in the hot component is 1.3×10^{48} molecules, while the ratio of the hot over warm number of molecules is about 0.2.

Similar results are obtained when the CO rotational temperatures and emitting molecules are correlated with the envelope masses (Figure 5.2). Small differences between the median values are due to a somewhat lower number of sources with known envelope masses. Note, however, that the correlations between numbers of emitting molecules and the envelope masses are **stronger** than those with bolometric luminosities (Table 5.1). In particular, the number of molecules in the warm component correlates with a higher, 5σ confidence level. Moreover, an additional correlation is found between the hot component and envelope mass. The strength of this correlations is at the 2σ correlation threshold when all 20 sources are considered, but increases to the 3.7σ level when the two outlying sources
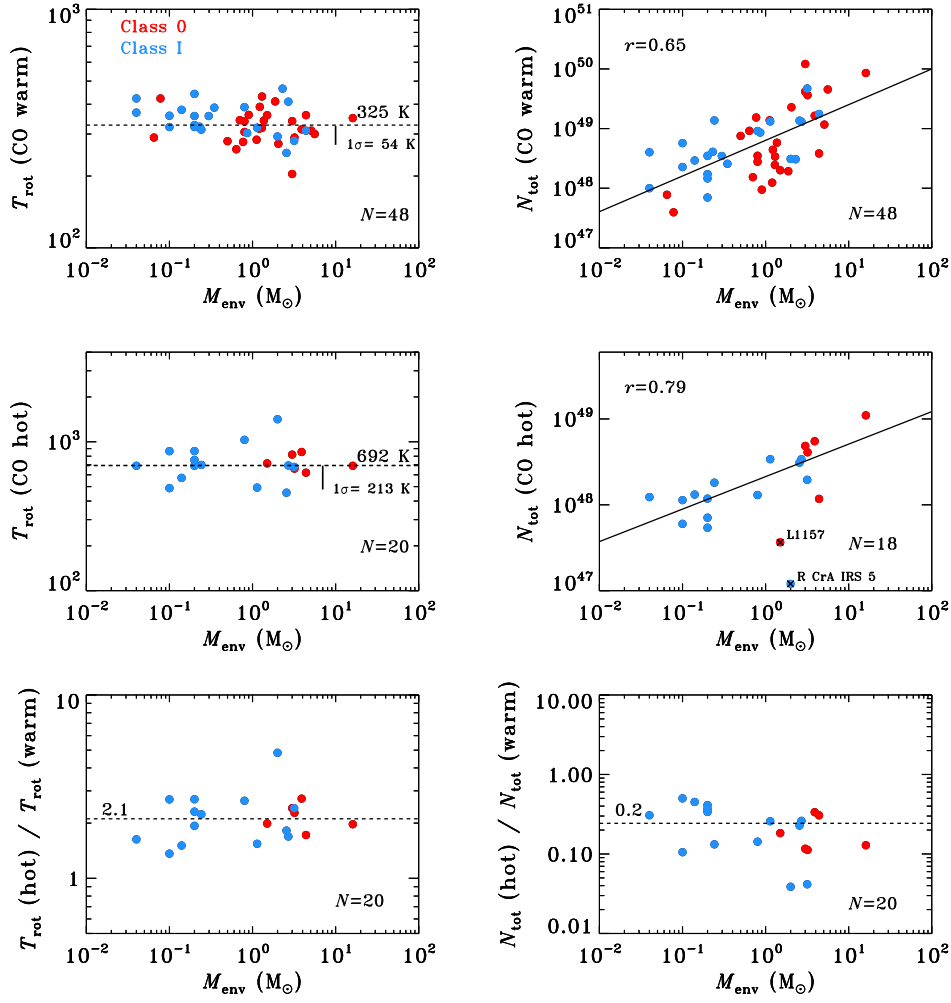
Figure 5.2 – Similar to Figure 5.1, except that all the quantities are shown as a function of envelope mass. Class 0 source L1157 and Class I source R CrA IRS 5A are not taken into account for the fit in the total number of hot molecules versus envelope mass plot (see text) and overplotted with a black cross.

are excluded. These outliers are the Class 0 source L1157 and Class I source R CrA IRS 5A.

Table 5.2 – CO excitation in selected molecular clouds

Cloud	CO warm component			CO hot component			Ratio[a]
	N (% obs)	T_{rot} (K)	$\mathcal{N}_w$ (10^{48})	N (% obs)	T_{rot} (K)	$\mathcal{N}_h$ (10^{48})	
Per	23 (77 %)	318	6.4	7 (23 %)	678	3.1	0.23
Tau	10 (71 %)	359	1.0	3 (21 %)	755	0.7	0.37
Oph	7 (78 %)	345	3.5	3 (33 %)	690	1.1	0.31
Aqu	2 (33 %)	281	14.5	0 (0 %)	–	–	–
W40	1 (14 %)	339	2.8	0 (0 %)	–	–	–
CrA	5 (100 %)	293	3.1	3 (60 %)	710	0.5	0.04
All	60 (67 %)	322	3.9	23 (26 %)	690	1.3	0.21

Notes. The bottom line refers to all sources and not only the ones from the clouds mentioned specifically in the table.
[a] The ratio of numbers of emitting CO molecules in the hot and warm components.

5.4.1.2 Cloud-to-cloud differences

Median rotational temperatures and numbers of emitting molecules are calculated separately for YSOs in different molecular clouds in Table 5.2. The warm component in the CO diagrams is most commonly detected in YSOs located in Corona Australis (all sources), Ophiuchus, Perseus, and Taurus (~70-80 %), and much less frequently detected for sources in the W40 and Aquila molecular clouds (15-30 % detection rate). Similarly, the hot component is detected most often in Corona Australis sources (60 %), less often in Ophiuchus (30 %), Perseus and Taurus (~20 %), and never detected in W40 and Aquarius.

As expected from the previous section, the spread in rotational temperatures between sources in different clouds is small. More significant differences are seen in the total numbers of emitting CO molecules. $\mathcal{N}_w$ is the largest in the Aquila (~15 10^{48}) and Perseus sources (~6 10^{48}), and smallest in the Taurus sources (~1 10^{48}), and of order of ~3 10^{48} for the remaining YSOs. The large number of emitting molecules in the warm component does not directly translate to detections of the hot component, as seen in the Aquila sources. Typically, $\mathcal{N}_h$ is of order of 1 10^{48} for all sources. The ratio of the hot-to-warm numbers of molecules is the lowest for Corona Australis sources (~0.04), and up to an order of magnitude larger, 0.2-0.4, for the remaining clouds.

Environment is therefore not a critical factor for the CO excitation. The differences between YSOs in Perseus and Taurus are not significant, and for the rest of the clouds the samples are too small for definitive conclusions. The CO non-detections in Aquila and W40 are more likely due to low-luminosities of the protostars and not intrinsic cloud differences.

5.4.2 Molecular and atomic cooling

Previous FIR surveys have shown that the proportion of atomic to molecular emission in low-mass protostars changes as they evolve (Nisini et al. 2002b, Podio et al. 2012, Karska

et al. 2013). We revisit these results using our larger sample of sources which is more evenly distributed over the Class 0 and I stages.

The total luminosity in the atomic lines is calculated by summing the fluxes of the two [O I] lines in the PACS spectra, at 63 and 145 μm. For the WILL sources where only the 63 μm line was targeted, the median ratio of the two oxygen lines from the WISH survey ([O I] 63 / [O I] 145 = 10.5, Karska et al. 2013) is used to correct for the missing flux of the [O I] 145 μm line. The [C II] line flux is not included in the atomic luminosities because it is either non-detected or contaminated by the larger-scale cloud emission for the majority of our sources. Unlike the surveys of Giannini et al. (2001) and Nisini et al. (2002b) using the single ISO beam of 80″, only objects with [O I] emission spatially associated with the studied sources are included in our analysis. As demonstrated in Table E.1. of Karska et al. (2013), PACS fluxes are up to a factor of a few lower than the ISO values for the same sources, most probably due to elimination of the cloud contribution to the [O I] emission.

The total far-infrared (55-210 μm) luminosity of the CO lines is calculated for our sources in two ways. For sources with full PACS spectra (from the DIGIT program), the total flux in the CO lines is simply the sum of fluxes from all detected lines. For sources for which only selected CO transitions were targeted (from the WISH and WILL programs), the CO rotational temperatures were used to obtain the fluxes of the missing lines. The procedure is applied only for sources with a minimum of three detected lines in each of the (warm and / or hot) components on the CO diagrams. In particular, for cases where the hot component temperature could not be well-determined, the warm component temperature is used for extrapolation. The extrapolation to lower$-J$ transitions not accessible to PACS ($J_\mathrm{u} < 14$) is not done due to the fact that the so-called 'cold' component on CO diagrams traces the entrained outflow gas of $T \lesssim 100$ K (Yıldız et al. 2013, Goicoechea et al. 2012), not the shocked, $T \gtrsim 300$ K gas seen by PACS.

The histograms of total CO and [O I] luminosities over bolometric luminosities (L_{CO} / L_{bol} and $L_{\mathrm{[OI]}}$ / L_{bol}) and of the ratio of the cooling in the two species (L_{CO} / $L_{\mathrm{[OI]}}$) are presented in Figure 5.3. The histogram of L_{CO} / L_{bol} peaks in the 10^{-3}-$10^{-2.5}$ bin for Class 0 sources and in the $10^{-3.5}$-10^{-3} bin for Class I sources, demonstrating that the fractional CO luminosity decreases for the more evolved sources. This is also reflected by the observed ranges of L_{CO} / L_{bol}, which extend to larger values for Class 0 sources and to smaller values for Class I sources.

Such a trend is not seen when histograms of $L_{\mathrm{[OI]}}$ / L_{bol} for the two classes of sources are compared. The ratio peaks in the 10^{-4}-10^{-3} bins with a small fraction of sources with higher or lower ratios up to an order of magnitude, irrespective of the evolutionary stage. These results are qualitatively different from previous studies with ISO, where the histogram for Class 0 sources peaked 2 orders of magnitude higher compared to the Class I sources, at about $10^{-2.5}$ (Nisini et al. 2002b, see also Podio et al. 2012). The large absolute values of $L_{\mathrm{[OI]}}$ / L_{bol} from ISO indicate significant contamination from nearby cloud emission, which could possibly be more severe in the surroundings of Class 0 sources.

The histograms of the L_{CO} / $L_{\mathrm{[OI]}}$ for Class 0 and I sources both peak in the 10^0-$10^{0.5}$ bin, showing that typically the CO luminosity is equal to or up to a factor ~ 3 larger than the [O I] luminosity. There is a tail of Class 0 sources with an even larger fraction of CO to [O I] luminosities. The histogram for the Class I sources is more symmetric, with only

195
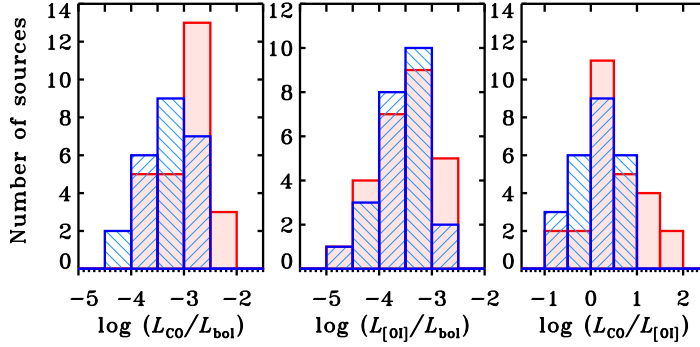
Figure 5.3 – Histograms of the CO (left) and [O I] (center) cooling over bolometric luminosity and the ratio of cooling in CO and [O I] (right). The red color shows the distributions for Class 0 sources and blue for Class I sources.

a slightly higher number of sources at lower L_{CO} / $L_{[OI]}$ ratios, corresponding to large fractions of atomic oxygen emission. In total, however, more sources in the Class I stage have more luminosity in CO than in atomic lines, but the maximum L_{CO} / $L_{[OI]}$ values are up to an order of magnitude lower than for the Class 0 sources. Similar trends have been reported in Nisini et al. (2002b) and Karska et al. (2013) for smaller samples of sources.

The large scatter in the rotational diagrams of H_2O and OH (Karska et al. 2013, Wampfler et al. 2013) implies that the accuracy of extrapolated fluxes of lines not targeted in the WISH and WILL programs is significantly lower than for the case of CO (Lee et al. submitted). Therefore, molecular cooling in H_2O and OH lines and, consequently, the total far-infrared cooling, can only be well-determined for a limited sample of sources with full PACS spectra observed in the DIGIT and WISH programs and is not presented here.

5.4.3 Mass flux rates in jets and outflows

Maps of outflows in low−J CO lines are commonly used to calculate outflow energetics of the entrained material in low-mass young stellar objects (e.g. Curtis et al. 2010, van der Marel et al. 2013, Yildiz et al. subm.). The outflow mass can be derived from the total column density of CO by conversion to H_2 mass over the whole area of the outflow (details in Appendix C in van der Marel et al. 2013). The mass outflow rate is then calculated by dividing the mass by the so-called 'dynamical age' of the outflow, which is obtained
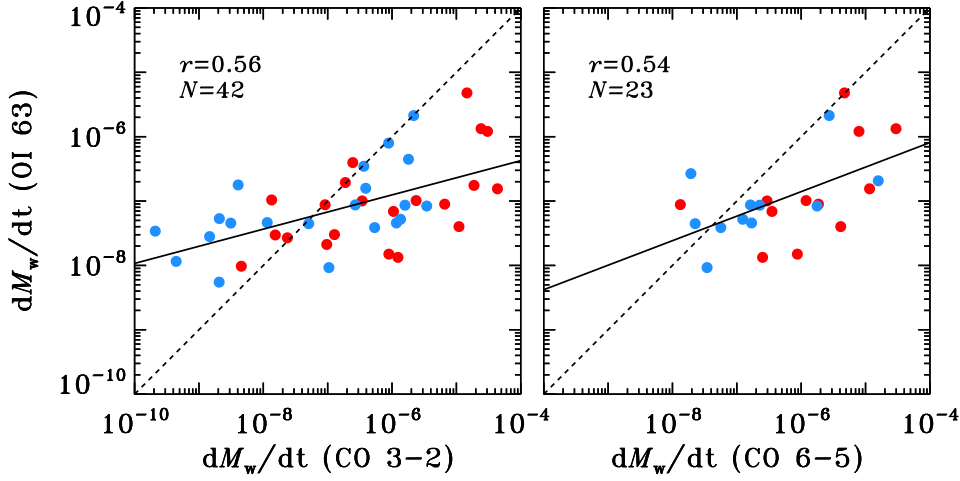
Figure 5.4 – Wind mass flux rates calculated from the [O I] line and CO 3-2 (left, from Mottram et al. in prep) and CO 6-5 (right, from Yildiz et al. subm.) lines. Solid lines show the best fit to the data and the dashed lines show the y = x function.

from the current outflow extent and the maximum velocity seen in the CO line wings. Therefore, the CO mass flux rate is by definition an 'integrated' mass flux rate over the outflow lifetime and is sensitive to the assumed outflow inclination. If momentum flux conservation applies, the wind mass flux rate implied by the CO lines, $dM_w(CO)/dt$, is subsequently calculated by multiplying the observed CO rate by the ratio of maximum velocity of CO line profiles and the assumed wind velocity of 100 km s^{-1}.

An alternative method of calculating the mass flux rates was proposed by Hollenbach (1985), who showed that for the range of physical conditions found in YSOs the mass flux rates scale with the [O I] line luminosity, $dM_w/dt=10\,L(O\,I\,63)$, in units of 10^{-5} M$_\odot$ yr^{-1}. The formula is valid under the assumption that the [O I] line traces primarily the dissociative shock caused by the impact of the jet / wind on the surrounding cloud. The contribution from the non-dissociative outflow shocks is assumed to be negligible and effects of outflow geometry are neglected.

Figure 5.4 and Table 5.3 compare the mass flux rates calculated using the two methods. The majority of the sources show higher mass flux rates inferred from the CO lines, with only a few sources lying on the y = x line. There are also about 10 sources with lower mass flux rates derived from CO 3-2 than [O I]. Those low CO / [O I] mass flux rates sources are typically Class I sources observed as part of the WILL program. Overall, the CO 3-2 and [O I] mass flux rates show a ~3.6σ correlation with the slope clearly deviating from the y = x function.

The median [O I] mass flux rate equals about 5 10^{-8} M$_\odot$ yr^{-1}, of the same order for both Class 0 and I sources (Table 5.3). The median CO 3-2 and CO 6-5 mass flux rates are of order 10^{-7}-10^{-6} M$_\odot$ yr^{-1}, but those are obtained for a subsample of sources observed in [O I]. The median ratios of the CO 3-2 / [O I] and CO 6-5 / [O I] are of the order

197

Table 5.3 – Jet / outflow mass loss rates from [O I] and CO lines

	dM_w/dt ($M_\odot$ yr^{-1})			Ratios of dM_w/dt	
	[O I] 63 μm	CO 3-2	CO 6-5	CO 3-2 / [O I]	CO 6-5 / [O I]
All (median)	$5.4\ 10^{-8}$	$1.2\ 10^{-7}$	$3.5\ 10^{-6}$	3	4
(mean)	$2.4\ 10^{-7}$	$3.3\ 10^{-6}$	$3.7\ 10^{-6}$	27	19
Class 0	$4.3\ 10^{-8}$	$1.2\ 10^{-7}$	$1.5\ 10^{-6}$	5	15
	$2.6\ 10^{-7}$	$3.0\ 10^{-6}$	$5.2\ 10^{-6}$	47	27
Class I	$7.0\ 10^{-8}$	$1.9\ 10^{-7}$	$1.6\ 10^{-7}$	1	2
	$2.1\ 10^{-7}$	$5.3\ 10^{-6}$	$1.9\ 10^{-6}$	27	10

Notes. CO 3-2 mass loss rates are from Mottram et al. (in prep.) and Yildiz et al. (subm.), for WILL and WISH / DIGIT sources respectively. CO 6-5 rates are calculated for the same WISH / DIGIT sources in Yildiz et al. (subm.).

of unity for both Class 0 and I sources. Larger differences between the two methods of determining wind mass flux rates are seen when the mean values are compared (Table 5.3). In particular, the mean CO / [O I] ratios are of the order of 10, indicating that some of the sources with the largest wind mass flux rates inferred from CO are at the same time weak in [O I].

Note that the CO maps were obtained in a uniform way and the mass outflow rates were calculated using the same method with absolute uncertainties of a factor of a few (van der Marel et al. 2013). Lower rates from the CO 3-2 with respect to CO 6-5 maps (Table 5.3) are due to the intrinsic differences in the sample of sources: the CO 3-2 data are obtained for a significantly larger number of sources, including the low luminosity sources from the WILL program. Despite these differences, the results are qualitatively the same for the CO 3-2 and CO 6-5 rates, as seen in Figure 5.3. For more detailed discussion of these results see §5.5.3.

5.4.4 Comparisons to models of shocks and photodissociation regions

Since PACS does not resolve the emitting regions of the molecules and atoms, comparisons of such observations with shock models have concentrated on line ratios (e.g. Santangelo et al. 2012, Vasta et al. 2012, Lee et al. 2013, Santangelo et al. 2013, Karska et al. subm.). Various molecular ratios indicate an origin in $C-$type shocks, which emit copiously in CO, H$_2$O, and OH, but produce very little [O I] emission.

[O I] shock predictions are calculated using the Flower & Pineau des Forêts (2003) model for a finely-sampled grid of shock velocities v, from 10 to about 50 km s^{-1}, and two pre-shock densities, $n_H = 10^4$ and 10^5 cm^{-3}. The model intensities in units of erg cm^{-2} s^{-1} sr^{-1} are translated to W cm^{-2} assuming that the emission entirely fills one spaxel in the PACS maps (1 sr $\sim$ 2.1 $10^{-9}\ \pi$). The one spaxel size is chosen despite the fact that PACS maps in the [O I] and [C II] lines often show emission extending to more than one spaxel (this work and Karska et al. 2013), because the actual emitting region observed
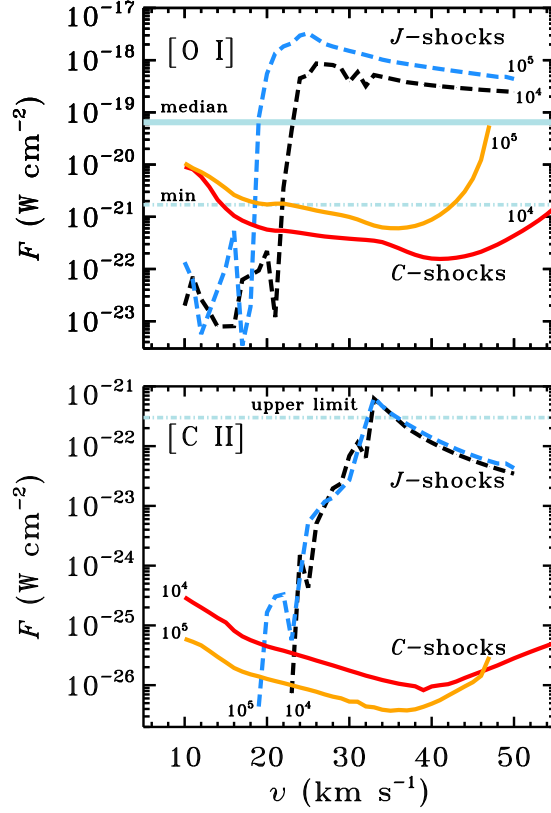
Figure 5.5 – Absolute fluxes of the [O I] line at 63 μm (top) and the [C II] line at 158 μm (bottom) predicted by C- and J-shock models of Flower & Pineau des Forêts (2003) and confronted with observations. Median observed fluxes of [O I] shown in the top panel are calculated only for those sources where the emission is associated with the source and not large-scale cloud emission. The minimum detected flux of [O I] is shown also for reference. In case of [C II], in the rare cases that the line is actually detected and spatially associated with the source, the fluxes exceed the range shown in the bottom panel. The instrumental upper limit for the line detection is shown as reference.

by each spaxel is likely only a fraction of the spaxel size ('filling factor' below unity). A possible underestimate of a factor of a few of the emitting region size does not affect the conclusions below given the orders of magnitude variations probed by the models and observations.

Comparison of absolute observed and model line fluxes of the [O I] 63 μm and [C II] 158 μm lines are shown in Figure 5.5 (top panel). The median observed [O I] flux, calculated for sources with emission spatially associated with YSOs, equals $\sim 10^{-19}$ W cm^{-2} and falls between the predictions for the $C-$ and $J-$type shock models for a wide range of shock velocities. The $C-$type shock model fluxes decrease from about 10^{-20} W cm^{-2}

199

by 1 and 2 orders of magnitude in the velocity range from 10 to about 40 km s^{-1} for the assumed pre-shock densities of 10^5 cm^{-3} and 10^4 cm^{-3}, respectively. Above 40 km s^{-1}, the fluxes increase to values as high as to 10^{-19} W cm^{-2} for the models with higher pre-shock densities, but still not sufficient to explain the [O I] emission in many of the brightest sources. The $J-$type shock model fluxes, on the other hand, fit even the brightest observed [O I] lines. A sharp increase from about 10^{-22} W cm^{-2} to 10^{-18} W cm^{-2} occurs when the shock becomes dissociative at velocities of about 20 km s^{-1}. Depending on the size of the emitting region, likely lower than the full spaxel area, the observations of all absolute line fluxes of [O I] can be reproduced with $J-$type shocks.

The observed fluxes and limits of the [C II] line at 158 μm greatly exceed the model predictions for both $C-$ and $J-$type shock models (Figure 5.5, bottom panel). Whenever the line is detected and associated with a YSO, the fluxes exceed 10^{-21} W cm^{-2}, 4 orders of magnitude above the model $C-$ shock fluxes and a factor of a few above the peak [C II] flux from the $J-$ shocks, at about 30 km s^{-1}. In many sources, however, the [C II] line is not detected and only the upper limit can be used for comparisons with the models. For those sources, the observed limit is consistent with both $J-$ and $C-$type shocks.

Since the shock models cannot reproduce the observed [C II] fluxes for the sources where it is detected, [C II] is most likely the result of CO photodissociation and photoionization of C. This requires hard UV photons with $\lambda < 1100$ Å, likely produced in the vicinity of the protostar, in accretion flows in the star-disk boundary layer and / or fast bow-shock (e.g. Spaans et al. 1995, van Kempen et al. 2009a). Models of photodissociation regions (PDRs, Tielens & Hollenbach 1985) can be used to constrain the UV field and densities using absolute intensities of atomic and ionic lines as well as molecules. In our case, where most of the molecular emission and a part of [O I] emission originates from shocks, comparisons to absolute line intensities of [C II] are the most reliable measure of FUV alone. To better constrain the range of possible parameters, the ratio of [C II] and [O I] can be used, taking into account that a fraction of the [O I] emission comes from the dissociative shocks. This ratio rapidly decreases with density, controlled mainly by [O I] with its high critical density of about $\sim 5\ 10^5$ cm^{-3}, two orders of magnitude higher than for [C II] (Kaufman et al. 1999).

Figure 5.6 compares the observed [C II] / [O I] versus [C II] intensities and the PDR model predictions from Kaufman et al. (1999). The [C II] intensities are calculated assuming a size of one spaxel and shown only for sources where the [C II] emission is spatially associated with YSOs. The range of observed [C II] intensities equals 10^{-5}-10^{-4} erg cm^{-2} s^{-1} sr^{-1}, whereas [C II] / [O I] ranges from 10^{-2}-10^0. The corresponding model densities are in the range from 10^5 cm^{-3} to 10^6 cm^{-3}. The majority of the sources show a very similar incident UV field, about 10^2 G_0 on scales of $\sim$1000 AU, with the exception of a more massive source – Serpens SMM1 (#66) – in the 10^3 G_0 regime.

Possible contributions from shocks to the [O I] intensity would decrease both the densities and the UV field matching the observations (see Figure 5.6). For example, if 90% of [O I] flux comes from the shock, corresponding to an increase of observed [C II] / [O I] by a factor of 10, the best fit densities are in the range 10^4-10^5 cm^{-3} and UV field of $\sim 10^1$-10^2 G_0.

Finally, we note that the diagnostic diagram from Figure 5.6 can be used to distinguish
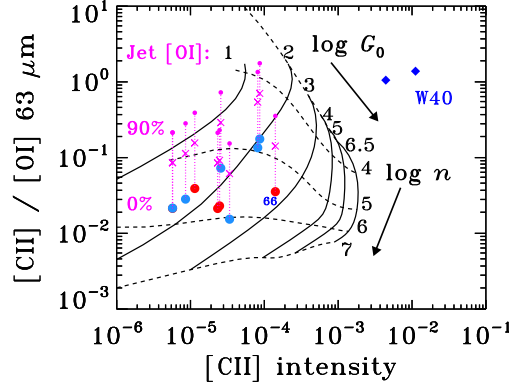
Figure 5.6 – Observed line ratio of the [C II] line at 158 μm and the [O I] line at 63 μm as function of the [C II] line intensity (red dots for Class 0 and blue dots for Class I objects) and models of photodissociation regions from Kaufman et al. (1999). Models are shown for densities from 10^3 to 10^7 cm^{-3} (in dashed lines) and for incident UV from 10^1 to $10^{6.5}$ G$_0$ (in solid lines). Small magenta dots and crosses indicate line ratios assuming that 90% and 75% of [O I] flux comes from the jet, respectively. Two cloud-related PDR regions in the W40 cloud are shown with blue diamonds.

between PDRs associated with YSOs and clouds. For comparison with the local PDRs, two sources observed within a strong PDR in the W40 cloud (W40-2 and W40-3) are shown. Both of them are located in the low-density and high-UV regime that is very distinct from our observed YSOs.

5.5 Discussion

As demonstrated in the previous sections, far-IR lines can inform about the physical processes in the surroundings of young protostars. First, the origin of the CO line emission is discussed based on excitation diagrams and correlations presented in §1.4.1. Second, possible scenarios responsible for the [O I] emission are considered, which are finally related to the mass loss rates calculated based on the [O I] luminosity.

5.5.1 Origin of CO emission: a two-shock scenario

Similar to individual and small subsample studies with *Herschel* / PACS, two temperature components are seen in CO rotational diagrams of Class 0/I. The median T_{rot} are $\sim$ 320 K and $\sim$ 690 K, for the 'warm' and 'hot' components, respectively, and do not correlate with physical parameters (bolometric luminosity and envelope mass). Such correlations are found for the total number of emitting CO molecules, in particular using the envelope mass, with the ratio of the hot-to-warm emitting molecules of order of 0.2. At the same

201

time, however, the detection rate for the 'hot' component is significantly higher for the Class I sources, which have lower envelope masses.

The above results quantitatively agree with the interpretation proposed for the 'hot' CO component by Kristensen et al. (2013) who linked it to the 'medium' or 'offset' component extracted from the complex H_2O and CO profiles from HIFI and arising from dense ($n \sim 5 \times 10^4 - 10^6$ cm^{-3}) and hot ($T \sim 750$ K) gas in the inner 100 AU of the protostellar envelope (see also Kristensen et al. 2012). Comparison to shock models from Neufeld & Dalgarno (1989) implied an origin in a dissociative shock with the dissociation due to the UV radiation from the accreting protostar (see also Kristensen et al. in prep.). The 'hot' CO component would then trace the part of the shock where H_2 reforms (Kristensen et al. 2013).

The larger detection rate of the highly-excited CO lines in the more evolved sources from our study could be therefore related to the smaller shielding (wide-angle outflows, more dispersed envelopes) of UV radiation in the Class I sources rather than the higher dust continuum shielding opacity in the Class 0 sources. The detection of highly-excited H_2O lines in the sources with high$-J$ CO emission suggest the same origin during the embedded phase. In the Class II sources, where the envelope is fully dispersed, the hot H_2O emission and non-detections of high$-J$ CO argue in favor of the disk origin (Fedele et al. 2012, Riviere-Marichalar et al. 2012).

The 'warm component', on the other hand, traces the part of the shock that is more shielded from UV, probably further out along the outflow or deeper into the envelope. High absolute intensities of CO lines cannot be accounted by dissociative shocks alone and require the non-dissociative shock component (Karska et al. subm.).

5.5.2 Origin of [O I] emission: disk, jet, or UV-heated cavity walls?

A possible contribution from the disk to the [O I] 63 μm line is investigated via comparisons with more evolved, Class II sources. The envelope mass of Class II sources is negligible and the corresponding accretion / ejection rates are much lower compared to Class 0/I sources. Therefore, the contribution from the jet is expected to be low, with the bulk of [O I] emission originating in the disk.

Figure 5.1 shows our protostars on a diagram comparing the [O I] line emission with continuum at 63 μm with separate fits to the non-outflow Class II sources and Class II sources with associated jet emission taken from Howard et al. (2013)[3]. Not surprisingly, almost all of our sources are located above the 'non-outflow' fit and follow the fit to the 'outflow' Class II sources instead.

The relative contribution of the jet and / or UV–heated cavity walls to the total [O I]

---

[3] We note a mistake in equation 4 of Howard et al. (2013), which relates the [O I] line emission and continuum flux at 63 μm for the outflow sources, and not the non-outflow sources as claimed in the text. Based on their Figure 6, we obtained the equation for the non-outflow sources:

$$\log F([\text{O I}]) = 0.737 \times \log(F_{\text{cont}}) - 0.67 \qquad (5.1)$$

where $F([\text{O I}])$ refers to the line flux of the [O I] 63 μm line in units of 10^{-16} W m^{-2} and F_{cont} to the continuum flux at 63 μm in Jy.
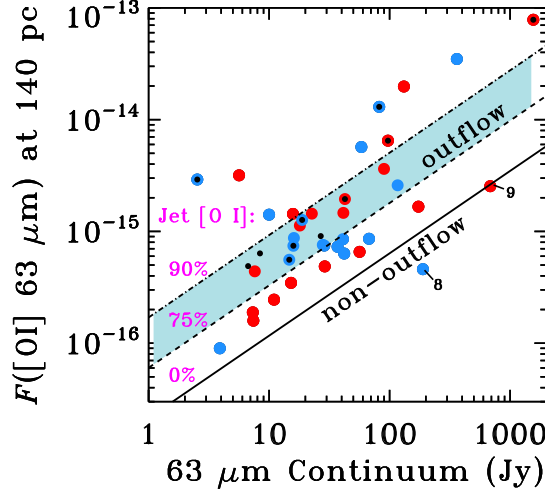
Figure 5.1 – Fluxes of the [O I] line at 63 μm as function of continuum flux at similar wavelength scaled to the common distance of 140 pc. The best fits to Class II sources in Taurus with jet / outflow emission (dashed line) and without (solid line) from Howard et al. (2013) are included for reference. Black dots denote sources with [C II] line detections (see Figure 5.6), three of them have less certain continuum values and as such have no corresponding blue / red circles. Sources lying on the dashed line have 25% contribution from the disk and 75% from the jet to the total [O I] emission, assuming that the solid line represents 100% contribution from the disk. The dash-dotted line represents sources with 90% jet contribution to [O I]. The shaded region denotes sources with 75% - 90% jet contribution to [O I] emission and includes the bulk of our sources.

emission can then be estimated assuming that the fit to the 'non-outflow' sources corresponds to the 100% emission coming from the disk. Accordingly, the sources on the 'outflow' fit have about 75% contribution from the jet / cavities to the [O I] flux, with a fraction of our sources showing more than 90% of these contributions (i.e. less than 10% contribution from the disk). As a consequence, we can rule out the disk emission to be an important factor influencing the [O I] emission observed in our protostars.

The excess [O I] emission is produced either in dissociative jet shocks, including a bow shock at the tip of the jet, or as a result of irradiation of outflow cavity walls by UV photons from these shocks and from a central protostar. A possible way to distinguish between the jet shocks and UV-heated cavity walls is to determine the densities of the emitting material. In the two-shock model, where the dissociative and non-dissociative shocks are assumed to be in a steady state, the higher-velocity jet shock propagates in smaller density material than the non-dissociative shock (Hollenbach 1997, Giannini et al. 2001).

For a subsample of our sources that show [C II] detections spatially associated with

protostars, the analysis of PDR emission provides an independent measure of material densities that can be compared with densities for CO and H_2O excited in a non-dissociative shock. Since all of those sources have at least 75% of jet / cavities contribution to the [O I] emission (Figure 5.1), the corresponding gas densities are of order 10^4-$10^{5.5}$ cm^{-3} (Figure 5.6). The pre-shock densities obtained from the ratios of pairs of CO and H_2O lines are of similar order ($\sim 10^5$ cm^{-3}, Karska et al. subm, this work), but become larger by about a factor of 10 when the compression factor for a non-dissociative shock is accounted for. As a consequence, the densities in the outflow cavity shocks are too high to explain the [O I] emission, confirming a different origin in a dissociative jet shock for the considered subsample of sources.

Generally, the relative fraction of emission from the jet shocks and UV-heated cavity walls will likely differ depending on the evolutionary stage of a protostar and species considered. Large OH intensities relative to H_2O found in the Class I sources (Figures 5.2 and 5.A.1) indicate the increasing importance of H_2O photodissociating UV photons as a protostar evolves. At the same time, no such difference is seen between [O I] emission relative to H_2O in Class 0/I sources. In fact, both the total cooling in the [O I] lines (Figure 5.3) and the fraction of sources with detected high-velocity emission in the [O I] 63 μm line (Figure 5.1) is similar in Class 0 and I stages. On the other hand, if the [O I] emission is produced in a slower ($v \sim 15 - 40$ km s^{-1}), $C-$ or $J-$type shock, it should decrease for the more evolved sources with lower envelope masses (Figure 5.5). A combination of this effect with the larger amount of UV photons penetrating such a dispersed envelope in the Class I stage could provide an explanation to all our observations.

5.5.3   Mass flux rates: evidence for jet evolution?

The origin of the [O I] emission has consequences for the interpretation of the differences in the mass flux rates obtained from the low$-J$ CO and [O I] lines (§4.3). The [O I] mass flux rates are equal to $\sim 10^{-8}$ M$_\odot$ yr^{-1} for Class 0/I sources and as such are similar or up to an order of magnitude lower than the CO mass loss rates for the same sources (Figure 5.4).

The opposite result was obtained in Giannini et al. (2001), based on *ISO* observations of [O I] towards ~10 Class 0 sources. Here, the [O I] mass loss rates were comparable or higher to the CO rates, clearly because of the cloud contamination within a single beam. Some discrepancy between mass flux rates from CO and [O I] lines was seen in a subsample of our sources analyzed in Karska et al. (2013). In contrast to this preliminary study, however, no decrease in the [O I] luminosity is found from Class 0 to Class I stage (Figure 5.3 and Figure 5.3).

The mass flux rates from the [O I] line are calculated on the assumption that all [O I] emission is produced in the jet shock, which is most likely not the case. If indeed part of the [O I] emission is a product of H_2O photodissociation in a slower shock, the calculated rates are only upper limits to the actual mass loss rates, and differ even more from the CO 3-2 and 6-5 rates, in particular for the more evolved sources. In such more evolved sources, the outflow cavity has widened and emptied, resulting in less efficient entrainment.

Interestingly, the majority of the sources with low CO / [O I] mass flux ratios are the more evolved Class I sources (Figure 5.4). Bright [O I] jets are also seen in Class II sources (Podio et al. 2012), where much weaker CO wind mass flux rates are found. In contrast, the most deeply embedded sources have large CO / [O I] mass flux ratios suggesting that [O I] underestimates the momentum flux, perhaps because the jet is partly molecular (Nisini et al. in prep.).

Altogether, this shows a possible evolution of the wind: in the most deeply embedded stages the jet is mostly molecular and evolves to the more atomic form as the envelope is dissipated, the outflow cavities widen, and the gas entrainment is reduced. Velocity-resolved observations of [O I] are needed to determine the relative jet and UV contributions and thus the details of the jet evolution.

5.6 Summary and conclusions

Herschel / PACS observations of hot gas in the surroundings of low-mass protostars allow to disentangle and characterize energetic physical processes associated with the earliest stages of star formation. CO and H_2O line are primary tracers of non-dissociative shocks occurring in the outflows on 10^3-10^4 AU scales. Dissociative shocks due to the fast-moving jet and H_2O photodissociation by UV photons contribute to the [O I] emission. The [C II] line is a unique tracer of the UV strength when spatially associated to a young protostar. The main conclusions are the following:
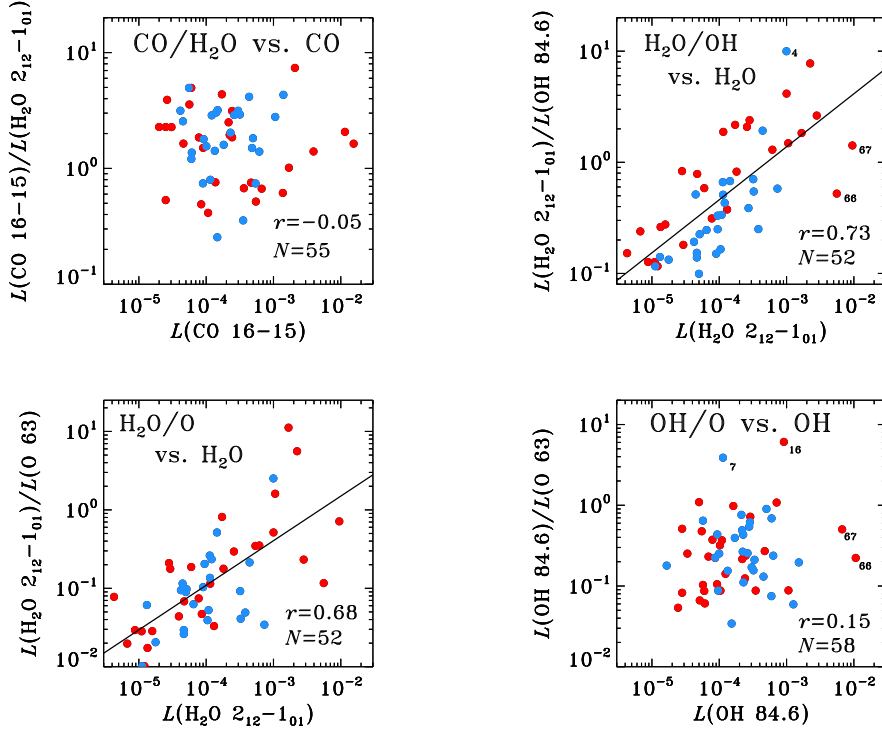
1. Two temperature components are found on CO diagrams, with $T_{rot} \sim 320$ K and ~ 690 K. Although the number of emitting molecules in the two components correlates with the envelope mass, the detection rates of the hot component are significantly lower for the Class 0 sources. These results are consistent with the interpretation proposed by Kristensen et al. (in prep.) that the hot component originates in a dissociative shock exposed to protostellar UV photons. The warm component, on the other hand, originates in non-dissociative shocks to account for the high absolute intensities of CO lines. The highly-excited H_2O line is most probably related to the same physical component.

2. Similar to previous studies, the CO molecular cooling over bolometric luminosity ratio is larger for the Class 0 sources. The total cooling in the [O I] line, on the other hand, is the same for Class 0/I sources, contrary to the *ISO* results from Nisini et al. (2002b). The contribution from the disk to the [O I] emission is negligible for the deeply-embedded protostars considered here. The [O I] flux originates in the jet shocks and in the UV irradiated cavity walls where H_2O photodissociates. The fraction of the jet emission decreases for more evolved sources, but the penetration by UV photons is enhanced, explaining a similar amount of [O I] cooling in Class 0/I sources.

3. Incident UV field and densities are calculated for a subsample of sources with detected [C II] emission using the Kaufman et al. (1999) models of photodissociation

205

regions. UV fields of $\sim 10 - 100\,\mathrm{G_0}$ and densities of $n \sim 10^4 - 10^{5.5}\,\mathrm{cm^{-3}}$ are determined. The densities are an order of magnitude lower than the values obtained from comparison of molecular emission to shock models indicating the origin inside the outflow cavities.

4. Mass flux rates in the jet/wind of order $\sim 10^{-8}\,\mathrm{M_\odot\,yr^{-1}}$ are calculated from the [O I] 63 μm line for both Class 0 and I sources. Those values are similar or up to an order of magnitude lower than the wind mass flux rates inferred from CO using momentum conservation and obtained for the same sources in a uniform manner. Differences are found between Class 0 and I sources, with the latter showing the [O I] mass flux rates exceeding the CO rates, suggesting that the atomic component of the jet dominates.

Acknowledgements

Figure 5.A.1 – Flux ratio - flux correlations between the CO 16-15 / H_2O 2_{12}-1_{01} and CO 16-15 lines (top left), the H_2O 2_{12}-1_{01} / OH 84.6 μm and H_2O 2_{12}-1_{01} lines (top right), the H_2O 2_{12}-1_{01} / [O I] 63 μm and H_2O 2_{12}-1_{01} lines (bottom left), and the OH 84.6 μm / [O I] 63 μm and OH 84.6 μm lines. Class 0 sources are shown in red and Class I sources in blue. Correlation coefficients (r) and number of sources with line detections (N) are shown on the plots. Solid lines show the best linear fits obtained with a least-squares method for cases where the correlation coefficient exceeds the 3σ threshold.

Appendix

5.A   Correlations of fluxes and flux ratios

Figure 5.A.1 shows correlations between line ratios of different species as functions of line fluxes of one of those species. Strong, ~5σ correlations are found between the H_2O 2_{12}-1_{01} / OH 84.6 μm ratio and the H_2O 2_{12}-1_{01} flux and between the H_2O 2_{12}-1_{01} / [O I] 63 μm ratio and the H_2O 2_{12}-1_{01} flux.

Table 5.B.1 – Correlation coefficients for line fluxes and sources parameters relations

|	L_{bol}		M_{env}	
	r	N	r	N
CO 16-15	**0.56**	70	**0.60**	57
CO 29-28	0.53	46	0.55	39
H_2O 2_{12}-1_{01}	0.45	57	**0.75**	47
H_2O 2_{21}-1_{10}	0.54	52	**0.72**	44
OH 84 μm	**0.58**	62	0.44	49
O I 63 μm	**0.65**	70	0.47	56

Notes. All correlation coefficients exceed the 3 σ threshold values, the ones exceeding the 4 σ threshold are shown in boldface.

5.B   Correlations with sources parameters

Figures 5.B.1 and 5.B.2 illustrate how line luminosities of molecules and [O I] correlate with two main physical parameters of the sources: bolometric luminosities and envelope masses. The correlations with source bolometric luminosities are particularly strong for the [O I] and OH lines (see Table 5.B.1) and to a smaller extent with the CO 16-15 line. Lack of correlation is found for H_2O and higher$-J$ CO transitions.

The envelope masses, on the other hand, correlate most strongly with the H_2O lines (at 5σ level) and CO 16-15 line (at 4.5σ level). In the sub-thermally excited H_2O lines this could be just an excitation effect, however a strong correlations with the CO line and the decrease of line with of H_2O lines for the Class I sources (Mottram et al. submitted) indicate that evolution also plays a role.
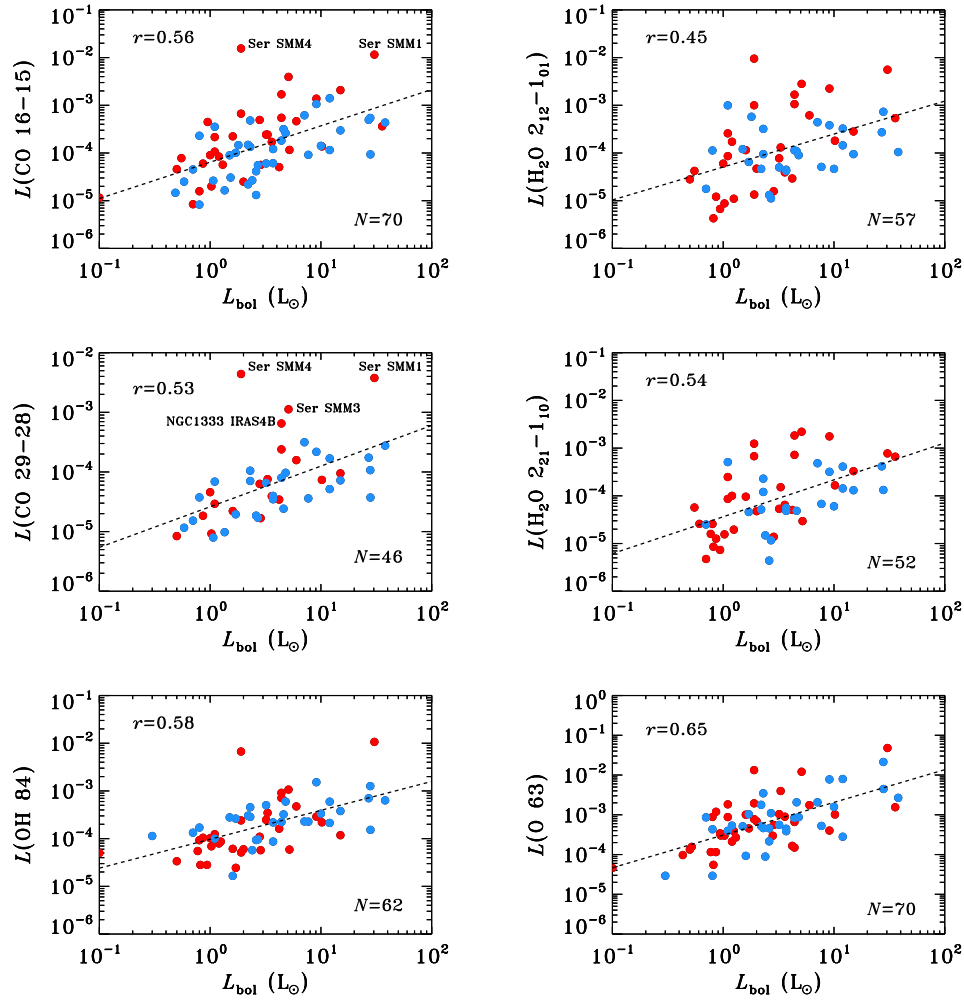
Figure 5.B.1 – Correlations of source bolometric luminosity and line fluxes of CO 16-15, CO 29-28, H_2O 2_{12}-1_{01}, H_2O 2_{21}-1_{10}, OH doublet at 84 μm, and [O I] line at 63 μm. Correlation coefficients (r) and number of sources with line detections (N) are shown on the plots and in Table 5.B.1.

5.C Rotational diagrams for the WILL sources

Figures 5.C.1 and 5.C.2 show CO rotational diagrams for the WILL sources. Separate linear fits are done to the transitions located in the 'warm' and 'hot' components, the same as used in Karska et al. (2013) and Green et al. (2013). Figures 5.C.3 and 5.C.4 show H_2O rotational diagrams with only one linear fit to all observed lines.
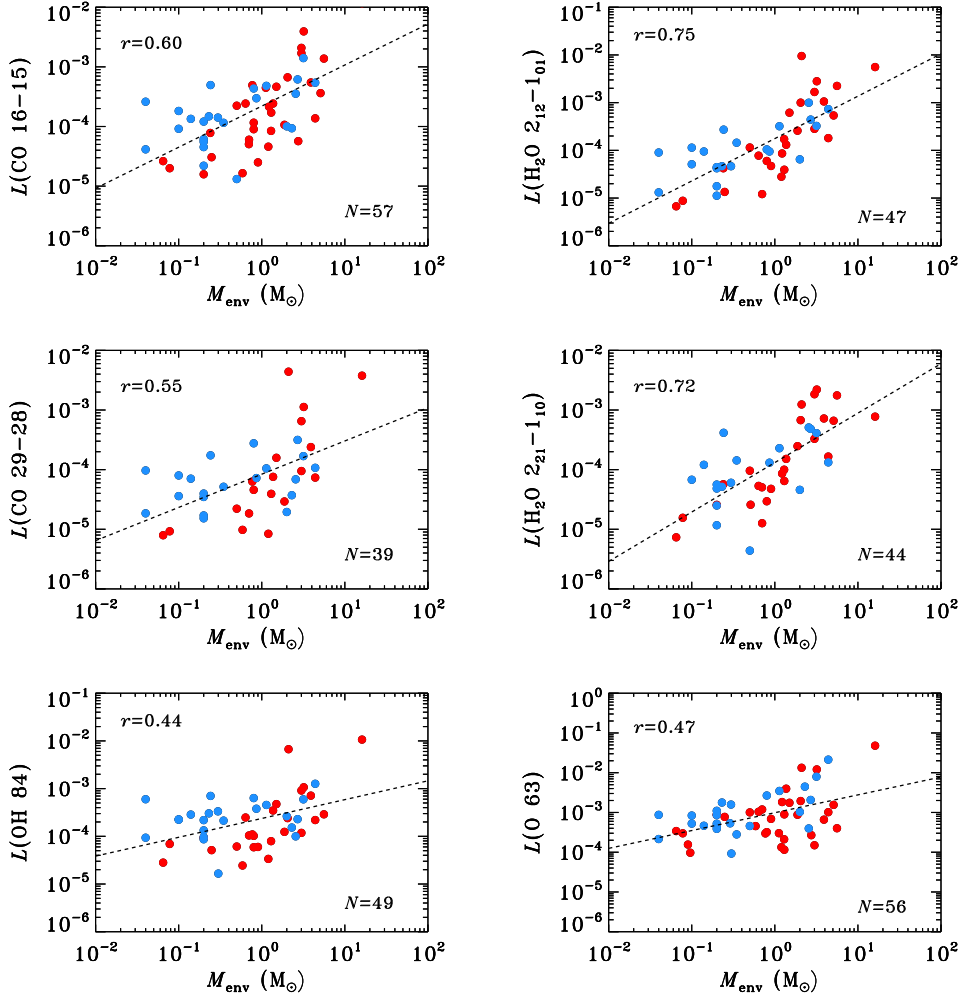
Figure 5.B.2 – Similar to Figure 5.B.1, except that the line fluxes are correlated with envelope masses.
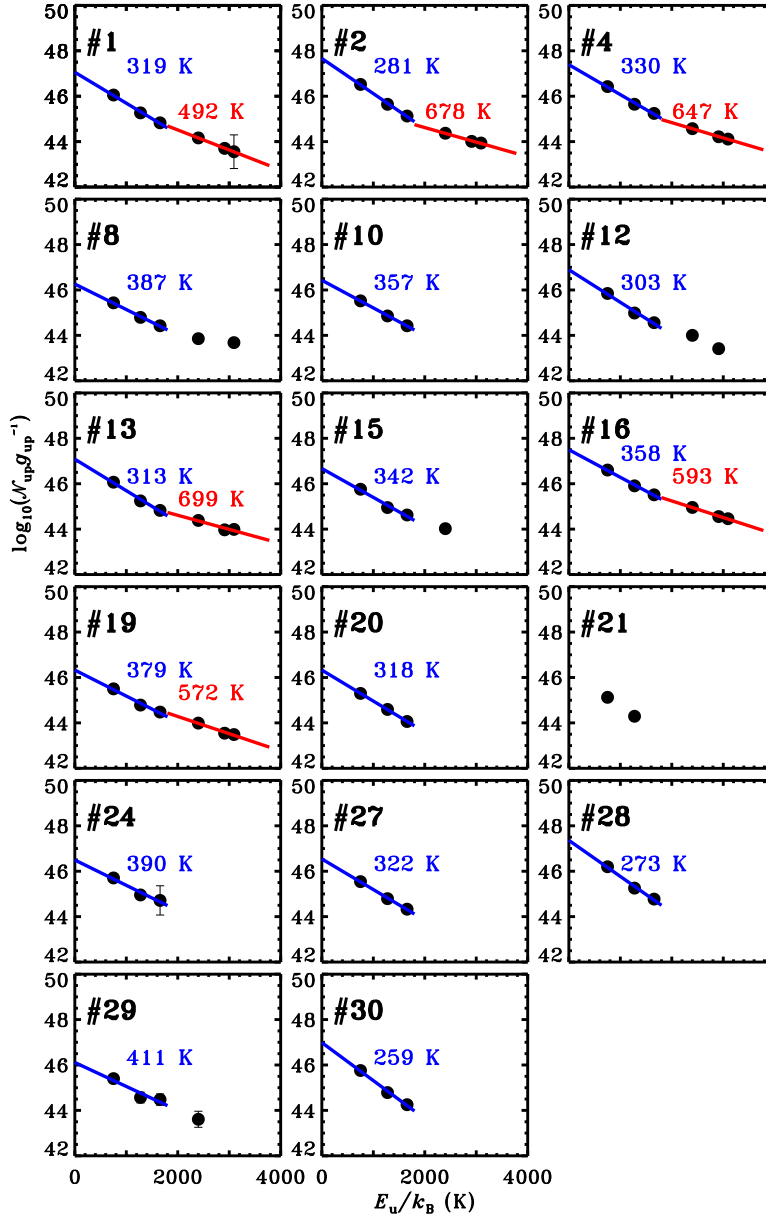
Figure 5.C.1 – Rotational diagrams of CO for Perseus sources not included in Karska et al. (2013) and Green et al. (2013). The base-10 logarithm of the number of emitting molecules from a level u, $\mathcal{N}_u$, divided by the degeneracy of the level, g_u, is shown as a function of energy of the upper level in kelvins, E_{up}. Blue and red solid lines show linear fits to the data and the corresponding rotational temperatures, when at least 3 lines are detected.
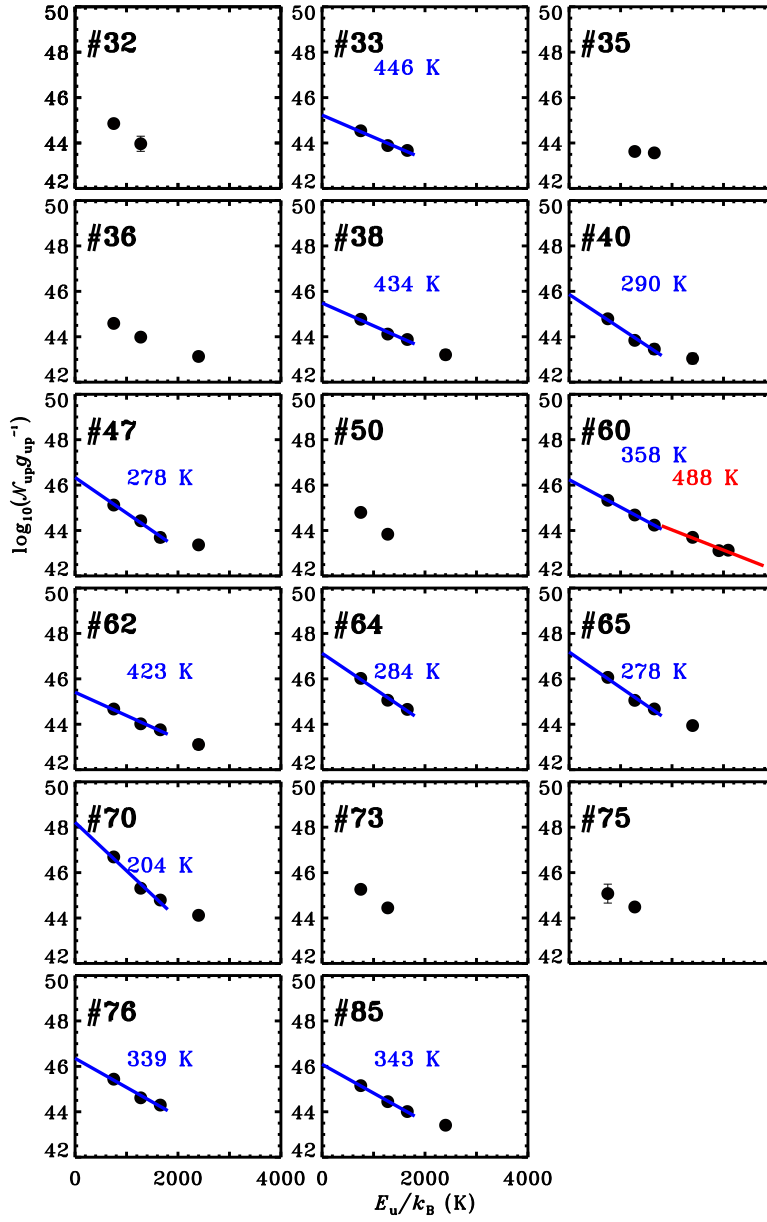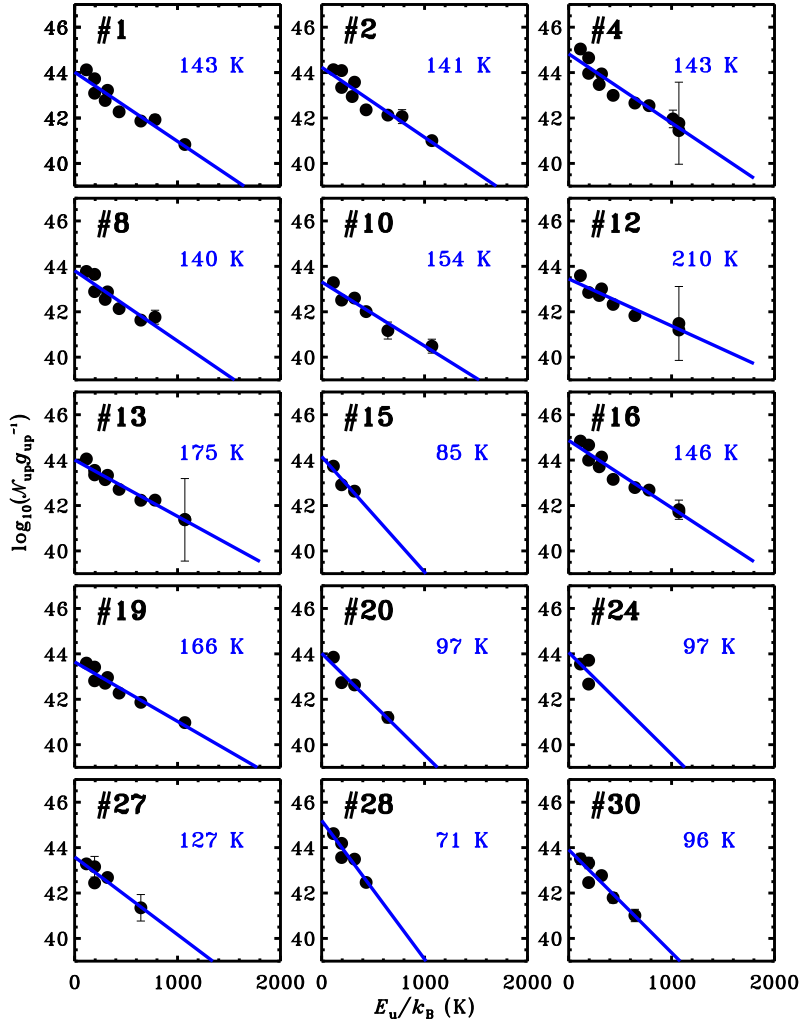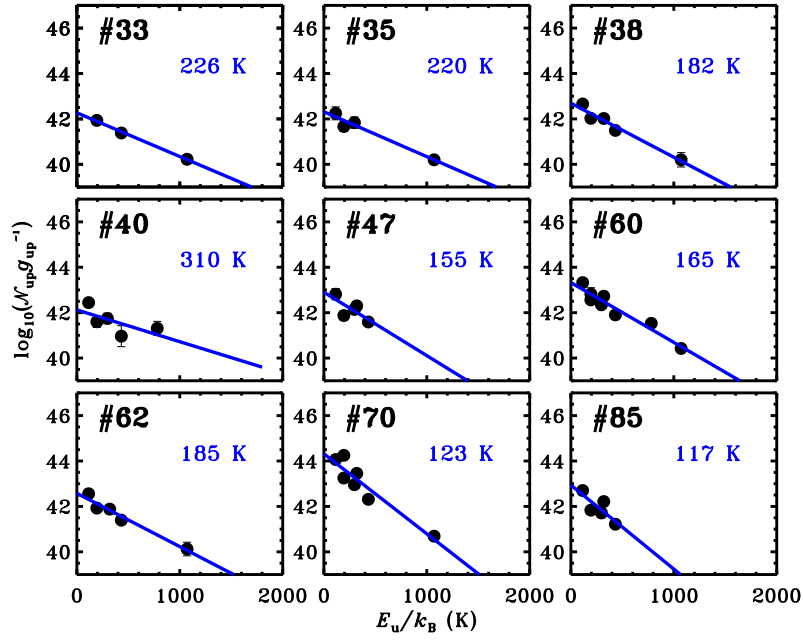
Figure 5.C.2 – The same as Figure 5.C.1, but for the remaining sources from the WILL program.

Figure 5.C.3 – Rotational diagrams of H_2O for Perseus sources not included in Karska et al. (2013) and Green et al. (2013).

Figure 5.C.4 – The same as Figure 5.C.3, but for the remaining sources from the WILL program.

Nederlandse samenvatting

De terugkoppeling van protosterren op hun omgeving.
Een onderzoek naar heet moleculair gas met *Herschel*

Stervorming

Het ontstaan van ons eigen zonnestelsel kan worden bestudeerd door waarnemingen te doen naar vormende protosterren in ons sterrenstelsel. Voor een beter begrip van ons eigen bestaan volgen we met name de evolutie van protosterren die uiteindelijk op onze zon zullen lijken (i.e. sterren met een massa M ~0.08–1.5 M$_\odot$, met M$_\odot$ de massa van de zon ~2×10^{33} gram). Sterren met een lage massa (zoals de zon) domineren stervorming, zowel qua totale massa als qua aantal. De weinige sterren met een hoge massa ($M \gtrsim 8$ M$_\odot$) hebben echter een groot effect op de vorming van de lichtere sterren, doordat ze sterke straling en winden veroorzaken, en daarnaast zware elementen in het interstellaire medium (ISM) injecteren.

Figuur 1 illustreert de belangrijkste fasen in het ontstaan van een lichte ster. Wanneer een dichte kern ineenstort onder zijn eigen zwaartekracht, leidt dat tot de vorming van een jonge stellaire kern die materie aan blijft trekken van het omhullende gas. Een deel van de materie wordt verdreven door bipolaire straalstromen die eerst gecollimeerd zijn (Klasse 0) maar later wijder worden (Klasse I). De ultraviolette (UV) straling van de groeiende ster dringt steeds dieper door in het omhullende gas. Tegelijkertijd is er minder materie dat door de straalstroom kan worden weggeblazen, omdat er minder materie door de ster wordt aangetrokken. Dit proces gaat door totdat de straalstroom helemaal verdwijnt. Wanneer het omhullende gas weg is (Klasse II), wordt de jonge hoofdreeksster met circumstellaire schijf zichtbaar. Het stof in de schijf klontert samen tot steeds grotere deeltjes, die uiteindelijk planetesimalen en planeten vormen (Klasse III). Het gas van de schijf komt deels terecht in grote gasplaneten, en wordt deels weggeblazen door de wind en de straling van de ster.

Doel van dit project

Uit het hierboven beschreven scenario blijkt dat protosterren een destructief effect hebben op de moleculaire wolken waaruit ze geboren worden. Terwijl de protoster groeit, verwarmt ze het ineenstortende omhullende gas, en stoot tegelijkertijd materie uit dat in de donkere wolk terecht komt. De ultraviolette straling kan deels ontsnappen door de
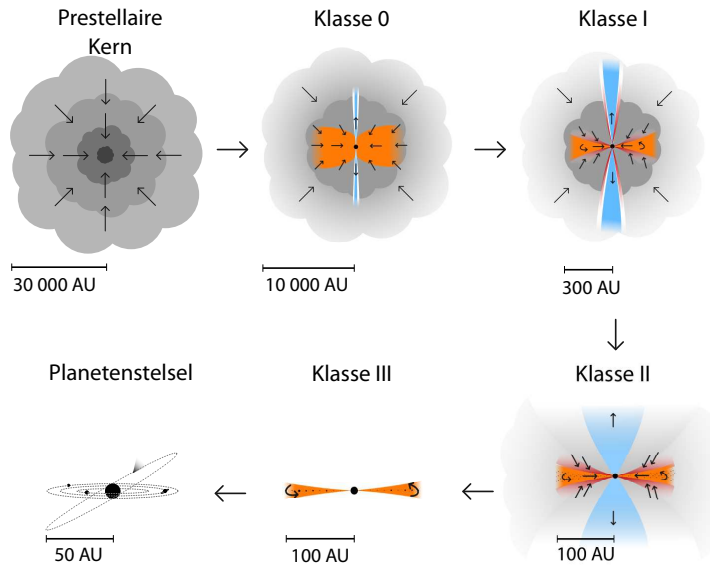
Figuur 5.5 – Schematische weergave van een protoster die uiteindelijk een ster wordt zoals onze zon. De schaal wordt aangegeven voor elke evolutionaire stap, waarbij 1 Astronomical Unit (AU) de afstand is tussen aarde en zon, 1 AU = 1.5×10^8 km. Overgenomen uit Persson (2013).

gaten die de straalstroom gemaakt heeft, en deels het gas verwarmen en de moleculen vernietigen. Het karakteriseren van deze processen is een belangrijke stap in het begrijpen waarom stervorming zo'n inefficient proces is, en welke materialen aanwezig zijn voor planeetvorming.

In dit proefschrift wordt geanalyseerd wat voor 'stempel' deze fysische processen achterlaten op het gas. Dit wordt gedaan met infrarood spectroscopie van het allernieuwste state-of-the art *Photodetector Array Camera and Spectrometer* (PACS) instrument aan boord van de *Herschel Space Observatory*. PACS is een uniek instrument dat deze hoog-energetische processen kan waarnemen met een ongeëvenaarde gevoeligheid en spatiële resolutie, en daardoor de omgeving van de protoster kan bekijken die in optisch licht niet zichtbaar is. In het bijzonder kunnen watermoleculen waargenomen worden met PACS, iets wat niet mogelijk is vanaf de aarde. Juist deze watermoleculen kunnen een unieke karakterisatie geven van warm gas en de energetische processen die plaatsvinden tijdens stervorming. Ook spelen ze een actieve rol in de koeling van het gas. Door de ver-infrarode emissielijnen te interpreteren kunnen we bepalen onder welke condities de protosterren vormen, maar er ook achter komen welke rol schokken en UV-straling spelen in dit proces.
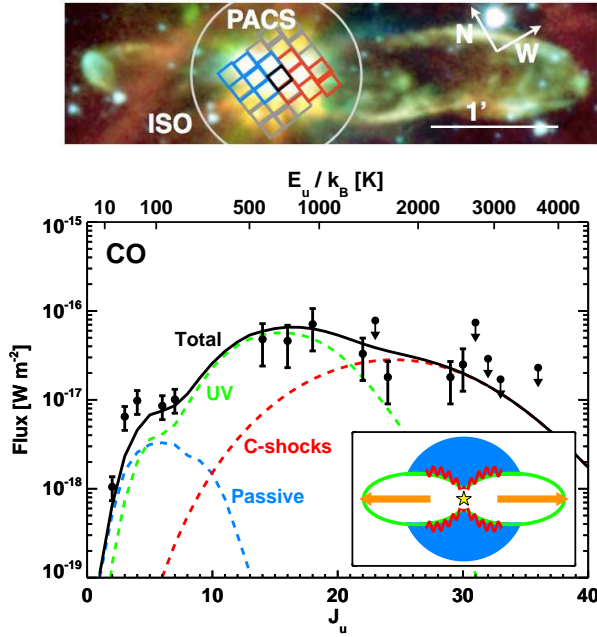
Figuur 5.6 – Boven: Moleculaire straalstroom van de Klasse I protoster HH 46. Het waargenomen gezichtsveld door *Herschel* / PACS en zijn voorganger ISO / LWS is aangegeven. De gekleurde blokjes zijn pixels van de PACS detector, waarbij rood de straalstroom detecteert die van ons weg beweegt, en blauw waar die naar ons toe beweegt. Onder: De helderheid van de CO lijnen waargenomen met Herschel/PACS en de APEX telescoop ($J_u < 10$), samen met voorspellingen van modellen van het gasomhulsel (blauw), de uitholling die de straalstroom gemaakt heeft in het gas verhit door ultraviolet fotonen (groen), en schokken op kleine schaal in de uitholling (rood). De zwarte lijn is de som van de drie. Een tekening van de verschillende componenten is rechts onder in de ingevoegde figuur gegeven. Overgenomen uit van Kempen et al. (2010b).

Herschel / PACS

Het eerste instrument dat het volledige ver-infrarode spectrum van een protoster heeft waar genomen is de Long-Wavelength-Spectrometer (LWS) aan boord van de *Infrared Space Observatory* (ISO). De telescoop had een vrij kleine diameter van 0.6 meter, waarmee groottes van $\gtrsim 20,000$ AU (1 AU = 1.5×10^8 km is de gemiddelde afstand tussen de aarde en de zon) bestudeerd kunnen worden in nabije protosterren. Daardoor vielen zowel het omhullende gas als de straalstroom op 1 enkele pixel (zie figuur 2), en was niet duidelijk waar het licht, dat was waargenomen met LWS, vandaan kwam.

Herschel / PACS, operationeel tussen halverwege 2009 en halverwege 2013, verbeterde de spatiële resolutie met een factor 8, en kon daardoor het uitgestraalde licht van ~2,000 AU rond nabije protosterren onderscheiden van de rest van het gezichtsveld (zie Figuur 2 voor een vergelijking tussen ISO en PACS). Door de combinatie van de reso-

lutie met de verbeterde gevoeligheid van PACS en astrochemische modellen, kunnen we de herkomst van de ver-infrarode straling bepalen, en daarmee de fysische processen die plaatsvinden tijdens de eerste fasen van de stervorming.

Figuur 2 is een voorbeeld van zo'n analyse, waarbij het opwarmen van omhullend gas, UV fotonen van de protoster, en schokken de koolmonoxide (CO) emissie van een Klasse I protoster verklaren. De modellen die voor deze analyse gebruikt worden geven echter geen unieke verklaring: de CO emissie kan ook gemodelleerd worden met een combinatie van schokken. Er moeten dus beperkingen aan het model toegevoegd worden door tegelijkertijd licht van alle atomen en moleculen te analyseren die in het ver-infrarood stralen – zoals water damp (H_2O), hydroxide (OH) en atomair zuurstof (O). Om erachter te komen welke fysische processen de vorming van protosterren domineren, moet onderzoek gedaan worden naar protosterren in verschillende fasen van hun ontwikkeling, met verschillende massa's en in verschillende omgevingen.

Dit proefschrift

Dit proefschrift behandelt de herkomst en evolutie van Klasse 0/I protosterren met een lage en hoge massa met ver-infrarode straling. Dit is gedaan met behulp van *Herschel* / PACS. Ver-infrarode straling is alomtegenwoordig in stervormingsgebieden (Hoofdstuk 2-5). In 80% van de lage massa protosterren worden CO, H_2O en OH lijnen waargenomen. 40% van deze objecten is ook zichtbaar in lijnen van hoog geëxciteerde toestanden van CO en H_2O (Hoofdstuk 5). Het stralingsgebied heeft een grootte van $\sim$1000 AU, hoewel een aantal objecten straling over $\sim$10, 000 AU vertoont in de richting van de CO straalstroom. Emissie van atomair zuurstof komt ook meestal op deze grote schalen voor.

Van lage massa protosterren nemen we CO excitatie waar met excitatietemperaturen van $\sim$320 K en $\sim$690 K (Hoofdstuk 2, 5). Wanneer protosterren met een grote verscheidenheid in massa wordt bestudeerd, blijkt dat ze allemaal gas van $\sim$300 K bevatten (Hoofdstuk 3). Ondanks de gelijkenissen in de CO emissie tussen protosterren met kleine en grote massa, is er een groot verschil tussen beide: het omhullende gas van een zware ster draagt 10 keer zoveel bij aan de totale emissie, dan het omhullende gas van een lichte ster (Hoofdstuk 3).

De verhouding tussen koeling door moleculen en koeling door atomen hangt sterker af van de leeftijd van de protoster dan van zijn massa. Daar staat tegenover dat de verhouding tussen koeling van het gas en de helderheid van de protoster maar een factor 4 kleiner wordt bij de overgang van Klasse 0 naar Klasse I (zie Figuur 3), terwijl het meer dan een factor 20 verschilt tussen protosterren met een lage en hoge massa (Hoofdstuk 2,3).

Schokken zijn de belangrijkste bron van heet ($T \gtrsim 300$ K) en dicht ($n \sim 10^6$ cm^{-3}) gas in de lage massa protosterren (Hoofdstuk 2, 4, 5). Niet-dissociatieve schokken produceren het overgrote deel van de waargenomen moleculaire lijnen, maar dissociatieve schokken zijn nodig om zowel de O en OH lijnen te verklaren, als ook de hoge excitatie van CO en H_2O (Hoofdstuk 4, 5). De huidige modellen van schokken zijn nog niet geheel correct. In een volgende generatie modellen zou UV straling, dat tijdens de schok ontstaat, ook geïmplementeerd moeten worden (Hoofdstuk 4, 5). Het gaat om UV velden van 10-100

218
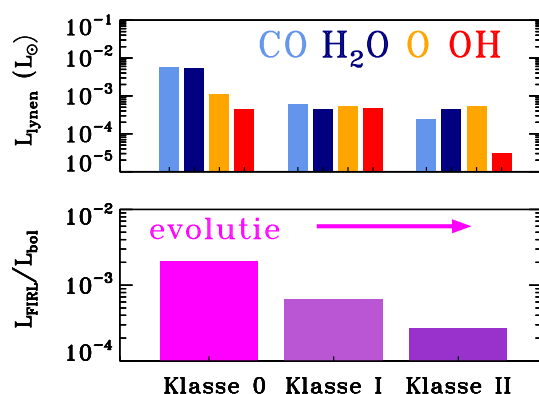
Figuur 5.7 – Boven: Gaskoeling in de lijnen van koolmonooxide (CO), water (H_2O), hydroxide (OH), en atomair zuurstof (O) voor Klasse 0, I en II protosterren. Onder: Evolutie in de hoeveelheid koeling in alle ver-infrarood lijnen ten opzichte van de helderheid van de bron.

keer het gemiddelde interstellaire stralingsveld (Hoofdstuk 5).

De toekomst

Het German Receiver for Astronomy at Terahertz-Frequencies (GREAT) instrument aan boord van de Stratospheric Observatory for Infrared Astronomy (SOFIA) kan spectra meten in het ver-infrarood met hoge spectrale resolutie, die een aanvulling zijn op de *Herschel* / PACS waarnemingen. In het komende jaar zijn waarnemingen van atomair zuurstof mogelijk, met ongeëvenaarde spectrale resolutie van 1 km s^{-1}, waarmee we kunnen bepalen hoeveel de straalstroom en het UV bijdragen aan de atomaire emissie tijdens de evolutie van de protoster.

Met sub-millimeter waarnemingen met de Atacama Large Millimeter/submillimeter Array (ALMA) zullen we nog meer inzicht krijgen in de effecten van jonge stellaire objecten op hun omgeving. De emissie van CO isotopologen op een schaal van ~100 AU zal de rol van UV straling duidelijk maken, terwijl SiO waarnemingen de sterkste schokken karakteriseren die ontstaan door interactie van de straalstroom met het omhullende gas en stof.

De spectrale kaarten met een resolutie van 0.4-0.8" van het Mid-Infrared Instrument (MIRI) op de James Webb Space Telescope (geplande lancering eind 2018), maken het mogelijk om heet gas rondom protosterren te bestuderen in het mid-infrarood (5-28 μm) op dezelfde ruimtelijke schaal als ALMA.

Hoewel de *Herschel* niet langer operationeel is, bevat het archief nog veel waarnemingen die niet geanalyseerd zijn. In het bijzonder de waarnemingen van nabije protosterren in moleculaire wolken, zullen bijdragen aan modellen van stervorming, evolutie, en het effect op de omgeving.

Streszczenie w języku polskim

Procesy oddziaływania protogwiazd na otoczenie.
Przeglądy gorącego gazu molekularnego przy pomocy *Herschela*

Powstawanie gwiazd

Odpowiedzi na pytanie, jak powstał nasz Układ Słoneczny, można poszukiwać poprzez obserwacje protogwiazd położonych w Drodze Mlecznej. Badanie protogwiazd, które w przyszłości staną się gwiazdami podobnymi do Słońca (tzn. utworzą małomasywne gwiazdy o masach M z zakresu $\sim 0,08$–$1,5\,M_\odot$, gdzie $M_\odot$ to masa Słońca równa $\sim 2 \times 10^{33}$ gramów), jest kluczowe do zrozumienia naszego własnego pochodzenia. Małomasywne gwiazdy są najbardziej liczne w galaktykach a ich sumaryczna masa przewyższa masę nielicznych masywnych gwiazd. Mimo to, badania masywnych gwiazd ($M \gtrsim 8\,M_\odot$) są również niezwykle istotne, ponieważ gwiazdy te w istotny sposób wpływają na obszary formujące mniej masywne gwiazdy poprzez silne promieniowanie, wiatry gwiazdowe oraz wzbogacanie ośrodka w ciężkie pierwiastki.

Rysunek 1 przedstawia kluczowe fazy ewolucji protogwiazd o małych masach. Grawitacyjny kolaps najgęstszych obszarów obłoków molekularnych powoduje powstanie centralnego jądra gwiazdowego. Jego masa rośnie w wyniku akrecji materii z otoczki wokół protogwiazdy. Część tej materii jest wyrzucana w postaci symetrycznych dżetów tworzących wypływy molekularne, początkowo o bardzo małym kącie rozwarcia (Klasa 0), który rośnie na późniejszych etapach ewolucji (Klasa I). Promieniowanie ultrafioletowe (UV) z tworzącej się gwiazdy dociera do coraz bardziej zewnętrznych warstw otoczki, w miarę jak jej masa zmniejsza się pod wpływem akrecji, a część jest rozpraszana przez dżety. Dżety z czasem wyprowadzają coraz mniej materii z powodu spadającego tempa akrecji i ostatecznie ich działalność ustaje. W momencie, gdy znika otoczka (Klasa II), w świetle widzialnym zaczyna być widoczna gwiazda centralna przed ciągiem głównym, otoczona przez dysk wokółgwiazdowy. Gaz z tego dysku zostaje uwięziony w gazowych olbrzymach, czyli planetach takich jak Jowisz czy Saturn, lub rozproszony przez silny wiatr gwiazdowy i promieniowanie. W tym samym czasie następuje zlepianie się pyłu w coraz większe struktury, tworząc w efekcie planetozymale oraz planety skaliste takie jak Ziemia (Klasa III).

221
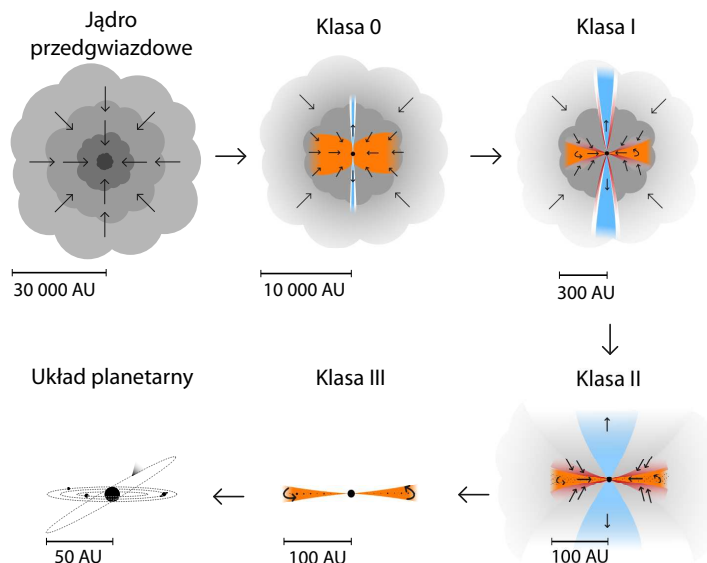
Rysunek 5.8 – Schemat ewolucji protogwiazd, które w przyszłości utworzą gwiazdy podobne do naszego Słońca. Każdy obrazek ma przypisane typowe rozmiary przestrzenne, przy czym 1 jednostka astronomiczna (AU) odpowiada odległości Ziemia-Słońce i wynosi 1 AU = $1,5 \times 10^8$ km. Na podstawie Persson (2013).

Główne cele pracy doktorskiej

Z przedstawionego scenariusza jasno wynika, że młode protogwiazdy gwałtownie oddziaływują na macierzyste obłoki molekularne. Gdy protogwiazdy zwiększają swoją masę, ogrzewają kurczącą się otoczkę i jednocześnie wyrzucają dżety gazu, które uderzają w otaczające je ciemne obłoki materii. W tym samym czasie promieniowanie ultrafioletowe przedostaje się do opróżnionej przez dżet wnęki wypływów molekularnych i dysocjuje oraz ogrzewa gaz. Dokładne scharakteryzowanie tego typu oddziaływań jest kluczowe do wyjaśnienia bardzo niskiej obserwowanej efektywności procesu formowania gwiazd oraz chemicznego przetwarzania materiału, który stanie się budulcem układu planetarnego.

Praca doktorska przedstawia analizę procesów fizycznych w otoczeniu młodych protogwiazd, które odzwierciedlają się w emisji gazu molekularnego w dalekiej podczerwieni. Obserwacje pochodzą z instrumentu PACS (ang. Photodetector Array Camera and Spectrometer) na *Kosmicznym Teleskopie Herschela*. Spektrofotometr PACS umożliwia badania i obrazowanie — z dotychczas najwyższą czułością i rozdzielczością przestrzenną — procesów energetycznych w pobliżu protogwiazd, które to procesy są całkowicie niewidoczne w świetle optycznym. Pozwala, między innymi, na obserwacje molekuł wody, które wskazują na obecność ciepłego gazu oraz procesów energetycznych zachodzących
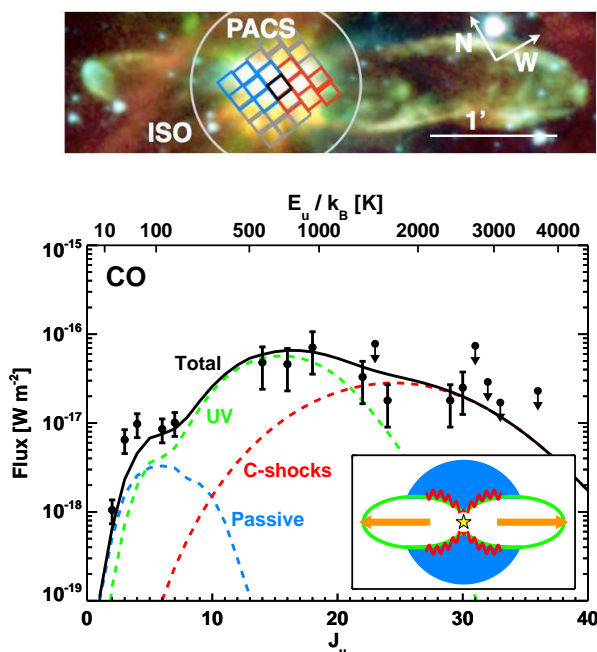
Rysunek 5.9 – Góra: Wypływ molekularny z HH 46, protogwiazdy Klasy I. Naniesione jest również pole widzenia PACSa na *Herschelu* oraz jego poprzednika, instrumentu LWS na ISO. Kolorowe kwadraty pokazują piksele detektora PACS, które obserwują część wypływu oddalającego się od nas (czerwone) oraz zbliżającego się do nas (niebieskie). Dół: Strumienie linii CO obserwowane przy pomocy PACSa na *Herschelu* oraz teleskopu submilimetrowego APEX (przejścia oznaczone jako $J_u < 10$) oraz model teoretyczny uwzględniający grzanie przez kolapsującą otoczkę (na niebiesko), ogrzewanie wnęk obłoków molekularnych przez promieniowanie UV (zielone), oraz lokalne szoki wzdłuż wnęk (czerwone). Czarna linia jest sumą tych trzech składników, które dodatkowo zobrazowane są na małej wstawce. Na podstawie van Kempen et al. (2010b).

podczas formowania się gwiazd, a także odgrywają ważną rolę w procesie chłodzenia gazu. Interpretacja pochodzenia linii emisyjnych w dalekiej podczerwieni pozwala na określenie warunków fizycznych gazu oraz roli szoków i promieniownia UV podczas 'przedszkolnych lat' protogwiazd o małych i dużych masach.

Herschel / **PACS**

Kompletne widmo protogwiazdy w podczerwieni zostało po raz pierwszy otrzymane przy pomocy Spektrometru Długich Fali (ang. Long-Wavelength Spectrometer, LWS) działającego na *Kosmicznym Obserwatorium Podczerwonym* (ang. *Infrared Space Observatory*, ISO). Teleskop miał średnicę 0, 6 m, co umożliwiało obserwacje najbliższych protogwiazd z rozdzielczością przestrzenną $\gtrsim$20 000 AU (1 AU = 1.5×10^8 km, odpo-

wiada odległości Ziemia-Słońce). W rezultacie, zarówno otoczka jak i wypływy molekularne przypadały na jeden piksel (zobacz Rysunek 2) i jednoznaczne określenie pochodzenia emisji podczerwonej było niemożliwe.

Instrument PACS działający na *Herschelu* od połowy 2009 do połowy 2013 roku umożliwił ośmiokrotne zwiększenie rozdzielności przestrzennej, aż do wielkości przestrzennych rzędu ~2 000 AU (porównanie pola widzenia ISO oraz PACSa pokazane jest na Rysunku 2). W połączeniu z większą czułością PACSa oraz nowymi modelami astrochemicznymi, możliwe stało się identyfikowanie źródeł emisji w dalekiej podczerwieni i tym samym opis procesów fizycznych mających miejsce podczas najwcześniejszych etapów formowania się gwiazd.

Rysunek 2 pokazuje przykład takiej analizy, gdzie grzanie gazu przez otoczkę, fotony UV z protogwiazdy oraz szoki zostało wymodelowane tak, aby wyjaśnić emisję we wszystkich liniach molekuły CO obserwowanej u protogwiazdy Klasy I. Niestety, tego typu modele nie są unikatowe – emisja w CO może być odtworzona używąjąc, przykładowo, tylko różnych rodzajów szoków (bez otoczki i promieniowania UV). Z tego powodu bardzo istotna jest jednoczesna analiza emisji w podczerwieni wszystkich obserwowanych molekuł i atomów: tlenku węgla (CO), pary wodnej (H_2O), wodorotlenku (OH) i tlenu atomowego (O). Przeglądy protogwiazd na różnych etapach ewolucji, w szerokim zakresie masy i położonych w różnorodnych środowiskach, są niezbędne, aby prawidłowo zidentyfikować i wyizolować główne procesy fizyczne prowadzące do powstania gwiazd.

Wyniki

W niniejszej pracy obserwacje przy pomocy PACSa na *Herschelu* użyte są do odpowiedzi na pytania o źródło emisji podczerwonej u protogwiazd Klasy 0 i I, o małych i dużych masach. Molekularna emisja podczerwona okazuje się być powszechna w obszarach formowania gwiazd (Rozdziały 2–5). Emisja w liniach CO, H_2O oraz OH została zaobserwowana u 80% małomasywnych protogwiazd. 40% tych obiektów wykazuje ponadto emisję w wysokowzbudzeniowych liniach CO oraz H_2O (Rozdział 5). Rozkład przestrzenny emisji molekularnej jest rzędu ~1000 AU, z wyjątkiem kilku obiektów w których rozciąga się ona aż do ~10 000 AU w kierunku wypływu molekularnego obserwowanego w niskich przejściach molekuły CO. Emisja tlenu atomowego jest zwykle rozciągła i ma podobny rozkład.

Emisja w przejściach molekuły CO odpowiada temperaturom wzbudzeniowym ~320 K i ~690 K u małomasywnych protogwiazd (Rozdziały 2 i 5). Komponent o temperaturze ~300 K widoczny jest również u protogwiazd o dużych masach (Rozdział 3). Pomimo tych podobieństw, udział otoczki w grzaniu gazu i chłodzeniu przy pomocy CO w przypadku masywnych protogwiazd wzrasta dziesięciokrotnie w stosunku do obiektów o małych masach (Rozdział 3).

Status ewolucyjny ma istotny wpływ na stosunek emisji molekularnej do atomowej, zdecydowanie większy niż masa protogwiazdy. Z kolei stosunek całkowitego chłodzenia gazu do jasności obiektów zmniejsza się jedynie czterokrotnie między Klasą 0 i I
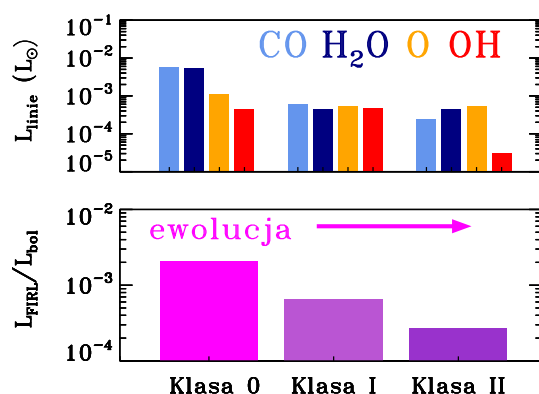
Rysunek 5.10 – Góra: Chłodzenie gazu w liniach tlenku węgla (CO), pary wodnej (H_2O), wodo-rotlenku (OH), oraz tlenu atomowego (O) dla obiektów Klasy 0, I i II. Dół: Zmiany ewolucyjne stosunku chłodzenia gazu w liniach dalekiej podczerwieni i jasności bolometrycznej (w całym zakresie widma) badanych obiektów.

(Rysunek 3) i aż dwudziestokrotnie między protogwiazdami o małych i dużych masach (Rozdziały 2 i 3).

Szoki są głównym źródłem gorącego ($T \gtrsim 300$ K) i gęstego ($n \sim 10^6$ cm^{-3}) gazu w małomasywnych protogwiazdach (Rozdziały 2, 4 i 5). Szoki, które nie powodują dysocjacji molekuł, odpowiedzialne są za większość emisji w liniach CO i H_2O, podczas gdy szoki dysocjujące są niezbędne do wyjaśnienia emisji w liniach tlenu atomowego oraz liniach OH, a także emisji w najbardziej wzbudzonych przejściach CO i H_2O (Rozdziały 4 i 5). Jednakże uwzględnienie wpływu promieniowania UV na szoki jest niezbędne do ścisłego określenia ich parametrów i musi zostać zaimplementowane w następnej generacji modeli szoków (Rozdział 4 i 5). Pole promieniowania UV w otoczeniu protogwiazd jest około 10–100 razy większe niż średnie międzygwiazdowe pole promieniowania (Rozdział 5).

Plany na przyszłość

Widma w dalekiej podczerwieni o większej rozdzielczości widmowej niż PACS mogą być otrzymywane przez Niemiecki Instrument na Częstościach Terahercowych (ang. The German REceiver for Astronomy at Terahertz Frequencies, GREAT), działający na Stratosferycznym Obserwatorium dla Astronomii Podczerwonej (ang. Stratospheric Observatory for Infrared Astronomy, SOFIA). W szczególności, w ciągu najbliższego roku wykonywane będą po raz pierwszy obserwacje tlenu atomowego z największą dotychczas rozdzielczością rzędu 1 km s^{-1}, co pozwoli na określenie stosunku emisji powodowanej przez dżety oraz promieniowanie UV od protogwiazd o różnym stopniu zaawansowania ewolucyjnego.

Komplementarny obraz procesów fizycznych wokół protogwiazd dostarczają obser-

wacje w paśmie (sub)milimetrowym prowadzone przy pomocy Wielkiej Sieci Telesko-pów Sub/Milimetrowych na Atacamie (ang. Atacama Large Millimeter/submillimeter Array, ALMA). ALMA umożliwia obserwacje izotopologów linii CO w obszarach wielko-ści ~100 AU, co w najbliższych latach pozwoli na określenie roli promieniowania UV w obszarze formowania gwiazd o małych masach. Z kolei obserwacje w liniach SiO pomogą określić parametry silnych szoków powstających w wyniku oddziaływań otoczki i dże-tów.

Podobną rozdzielczość przestrzenną (0.4-0.8") w podczerwieni będzie oferował In-strument Podczerwony (ang. Mid-Infrared Instrument, MIRI), który znajdzie się na po-kładzie planowanego do wystrzelenia pod koniec 2018 roku *Teleskopu Kosmicznego Ja-mesa Webba* (ang. James Webb Space Telescope, JWST). Instrument dostarczy informacji o rozkładzie przestrzennym gorącego gazu i jego właściwościach ukazanych przez linie widmowe w zakresie 5-28 μm.

Pomimo zakończenia misji *Herschela* w połowie 2013 roku, ogromna ilość danych ciągle nie została jeszcze opracowana. Tymczasem kompletny przegląd protogwiazd w pobliskich obłokach molekularnych jest potrzebny do opracowania modeli teoretycznych powstawania gwiazd oraz ich ewolucji, a także wpływu protogwiazd na najbliższe oto-czenie.

Bibliography

Alves, J., Lombardi, M., & Lada, C. J. 2007, A&A, 462, L17

Anderl, S., Guillet, V., Pineau des Forêts, G., & Flower, D. R. 2013, A&A, 556, A69

André, P., Di Francesco, J., Ward-Thompson, D., et al. 2014, Protostars and Planets VI, University of Arizona Press (2014), eds. H. Beuther, R. Klessen, C. Dullemond, Th. Henning

André, P., Men'shchikov, A., Bontemps, S., et al. 2010, A&A, 518, L102

André, P., Ward-Thompson, D., & Barsony, M. 1993, ApJ, 406, 122

André, P., Ward-Thompson, D., & Barsony, M. 2000, Protostars and Planets IV, University of Arizona Press (1999), eds. V. Mannings, A. P. Boss, and S.S. Russell, 59

Arce, H. G., Borkin, M. A., Goodman, A. A., Pineda, J. E., & Halle, M. W. 2010, ApJ, 715, 1170

Arce, H. G., Shepherd, D., Gueth, F., et al. 2007, Protostars and Planets V, University of Arizona Press (2006), eds. B. Reipurth, D. Jewitt, and K. Keil, 245

Bachiller, R., Pérez Gutiérrez, M., Kumar, M. S. N., & Tafalla, M. 2001, A&A, 372, 899

Bachiller, R. & Tafalla, M. 1999, in NATO ASIC Proc. 540: The Origin of Stars and Planetary Systems, Dordrecht; Boston: Kluwer Academic Publishers, eds. C.J. Lada, N. Kylafis, 227

Bastian, N., Covey, K. R., & Meyer, M. R. 2010, ARA&A, 48, 339

Bate, M. R., Tricco, T. S., & Price, D. J. 2014, MNRAS, 437, 77

Baulch, D., Cobos, C., Cox, R., et al. 1992, J. Phys. Chem. Ref. Data, 21, 411

Benedettini, M., Busquet, G., Lefloch, B., et al. 2012, A&A, 539, L3

Bergin, E. A., Neufeld, D. A., & Melnick, G. J. 1998, ApJ, 499, 777

Bergin, E. A. & Tafalla, M. 2007, ARA&A, 45, 339

Beuther, H., Churchwell, E. B., McKee, C. F., & Tan, J. C. 2007, Protostars and Planets V, University of Arizona Press (2006), eds. B. Reipurth, D. Jewitt, and K. Keil, 165

Bjerkeli, P., Liseau, R., Larsson, B., et al. 2012, A&A, 546, A29

Bjerkeli, P., Liseau, R., Nisini, B., et al. 2011, A&A, 533, A80

Bontemps, S., Andre, P., Terebey, S., & Cabrit, S. 1996, A&A, 311, 858

Boonman, A. M. S., Doty, S. D., van Dishoeck, E. F., et al. 2003, A&A, 406, 937

Boonman, A. M. S. & van Dishoeck, E. F. 2003, A&A, 403, 1003

Brinch, C. & Hogerheijde, M. R. 2010, A&A, 523, A25

Busquet, G., Lefloch, B., Benedettini, M., et al. 2014, A&A, 561, A120

Ceccarelli, C., Boogert, A. C. A., Tielens, A. G. G. M., et al. 2002, A&A, 395, 863

Ceccarelli, C., Caux, E., Loinard, L., et al. 1999, A&A, 342, L21

Ceccarelli, C., Hollenbach, D. J., & Tielens, A. G. G. M. 1996, ApJ, 471, 400

Cernicharo, J., Goicoechea, J. R., & Caux, E. 2000, ApJ, 534, L199

Cernicharo, J., Goicoechea, J. R., Daniel, F., et al. 2006, ApJ, 649, L33

Cesaroni, R. 2005, Ap&SS, 295, 5

Chabrier, G. 2003, PASP, 115, 763

Chavarría, L., Herpin, F., Jacq, T., et al. 2010, A&A, 521, L37

Chen, H., Myers, P. C., Ladd, E. F., & Wood, D. O. S. 1995, ApJ, 445, 377

Chieze, J.-P., Pineau des Forets, G., & Flower, D. R. 1998, MNRAS, 295, 672

Clegg, P. E., Ade, P. A. R., Armand, C., et al. 1996, A&A, 315, L38

Codella, C., Ceccarelli, C., Lefloch, B., et al. 2012a, ApJ, 757, L9

Codella, C., Ceccarelli, C., Lefloch, B., et al. 2012b, ApJ, 757, L9

Codella, C., Lefloch, B., Ceccarelli, C., et al. 2010, A&A, 518, L112

Crapsi, A., van Dishoeck, E. F., Hogerheijde, M. R., Pontoppidan, K. M., & Dullemond, C. P. 2008, A&A, 486, 245

Curiel, S., Raymond, J. C., Wolfire, M., et al. 1995, ApJ, 453, 322

Curtis, E. I., Richer, J. S., Swift, J. J., & Williams, J. P. 2010, MNRAS, 408, 1516

Daniel, F., Dubernet, M.-L., & Grosjean, A. 2011, A&A, 536, A76

Davis, C. J., Scholz, P., Lucas, P., Smith, M. D., & Adamson, A. 2008, MNRAS, 387, 954

de Graauw, T., Haser, L. N., Beintema, D. A., et al. 1996, A&A, 315, L49

de Graauw, T., Helmich, F. P., Phillips, T. G., et al. 2010, A&A, 518, L6

di Francesco, J., Evans, II, N. J., Caselli, P., et al. 2007, Protostars and Planets V, University of Arizona Press (2006), eds. B. Reipurth, D. Jewitt, and K. Keil, 17

Di Francesco, J., Johnstone, D., Kirk, H., MacKenzie, T., & Ledwosinska, E. 2008, ApJS, 175, 277

Dionatos, O., Jørgensen, J. K., & Green, J. D. subm., A&A

Dionatos, O., Jørgensen, J. K., Green, J. D., et al. 2013, A&A, 558, A88

Doty, S. D. & Neufeld, D. A. 1997, ApJ, 489, 122

Draine, B. T. 1980, ApJ, 241, 1021

Draine, B. T. & McKee, C. F. 1993, ARA&A, 31, 373

Draine, B. T., Roberge, W. G., & Dalgarno, A. 1983, ApJ, 264, 485

Dunham, M. M., Evans, II, N. J., Terebey, S., Dullemond, C. P., & Young, C. H. 2010, ApJ, 710, 470

Dunham, M. M., Stutz, A. M., Allen, L. E., et al. 2014, Protostars and Planets VI, University of Arizona Press (2014), eds. H. Beuther, R. Klessen, C. Dullemond, Th. Henning

Elitzur, M. & de Jong, T. 1978, A&A, 67, 323

Elitzur, M. & Watson, W. D. 1978, A&A, 70, 443

Enoch, M. L., Evans, II, N. J., Sargent, A. I., & Glenn, J. 2009, ApJ, 692, 973

Enoch, M. L., Young, K. E., Glenn, J., et al. 2006, ApJ, 638, 293

Evans, II, N. J. 1999, ARA&A, 37, 311

Evans, II, N. J., Dunham, M. M., Jørgensen, J. K., et al. 2009, ApJS, 181, 321

Evans, II, N. J., Heiderman, A., & Vutisalchavakul, N. 2014, ApJ, 782, 114

Faure, A., Crimier, N., Ceccarelli, C., et al. 2007, A&A, 472, 1029

Fedele, D., Bruderer, S., van Dishoeck, E. F., et al. 2013, A&A, 559, A77

Fedele, D., Bruderer, S., van Dishoeck, E. F., et al. 2012, A&A, 544, L9

Fich, M., Johnstone, D., van Kempen, T. A., et al. 2010, A&A, 518, L86

Fischer, J., Luhman, M. L., Satyapal, S., et al. 1999, Ap&SS, 266, 91

Flower, D. R. & Gusdorf, A. 2009, MNRAS, 395, 234

Flower, D. R. & Pineau des Forêts, G. 2003, MNRAS, 343, 390

Flower, D. R. & Pineau des Forêts, G. 2010, MNRAS, 406, 1745

Flower, D. R. & Pineau des Forêts, G. 2012, MNRAS, 421, 2786

Flower, D. R. & Pineau des Forêts, G. 2013, MNRAS, 436, 2143

Frank, A., Ray, T. P., Cabrit, S., et al. 2014, Protostars and Planets VI, University of Arizona Press

(2014), eds. H. Beuther, R. Klessen, C. Dullemond, Th. Henning

Giannini, T., Nisini, B., & Lorenzetti, D. 2001, ApJ, 555, 40

Giannini, T., Nisini, B., Neufeld, D., et al. 2011, ApJ, 738, 80

Goicoechea, J. R. & Cernicharo, J. 2001, ApJ, 554, L213

Goicoechea, J. R., Cernicharo, J., Karska, A., et al. 2012, A&A, 548, A77

Goicoechea, J. R., Cernicharo, J., Lerate, M. R., et al. 2006, ApJ, 641, L49

Goldsmith, P. F. & Langer, W. D. 1978, ApJ, 222, 881

Goldsmith, P. F. & Langer, W. D. 1999, ApJ, 517, 209

Green, J. D., Evans, II, N. J., Jørgensen, J. K., et al. 2013, ApJ, 770, 123

Green, S., Maluendes, S., & McLean, A. D. 1993, ApJS, 85, 181

Greene, T. P., Wilking, B. A., Andre, P., Young, E. T., & Lada, C. J. 1994, ApJ, 434, 614

Griffin, M. J., Abergel, A., Abreu, A., et al. 2010, A&A, 518, L3

Gueth, F. & Guilloteau, S. 1999, A&A, 343, 571

Guillet, V., Jones, A. P., & Pineau Des Forêts, G. 2009, A&A, 497, 145

Guillet, V., Pineau Des Forêts, G., & Jones, A. P. 2007, A&A, 476, 263

Guillet, V., Pineau Des Forêts, G., & Jones, A. P. 2011, A&A, 527, A123

Gusdorf, A., Giannini, T., Flower, D. R., et al. 2011, A&A, 532, A53

Gusdorf, A., Pineau Des Forêts, G., Cabrit, S., & Flower, D. R. 2008, A&A, 490, 695

Gutermuth, R. A., Bourke, T. L., Allen, L. E., et al. 2008, ApJ, 673, L151

Gutermuth, R. A., Megeath, S. T., Myers, P. C., et al. 2009, ApJS, 184, 18

Gutermuth, R. A., Megeath, S. T., Myers, P. C., et al. 2010, ApJS, 189, 352

Harwit, M., Neufeld, D. A., Melnick, G. J., & Kaufman, M. J. 1998, ApJ, 497, L105

Hatchell, J., Fuller, G. A., & Richer, J. S. 2007a, A&A, 472, 187

Hatchell, J., Fuller, G. A., Richer, J. S., Harries, T. J., & Ladd, E. F. 2007b, A&A, 468, 1009

Hatchell, J., Terebey, S., Huard, T., et al. 2012, ApJ, 754, 104

Helmich, F. P. & van Dishoeck, E. F. 1997, A&AS, 124, 205

Herczeg, G. J., Brown, J. M., van Dishoeck, E. F., & Pontoppidan, K. M. 2011, A&A, 533, A112

Herczeg, G. J., Karska, A., Bruderer, S., et al. 2012, A&A, 540, A84

Hirano, N., Ho, P. P. T., Liu, S.-Y., et al. 2010, ApJ, 717, 58

Hirota, T., Bushimata, T., Choi, Y. K., et al. 2008, PASJ, 60, 37

Hogerheijde, M. R. & van der Tak, F. F. S. 2000, A&A, 362, 697

Hogerheijde, M. R., van Dishoeck, E. F., Blake, G. A., & van Langevelde, H. J. 1997, ApJ, 489, 293

Hollenbach, D. 1985, Icarus, 61, 36

Hollenbach, D. 1997, in IAU Symposium, Vol. 182, Herbig-Haro Flows and the Birth of Stars, ed. B. Reipurth & C. Bertout, 181–198

Hollenbach, D. & McKee, C. F. 1989, ApJ, 342, 306

Hollenbach, D. J., Chernoff, D. F., & McKee, C. F. 1989, in ESA Special Publication, Vol. 290, Infrared Spectroscopy in Astronomy, ed. E. Böhm-Vitense, 245–258

Howard, C. D., Sandell, G., Vacca, W. D., et al. 2013, ApJ, 776, 21

Jeans, J. H. 1928, Astronomy and cosmogony (Cambridge University Press)

Johnstone, D., Boonman, A. M. S., & van Dishoeck, E. F. 2003, A&A, 412, 157

Jørgensen, J. K., Bourke, T. L., Myers, P. C., et al. 2007a, ApJ, 659, 479

Jørgensen, J. K., Harvey, P. M., Evans, II, N. J., et al. 2006, ApJ, 645, 1246

Jørgensen, J. K., Johnstone, D., Kirk, H., & Myers, P. C. 2007b, ApJ, 656, 293

Jørgensen, J. K., Johnstone, D., Kirk, H., et al. 2008, ApJ, 683, 822

Jørgensen, J. K., Schöier, F. L., & van Dishoeck, E. F. 2002, A&A, 389, 908

Karska, A., Herczeg, G. J., van Dishoeck, E. F., et al. 2013, A&A, 552, A141

Karska, A., Herpin, F., Bruderer, S., et al. 2014, A&A, 562, A45

Kaufman, M. J. & Neufeld, D. A. 1996, ApJ, 456, 611

Kaufman, M. J., Wolfire, M. G., Hollenbach, D. J., & Luhman, M. L. 1999, ApJ, 527, 795

Kessler, M. F., Steinz, J. A., Anderegg, M. E., et al. 1996, A&A, 315, L27

Knee, L. B. G. & Sandell, G. 2000, A&A, 361, 671

Kristensen, L. E., Ravkilde, T. L., Field, D., Lemaire, J. L., & Pineau Des Forêts, G. 2007, A&A, 469, 561

Kristensen, L. E., van Dishoeck, E. F., Benz, A. O., et al. 2013, A&A, 557, A23

Kristensen, L. E., van Dishoeck, E. F., Bergin, E. A., et al. 2012, A&A, 542, A8

Kristensen, L. E., van Dishoeck, E. F., Tafalla, M., et al. 2011, A&A, 531, L1

Kristensen, L. E., Visser, R., van Dishoeck, E. F., et al. 2010, A&A, 521, L30

Kroupa, P. 2002, Science, 295, 82

Krumholz, M. R. 2014, ArXiv No. 1402.0867

Krumholz, M. R., Bate, M. R., Arce, H. G., et al. 2014, Protostars and Planets VI, University of Arizona Press (2014), eds. H. Beuther, R. Klessen, C. Dullemond, Th. Henning

Kwon, W., Looney, L. W., Crutcher, R. M., & Kirk, J. M. 2006, ApJ, 653, 1358

Lada, C. J. 1999, in NATO ASIC Proc. 540: The Origin of Stars and Planetary Systems, Dordrecht; Boston: Kluwer Academic Publishers, eds. C.J. Lada, N. Kylafis, 143

Lada, C. J. & Wilking, B. A. 1984, ApJ, 287, 610

Larson, R. B. 1969, MNRAS, 145, 271

Lee, J., Lee, J.-E., Lee, S., et al. 2013, ApJS, 209, 4

Lefloch, B., Cabrit, S., Busquet, G., et al. 2012a, ApJ, 757, L25

Lefloch, B., Cabrit, S., Busquet, G., et al. 2012b, ApJ, 757, L25

Leroy, A. K., Walter, F., Brinks, E., et al. 2008, AJ, 136, 2782

Lesaffre, P., Chièze, J.-P., Cabrit, S., & Pineau des Forêts, G. 2004a, A&A, 427, 147

Lesaffre, P., Chièze, J.-P., Cabrit, S., & Pineau des Forêts, G. 2004b, A&A, 427, 157

Leurini, S., Wyrowski, F., Herpin, F., et al. 2013, A&A, 550, A10

Lindberg, J. E., Jørgensen, J. K., Green, J. D., et al. 2014, A&A, 565, A29

Lindberg, J. E., Jørgensen, J. K., Green, J. D., et al. 2013, ArXiv e-prints

Liseau, R., Justtanont, K., & Tielens, A. G. G. M. 2006, A&A, 446, 561

Liu, C.-F., Shang, H., Pyo, T.-S., et al. 2012, ApJ, 749, 62

Looney, L. W., Mundy, L. G., & Welch, W. J. 2000, ApJ, 529, 477

Manoj, P., Watson, D. M., Neufeld, D. A., et al. 2013, ApJ, 763, 83

Maret, S., Bergin, E. A., Neufeld, D. A., et al. 2009, ApJ, 698, 1244

Maret, S., Ceccarelli, C., Caux, E., Tielens, A. G. G. M., & Castets, A. 2002, A&A, 395, 573

Marseille, M. G., van der Tak, F. F. S., Herpin, F., & Jacq, T. 2010, A&A, 522, A40

Maury, A. J., André, P., Men'shchikov, A., Könyves, V., & Bontemps, S. 2011, A&A, 535, A77

McElroy, D., Walsh, C., Markwick, A. J., et al. 2013, A&A, 550, A36

Melnick, G. J., Stauffer, J. R., Ashby, M. L. N., et al. 2000, ApJ, 539, L77

Mitchell, G. F., Maillard, J.-P., Allen, M., Beer, R., & Belcourt, K. 1990, ApJ, 363, 554

Mottram, J. C., van Dishoeck, E. F., Schmalzl, M., et al. 2013, A&A, 558, A126

Müller, H. S. P., Schlöder, F., Stutzki, J., & Winnewisser, G. 2005, Journal of Molecular Structure, 742, 215

Müller, H. S. P., Thorwirth, S., Roth, D. A., & Winnewisser, G. 2001, A&A, 370, L49

Myers, P. C. & Ladd, E. F. 1993, ApJ, 413, L47

Neufeld, D. A. 2012, ApJ, 749, 125

Neufeld, D. A. & Dalgarno, A. 1989, ApJ, 344, 251

Neufeld, D. A. & Kaufman, M. J. 1993, ApJ, 418, 263

Neufeld, D. A., Nisini, B., Giannini, T., et al. 2009, ApJ, 706, 170

Nisini, B., Benedettini, M., Codella, C., et al. 2010a, A&A, 518, L120

Nisini, B., Benedettini, M., Giannini, T., et al. 1999, A&A, 350, 529

Nisini, B., Benedettini, M., Giannini, T., et al. 2000, A&A, 360, 297

Nisini, B., Caratti o Garatti, A., Giannini, T., & Lorenzetti, D. 2002a, A&A, 393, 1035

Nisini, B., Giannini, T., & Lorenzetti, D. 2002b, ApJ, 574, 246

Nisini, B., Giannini, T., Neufeld, D. A., et al. 2010b, ApJ, 724, 69

Nisini, B., Santangelo, G., Antoniucci, S., et al. 2013, A&A, 549, A16

Offner, S. S. R., Clark, P. C., Hennebelle, P., et al. 2014, Protostars and Planets VI, University of Arizona Press (2014), eds. H. Beuther, R. Klessen, C. Dullemond, Th. Henning

Ott, S. 2010, in Astronomical Society of the Pacific Conference Series, Vol. 434, Astronomical Data Analysis Software and Systems XIX, ed. Y. Mizumoto, K.-I. Morita, & M. Ohishi, 139

Padoan, P., Federrath, C., Chabrier, G., et al. 2014, Protostars and Planets VI, University of Arizona Press (2014), eds. H. Beuther, R. Klessen, C. Dullemond, Th. Henning

Panoglou, D., Cabrit, S., Pineau Des Forêts, G., et al. 2012, A&A, 538, A2

Persson, M. 2013, PhD thesis, University of Copenhagen

Peterson, D. E., Caratti o Garatti, A., Bourke, T. L., et al. 2011, ApJS, 194, 43

Pickett, H. M., Poynter, R. L., Cohen, E. A., et al. 1998, J. Quant. Spec. Radiat. Transf., 60, 883

Pilbratt, G. L., Riedinger, J. R., Passvogel, T., et al. 2010a, A&A, 518, L1

Pilbratt, G. L., Riedinger, J. R., Passvogel, T., et al. 2010b, A&A, 518, L1

Podio, L., Kamp, I., Flower, D., et al. 2012, A&A, 545, A44

Poglitsch, A., Waelkens, C., Geis, N., et al. 2010, A&A, 518, L2

Rebull, L. M., Padgett, D. L., McCabe, C.-E., et al. 2010, ApJS, 186, 259

Rebull, L. M., Stapelfeldt, K. R., Evans, II, N. J., et al. 2007, ApJS, 171, 447

Riviere-Marichalar, P., Ménard, F., Thi, W. F., et al. 2012, A&A, 538, L3

Robitaille, T. P. 2011, A&A, 536, A79

Robitaille, T. P., Whitney, B. A., Indebetouw, R., & Wood, K. 2007, ApJS, 169, 328

Robitaille, T. P., Whitney, B. A., Indebetouw, R., Wood, K., & Denzmore, P. 2006, ApJS, 167, 256

Rosenthal, D., Bertoldi, F., & Drapatz, S. 2000, A&A, 356, 705

Rosolowsky, E. 2005, PASP, 117, 1403

Sales, L. V., Marinacci, F., Springel, V., & Petkova, M. 2014, MNRAS, 439, 2990

San José-García, I., Mottram, J. C., Kristensen, L. E., et al. 2013, A&A, 553, A125

Santangelo, G., Nisini, B., Antoniucci, S., et al. 2013, A&A, 557, A22

Santangelo, G., Nisini, B., Codella, C., et al. 2014, ArXiv No. 1406.6302

Santangelo, G., Nisini, B., Giannini, T., et al. 2012, A&A, 538, A45

Schöier, F. L., van der Tak, F. F. S., van Dishoeck, E. F., & Black, J. H. 2005, A&A, 432, 369

Sempere, M. J., Cernicharo, J., Lefloch, B., González-Alfonso, E., & Leeks, S. 2000, ApJ, 530, L123

Shirley, Y. L., Evans, II, N. J., Rawlings, J. M. C., & Gregersen, E. M. 2000, ApJS, 131, 249

Shu, F. H., Adams, F. C., & Lizano, S. 1987, ARA&A, 25, 23

Skrutskie, M. F., Cutri, R. M., Stiening, R., et al. 2006, AJ, 131, 1163

Snell, R. L., Hollenbach, D., Howe, J. E., et al. 2005, ApJ, 620, 758

Solomon, P. M., Rivolo, A. R., Barrett, J., & Yahil, A. 1987, ApJ, 319, 730

Spaans, M., Hogerheijde, M. R., Mundy, L. G., & van Dishoeck, E. F. 1995, ApJ, 455, L167

Sturm, E., Lutz, D., Verma, A., et al. 2002, A&A, 393, 821

Suutarinen, A. N., Kristensen, L. E., Mottram, J. C., Fraser, H. J., & van Dishoeck, E. F. 2014, MNRAS, 440, 1844

Tafalla, M., Liseau, R., Nisini, B., et al. 2013, ArXiv e-prints

Takahashi, T., Silk, J., & Hollenbach, D. J. 1983, ApJ, 275, 145

Tennyson, J. 2005, Astronomical spectroscopy : an introduction to the atomic and molecular physics of astronomical spectra (World Scientific Publishing Company)

Tielens, A. G. G. M. 2010, The Physics and Chemistry of the Interstellar Medium (Cambridge University Press)

Tielens, A. G. G. M. & Hollenbach, D. 1985, ApJ, 291, 722

Tobin, J. J., Hartmann, L., Chiang, H.-F., et al. 2011, ApJ, 740, 45

Valenti, J. A., Johns-Krull, C. M., & Linsky, J. L. 2000, ApJS, 129, 399

van der Marel, N., Kristensen, L. E., Visser, R., et al. 2013, A&A, 556, A76

van der Tak, F. F. S., Black, J. H., Schöier, F. L., Jansen, D. J., & van Dishoeck, E. F. 2007, A&A, 468, 627

van der Tak, F. F. S., Chavarría, L., Herpin, F., et al. 2013, A&A, 554, A83

van der Tak, F. F. S., van Dishoeck, E. F., Evans, II, N. J., & Blake, G. A. 2000, ApJ, 537, 283

van der Wiel, M. H. D., Pagani, L., van der Tak, F. F. S., Kaźmierczak, M., & Ceccarelli, C. 2013, A&A, 553, A11

van Dishoeck, E. F. 2004, ARA&A, 42, 119

van Dishoeck, E. F., Herbst, E., & Neufeld, D. A. 2013, Chemical Reviews, 113, 9043

van Dishoeck, E. F., Kristensen, L. E., Benz, A. O., et al. 2011, PASP, 123, 138

van Dishoeck, E. F., Wright, C. M., Cernicharo, J., et al. 1998, ApJ, 502, L173

van Kempen, T. A., Green, J. D., Evans, N. J., et al. 2010a, A&A, 518, L128

van Kempen, T. A., Kristensen, L. E., Herczeg, G. J., et al. 2010b, A&A, 518, L121

van Kempen, T. A., van Dishoeck, E. F., Güsten, R., et al. 2009a, A&A, 501, 633

van Kempen, T. A., van Dishoeck, E. F., Hogerheijde, M. R., & Güsten, R. 2009b, A&A, 508, 259

van Kempen, T. A., van Dishoeck, E. F., Salter, D. M., et al. 2009c, A&A, 498, 167

Van Loo, S., Ashmore, I., Caselli, P., Falle, S. A. E. G., & Hartquist, T. W. 2013, MNRAS, 428, 381

Vasta, M., Codella, C., Lorenzani, A., et al. 2012, A&A, 537, A98

Vastel, C., Spaans, M., Ceccarelli, C., Tielens, A. G. G. M., & Caux, E. 2001, A&A, 376, 1064

Velusamy, T., Langer, W. D., & Thompson, T. 2013, ArXiv e-prints

Visser, R., Kristensen, L. E., Bruderer, S., et al. 2012, A&A, 537, A55

Vogelsberger, M., Genel, S., Springel, V., et al. 2014, Nature, 509, 177

Wagner, A. F. & Graff, M. M. 1987, ApJ, 317, 423

Walter, F. M., Herczeg, G., Brown, A., et al. 2003, AJ, 126, 3076

Wampfler, S. F., Bruderer, S., Karska, A., et al. 2013, A&A, 552, A56

Wampfler, S. F., Bruderer, S., Kristensen, L. E., et al. 2011, A&A, 531, L16

Wampfler, S. F., Herczeg, G. J., Bruderer, S., et al. 2010, A&A, 521, L36

Whitney, B., Robitaille, T., & Bjorkman, J. 2013, APJS, subm.

Wilson, T. L. & Rood, R. 1994, ARA&A, 32, 191

Wright, C. M., van Dishoeck, E. F., Black, J. H., et al. 2000, A&A, 358, 689

Wyrowski, F., Menten, K. M., Schilke, P., et al. 2006, A&A, 454, L91

Yang, B., Stancil, P. C., Balakrishnan, N., & Forrey, R. C. 2010, ApJ, 718, 1062

Yang, H., Herczeg, G. J., Linsky, J. L., et al. 2012, ApJ, 744, 121

Yıldız, U. A., Kristensen, L. E., van Dishoeck, E. F., et al. 2012, A&A, 542, A86

Yıldız, U. A., Kristensen, L. E., van Dishoeck, E. F., et al. 2013, A&A, 556, A89

Yıldız, U. A., van Dishoeck, E. F., Kristensen, L. E., et al. 2010, A&A, 521, L40

Young, C. H. & Evans, II, N. J. 2005, ApJ, 627, 293

Zinnecker, H. & Yorke, H. W. 2007, ARA&A, 45, 481

Publications

Publications in refeered journals

14. **Shockingly low water abundances in Herschel / PACS observations of low-mass protostars in Perseus**
A. Karska, L. E. Kristensen, E. F. van Dishoeck, M. N. Drozdovskaya, J. C. Mottram, G. J. Herczeg, S. Bruderer, S. Cabrit, N. J. Evans II, D. Fedele, A. Gusdorf, J. K. Jørgensen, M. J. Kaufman, G. J. Melnick, D. A. Neufeld, B. Nisini, G. Santangelo, M. Tafalla, S. F. Wampfler, 2014, accepted by Astron. Astrophys. (Chapter 4 of this thesis)

13. **Far-infrared molecular lines from low- to high-mass star forming regions observed with Herschel**
A. Karska, F. Herpin, S. Bruderer, J. R. Goicoechea, G. J. Herczeg, E. F. van Dishoeck, I. San José-García, A. Contursi, H. Feuchtgruber, D. Fedele, A. Baudry, J. Braine, L. Chavarría, J. Cernicharo, F. F. S. van der Tak, and F. Wyrowski, 2014, Astron. Astrophys., **562**, 45

12. **Water in star-forming regions with Herschel (WISH). V. The physical conditions in low-mass protostellar outflows revealed by multi-transition water observations**
J.C. Mottram, L.E. Kristensen, E.F. van Dishoeck, S. Bruderer, I. San José-García, A. Karska, R. Visser, G. Santangelo, and 12 co-authors, 2014, Astron. Astrophys., in press

11. **APEX CHAMP$^+$ high-J CO observations of low-mass young stellar objects. IV. Mechanical and radiative feedback**
U.A. Yıldız, L.E. Kristensen, E.F. van Dishoeck, T.A. van Kempen, M.R. Hogerheijde, A. Karska, and 9 co-authors, 2014, submitted to Astron. Astrophys.

10. **Herschel/DIGIT observations of warm gas associated with young stellar objects in Corona Australis**
J.E. Lindberg, J.K. Jørgensen, J.D. Green, G.J. Herczeg, O. Dionatos, N.J. Evans, A. Karska, S.F. Wampfler, 2014, Astron. Astrophys. **565**, 29

9. **High-J CO survey of low-mass protostars observed with Herschel-HIFI**
U.A. Yıldız, L.E. Kristensen, E.F. van Dishoeck, I. San Jose-Garcia, A. Karska, D. Harsono, M. Tafalla, A. Fuente, R. Visser, J.K. Jørgensen, and M.R. Hogerheijde, 2013, Astron. Astrophys., **556**, 89

8. **Embedded protostars in the dust, ice, and gas in time (DIGIT) Herschel key program: Continuum SEDs, and an inventory of characteristic far-infrared lines from PACS spectroscopy**
   J.D. Green, N.J. Evans II, J.K. Jørgensen, and 18 co-authors, including A. Karska, 2013, Astrophys. J., **770**, 123

7. **Water in star-forming regions with Herschel (WISH). III. Far-infrared cooling lines in low-mass young stellar objects**
   A. Karska, G.J. Herczeg, E.F. van Dishoeck, and 22 co-authors, 2013, Astron. Astrophys., **552**, 141

6. **OH far-infrared emission from low- and intermediate-mass protostars surveyed with Herschel-PACS**
   S.F. Wampfler, S. Bruderer, A. Karska, G.J. Herczeg, E.F. van Dishoeck, L.E. Kristensen, J.R. Goicoechea, A.O. Benz, S.D. Doty, C. McCoey, A. Baudry, T. Giannini, and B. Larsson, 2013, Astron. Astrophys., **552**, 56

5. **The complete far-infrared and submillimeter spectrum of the Class 0 protostar Serpens SMM1 obtained with Herschel. Characterizing UV-irradiated shocks heating and chemistry**
   J.R. Goicoechea, J. Cernicharo, A. Karska, E.T. Polehampton, S.F. Wampfler, L.E. Kristensen, E.F. van Dishoeck, M. Etxaluze, O. Berné, and R. Visser, 2012, Astron. Astrophys., **548**, 77

4. **Water in star-forming regions with Herschel (WISH). II. Evolution of 557 GHz $1_{10} - 1_{01}$ emission in low-mass protostars**
   L.E. Kristensen, E.F. van Dishoeck, E.A. Bergin, and 22 co-authors, including A. Karska, 2012, Astron. Astrophys., **540**, 8

3. **Water in star-forming regions with Herschel: highly excited molecular emission from the NGC 1333 IRAS 4B outflow**
   G.J. Herczeg, A. Karska, S. Bruderer, L.E. Kristensen, E.F. van Dishoeck, J.K. Jørgensen, R. Visser, S.F. Wampfler, E.A. Bergin, U.A. Yıldız, K.M. Pontoppidan, and J. Gracia-Carpio, 2012, Astron. Astrophys., **540**, 84

2. **Water in Star-forming Regions with the Herschel Space Observatory (WISH). I. Overview of Key Program and First Results**
   E.F. van Dishoeck, L.E. Kristensen, A.O. Benz, and 68 co-authors, including A. Karska, 2011, PASP **123**, 138

1. **The interface between the stellar wind and interstellar medium around R Cassiopeiae revealed by far-infrared imaging**
   T. Ueta, R.E. Stencel, I. Yamamura, K.M. Geise, A. Karska, H. Izumiura, Y. Nakada, M. Matsuura, Y. Ita, T. Tanabé, H. Fukushi, N. Matsunaga, H. Mito, and A.K. Speck, 2010, Astron. Astrophys., **514**, 16

Publication in preparation

1. **Physics of deeply-embedded low-mass protostars: evolution of shocks, ultraviolet radiation, and mass flux rates**
A. Karska, E. F. van Dishoeck, N. J. Evans II, L. E. Kristensen, J. C. Mottram, J. D. Green, G. J. Herczeg, J. K. Jørgensen, and DIGIT, WISH, and WILL teams 2014, to be submitted (Chapter 5 of this thesis)

Conference contributions

9. **High mass star formation revealed by Herschel PACS spectroscopy**
W. Kwon, F.F.S. van der Tak, A. Karska, G.J. Herczeg, J. Braine, F. Herpin, F. Wyrowski, E.F. van Dishoeck, 2013, Protostars & Planets VI

8. **Photometric observations of Epsilon Aurigae during the eclipse of 2009–2011**
K. Iłkiewicz, P. Wychudzki, C. Gałan, M. Gładkowski, A. Karska, M. Więcek, T. Tomov, M. Mikołajewski, 2013, AASP, 3, 23

7. **Herschel/PACS observations of Class 0/I low-mass young stellar objects**
A. Karska, G.J. Herczeg, E.F. van Dishoeck, L.E. Kristensen, S. Bruderer, R. Visser, S.F. Wampfler and WISH team, 2011, IAUS 280, 214

6. **Warm water in Herschel/PACS observations of NGC 1333 IRAS 4B: the outflow, not the disk!**
G.J. Herczeg, A. Karska, L.E. Kristensen, E.F. van Dishoeck et al. 2011, IAUS 280, 195

5. **V2467 Cygni as a possible intermediate polar**
E. Świerczyński, M. Mikołajewski, T. Tomov, E. Ragan, C. Gałan, A. Karska, P. Wychudzki, M. Więcek, M. Cikała, and M. Lewandowski, 2010, ASPC (eds. A. Prsa, M. Zejda) 435, 297

4. **How do we observe a birth of planetary nebula? The example of V886 Her**
A. Karska, M. Mikołajewski, 2008, YSC'15 (eds. V. Ya. Choliy, G. Ivashchenko), 17

3. **Gemini & HST observations of post-AGB objects**
A. Karska, N. Siódmiak, R. Szczerba, M. Meixner, T. Ueta, 2007, APNIV (eds. R.L.M. Corradi, A. Manchado, N. Soker), 379

2. **Optical study of V886 Her - a rapidly changing post-AGB star**
A. Karska, M. Mikołajewski, E. Ragan, E. Świerczyński, T. Brożek, A. Majcher, J.L. Janowski, M. Gromadzki, T. Tomov, I. Bellas-Velidis, A. Dapergolas, 2007, APNIV (eds. R.L.M. Corradi, A. Manchado, N. Soker), 373

1. **UBV(RI)$_C$ Photometry of the Contact W UMa Binary BD+14°5016**
A. Karska, M. Mikołajewski, G. Maciejewski, C. Gałan, and P. Ligęza, 2005, Ap&SS, 296, 309

Non-refereed publications

12. **Multicolor photometry of SU UMa and U Gem during quiescence, outburst and superoutburst**
    P. Wychudzki, M. Mikołajewski, M. Więcek, <u>A. Karska</u>, C. Gałan, E. Świerczyński, S. Frackowiak, T. Tomov, 2010, ArXiv No. 1006.2971

11. **Four unusual novae observed in Torun: V2362 Cyg, V2467 Cyg, V458 Vul, V2491 Cyg**
    E. Ragan, M. Mikołajewski, T. Tomov, and 21 co-authors, including A. Karska, 2010, ArXiv No. 1004.0420

10. **V2467 Cyg - A Nova with extremely strong O I 8446 emission**
    T. Tomov, M. Mikołajewski, E. Ragan, and 14 co-authors, including A. Karska, 2007, IBVS 5779

9. **Microlensing of GSC 3656-1328**
   M. Mikolajewski, T. Tomov, A. Niedzielski, A. Strobel, T. Brożek, K. Czart, C. Gałan, <u>A. Karska</u>, E. Świerczyński, and M. Wiecek, 2006, ATel 943

8. **GRB 060605, optical observations**
   <u>A. Karska</u>, P. Garnavich, 2006, GCN 5260

7. **GRB 060604, optical observations**
   P. Garnavich, <u>A. Karska</u>, 2006, GCN 5253

6. **CCD times of minima of some eclipsing binaries in 2003**
   G. Maciejewski and <u>A. Karska</u>, 2004, IBVS 5494

5. **Four new short-period eclipsing binary stars**
   G. Maciejewski, K. Czart, A. Niedzielski, and <u>A. Karska</u>, 2003, IBVS 5431

4. **Spectroscopic and photometric solution of the binary system BD+14°5016**
   G. Maciejewski, P. Ligęza, and <u>A. Karska</u>, 2003, IBVS 5400

3. **CCD times of minima of some eclipsing binaries in 2002**
   <u>A. Karska</u> and G. Maciejewski, 2003, IBVS 5380

2. **GSC 02757-00769 - a new EW binary system**
   G. Maciejewski, <u>A. Karska</u>, and A. Niedzielski, 2003, IBVS 5370

1. **BD+14°5016 - A new EW eclipsing binary**
   G. Maciejewski, <u>A. Karska</u>, and A. Niedzielski, 2002, IBVS 5343

Popular papers

2. **Dlaczego powinniśmy przystąpić do ESO** A. Karska, 2011, Urania-PA 6

1. **Poszukiwanie gwiazd zmiennych w Piwnicach** A. Karska, G. Maciejewski, 2003, Urania-PA 5

Curriculum vitae

My interests in astronomy began at primary school when I was first introduced to astronomy during geography lessons. A few years later I attended a summer camp organized by a Polish astronomy club 'Almukantarat', which demythologized for me the job of an astronomer and that is when – at the age of 15 – I decided to pursue this career path.

I was very lucky to have many 'hands-on' experiences with research already in my high school years. The most important was a participation in the 'Semi-Automatic Variability Search' project in Piwnice, where we surveyed the northern sky to search for new variable stars and analyzed in more detail some short-period close binary systems such as W UMa type stars. I also visited many times the Observatory at the Mount Suhora to observe and model such multiple systems. The results were presented in a series of (short) papers and some conferences and competitions for high-school students, such as 'Ogólnopolskie Młodzieżowe Seminarium Astronomiczne', 'European Union Contest for Young Scientists', and 'First Step to Nobel Prize in Physics'. All of those experiences convinced me that there is no better job for me than becoming a professional astronomer.

In 2004-2009 I studied astronomy in Toruń, the birthplace of Nicolaus Copernicus and, for good reasons, a twin city of Leiden. From very early on, all the students were encouraged to optical observations and thus during this period I focused on observations of symbiotic variable stars and novae. After my 2nd year of studies I had an opportunity to participate in a summer project at the Notre Dame University in the USA (as part of the Research Experience for Undergraduates). As part of this project I made photometric observations of white dwarfs at the Vatican Observatory on Mount Graham in Arizona. The subsequent summer, I got my first experience with infrared data at Denver University, working on the *Spitzer* images of dust shells around evolved stars. My Master thesis back in Poland focused on comparisons of infrared properties of planetary nebulae in the Milky Way and Large Magellanic Clouds using the ISO spectra, the *Spitzer* photometry and the CLOUDY photoionization code. At this point, I anticipated the amazing improvement in the data quality that will be offered by the new far-infrared telescope *Herschel* and looked for PhD projects based on those data.

I was fortunate to get a position in the group led by Ewine van Dishoeck in Leiden and Garching as part of the 'Water in star-forming regions with Herschel' (WISH) project. Since I was going to work on the data specifically from the PACS instrument, built at MPE in Garching, I was supposed to spend the first three years in Garching and then move for the final year to Leiden. My personal life led to the modification of those plans – with two small children born during the PhD and a good job of my husband at the Technische Universität in Garching, so we decided to stay in Germany until the end of my PhD.

The pace of my PhD was 'measured' by participation in the *Herschel* group meetings, including 6 WISH only team meetings (5× in Leiden, 1 in Toledo, and 1 in Ringberg), 1 DIGIT team meeting in Pasadena, and 1 joined meeting at the Lorentz Center in Lei-

den. Together with regular telecons and shorter meetings during the conferences, this has been a very tight, fruitful and inspiring collaboration. Apart from the team meetings, I presented my results at several conferences: in Garching, Ringberg, Toledo, Grenoble, and Noordwijk. I also attended two interferometry summer schools, in Grenoble and Rimini, and participated in the joint Max-Planck and Dutch observing run at the APEX telescope in Chile. I enjoyed a lot the annual Star Formation Workshop at ESO and the Leiden-Garching group retreats, and the biannual MPE / Infrared Group retreats.

From October, I will start a position in the Adam Mickiewicz University in Poznań (Poland) as an assistant professor of astrophysics and the principal investigator of the PRELUDIUM grant of the National Science Center.

Acknowledgments

Doing a PhD is a challenging experience, with long periods of 'invisible' work (not always progress..) and just a few moments of glory that we have to learn how to appreciate properly. I was very lucky to have a supportive group of collaborators and colleagues that helped me to become motivated and ambitious despite the difficulties. Certainly the biggest challenge in the last few years was not that much the science itself (I cannot complain on the quality of the *Herschel* spectra!), but the balance between the PhD workload and my growing family.

At the very beginning of my PhD I got pregnant and 9.5 months later gave birth to my son Maciej (on June 24th, 2010). It was not an easy start and I felt very insecure about the whole situation. I would not have survived this challenge, of combining a motherhood with a PhD, if not for many, many discussions with Greg, Linda, and Amelie at MPE, and Lars in Leiden. A very supportive approach of my employers, and the WISH and DIGIT teams, including the policy to secure the data for PhD students, helped enormously. A place in the institute's nursery for Maciej and additional financial support from the Max-Planck Society, the German government and the Christiane Nüsslein-Volhard-Foundation made it possible for me to continue my PhD. It also encouraged me to have a second baby, Joanna (born on May 31st, 2013), who has luckily stayed at home with my husband for the entire first year of her life (paternity leaves are fantastic!).

From the science point of view, I highly benefited from the meetings of the WISH and DIGIT teams, with their friendly atmosphere and collaborative effort to make the best possible science. Science is currently more competitive than ever but I did not feel it when interacting with my fantastic collaborators. Many people contributed to my papers and I am very indebted to all of them for all the small and big comments. In particular, I would like to thank Lars Kristensen and Gregory Herczeg, at the time post-docs in Leiden and Garching, who helped me to develop as a scientist, never stopped supporting me in the hard times and probably had the largest impact on my papers (together with 'those who only do their job' and cannot be mentioned explicitly here). I learned a lot and also enjoyed the collaboration with Simon Bruderer, Susanne Wampfler, Fabrice Herpin, Davide Fedele, Joe Mottram, Javier Goicoechea, and many many other WISH and DIGIT people. I would also like to acknowledge the support from some of the PACS team members on the corridor, in particular Albrecht Poglitsch, Eckhard Sturm, Helmut Feuchtgruber, Alessandra Contursi, and Javier Graciá Carpio.

It is always useful to chat with other PhD students suffering from the same or similar frustrations, be it science or life. In many cases the common experience leads to the life-long friendships. I owe a lot to Nienke van der Marel and Irene San José-García (my dear paranymphs!), Annemieke Jansen (thank you for translating the Dutch summary!), Daniel Harsono (so nice to wrap-up the thesis and organize the defense together!), Umut Yıldız (my HIFI and APEX expert), Heike Modest (I wouldn't make the room for children if

"We gain strength, and courage, and confidence by each experience in which we really stop to look fear in the face... we must do that which we think we cannot."

– Eleanor Roosevelt